The Dissertation Committee for Ryann Elizabeth Rupp
certifies that this is the approved version of the following dissertation:

Dynamic Normal Grain Growth in BCC Interstitial-Free Steel During Hot Deformation

Committee:

Eric M. Taleff, Supervisor

David L. Bourell

Maria C.G. Juenger

Desiderio Kovar

Carolyn C. Seepersad

Dynamic Normal Grain Growth in BCC Interstitial-Free Steel During Hot Deformation

by

Ryann Elizabeth Rupp

DISSERTATION

Presented to the Faculty of the Graduate School of

The University of Texas at Austin

in Partial Fulfillment

of the Requirements

for the Degree of

DOCTOR OF PHILOSOPHY

THE UNIVERSITY OF TEXAS AT AUSTIN

August 2018

Dedicated to my loved ones.

Acknowledgments

I am deeply grateful to so many people and organizations who helped make this research possible. I am extremely thankful to Dr. Eric Taleff. It has been an honor and privilege to be a member of his research group. I appreciate the dissemination of knowledge on research, soft-skills, and virtues. I would also like to thank my committee members, Dr. David Bourell, Dr. Maria Juenger, Dr. Desiderio Kovar, and Dr. Carolyn Seepersad, whose input has been invaluable.

I would like to take a moment to acknowledge the following people and organizations that make this research possible: Mr. Ukena whose original research in low carbon steels was the basis for this project; Mr. Thomas Cayia from Arcelor Mittal who donated the Ti-IF steel sheet material; support from the National Science Foundation, who funded this research under grant DMR-1507417 and some of the equipment under DMR-9974476; The Department of Geological Science at the University of Texas at Austin, who permitted us to use their FEI XL30 ESEM to collect EBSD data sets; and finally, Ms. Emily Brady Dukes who worked with me as an undergraduate researcher.

I am amazed by the generosity of the materials science and research community who willingly share their expertise in order to advance knowledge. I would like to specifically acknowledge Tim Ruggles and Bret Dunlap for

helping me learn OpenXY. I am also grateful to the Taleff research group, specifically Drs. Thomas Ivanoff and Philip Noell.

And finally, I would be nothing without my support system: Joseph, Mom, Dad, and sisters. Thank you so much for everything.

Dynamic Normal Grain Growth in BCC Interstitial-Free Steel During Hot Deformation

Publication No. _____

Ryann Elizabeth Rupp, Ph.D.
The University of Texas at Austin, 2018

Supervisor: Eric M. Taleff

Concurrent plastic deformation at elevated temperature can produce dynamic normal grain growth (DNGG). DNGG significantly impacts microstructure by accelerating grain growth and/or evolving texture. Both of these were observed in an interstitial-free steel deformed in uniaxial tension at 850 °C at a constant true-strain rate of 10^{-4} s^{-1}. Two complementary analysis methodologies were used to investigate DNGG and its mechanisms. The first analysis method determined the contributions from (i) lattice rotation during slip and (ii) DNGG to texture evolution during high-temperature deformation. Lattice rotation and DNGG were isolated by determining the texture of three states: (i) undeformed (recrystallized), (ii) deformed at room temperature, and (iii) deformed at high temperature. The second analysis method segmented EBSD data into individual grains, which included their sizes and orientations. This

analysis method probed the relationships between crystallographic orientation and changes in grain area fraction, number fraction, and size with strain. A statistical analysis identified the characteristics of grains that were preferred for growth in order to investigate DNGG and its mechanisms. DNGG preferentially grew grains of specific orientations at the expense of other orientations. Grains that preferentially grew by DNGG were observed to be from orientations with specific crystallographic planes parallel to the plane of the sheet material. Grains oriented with the {111}, {332}, or {322} planes parallel with the plane of the sheet material were preferred for growth. Among grains with these planes parallel to the sheet plane, a specific subset of orientations were most preferred for growth. The reference orientations most favored for growth depended on the initial recrystallized texture relative to the specimen tensile direction. Subgrains were observed to occur in grains during hot deformation and concurrently with DNGG. High-resolution EBSD (HR-EBSD) resolved subgrains and associated hot deformation substructure that is hypothesized to be important to DNGG.

Table of Contents

List of Abbreviations

BCC:	Body centered cubic
BSE:	Back-scattered-electron
CSL:	Coincidence site lattice
DAGG:	Dynamic abnormal grain growth
DNGG:	Dynamic normal grain growth
DRV:	Dynamic recovery
DRX:	Dynamic recrystallization
EBSD:	Electron backscattered diffraction
FCC:	Face centered cubic
GOS:	Grain orientation spread
HAGB:	High-angle grain boundary
HCP:	Hexagonal close packing
HEM:	Homogeneous equivalent medium
HR-EBSD:	High-resolution EBSD
IPF:	Inverse pole figure
LAGB:	Low-angle grain boundary
LC-AK:	Low-carbon, aluminum-killed
LTD:	Long transverse direction
$\boldsymbol{M}$**:**	Grain boundary mobility
$\boldsymbol{M_0}$**:**	Pre-exponential factor for mobility
MRD:	Multiples of random
N/A:	Not applicable
NaN:	Not a number
ND:	Normal direction
ODF:	Orientation distribution function
P:	Driving pressure for migration
$\boldsymbol{Q}$**:**	Activation energy
$\boldsymbol{R}$**:**	Universal gas constant
$\bar{\mathbf{r}}$**-value:**	Lankford coefficient
RD:	Rolling direction
ROD:	Reference orientation deviation
ROI:	Region of interest

RT:	Room-temperature
SAGG:	Static abnormal grain growth
STD:	Short transverse direction
SNGG:	Static normal grain growth
$\boldsymbol{T}$**:**	Absolute temperature
TD:	Tensile direction
Ti-IF:	Titanium-added interstitial-free
TLTD:	Tensile long transverse direction
$\boldsymbol{T_m}$**:**	Melting temperature
v:	Grain boundary migration rate
VPSC:	Visco-plastic self-consistent
w.r.t.:	with respect to
Z:	Zenner-Holloman parameter

Chapter 1

Introduction

1.1 Motivation

Industry uses hot and warm working for a wide range of processing, during which dynamic grain growth can occur. Dynamic grain growth is grain growth that occurs during plastic deformation. Static grain growth, by comparison, occurs during static annealing with no concurrent plastic deformation. Dynamic grain growth significantly impacts microstructure and, therefore, mechanical properties. Deformation at elevated temperature can accelerate grain growth, leading to the general observation that dynamic grain growth is faster than static grain growth. Dynamic normal grain growth (DNGG) can alter microstructure to potentially produce an improved Lankford Coefficient ($\bar{r}$-value). The Lankford coefficient is a measure of plastic anisotropy, and a higher $\bar{r}$-value results in better sheet formability [1]. Dynamic abnormal grain growth (DAGG) can create large single crystals in the solid-state, some several centimeters in length [2–6]. Despite the significant impact dynamic grain growth can have on microstructure, our understanding of dynamic grain growth is very limited [7]. An improved fundamental understanding of dynamic grain growth is expected to enable more economical tailoring of microstructure and therefore properties for specific applications. The goal of this dissertation is

to develop a fundamental understanding of the mechanisms responsible for dynamic grain growth in a body centered cubic metal.

1.2 Background

1.2.1 The nature of grain boundaries

Grains are regions in a crystal of relatively constant crystalline orientation that are bounded by grain boundaries. A grain boundary is a non-equilibrium defect that separates two grains of the same crystal structure with different orientations [8]. To unambiguously define a grain boundary in three-dimensions, eight parameters are needed to express its orientation relationship, spatial orientation, and translation vector. The orientation relationship, expressed as three angles, describes the crystallographic orientation difference between the two grains. The spatial orientation of a grain boundary is the orientation of that grain boundary plane with respect to the crystallographic orientation of one of the adjacent grains. It is usually represented by two angles. The translation vector characterizes the displacement of the two grains with respect to one another and is described by three parameters [8]. Only the five parameters related to the crystallographic and spatial orientation of the boundary are necessary to fully describe the boundary crystallography [9]. A single planar section characterized by microscopy techniques, such as electron backscatter diffraction (EBSD), provides only four of these five grain boundary parameters. The spatial orientation parameter related to the inclination angle of the grain boundary with respect to the plane inspected cannot be de-

termined without additional data. Techniques such as serial sectioning can be utilized to measure this inclination angle of the grain boundary, thus providing all five parameters necessary to fully characterize the boundary crystallography [10].

The orientation relationship between two grains can be defined by the transformation necessary to bring the crystal lattice of one grain into coincidence with the other. A convenient representation of this is a rotation about a common axis between the two grains. The rotation angle required to bring the two grains into crystallographic coincidence is called the misorientation angle, or simply the misorientation. This single measure is the first parameter typically used to understand the nature of a grain boundary. Because several different misorientation angles might bring two lattices into coincidence, it is usual to refer to the smallest angle that does so, which is termed the disorientation (angle) [8, 11].

Grain boundaries can be separated into three distinct classifications: low-angle, high-angle, and 'special' high-angle. Low-angle grain boundaries (LAGBs) have a misorientation of less than 10 to 15° and are composed of dislocation networks. Their structure and properties depend on the boundary misorientation. High-angle grain boundaries (HAGBs) have a misorientation larger than than 10 to 15°. A high-angle boundary appears as approximately a plane of random atomic arrangement. The structure and properties of HAGBs are generally independent of misorientation, with the exception of 'special' high-angle boundaries. 'Special' high-angle boundaries have atomic

sites within the grain boundary that coincide with a lattice site for both of the adjacent grains. These atomic sites are known as coincidence sites. These coincidence sites, as in the adjacent grains, are periodic and form a lattice known as the coincidence site lattice (CSL). A CSL boundary is denoted as a Σx boundary where x equals the ratio of total lattice sites to coincident sites in the boundary. A smaller Σ value correlates to a more ordered grain boundary. Nearly all of the atomic sites in a low-angle boundary are in coincidence, aside from the dislocation cores. As a result, low-angle boundaries are often described as $\Sigma 1$ boundaries [7, 8].

1.2.2 The characteristics of grain growth

Grain growth occurs by the migration of grain boundaries to lower the total free energy of the microstructure. A grain grows at the expense of its neighbors. Grain growth occurs by the creation and destruction of lattice sites at the boundary between the growing and shrinking grains, respectively. The grain boundary migration rate, v, is typically assumed to be the product of the grain boundary mobility, M, and the driving pressure for migration, P, such that [7, 8],

$$v = M \cdot P. \tag{1.1}$$

In principal, a gradient in any intensive thermodynamic property can act as a source for the driving pressure. A drop in the total free energy of the system is required for boundary migration. Typically, the driving pressure does not depend on temperature. It has units of energy per unit volume.

Sources for driving pressures that are applicable to this work are listed in Table 1.1 [8].

Table 1.1: Driving pressures for grain boundary migration, modified from Gottstein and Shvindlerman [8]

Source	Equation	Approximate value of parameters	Estimated driving pressure, MPa
Stored deformation energy	$P = \frac{1}{2}\rho\mu b^2$	ρ = dislocation density $\sim 10^{15}/\text{m}^2$ $\frac{\mu b^2}{2}$ = dislocation energy $\sim 10^{-8}$ J/m	10
Grain boundary energy	$P = \frac{2\gamma}{R}$	γ = grain boundary energy ~ 0.5 J/m^2 R = grain boundary radius of curvature $\sim 10^{-4}$ m	10^{-2}
Surface energy	$P = \frac{2\Delta\gamma^s}{d}$	d = sample thickness $\sim 10^{-3}$ m $\Delta\gamma^s$ = surface energy difference of two neighboring grains ~ 0.1 J/m^2	2×10^{-4}
Elastic energy	$P = \frac{\tau^2}{2}(\frac{1}{E_1} - \frac{1}{E^2})$	τ = elastic stress ~ 10 MPa E_1, E_2=elastic moduli of neighboring grains $\sim 10^5$ MPa	2.5×10^{-4}

Grain boundary mobility generally follows the Arrhenius relationship with temperature,

$$M = M_0 \exp\left(\frac{-Q}{RT}\right), \tag{1.2}$$

where M_0 is the pre-exponential factor, R is the universal gas constant, T is the absolute temperature, and Q is the associated activation energy [7]. The

physical process of grain boundary migration is highly dependent upon temperature, boundary forces, and boundary structure [7]. Alloy composition, impurities, second phases, and defects strongly affect grain boundary mobility [7, 8]. Our knowledge of the physical processes involved in grain boundary migration is extremely limited [8]. A general discussion on the theories associated with grain boundary mobility is provided in the following paragraphs.

As mentioned earlier, the structure and energy of LAGBs are dependent upon misorientation. Therefore, the boundary mobility of LAGBs is also expected to be sensitive to misorientation. Theories that agree with experimental research predict three mobility regimes for LAGBs. The first regime is when the boundary misorientation is less than a degree, which includes special symmetrical tilt boundaries under stress [7]. The dominant mechanism in this regime is the climb of dislocations. An increase in misorientation decreases the spacing between boundary dislocations, resulting in reduced mobility. Therefore, in this region boundary mobility is inversely related to misorientation. A different mechanism dominates when the boundary misorientation ranges from 5° up to the boundary structure transitions to a HAGB. This regime is likely controlled by the diffusion of atoms between dislocations. The boundary mobility in this regime is expected to be proportional to the misorientation. Between these two regions is a transition regime. The two dominant mechanisms described above compete. Consequently, a minimum in the boundary mobility exists in this transition regime [7].

Compared to a general LAGB, HAGB mobility is significantly faster.

The physical process of HAGB migration is independent of misorientation. The general mechanism is thermally-activated diffusion of atoms across the grain boundary from the shrinking grain to the growing grain. Experiments suggest, for specific cases, the occurrence of atoms migrating as clusters. These include specific boundaries identified by consideration of the activation volume and migration at high homologous temperatures [7, 8].

The dependence of HAGB mobility on boundary misorientation is related to the dependence of boundary orientation on solute segregation. Grain boundaries are defects with a free volume that is dependent upon the boundary structure. This free volume tends to attract solute atoms, leading to a solute atmosphere at the grain boundary. Special HAGBs are more structured than random HAGBs. Therefore, special HAGBs have a lower free volume. Thus, solutes are less likely to segregate to special HAGBs [7, 8].

For ultra-pure materials, special and random HAGBs have essentially the same mobility. Boundary mobility decreases by several orders of magnitude with the addition of trace amounts of solute. With increasing solute concentration, a small drop in the mobility of special HAGBs is observed, but significant reductions are observed in random HAGBs. The dependence of HAGB mobility on orientation disappears with increasing solute concentration. The mobility of grain boundaries in low-purity material is much less than in ultra-high purity material. HAGB mobility dependence on boundary misorientation because of solute segregation is limited to a very narrow solute concentration range at very low concentrations [7, 8].

The impact of solute atmospheres on grain boundary migration depends on the driving pressure, solute concentration, and temperature. For low driving pressures, the solute atmosphere moves with the boundary. This reduces the migration rate of the boundary because its velocity is controlled by the diffusion of the slowly migrating solutes. The solutes lag behind the moving boundary resulting in an asymmetric concentration profile. This lag increases with increasing boundary velocity. At a critical driving pressure and corresponding boundary velocity, the grain boundary is extricated from the solute atmosphere. The boundary then migrates as a solute-free boundary. The critical driving pressure depends on solute concentration and temperature. The critical driving pressure decreases with a decrease in the solute concentration and an increase of temperature. A transition region between a solute loaded boundary to a solute free boundary exists at intermediate boundary velocities. In this region, increasing driving pressure results in a rapid increase in velocity [7, 8].

It is apparent that even low solute concentrations have significant consequences on boundary mobility. This makes it difficult to ascertain if the innate mechanism(s) for boundary migration are captured by the mobilities determined for 'pure' materials. It is possible that for a completely pure material, grain boundary mobility is dependent upon boundary misorientation. Since special HAGBs are more structured than HAGBs, it is reasonable to expect special HAGBs to have a lower mobility in that case [7, 8].

To categorize the types of grain growth, one must answer the following:

(i) is there concurrent plastic straining during the grain growth, and (ii) which grains grow? If grain growth occurs during plastic straining, the grain growth is dynamic. Otherwise, it is static. Grain growth is normal if there is a uniform coarsening of grains, and abnormal if one or a few grains grow to become several times the size of the rest of the grains in the microstructure. This produces four distinct categories of grain growth: static normal grain growth (SNGG), static abnormal grain growth (SAGG), dynamic normal grain growth (DNGG), and dynamic abnormal grain growth (DAGG). The focus of this dissertation is on dynamic normal grain growth, but all four categories are described in the following.

1.2.3 Static abnormal grain growth (SAGG)

With additional annealing after primary recrystallization, static abnormal grain growth can occur when one or a few grains grow preferentially. These grains possess a growth advantage and grow to become several times larger than the rest of the grains. SAGG involves a change in the grain size distribution. SNGG, on the other hand, involves shifting of the same grain distribution shape to a higher grain size range [7, 12].

Like SNGG, the primary driving pressure for SAGG is grain boundary surface energy. SAGG kinetics are similar to primary recrystallization kinetics. This has resulted in this phenomenon being called secondary recrystallization. The incubation time for SAGG is the time for the preferred grain(s) to become approximately twice the size as the rest of the microstructure [7, 12].

Typically, the preferentially growing grain(s) for SAGG requires an advantage other than size for abnormal grain growth. This advantage is commonly attributed to SNGG growth inhibited by (i) inclusions or (ii) texture. Inclusions or precipitates can pin grain boundaries, resulting in the suppression of SNGG. During annealing, the inclusions may coarsen or dissolve into the microstructure. Localized destabilization of inclusions may provide the opportunity for a grain to reach the critical size for abnormal grain growth. Growth inhibited by texture is associated with a strongly textured microstructure. It is based on the premise that HAGBs have a higher mobility than LAGBs. In a strongly textured microstructure, grain growth is limited when the LAGBs between similarly oriented grains have a low mobility. However, a disparately oriented grain with primarily HAGBs in the textured microstructure may have the mobility advantage necessary to permit abnormal grain growth [7, 12].

In general, SAGG occurs more readily in thin sheet than in bulk material. Free surfaces inhibit normal grain growth through two different mechanisms. First, if the grains are approximately the same size as the sheet thickness, than the grain boundary curvature is reduced. This results in a decrease in the driving pressure compared to the bulk. Second, as a result of the surface and grain boundary tensions, thermal grooves form at the junction between the free surface and the grain boundary. Thermal grooves can pin the grain boundaries. In thin films and sheets, the dependence of surface energy on grain orientation acts as the driving pressure for SAGG. A difference of only a few percent is necessary to permit SAGG. The SAGG grain growth

rate is inversely related to the thickness of the sheet [7].

An important commercial application of SAGG is the manufacturing of silicon steel sheets for transformer cores. The <100> direction is the easiest for magnetization. Therefore during material processing, it is desired to tailor the microstructure to have a strong texture with grains oriented along the <100> parallel to the sheet rolling direction (RD). This has been accomplished by utilizing SAGG to preferentially grow grains from the {110}<001> Goss texture during the final elevated temperature heat treatment of the sheet material [7].

1.2.4 Dynamic abnormal grain growth (DAGG)

DAGG has been observed in sheet materials of commercial purity Mo, commercial purity Ta, and a Ta alloy. During displacement-controlled tensile straining of these materials at elevated temperature, flow stress approaches or reaches a steady-state stress, as expected for a polycrystalline material under creep conditions. At a critical strain, ε_c, DAGG initiates and produces a rapid drop in flow stress, as shown in Figure 1.1. This decrease in flow stress is the result of a single or a few abnormal, or DAGG, grains consuming the polycrystalline microstructure. These large DAGG grains have little resistance to creep flow, which causes the observed stress drop. The DAGG grain(s) will continue to grow until they span the entire gauge length of the specimen. This corresponds to the bottom of the stress drop; see Figure 1.1. Further straining at temperature beyond the stress minimum simply deforms the DAGG grain(s).

DAGG initiation and propagation will typically stop if straining is interrupted [2–6]. Figure 1.1 provides true stress *versus* true strain curves showing the initiation and propagation of DAGG in a commercial-purity Mo sheet material deformed at 1540 °C and 10^{-4} s^{-1} [3]. DAGG has produced single crystals several centimeters in length in Mo materials [4, 5]. It has been observed at homologous temperatures between 0.52 and 0.72 and at strain rates between 10^{-6} and 10^{-4} s^{-1} [2–6].

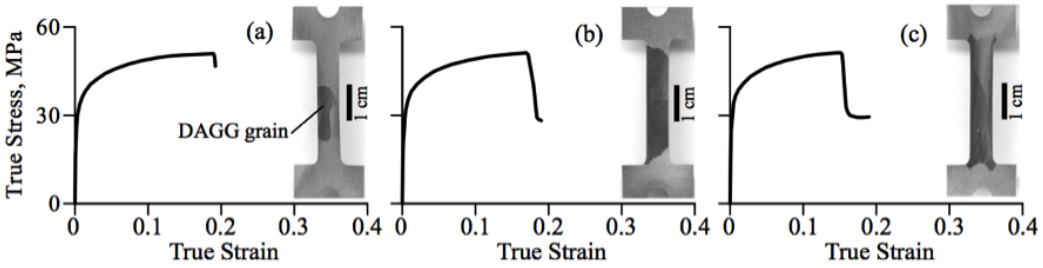

Figure 1.1: True stress versus true strain curves are shown for three different commercial purity Mo specimens. The specimens were deformed in tension to various strains, increasing from (a) to (c). The specimens were deformed at 1540 °C and 10^{-4} s^{-1}. Compiled from [3].

The following are characteristics of DAGG observed in Mo and Ta sheet materials [2–6]:

1. Above a minimum strain required to initiate DAGG, initiation is a stochastic event, the probability of which increases as the strain increases. The critical strain to initiate DAGG is largely insensitive to strain rate across the range of rates investigated to date.

2. A minimum temperature, unique to each material, is required for DAGG to initiate.

3. Grain boundary curvature provides the most important driving pressure for DAGG propagation.

4. DAGG in Mo appears from experimental data to be a direct function of plastic strain accumulation and not time.

5. DAGG grains are preferentially oriented with the <110> direction approximately parallel to the tensile direction (TD).

In general, deformation temperature has a strong effect on the critical strain; as the deformation temperature increases, the critical strain decreases [2–6]. An exception is Ta sheet material, for which no effect of temperature was observed across the range of temperatures studied, 1450 to 1850 °C. This is potentially the result of excessive normal grain growth in the Ta prior to DAGG initiation [4]. A potential for normal grain growth prior to DAGG initiation is associated with a lowering of the critical strain and with the production of multiple DAGG grains and island grains. Island grains are coarse grains that DAGG grains are unable to consume. In the Ta material, grain boundaries between DAGG grains, as well as boundaries between DAGG and island grains, were frequently observed to be special boundaries, particularly of the Σ 3 type [4, 5]. This was not observed in Mo sheet materials [5, 13]. DAGG has also been observed in commercial purity Mo wire and rod materials [3, 4, 13].

The DAGG phenomenon has likely not been observed by other investigators because of the prevalence of load-controlled testing. During load-controlled testing, the rapid drop in flow stress associated with the DAGG phenomenon would likely lead to specimen failure. This is because of the rapid strain rate acceleration required to maintain a constant load following DAGG initiation, which is easily interpreted as material failure [2]. Attempts by Groza *et al.* to observe DAGG in high-purity iron were thwarted by extensive normal grain growth [14].

1.2.5 Static and dynamic normal grain growth (SNGG and DNGG)

Because the grains that grow during normal grain growth do so at the expense of the grains consumed by growth, it is important to understand why particular grains grow and others do not. It is often observed that grains with particular crystallographic orientations are preferred for growth. Texture evolution by the selective growth of grains of preferred orientations implies that these grains possess an advantage over other grains. Three different theories regarding this advantage will be presented. These are grain growth controlled by (i) boundary character, (ii) strain accumulation, and (iii) subgrain structure.

1.2.5.1 SNGG controlled by boundary character

Grain boundary mobility has been reported to depend on the character of the grain boundary, particularly its disorientation [15]. During annealing

after cold deformation, it is theorized that the recrystallization texture is a consequence of the differences in grain boundary mobility as a function of boundary disorientation [16]. Termed growth selection or oriented growth, grain boundary mobility dependence on disorientation has been reported in face centered cubic (FCC), body centered cubic (BCC), and hexagonal close packing (HCP) metals [15, 16].

Growth-selection experiments to determine the grain boundary disorientations with the maximum mobility were performed by Lücke and associates. Lightly deformed, wire-shaped single crystals were heavily deformed at one end. These specimens were then statically annealed. During annealing, a large number of recrystallization nuclei formed at the heavily deformed end of the specimen. It was usually observed that one recrystallized grain was favored for growth over the rest. The favored grain would grow to occupy the entire cross section of the wire specimen. Typically, these favored grains possessed a very specific misorientation with respect to the original lightly deformed single crystal. This orientation relationship defines the grain boundary disorientation with the highest mobility. It should be noted that the texture of the recrystallized nuclei at the beginning of the growth process was usually close to random. For all cases, the grain orientations preferred for growth were not preferred for nucleation. These grains occurred in number fractions equal to other orientations among the initially recrystallized grains, which evidenced a random recrystallization texture [15].

Growth-selection experiments with high purity aluminum (FCC) deter-

mined that grains misoriented 40° about the common <111> axis with respect to the deformed matrix had the highest mobility. This misorientation angle is only approximate. The majority of the grain boundary misorientation angles deviated by less than 12° from 40°, and almost all of the grain boundaries were within 18° of this. The addition of 0.5 at.% Mn was observed to affect the disorientation of the grain boundary with the highest mobility. For an Al-Mn alloy, the highest mobility grain boundary was the 153°<335> boundary. The scatter about this misorientation angle was approximately 10°. Growth selection experiments for a Fe-3%Si (BCC) alloy determined that 90% of the crystals preferred for growth had a 27°<110> misorientation with respect to the deformed crystal and an 84°<110> misorientation for the remaining 10%. A scatter of approximately 10° for both of these misorientations was reported. Two grain misoreintations were reported to have the highest mobility in zinc and cadmium, both HCP metals. These two had an approximately 12° scatter about a high-index orientation not clearly defined in that study. A 30°<111> misorientation with approximately 12° of scatter was observed in silver (FCC). The silver growth selection experiments were complicated by the formation of recrystallization twins. Copper (FCC) was reported to produce results similar to silver [15].

There are several observations from these growth selection experiments that merit consideration. First, for oriented growth to be observed, the recrystallization nuclei must impinge each other to require growth competition between the nuclei. Cases of spontaneous nucleation have resulted in the for-

mation of a random texture because the distance between recrystallization nuclei was so large that the nuclei were able to grow significantly without impingement on other nuclei [17]. Second, the scatter in the angle of rotations related to the highest boundary mobility disorientation can be quite large [15, 17, 18]. The orientation of the single crystal was also observed to affect the scatter in the measured disorientation angles of the highest mobility boundary [15]. Scatter was observed to decrease with increasing deformation and wire diameter [15, 18]. However, with extremely large deformations, the highest mobility boundary disorientation was observed to change. For 80% cold-rolled aluminum, the highest mobility boundary disorientation axis shifted 5° from the <111> axis that is favored for 20 to 50% strained aluminum [15, 17, 18]. Finally, it is expected that symmetrically equivalent axes have the same mobility. Therefore, within a family, all common misorientation axes should be equally favored during growth-selection experiments. However, this logic is not met by data reported from the growth-selection experiments performed by Lücke [15, 17, 18]. Lücke reported data that contradicts this expectation for both Al and Fe-3%Si [15]. The meaning of these results, and even their correctness, is still a matter of debate.

Graham and Cahn investigated the orientation dependence of grain boundary mobility in aluminum. They observed the recrystallized grain mobility to be insensitive to boundary disorientation [19]. There are some fundamental differences between the work of Graham *et al.* [19] and Yoshida, Liebman, and Lücke [17]. Graham *et al.* utilized a uniform temperature fur-

nace, while Yoshida *et al.* employed a gradient furnace [17, 19]. The difference in heating between these two furnaces results in a dissimilarity in the recovery of the deformed single crystals, which may be important. Another difference is the amount of deformation imparted to the single crystal. Graham *et al.* imparted 10 and 15% deformation, while Yoshida *et al.* deformed the single crystals by 10, 20, 30, and 50% [17, 19]. Yoshida *et al.* note that growth selection was not observed during recrystallization of the 10% deformed single crystals, when recrystallization occurred [17]. Yoshida *et al.* speculate that impurity differences in the aluminum are likely the culprit for the contradicting results from the two bodies of work [17].

Grains in growth-selection experiments grow into a deformed matrix comprised of a single initial crystallographic orientation. However, in polycrystalline materials, the deformed matrix can consist of numerous orientations. One theory holds that a "compromise texture" will result. This implies that the resulting texture components after growth selection are not those with the highest boundary mobility with respect to one disorientation. Instead, the resulting texture consists of grains oriented to have high mobility boundaries with respect to several of the deformed matrix orientations [16, 18, 20, 21]. Beck, however, mentions that for FCC metals most of the known recrystallization textures consist of orientations that are close to the highest mobility boundary disorientation with at least one of the deformed matrix texture components [16]. Beck noted some objections to the oriented growth theory and attempted to rebut these [16, 22]. The validity of the oriented growth theory

is still a matter for debate. That debate is beyond the scope of this work. Interested readers are referred to the literature for more details on this topic [16, 22].

Several investigations were performed to examine texture evolution in low-carbon steel after hot rolling, cold rolling, and annealing [23–26]. Recrystallization during annealing after significant cold-rolling reductions was reported to strengthen the <111> parallel to the normal direction (ND) i.e. the γ-fiber and weaken the <110>||RD i.e. the α-fiber [23–26]. There is an approximate 35°<110> misorientation between the {111}<112> γ-fiber and the {112}<110> α-fiber. It was theorized that this grain boundary type has a high mobility because of its similarity to the 27°<110> misorientation observed to have the highest mobility in Fe-3%Si growth selection experiments performed by Lücke *et al.* Lücke and coworkers therefore concluded that growth selection plays a role in microstructural evolution during recrystallization [25, 26].

Lindh *et al.*, however, did not observe growth selection during the recrystallization of an interstitial-free steel. Lindh observed very similar cold-rolled and recrystallized textures to those reported by Lücke and coworkers. However, during recrystallization, consumption of the {112}<110> component was not observed to strengthen the {111}<112> texture component, but rather a slight strengthening of the {111}<110> component and the development of other minor texture components was observed. Lindh goes on to say that compromise growth models are inappropriate to explain these data [27].

1.2.5.2 DNGG controlled by strain accumulation in individual grains

Fukutomi and colleagues have reported a DNGG phenomenon that results in texture evolution during hot deformation by the selective growth of grains with a specific orientation. Labeled preferential dynamic grain growth, it was reported when deformation occurs in the solute drag creep regime. It was theorized by Fukutomi and his collaborators that the preferred grain orientation for growth is one having stability during deformation and a low Taylor factor. It was further predicted that preferential dynamic grain growth can occur independent of deformation type, alloy, and crystal structure. Fukutomi observed the preferential growth of grains with the {001} plane normal along the compression axis in Al-Mg, AA5182, Al-Cu, and Fe-3mass%Si deformed both by uniaxial and plane strain compression. Extruded AA5182 was reported to also exhibit preferential grain growth of grains with the {001} plane normal along the extrusion axis. Fukutomi *et al.* investigated Mg alloy AZ80 in uniaxial and plane-strain compression and reported increased growth of grains with the {0001} plane normal along the compression axis. Precipitates, second phases, carbides, and alloying elements beyond the two elements of binary alloys were observed to suppress preferential grain growth [28–38].

1.2.5.3 Effects from subgrains

Subgrains are regions of constant crystalline orientation within a grain that are separated by dislocation walls. The dislocation walls are low-angle boundaries, and the misorientation between neighboring subgrains can be as

low as 0.001° [39]. Figure 1.2 shows a back-scattered-electron (BSE) image of subgrains in an interstitial-free steel water-quenched following high-temperature steady-state creep deformation.

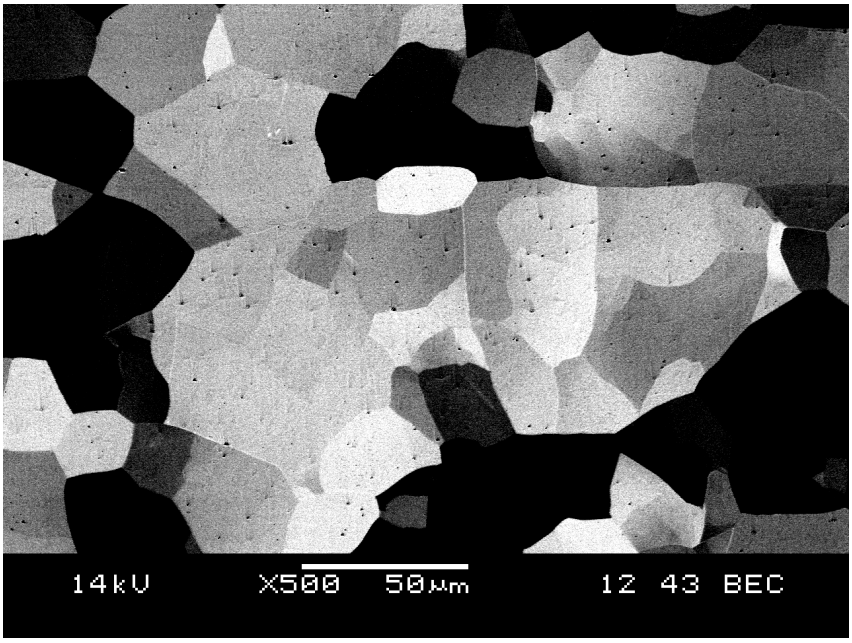

Figure 1.2: A BSE image of subgrains in an interstitial-free steel deformed at 850 °C to $\varepsilon = 0.2$ at $\dot{\varepsilon} = 10^{-4}$ s^{-1} and water-quenched.

Subgrains form during the primary stage of dislocation-climb (five-power) creep [40]. Subgrain size is inversely related to the applied stress and is independent of temperature, strain, grain size, thermal-mechanical history, and impurities during steady-state deformation [7, 39, 40]. During deformation, subgrains rearrange themselves to remain approximately equiaxed [7, 39]. The misorientation between subgrains was observed by Humphreys and Ashton to increase with strain [7].

The selective growth of grains with specific orientations at the expense of others requires that the growing grains possess an advantage of some form for growth. Driver *et al.* and Bardal *et al.* reported substructure to be strongly dependent on grain orientation in hot-deformed aluminum and its alloys [41, 42] This dependence suggests a connection between subgrains and the growth advantage for preferred orientations by two possible mechanisms: (i) stored energy or (ii) interfacial tension forces from subgrains on the grain boundary.

As mentioned previously, grain orientation was reported to impact substructure by affecting subgrain size and misorientation in hot-deformed aluminum and its alloys. This dependence was consequently reported to result in differences in the stored energy between grains with different orientations [41, 42]. Driver theorizes that this stored energy difference generates the driving pressure for grain growth of particular grains in the aluminum [41]. Such a stored energy dependence on grain orientation as a result of substructure may be the mechanism driving DNGG.

Subgrains interact with the grain boundary. During creep, wavy grain boundaries are sometimes observed. This is a result of interfacial tension from the intersecting subgrain boundaries pulling on the grain boundary [43]. This grain boundary modification may also provide the advantage required for DNGG.

The dependence of substructure on grain orientation was reported by Samajdar *et al.* to be highly dependent on Z [44]. The Z value is the Zenner-

Holloman parameter:

$$Z = \dot{\varepsilon} \exp\left(\frac{Q}{RT}\right) \tag{1.3}$$

where $\dot{\varepsilon}$ is the strain rate, Q is the activation energy, R is the universal gas constant, and T is the absolute temperature. Samajdar observed an effect of grain orientation or Taylor factor on substructure during hot deformation of an aluminum alloy at Z values of 10^{12} to 10^{13} s^{-1}. No orientation dependence on substructure was observed at lower Z values of 10^{9} to 10^{10} s^{-1} [44]. Z values of 1.31×10^{11} s^{-1} and 10^{15} s^{-1} were reported by Driver and Bardal, respectively, when substructure depended on grain orientation [41, 42].

1.2.6 IF steel

The capability to deep draw low and and extra low carbon steel makes them attractive to industry [45]. This capability depends in part upon the material's texture. The normal plastic anisotropy ratio, r, affects the relationship between the material flow for shape forming and sheet thinning. The value of r is formally defined as

$$r = \epsilon_w / \epsilon_t, \tag{1.4}$$

where ϵ_w and ϵ_t are the width and thickness strain in the sheet, respectively, after tensile deformation [46]. The planar anisotropy value Δr is defined as

$$\Delta r = \frac{r_0 + r_{90} - 2r_{45}}{2}, \tag{1.5}$$

where r_0, r_{90}, and r_{45} correspond to the r values from tensile tests at 0°, 90°, 45° within the plane of the sheet with respect to the rolling direction [46].

When planar anisotropy is present, the yield stress varies with direction within the plane of the sheet. To approximate the planar anisotropy as normal, an average value $\overline{r}$ is often defined as [46]

$$\overline{r} = \frac{r_0 + 2r_{45} + r_{90}}{4}. \tag{1.6}$$

For good deep drawability, a high $\overline{r}$ and low Δr values are desired [47]. For low carbon steels, a high $\overline{r}$ value is connected to the microstructure possessing a strong uniform {111} fiber texture along the sheet normal direction [45]. The value of $\overline{r}$ for interstitial steel typically ranges from approximately 1.5 to 2.1 [48].

Interstitial free steels have a carbon content that typically ranges from 0.002 to 0.008 wt.% [48]. The addition of titanium to low and extra low carbon steels serves to scavenge carbon and nitrogen by producing TiC and TiN particles. This results in an essentially interstitial-free microstructure [45]. As a result, Ti-IF steel remains BCC for a wide range of temperatures [49].

1.2.7 Prior work on dynamic recrystallization and normal grain growth in IF steels

IF steels have been engineered to improve deep drawability [45]. As a result there was extensive prior research focused on their microstructure and properties. A subset of this research was focused on the microstructural evolution from warm rolling in the ferritic range [50–58]. Rolling, torsion, and compression were often used to hot deform BCC interstitial-free steel and α-

iron for study. The strain rates and strains in these studies were typically much higher than those used in this dissertation. These investigations focused on whether dynamic recovery (DRV) or dynamic recrystallization (DRX) occurred as well as DRX classification. Therefore, characterization was limited to these two effects. Possible evidence of dynamic normal grain growth was not recognized [58]. The limited prior research on dynamic normal grain growth in IF steels will now be presented.

1.2.7.1 Ukena's results

Ukena reported $\overline{r}$ in low-carbon, aluminum-killed (LC-AK) steel at ambient temperature to improve with increased annealing times during a prior heat treatment. Static annealing at 800 °C for approximately 500 seconds was observed to increase $\overline{r}$ from 1.9 to 2.03. When a stress of 2 kg/mm^2 was applied in uniaxial tension during the anneal, $\overline{r}$ was found to improve faster. Annealing at 800 °C for approximately 500 seconds with an applied uniaxial stress of 2 kg/mm^2 was observed to increase $\overline{r}$ from 1.9 to 2.16 [1].

This behavior was the result of an atypical crystallographic texture evolution during annealing under a uniaxial tensile load. A strengthening of the {111}<110> texture component was observed after tensile loading while annealing but was not observed after static annealing alone [1, 59]. This is also a texture component preferred by DAGG grains in BCC refractory metals [2–6]. The plastic strain induced during loading is likely too small for lattice rotation to be solely responsible for the reported texture evolution. LC-AK

and Ti-IF steels remain BCC during the high-temperature annealing studied by Ukena because of their low interstitial element concentration [1, 59].

1.2.7.2 Noell's results

Dr. Philip Noell, as part of his dissertation research, reproduced the work of Ukena in order to (i) establish repeatability and (ii) characterize the microtexture. Ti-IF steel was hot deformed in tension at true-strain rates between 10^{-4} and 10^{-3} s^{-1} and temperatures between 0.56 to 0.64 T_m, where T_m is the melting temperature. For all tests, the tensile direction (TD) was aligned to be parallel to the final rolling direction of the sheet. The gauge and the grip regions of the tensile specimens were used to analyze the deformed and undeformed microstructures, respectively. DAGG did not occur in any of these specimens. Data suggest that at strain rates faster than 10^{-4} s^{-1}, DRX may occur, as indicated by fluctuations in the flow stress illustrated in Figure 1.3. However, metallography to confirm this suspicion of DRX was not performed [13].

High-temperature tensile deformation in Ti-IF steel at a true-strain rate of 10^{-4} s^{-1} strengthened the {111}<110> and {112}<110> texture components and weakened the {111}<112> and {554}<225> texture components [13]. This is illustrated by the {200} pole figures in Figure 1.4. A reference {200} pole figure showing important BCC texture components in presented in Figure 1.5. This is the same texture evolution reported by Ukena [1, 59]. Increasing temperature during static annealing did not have any significant af-

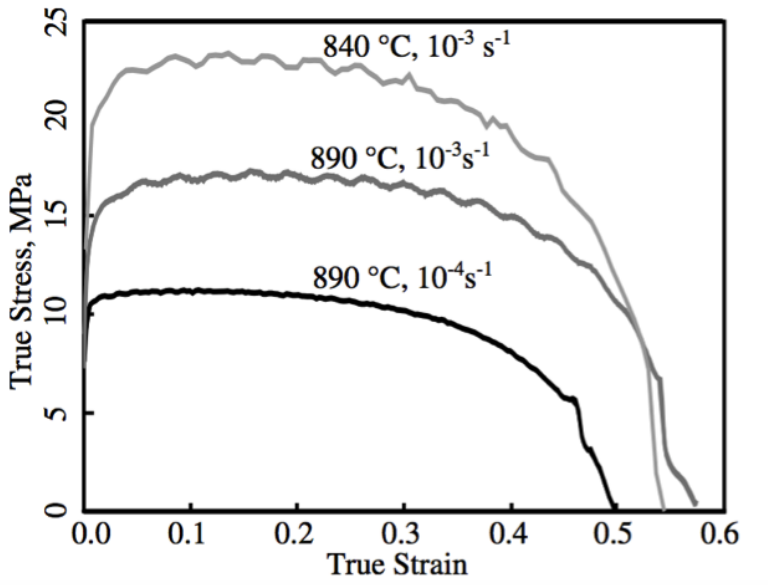

Figure 1.3: True-stress *versus* true-strain curves, calculated without accounting for necking, of Ti-IF steel specimens deformed in uniaxial tension at various temperatures and strain rates and elongated to failure. The fluctuations in the flow stress for the specimens deformed at 10^{-3} s^{-1} suggest the occurrence of dynamic recrystallization. This figure is from reference [13].

fect on texture. However, significant changes in texture were observed to occur with an increase in temperature during annealing under a tensile load. The strongest intensities observed were the {111}<110> and {112}<110> texture components for the specimen deformed at 850 °C. The {200} pole figures for these data are presented in Figure 1.6. These results suggest that DNGG caused the observed texture evolution. Dynamic grain growth occurred much more rapidly than did static grain growth. Noell theorized that the texture evolution observed is the result of dynamic normal grain growth preferentially accelerating the growth of grains with specific crystallographic orientations,

those that are also favored for DAGG [13].

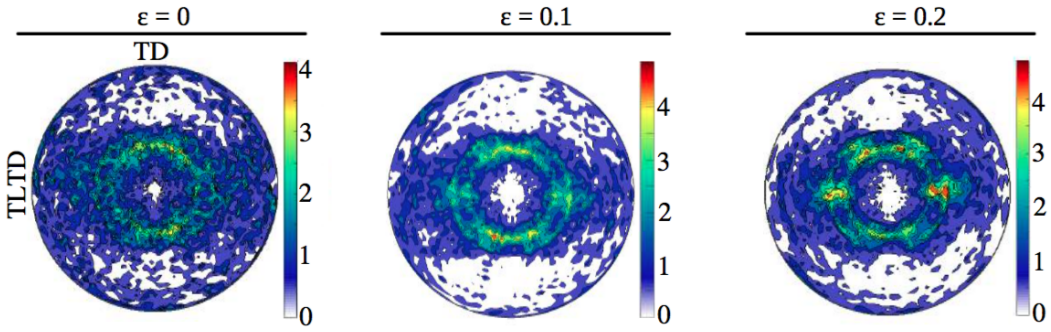

Figure 1.4: {200} pole figures for the Ti-IF steel deformed at 850 °C at $\dot{\varepsilon} = 10^{-4}$ s^{-1} to varying strains. This figure is from reference [13].

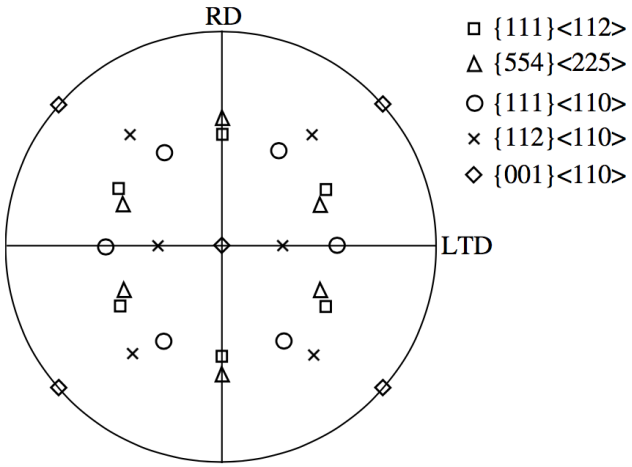

Figure 1.5: A {200} pole figure highlighting typical BCC texture components. This figure is from reference [13].

From Noell's work, it is apparent that a microstructural texture evolution occurs during high temperature tensile deformation that is not observed by static annealing alone. Two different effects may be contributing to this texture: (i) DNGG and (ii) lattice rotation. Lattice rotation is a consequence

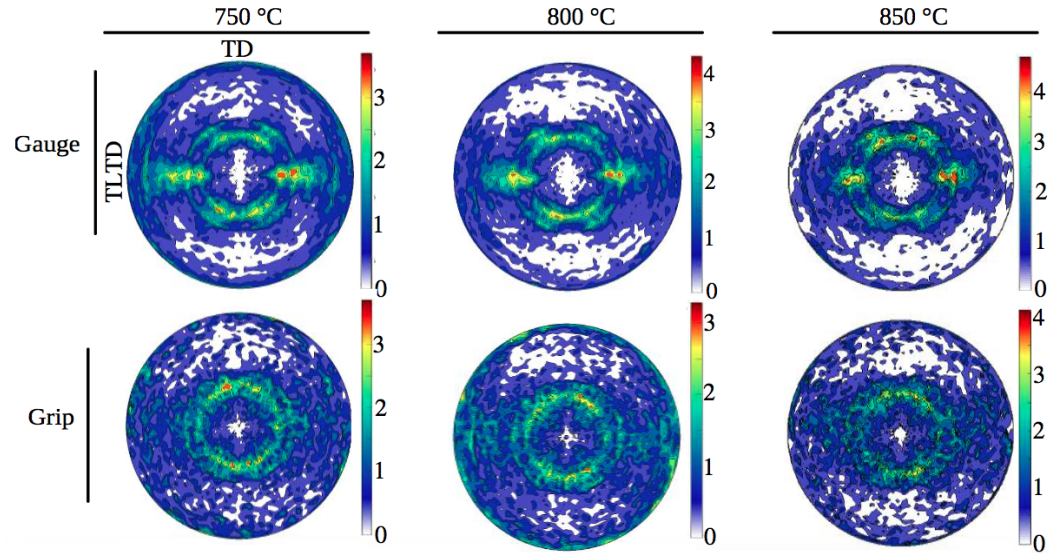

Figure 1.6: {200} pole figures for the Ti-IF steel deformed at $\dot{\varepsilon} = 10^{-4}$ s^{-1} to $\varepsilon = 0.2$ at varying strains. The deformed and undeformed macrotexture was investigated by analyzing the gauge and grip regions of the tensile specimen, respectively. The grip region represents static annealing. This figure is from reference [13].

of slip. As a specimen is deformed, individual grains gradually rotate in order to maintain compatibility [60]. Additional data and analysis are necessary to separate and isolate these individual effects on the observed texture evolution.

Chapter 2

Hypotheses

This study attempts to test the following hypotheses:

1. Dynamic normal grain growth impacts texture evolution during high temperature tensile deformation by preferentially growing grains of specific orientations at the expense of other orientations.

2. Grains that are preferred for dynamic grain growth possess an intrinsic characteristic(s) that provides a growth advantage.

The methods used to test each of these hypotheses will now be discussed.

2.1 Test methodology: hypothesis #1

To test the first hypothesis, it is necessary to identify the effects of lattice rotation from plastic straining and DNGG on texture evolution during high-temperature tensile deformation. This is achieved by first determining the texture of the recrystallized state and the textures produced by room- and high-temperature deformation. By comparing the textures of these three different states, the effects of lattice rotation and DNGG can be isolated. This methodology will provide a measurement of the contribution from DNGG to

the texture evolved during high-temperature deformation, a direct test of the first hypothesis. Furthermore, the specific texture components increased by DNGG will be identified.

The role of the initial recrystallized sheet texture on texture evolution during high-temperature tensile deformation will also be investigated. The TD is varied with respect to the RD to effectively alter the initial recrystallized texture with respect to the TD. Tensile tests include orientations with the TD at 0°, 45°, and 90° with respect to the RD. The effects of these three initial recrystallized sheet textures with respect to the TD will be evaluated.

2.2 Test methodology: hypothesis #2

Three theories are proposed here and in the literature regarding the advantage of grains favored for DNGG. These are growth controlled by (i) boundary character, (ii) strain accumulation, and (iii) subgrain structure. Individual grain characteristics will be collected from recrystallized grains and grains after high-temperature deformation. A statistical analysis will be performed to identify the characteristics of grains that are preferred as well as ill-favored for growth. These characteristics will then be compared to the boundary character and strain accumulation theories to determine if there is any correlation. High-resolution EBSD (HR-EBSD) will be used to evaluate the effects of subgrains. HR-EBSD improves the angular resolution of lattice measurements by using cross-correlation for orientation indexing rather than the Hough transformation that is utilized for standard-resolution EBSD. By

using HR-EBSD, the identification and measurement of subgrains is greatly improved. Ideally, individual subgrains can be segmented and characterized from HR-EBSD data sets to determine if they play an important role in DNGG.

Chapter 3

Experimental Procedures

3.1 Characteristics of the Ti-IF steel in this work

The Ti-IF steel used in this work was donated by I/N Tek and I/N Kote (New Carlisle, IN), a collaboration between ArcelorMittal and Nippon Steel & Sumitomo Metal Corporation. Table 3.1 is the mill composition in weight percent as reported by the manufacturer. The Ti-IF steel was rolled to a final sheet thickness of 0.69 mm.

Table 3.1: The Ti-IF steel chemical composition in weight percent as reported by the manufacturer.

Mn	Al	Ti	Cr	Cu	Ni	S
0.1319	0.065	0.0428	0.0294	0.0188	0.0185	0.0118
P	Nb	Si	Mo	As	N	C
0.0112	0.0097	0.0049	0.004	0.0034	0.00248	0.0024
Pb	Sn	V	Sb	B	Ca	Fe
0.001	0.001	0.001	0.0007	0.0001	0.0001	bal.

The final rolling direction of the sheet was noted and used as a reference direction for the sheet material. This was important for determining the alignment of the tensile specimens with respect to the sheet material. The other two sheet reference directions are the long transverse direction (LTD)

and the normal direction (ND). The LTD is in the plane of the sheet and perpendicular to the RD. The ND is normal to the sheet plane, i.e. along the thickness of the sheet.

It is desired for the Ti-IF steel material to remain BCC during elevated temperature tensile testing. BCC ferrite begins to transform into FCC austenite at a critical temperature A_{c1} for Fe-C alloys with less than 0.022 wt.% carbon. This critical temperature can be calculated in °C from the phase diagram as

$$A_{c1} = 912 - 8409.1C, \tag{3.1}$$

where, C is the wt.% of carbon in the steel [49]. Thus, for the Ti-IF steel used in this work to remain BCC, elevated temperature tensile testing up to 892 °C can be performed. This is likely an underestimation of the transformation temperature because the titanium removes almost all of the carbon from the solid solution. To verify the accuracy of these predictions and ensure that the transition to austenite did not occur, the following checks were made. One check occurred during the specimen heat-up when testing at elevated temperature. A transformation to austenite during heat-up under a constant preload would be recorded as a change in instrument displacement. Transformation from ferrite to austenite requires a length contraction of 1.2%, which would be readily measurable. Therefore, it was verified that no abnormal shifts in the instrument displacement occurred during specimen heat up. It is expected

that a transformation to austenite and back to ferrite would refine the microstructure. Therefore, for all the specimens, it was confirmed that there was not any unexpected microstructure refinement.

3.2 Mechanical test methods

3.2.1 Test specimen geometries

3.2.1.1 Annealing tests

Specimens were excised from the as-received material for annealing. The annealing specimen dimensions were approximately 25.4 mm by 25.4 mm (1 in. by 1 in.) squares with thickness the same as the as-received sheet (0.69 mm). The reference directions of these specimens are the same as those of the sheet material.

A salt pot was utilized for some of the annealing. Nickel wire was used to insert and remove the specimens from the salt pot. This required the addition of a hole punched into the corner of these specimens so that the wire could be attached.

3.2.1.2 Tensile tests

The as-received Ti-IF steel sheet material was fabricated into tensile specimens using water jet machining, which produced very minor edge rounding on the machined edge of the thin sheet. The tensile specimens were machined to have a gauge length and width of 25.4 mm and 6.44 mm, respectively. The thickness of the sheet was 0.69 mm. The filet radius between the grip and

gauge is 1.6 mm. The tensile specimens were designed to include the capability to be pin-loaded. The pin diameter is 6.35 mm (0.25 in.). Figure 3.1, below, is a schematic of the "dog-bone" geometry.

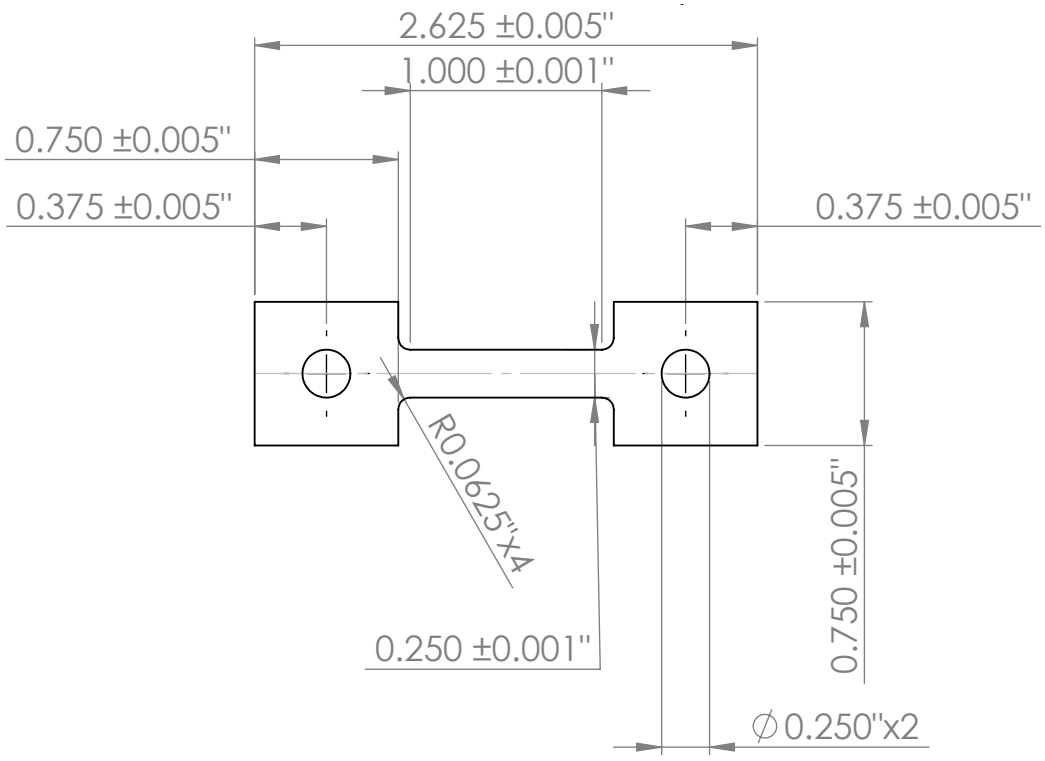

Figure 3.1: A schematic with dimensions in inches of the "dog-bone" tensile specimens used in this study.

Specimens were fabricated with the tensile direction at 0°, 45°, and 90° with respect to the final rolling direction of the sheet. Besides the tensile direction, the other reference directions are the tensile long transverse direction (TLTD) and the short transverse direction (STD). The TLTD is perpendicular to the tensile direction and is in the plane of the sheet. The STD is normal to

the plane of the sheet and is always aligned with the ND of the sheet.

3.2.2 Static annealing and recrystallization

Ti-IF steel specimens were statically annealed in a box, tube, or salt pot furnace. The annealing requirements determined which furnace type was used for a given application. Each furnace type and its applications are discussed in the following.

Box and tube furnaces were used to fully recrystallize the as-received Ti-IF steel sheet material. Recrystallization was achieved by statically annealing specimens at 850 °C for 30 minutes. To reduce oxidation during the anneal, the specimens were placed inside a stainless steel bag, sealed by folding over its open end, with Ti chips added to scavenge O_2. The annealing time was recorded from when the thermocouple attached to the stainless steel bag registered a temperature of 840 °C. Temperature was monitored throughout the anneal, and the temperature of the stainless steel bag never deviated more than $\pm$ 10 °C from the desired annealing temperature. Specimens were recrystallized in both the annealing test geometry and the tensile test geometry. The one specimen with the annealing test geometry was used to characterize the recrystallized texture. The specimens with the tensile test geometry were used for room-temperature tensile testing.

Salt pot furnaces were employed for a recrystallization study (STA-Hard 17: trade name of salt). The goal of this study was to determine the annealing time necessary to fully recrystallize the as-received Ti-IF steel sheet material.

Specimens with the annealing test geometry were annealed at 850 °C for times ranging from 4 to 1802 seconds. Short annealing times require rapid specimen heat-up, which is supplied by the salt pot furnace. The annealing time was recorded from when the specimen first contacted the molten salt. The annealing time recording was stopped at the beginning of the subsequent water-quench. Care was taken to anneal the specimens within ± 10 °C of the desired temperature. SiC paper was used to remove oxidation from the heat-treated specimens. A minimum of five Rockwell B hardness measurement were taken using a 1/16-in high-speed steel ball indenter. The minimum indention spacing guidelines for hardness measurements outlined in ASTM Standard E18-17$^{\varepsilon 1}$ were followed [61]. Specimens that significantly warped during annealing were excluded from analysis.

3.2.3 Room-temperature tensile testing

Uniaxial tensile testing in ambient air was performed on an electromechanical testing frame. The test frame was a Series 1600 Computer-Controlled Universal Testing Machine from Applied Test Systems (Butler, PA). A 3542-010M-025-HT1 extensometer from Epsilon Technology Corp (Edina, MN) was used to record the strain. The extensometer has a 10 mm gauge length with a measuring range of positive or negative 2.5 mm in tension or compression, respectively. The operable temperature range for the extensometer is -40 °C to 150 °C. The maximum excitation and sensitivity of the extensometer is 10 VDC and 1.999 mV/V, respectively.

Specimens of the as-received material were fully recrystallized prior to testing in a tube furnace. Mechanical wedge grips were used to attach the specimens to the test frame. The extensometer was attached to the specimen using rubber bands or springs. Score marks, in the gauge region on the opposite side relative to the extensometer, were used to determine the final strain.

The guidelines from ASTM standards E8/E8M-16a [62] and A370-17a [63] were generally followed when designing and implementing this test. The tension test was displacement controlled with a crosshead rate of 0.021 mm/s (0.05 in./min.). Specimens were deformed to a true strain of 0.1 or 0.2. The TD was orientated at 0°, 45°, or 90° with respect to the RD.

3.2.4 Elevated-temperature tensile testing in air

3.2.4.1 Furnace and test frame

Constant true-strain rate uniaxial tension tests were performed at elevated-temperature in air. An Applied Test Systems (Butler, PA) Series 3210 3-zone furnace was attached to a MTS Systems (Eden Prairie, MN) 810 servohydraulic test frame. The MTS TestSuite Multipurpose Elite software version 2.2.1 controlled the test frame. The servohydraulic frame is capable of switching between load and displacement control. A load cell located outside the furnace was used to monitor the force on the pull rods throughout the entirety of the test run. This test setup enabled substructure characterization by providing the ability to quench specimens upon test completion.

Pin-loaded grips were used for testing. Specimens remained inside the

furnace for the entirety of the test-run. To record the temperature during heat-up and testing, two thermocouples were inserted into the furnace. The thermocouples were on opposite sides of the sheet specimen. They were arranged so that one thermocouple was in contact with the bottom portion of the specimen gauge region and the other was near the top. During testing, the temperature remained within $\pm$ 5 °C of the desired test temperature.

3.2.4.2 Heat-up and quenching

Two different Series 3210 furnaces were used for these tests. The heat-up time necessary for the older furnace to reach the desired test temperature of 850 °C was 3 hours. This furnace was used for one test before being replaced. The replacement furnace was used for the remainder of the tests and required approximately 40 minutes to reach the 850 °C test temperature.

During heat-up, thermal expansion of the pull rods and specimen occur. In order to prevent a compressive load from being placed on the specimen, a software program continuously adjusted the axial displacement of the bottom pull rod to maintain a specified preload. This preload was set at either 10 N (2.25 lbs.) or 3.6 N (0.81 lbs.). Once the desired temperature was reached, this preloading was continued for 2 to 10 minutes. This ensured that the specimen was fully recrystallized prior to testing, according to the time for recrystallization determined by a recrystallization study.

After test completion, a quenching procedure was employed to enable quenching of the specimens in an attempt to preserve the specimen microstruc-

ture. Once the desired strain was reached during testing, the test program switched from displacement to load control. The bottom pull rod continuously adjusted itself to maintain the current load at the completion of the test on the specimen for 420 seconds. During this time, the furnace was turned off and opened. Water was then continuously sprayed onto the specimen. After the 420 seconds, the computer program reduced the load on the specimen, and the pins were removed. During this time, the specimen was continuously sprayed with water. Once the specimen was fully removed from the grips, the specimen was immersed in water.

3.2.4.3 Tensile tests in air

Uniaxial tension tests in air at 850 °C at a constant true-strain rate of 10^{-4} s^{-1} to a true strain of 0.1 or 0.2 were performed. The purpose of these tests was to produce specimens specifically for microstructural characterization by rapidly quenching to preserve microstructure from elevated-temperature deformation. The TD was oriented at 0°, 45°, and 90° with respect to the RD. A specimen was also deformed in uniaxial tension at 850 °C at a constant true-strain rate of 10^{-3} s^{-1} to a true strain of 0.2. This specimen was oriented with its TD parallel to the RD.

Prior to testing, the loading pins were coated with boron nitride in order to prevent seizing and to ease specimen removal during quenching. A specimen in the as-received condition was then pin-loaded into the grips for testing. The specimen fully recrystallized during the heat-up procedure.

A "test-run" included heat-up, the tensile test, and subsequent quenching. The entire test-run was controlled by a single computer-controlled test program using the MTS TestSuite Multipurpose Elite software. While this program went through several minor alterations, the block diagram of the ultimate version is shown in Figures 3.2 through 3.6. These figures are separated into the test-run initiation, five loops, and termination. Data acquisition occurred parallel to the five loops. The running time, the axial displacement of the bottom pull rod, and the axial force on the pull rods were recorded. Individual aspects regarding the full test run will now be discussed.

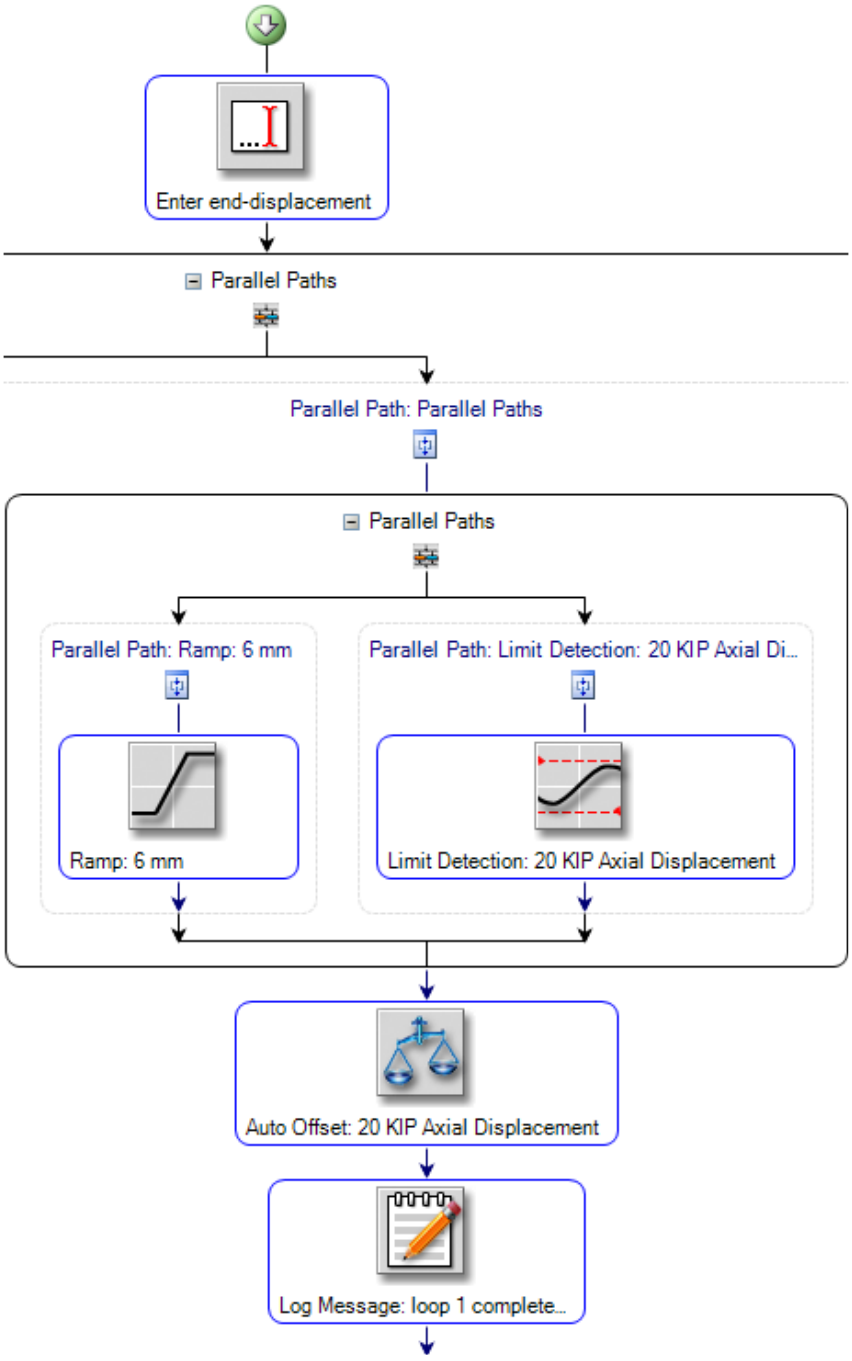

Figure 3.2: The block diagram of the initiation and Loop 1 of the test-run. The initiation controls the final strain of the tensile test. Loop 1 begins the heat-up portion of the test-run.

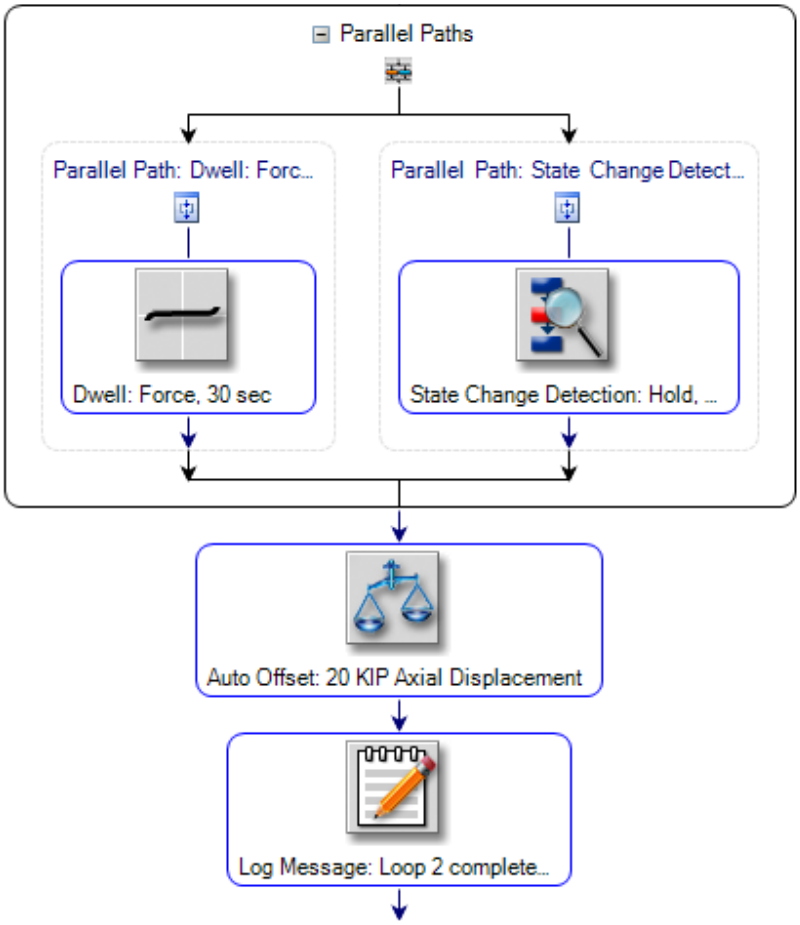

Figure 3.3: The block diagram of Loop 2 of the test-run. The completion of this loop concludes the test-run's heat-up.

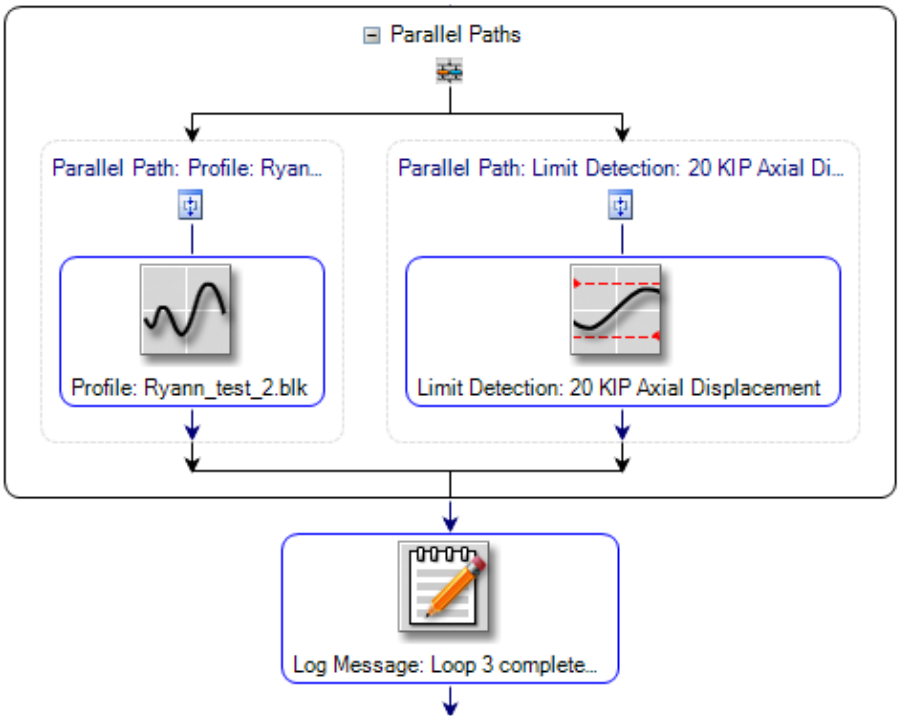

Figure 3.4: The block diagram of Loop 3 of the test-run. Uniaxial tension at a constant true-strain rate occurs during this loop.

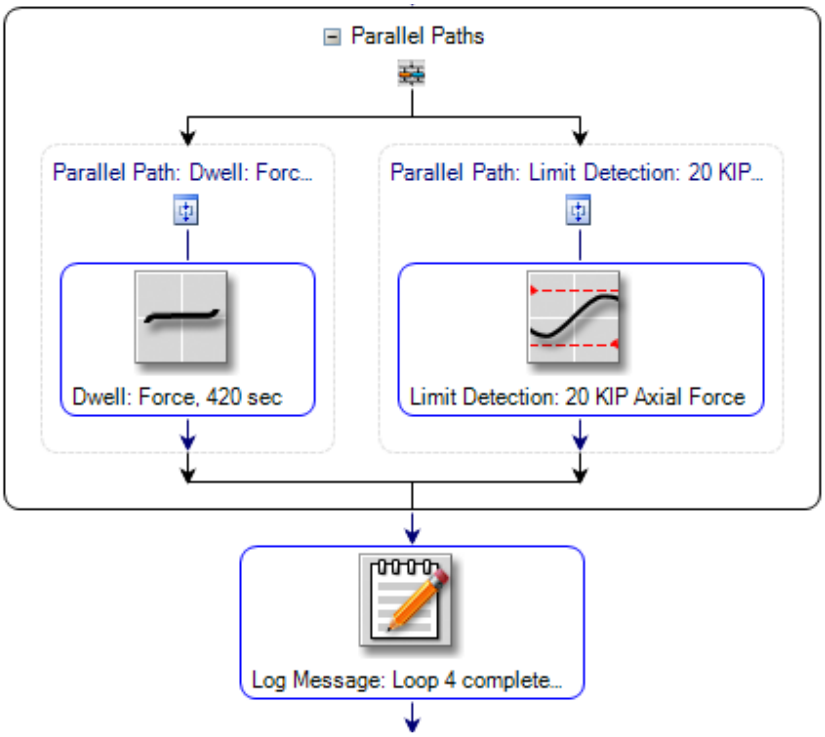

Figure 3.5: The block diagram of Loop 4 of the test-run. This loop marks the beginning of the quenching procedure. The crosshead continuously dwells at the load at the end of Loop 3 in order to preserve substructure.

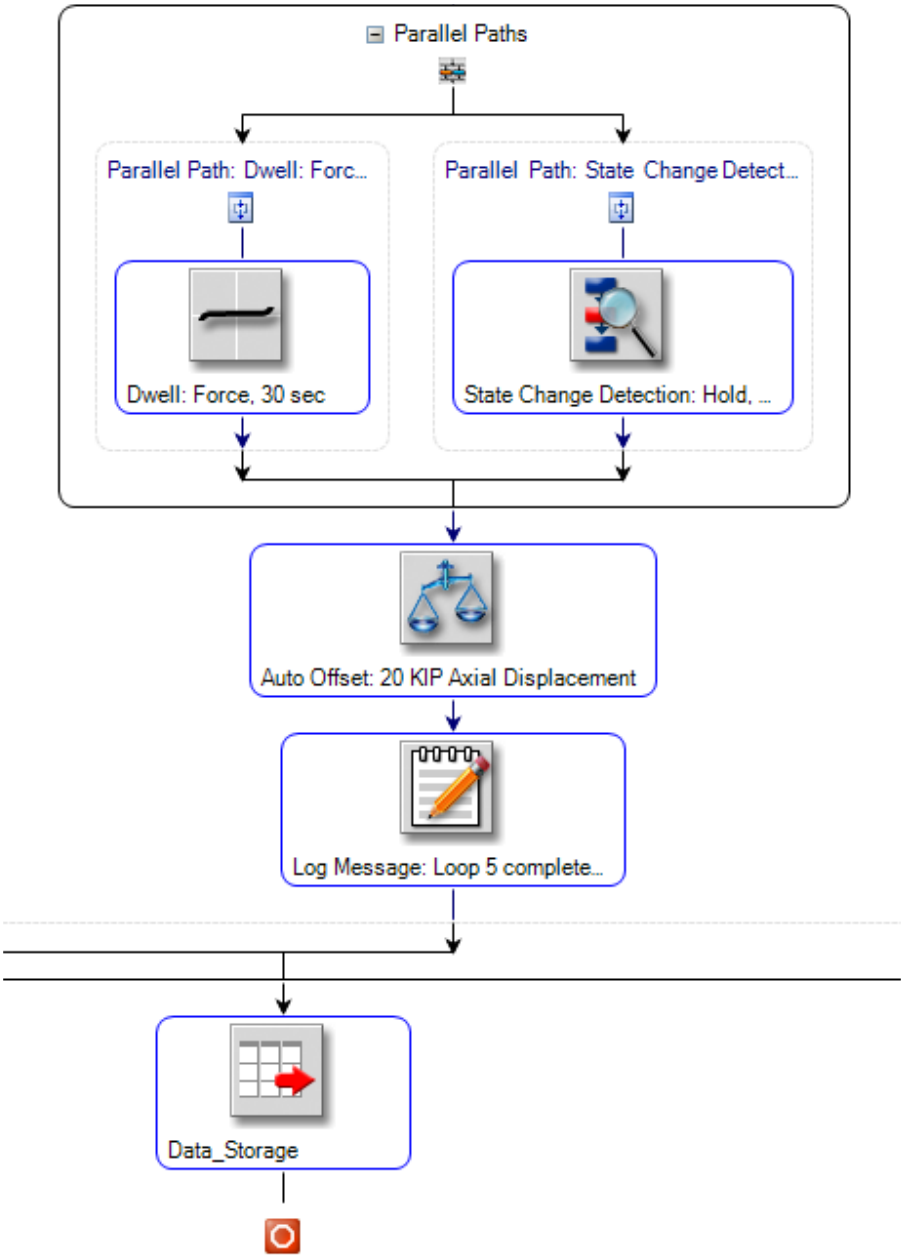

Figure 3.6: The block diagram of Loop 5 and termination of the test-run. The specimen is removed during this loop and completes the quenching procedure. Data from the entire test-run is stored. The test-run is then terminated.

The test-run began by inputting the desired end-displacement into the program shown in Figure 3.2. This value was calculated from the desired final strain. Once this value was entered, Loop 1 began. During this loop, the axial displacement increased at a rate of 0.005 mm/s until the desired preload was reached. The axial displacement was then zeroed, Loop 1 was exited, and Loop 2 began. Loop 2, Figure 3.3, held the desired preload indefinitely until the "Hold" button was pressed. The axial displacement was again zeroed. Loop 2 was then exited. Loops 1 and 2 controlled during the heat-up portion of the test-run. During these loops, the furnace was turned on and ramped up to the desired test temperature. The "Hold" button was pressed after the furnace was at temperature for a prescribed time of 2 min. to ensure the specimen was fully recrystallized.

The tension test occurred in Loop 3, which is illustrated in Figure 3.4. A test profile directed the test frame's hydraulic piston displacement in order to deform the specimens at a constant true-strain rate. The files used to specify the crosshead displacement are provided in Appendix A. The test stoped automatically once the desired end-displacement that was input at the beginning of the test-run was reached, ending Loop 3.

Loops 4 and 5 are displayed in Figures 3.5 and 3.6. These loops are the quenching portion of the test-run. Loop 4 instructed the instrument to dwell for 420 s at the load at the end of Loop 3. At the beginning of this loop, the furnace was promptly turned off and opened. The specimen was then continuously sprayed with water. After the 420 s, Loop 4 exited. Loop

5 adjusted the dwell load to a value just above zero. In the final iteration of the test procedure, this value was set to 0.001 kN. The instrument maintained this load indefinitely until the "Hold" button is pressed. During this time, the specimen is continuously sprayed with water, and the pins holding the specimen removed. Once the specimen was removed from the test rig, the "Hold" button was pressed. The axial displacement was zeroed and Loop 5 was exited. Data collected throughout the entirety of the test-run was stored. The test-run was then terminated.

3.2.4.4 Data processing

The Ti-IF steel specimens oxidized during tensile testing at elevated-temperature in air. Oxidation eats away at the specimen surface and reduces the cross-sectional area. Even though the initial cross-sectional area is documented prior to testing, the cross-sectional area is not known after the specimen reaches the test temperature. Oxidation continues during testing, breaking the assumption that the volume in the gauge remains constant. Therefore, stress cannot be calculated accurately because the cross-sectional area is unknown. The tensile strain, however, is known.

Approximate engineering and true stress-strain curves were calculated after each test-run to check for any test anomalies. Care was taken to correct the recorded axial displacement by removing the "setting" effect from the grips and effects of the machine compliance. Corrections were also made to the elastic portion of the load-displacement curves. The slope was adjusted to con-

form to the Young's modulus of the material at the testing temperature [64]. Since the stress calculated for stress-strain curves is only an approximation, the stress-strain curves from tests in air are not be presented. Elevated temperature tensile testing in a vacuum was performed to accurately determine true stress-strain curves.

3.2.5 Elevated temperature tensile testing in vacuum

3.2.5.1 Furnace and test frame

Elevated temperature tensile testing in vacuum used a Thermal Technology LLC (Santa Rosa, CA) Testmaster 3-8-3W vacuum furnace. This furnace was fitted to an Alliance RF/100 electromechanical, computer-controlled testing frame from MTS Systems. The MTS TestWorks 4 software version 4.12 D controlled crosshead displacement. The furnace employs tungsten heating elements and can reach the desired test temperature within minutes. The tensile gauge region of the test specimen remains within the furnace hot-zone for the entirety of the test. Independent temperature profiling of the furnace hot zone determined the temperature is held within $\pm$ 10 °C of the desired test temperature. The interested reader is directed to [65] for more information on temperature profiling. The purpose of these tests was to measure accurate stress-strain data by avoiding oxidation of the specimen and its associated material loss. The configuration of the vacuum furnace prevents rapid quenching after testing to preserve the microstructure from elevated-temperature deformation. This is the reason that tests in air, described previously, were used to

produce specimens for microstructural characterization.

Pins were used to connect the tensile specimens to tungsten pull rods. The pull rods exited the furnace through bellow assemblies located at the top and bottom of the furnace. The bellows seal the furnace so that a vacuum may be maintained. A vacuum of 10^{-5} to 10^{-6} Torr was attained during testing. During testing, the bottom pull rod remained stationary. The top pull rod can travel up to 76 mm (3 in.), as permitted by the upper bellows assembly. An image of the electromechanical test frame and vacuum furnace assembly is presented in Figure 3.7.

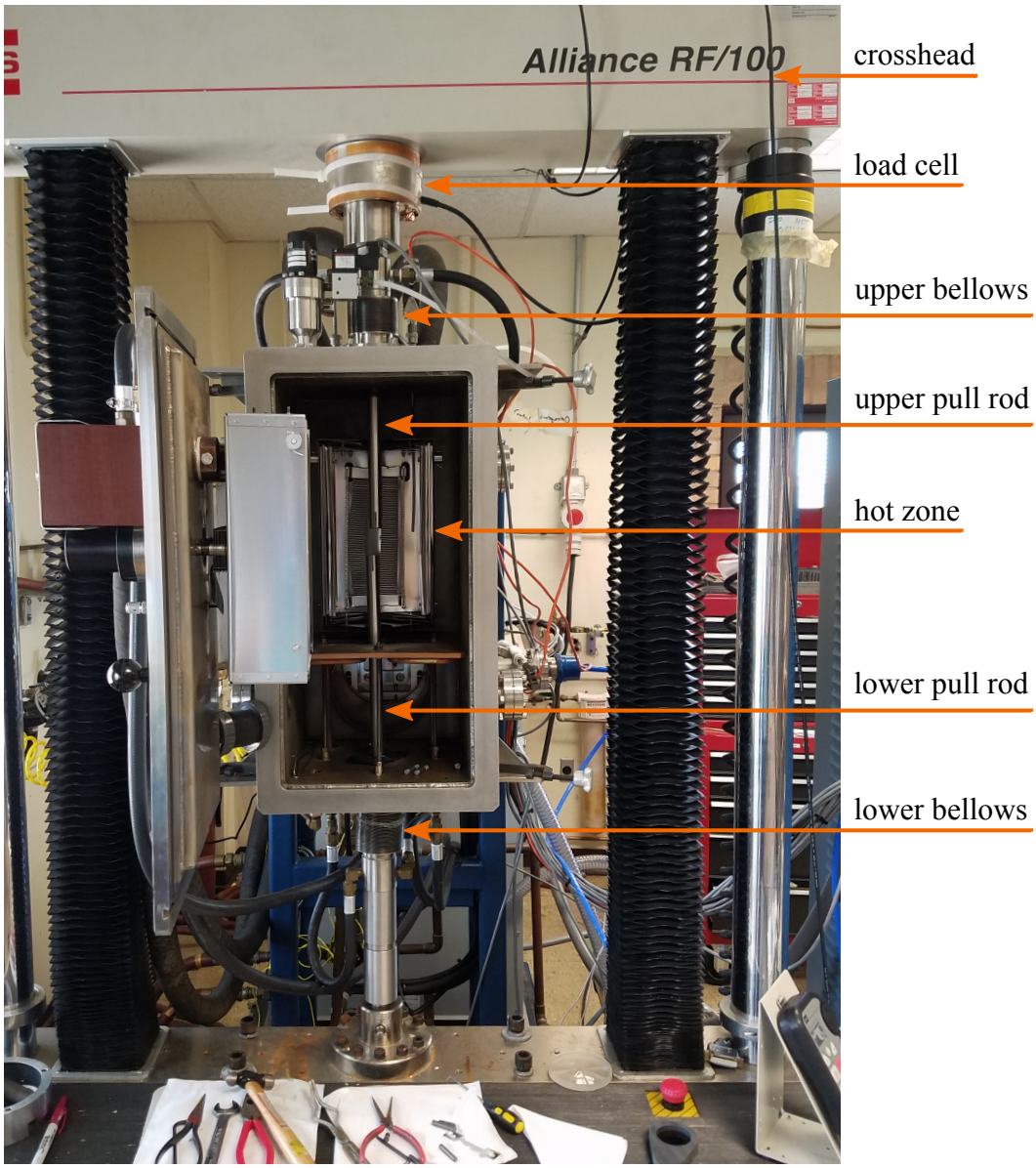

Figure 3.7: The vacuum tensile furnace assembly. This photograph was taken by Mrs. Emily Brady.

3.2.5.2 Heat-up and cool-down

In order to maintain the vacuum during heat-up, the furnace was programed to gradually ramp up to the desired set point. This ramp up occurred over a 15 minute period. Thermal expansion of the pull rods and specimen occur during heat-up. To prevent a compressive load from being placed on the specimen, a preload of 22 N (5 lbs.) was applied to the specimen. A computer-controlled program continuously adjusted the crosshead to apply this preload. Upon reaching the desired set point, this temperature was held for approximately one hour. During this hold time, thermal expansion of the specimen and pull rods gradually went to completion. Stabilization of the system at the set-point temperature was necessary to accurately determine the specimen elongation from the crosshead displacement during testing. The crosshead displacement was measured during heat-up to determine the rate of thermal expansion in the system. A test was started when the thermal expansion rate was less than 5% of the test strain rate. The crosshead extension *versus* time for a typical cycle of heating and temperature hold is displayed in Figure 3.8. The specimens fully recrystallized during this process prior to tensile straining.

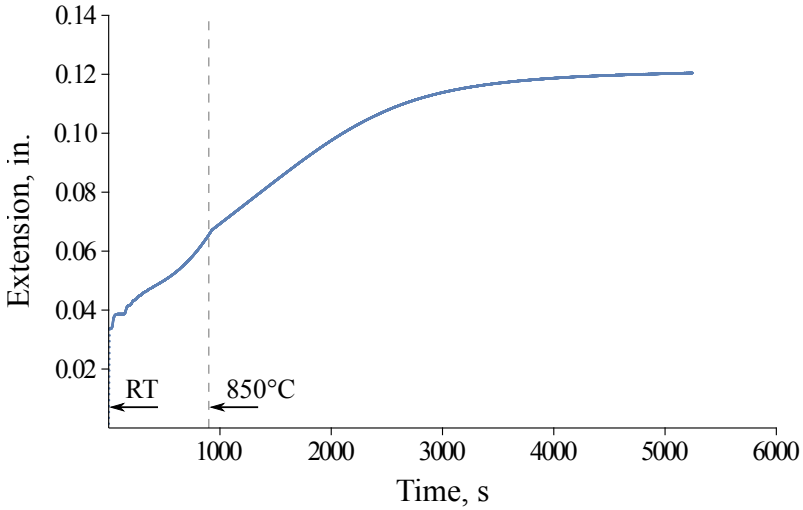

Figure 3.8: The extension *versus* running time profile for a typical heating and hold cycle is shown. The arrows indicate when the hot zone was at room temperature (RT) and reached the 850 °C test temperature.

A cool-down procedure was employed after tensile testing in an attempt to protect the load cell and specimen. Once the desired strain was reached during testing, the test program was terminated, and the load on the specimen was manually removed. Once the specimen was unloaded, the furnace was turned off with the specimen still inside. As the furnace cooled, the specimen and pull rods contracted. A computer-controlled software program continuously adjusted the crosshead displacement in order to prevent loading of the specimen during this thermal contraction.

3.2.5.3 Tensile tests in vacuum

Uniaxial tensile tests in vacuum at 850 °C were performed at a constant true-strain rate of 10^{-4} s^{-1} to a true strain of 0.1 or 0.2. The TD was oriented

at 45° and 90° with respect to the RD. Specimens with TD parallel to the RD were tested by Noell, and those data are presented in this dissertation. A specimen in the as-received condition was pin-loaded into the grips for testing. During the heat-up procedure, the specimen fully recrystallized.

A software program was used to deform the specimens at a constant true-strain rate. This was executed by the computer-controlled program continuously varying the test frame's crosshead displacement rate. The interested reader is directed to [65] for more information regarding constant true-strain rate testing. During the test, the crosshead displacement and force on the pull rods were recorded. The force on the pull rods was monitored by a load cell located outside the furnace. The specimen gauge region was assumed to conserve volume and deform uniformly. These assumptions were verified by measuring the specimen gauge region after testing.

3.2.5.4 Data processing

Before the true stress-strain curves could be produced, the force and displacement data required several corrections. As the crosshead moved, the upper bellows applied a force to the top pull rod. To accurately determine the load on the specimen, the load from the bellows must be accounted for. Independent calibration tests were performed to measure the load from the bellows as a function of crosshead position. This calibration involved measuring the load as a function of crosshead displacement without a specimen inserted and with no vacuum applied. When the specimen was under vacuum,

shortly before testing, the load and displacement was tared to zero. By taring the load of specimen under vacuum, the force on the load cell from the atmospheric pressure differential force was removed from the measurement. Figure 3.9 shows an example of the load *versus* extension data used to correct for the load of the bellows. A fourth order polynomial was fitted to the data. This fitted polynomial was used to subtract the load of the bellows from the raw force data measured during testing. To accurately report the crosshead displacement during testing, the following corrections to the raw displacement data were necessary. The "setting" effect from the grips and effect of machine compliance were removed from the recorded axial displacement. The elastic slope of the data was corrected in order to conform to the Young's modulus reported by Köster and Rauscher [64].

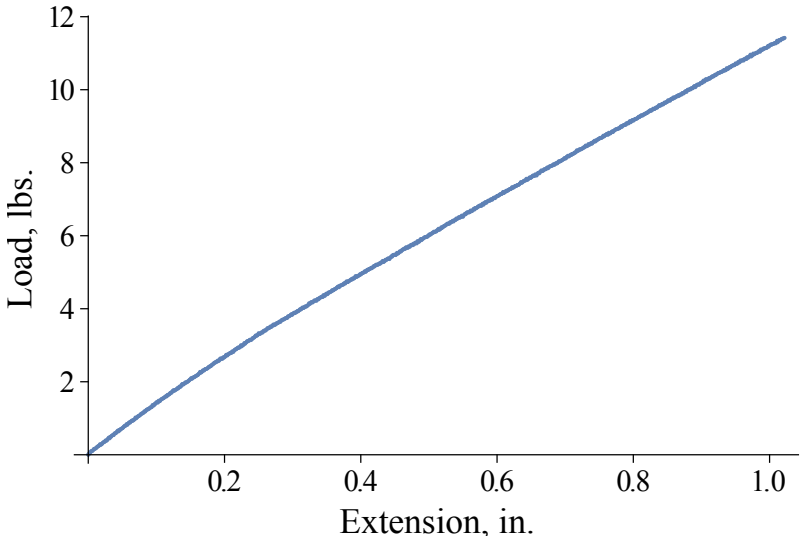

Figure 3.9: The load from the bellows *versus* the crosshead extension is shown. These data are from an independent calibration test. No specimen was present during the calibration and no vacuum was applied.

3.3 Microstructure characterization

3.3.1 Metallography specimen preparation

The specimens that were deformed in air at elevated temperature oxidized, forming a scale on the surface. To remove the scale, the specimens were pickled. This involved dipping and agitating the specimen in 6 to 12 wt.% sulfuric acid heated between 77 and 88 °C (170 to 190 °F). The specimens were pickled for up to 10 minutes.

All of the Ti-IF steel specimens regardless of testing condition were sectioned, ground, and polished for characterization with BSE channeling contrast and EBSD. A Struers (Cleveland, OH) Minitom low speed precision abrasion saw was used with a diamond blade to section each specimen to size. The typical grinding and polishing procedure for preparing Ti-IF steel specimens is presented in Table 3.2. To grind the specimens an Allied High Tech Products, Inc. (Rancho Dominguez, CA) Techprep base with Multiprep head or Struers Rotopol-15TM automated polisher was used. The Struers Rotopol-15TM automated polisher was used for the polishing steps.

Some key things to note from Table 3.2 are the following. The listed times are the minimum times spent at each step. The actual polishing time for a given step was approximately double the time it took to remove the surface scratches from the previous step. This ensured the removal of the residual deformation below the surface from the previous step. The exact metallographic products and procedures varied. The metallographic products used depended upon what was available. For a given step, the equivalent Leco (Saint Joseph,

MI) and Struers products were used. Occasionally an Allied lubricant was used. The procedure varied depending upon the method used to mount the specimen for metallographic preparation. Three methods were used. Some specimens were embedded in bakelite pucks. The exact procedure listed in Table 3.2 was followed for these specimens. Other specimens were glued to a bakelite puck using cyanoacrylate adhesive. Upon completion of the listed procedures, these specimens were inspected using BSE channeling contrast. If the specimen preparation was adequate, the 3 and 1 μm diamond polishing steps were repeated. Acetone was then used to remove the specimen from the bakelite puck. Care was taken to minimize contact between the acetone and the polished surface of the specimen. The specimen was then attached to a bakelite puck using double-sided adhesive tape. The colloidal silica polishing step was then repeated. The third method involved using the double-sided adhesive tape alone to mount the specimen to a bakelite puck. The exact procedure listed in Table 3.2 was followed for these specimens. The specimen was removed after each step and reattached with new tape. The purpose of using the glue and double-sided adhesive tape was to reduce specimen size. This permitted EBSD scans at the optimal working distance to be collected. This ensured that Kikuchi patterns were centered with respect to the EBSD camera in order to improve high-resolution EBSD (HR-EBSD) cross-correlation indexing. The size of the specimen determined whether using double-sided adhesive tape or glue was better for mounting. For large specimens, with a contact area in the vicinity of 58 mm^2 (0.09 in.^{2}), double-sided adhesive tape

was best. For small specimens, with a contact area of approximately 19 mm^2 (0.03 $in.^2$), glue was the better choice.

A recrystallized specimen annealed in a box furnace was sectioned and mounted for characterization on three orthogonal surfaces. These are the RD-LTD, RD-ND, and LTD-ND planes. The specimens deformed in tension were characterized on the TD-TLTD plane.

Table 3.2: The typical grinding and polishing procedures used to prepare Ti-IF steel specimens for BSE channeling contrast and EBSD characterization are listed. The products listed are Leco consumables. The equivalent Struers or Allied products may have been used, depending on what was available to the user. The times given are the minimum spent at each step.

Polishing Surface	Polishing Media	Lubricant	RPM	Force	Time
1200 grit SiC	-	Water	300	5 N	Until scale and any adhesives are removed
Pan-W	15 μm Premium	Aqua Lube	150	Hand	15 min.
Pan-W	9 μm Premium	Aqua Lube	150	Hand	10 min.
Pan-W	6 μm Premium	Aqua Lube	150	Hand	5 min.
Lecloth	3 μm Premium	Aqua Lube	150	Hand	10 min.
Lecloth	1 μm Premium	Aqua Lube	150	Hand	15 min.
Imperial	Colloidal silica slurry	Deionized water	90	Hand	20 min.

3.3.2 SEM and EBSD data acquisition

BSE channeling contrast using a JEOL JSM-5610 SEM was used for microstructural characterization. Typically a low accelerating voltage, small working distance, and large spot size are desired. These values, for the Ti-IF steel, were typically in the vicinity of 14 kV, 14 mm, and 45, respectively.

A Philips/ FEI XL30 environmental scanning electron microprobe (ESEM) equipped with an Oxford HKL Nordlys detector using Oxford AZtecHKL software was used to collect EBSD data. The size of the camera was 1,344 pixels by 1,024 pixels. A 2 μm step size was deemed appropriate for the Ti-IF steel and was used for every scan. The following settings were used for collecting standard-resolution EBSD data. An accelerating voltage of 20 kV with a spot size of 5 was used. The working distance was typically at 15 mm $\pm$ 3 mm. The specimen was tilted 70°. For phase acquisition, 27 reflectors were used. When optimizing the pattern, 4×4 binning was used with high gain and the exposure determined by pressing the auto button. Both the auto and static background were turned on. Ten (10) frames were collected for the static background. When optimizing the solver, the software was directed to detect the edges of 12 bands. The Hough resolution was set to 70. For most specimens, frame averaging was not used.

The settings used to collect high-resolution EBSD (HR-EBSD) data were the same as those used for standard-resolution EBSD data with the following exceptions. No binning (1×1) was used. Typically, auto background was turned off. No frame averaging was used. The scans were kept small

to minimize beam shift. Care was taken to never scan an area larger than 300 μm $\times$ 300 μm. Kikuchi patterns were saved whenever the capability to perform HR-EBSD was desired.

The Oxford AZtecHKL software, for each EBSD session, produces .oip, .crc, and .dat files. For each individual scan, .cpr and .ctf files were exported. These files are necessary for additional analysis. The .cpr file records data from the EBSD settings. Data from each pixel in the EBSD data is recorded in the .ctf file. The most important information is a pixel's phase id, spatial orientation, and crystallographic orientation. Other values such as the MAD number, image quality, and band contrast are also recorded for each pixel. The .ctf file documents some of the EBSD settings. The .ctf file was imported into a program called Manager Data to export a .txt file of the information in the .ctf file. The .txt file includes all of the information that was recorded in the .ctf file as well as the direction cosine matrix for each pixel. When storing Kikuchi patterns, a .ebsp file is produced. The individual Kikuchi pattern images were exported in a .tiff format from the AZtecHKL software.

Chapter 4

Data and Numerical Analysis Procedures

4.1 Software used

Numerous software programs were utilized to perform the data and numerical analysis in this work. A brief description of each program and its capabilities will now be provided.

4.1.1 Pedrazas' Mathematica code

A custom Mathematica [66] script by Pedrazas [65] is capable of performing basic EBSD analysis, including boundary type characterization, strain accumulation, and grain size. Pole figures, inverse pole figures, and various maps can be output. The algorithms used are well documented, transparent, and accessible. The script can be easily modified to meet specific needs. A robust algorithm handles unindexed pixels particularly well. The .txt input file from an EBSD scan is required.

4.1.2 MTEX and Matlab

MTEX [67], a free toolbox in Matlab [68], is used by an extensive community for crystallographic texture analysis and modeling. MTEX has a voluminous catalog of functions available for analysis, including the capabil-

ity to calculate orientation distribution functions (ODFs). MTEX has a few drawbacks. First, the documentation for some of these functions is limited. It can also be difficult to modify and apply the functions to specific needs. MTEX does not handle unindexed pixels well. MTEX version 4.0.23 using Matlab R2014B was used in this work to process EBSD data. For EBSD data analysis, the .ctf file from an EBSD scan is required.

4.1.3 OpenXY

OpenXY [69] developed by Bringham Young University is an open source code written in Matlab [68] to produce HR-EBSD data. This software improves the accuracy of orientation indexing by implementing cross-correlation instead of the standard Hough transformation. OpenXY requires the .ctf and .cpr files as well as the individual .tiff image files of the Kikuchi patterns to be input. A .ctf file with the crystallographic orientation angles indexed using cross-correlation is output.

4.1.4 VPSC

R. A. Lebensohn and C. N. Tomé developed and maintain the visco-plastic self-consistent (VPSC) software [70, 71]. The software is free and generally available upon request, subject to some export restrictions. The VPSC code simulates texture changes from plastic deformation. Version 7c of the VPSC software was used in this work.

The VPSC software requires several input files. The input files used in

this work are provided in Appendix D. These files will now be discussed. The "vpsc7_x0.in" file used in this work provides information regarding the input files to read in, the test conditions, and the simulation deformation path. The "tension_x0_298", "tension_x90_298", and "tension_x45_298" files were used to designate the time increments and components of the velocity gradient. The initial microtexture is supplied in the "tifsteel.tex" file. This file specifies the type of Euler angles used and the number of grains in the file. For each grain in the file, the mean orientation of the grain and its volume fraction are provided. The "Fe.sx" file used in this work consists of information regarding the deformation modes and initial parameters of an Fe single crystal [70].

An assortment of files are output by the VPSC software. The "TEX_PHn.OUT" file is of interest to this work. This file outputs the predicted microtexture as a list of individual grain orientations in the simulated deformation produced from the initial microtexture [70, 71].

4.2 Standard-resolution EBSD data analysis

4.2.1 Adjustments for specimen alignment

Prior to analyzing the EBSD data, the raw EBSD data were corrected for misalignment of the specimen in the SEM chamber. Misalignment was the result of the sample not being completely flat and parallel to the detector. The rotations necessary to correct for misalignment were determined by enforcing the sample symmetry on the {200} pole figure. Sample symmetry is a statistical symmetry that is the result of the sample's processing history. There are

three types of sample symmetry: triclinic, monoclinic, and orthotropic [72].

The samples oriented with their tensile direction at 0° and 90° with respect to the rolling direction exhibit orthotropic sample symmetry. Orthotropic sample symmetry has three mirror planes perpendicular to each of the sample's three reference directions [72]. This implies that the discrete data points in the {200} pole figure should be centered about the origin. To determine the specimen misalignment, a custom, automated Mathematica [66] routine using algorithms from Pedrazas' Mathematica script [65] was created. This script determined the center of the discrete {200} pole figure data and the rotations necessary to center the data about the origin. The raw EBSD data was rotated by these amounts in MTEX to correct for specimen misalignment.

Orthotropic sample symmetry is destroyed when the samples are deformed with their tensile direction at 45° with respect to the rolling direction. Instead, a monoclinic sample symmetry, 2/m, is present [73]. This is equivalent to a mirror plane perpendicular to the short transverse direction (STD) and a two-fold rotation axis in the TD-TLTD plane. Monoclinic sample symmetry also implies the {200} pole figure data should be centered about the pole figure's origin. The same process was thus used to correct the specimens oriented with their TD at 45° with respect to the RD as the specimens oriented at 0° and 90°.

For a population of 28 standard-resolution EBSD scans, the largest alignment correction was 5.38°. The mean standard error for the alignment correction was ± 1.73°. The mean standard error of the specimen misalign-

ment that remained after correcting the data was ± 0.20° for the same population. Once the data were corrected, EBSD data analysis using Pedrazas' Mathematica script and/or MTEX were performed.

4.2.2 Microstructure analysis

4.2.2.1 Pole figures

Any crystal vector can be characterized by its intersection with the unit reference sphere. Typically a plane or a direction is described. A pole is the point of intersection of the orientation of a specific crystallographic direction or plane with the reference sphere. The unit reference sphere is linked to the specimen coordinate frame. The sphere is then projected onto a 2D plane to create a pole figure [11]. Therefore, a pole figure is the projection of the orientation of a crystal with respect to the sample coordinate frame [60].

The fundamental area for a pole figure depends on the sample symmetry. A uniform distribution of data points in a pole figure indicates that the polycrystal has a random texture. Conversely, a texture in a polycrystal is represented by the clustering of data points [74].

From the EBSD data, the {200}, {110}, and {211} pole figures were plotted in MTEX. The {200} pole figure is particularly useful for BCC materials. A reference {200} pole figure is presented in Figure 1.5. Pole figures of both the discrete data and the ODF derived from those data were produced.

4.2.2.2 Inverse pole figures

An inverse pole figure (IPF) is the projection of the orientation of the specimen coordinate frame with respect to the crystal coordinate frame [11, 60]. The fundamental area depends on the crystal symmetry. For cubic crystals, the fundamental area is the stereographic triangle with the corners corresponding to the {100}, {110}, and {111} poles [60].

For the annealed specimens, MTEX was used to plot the RD, LTD, and ND inverse pole figures. The TD, TLTD, and STD inverse pole figures were produced for the tensile specimens. Inverse pole figures of both the discrete data and the ODF derived from those data were calculated.

4.2.2.3 ODFs and Euler plots

An ODF uses spherical harmonics to mathematically represent texture [60, 74]. A more in depth discussion on the calculation of ODFs is outside the scope of this dissertation. ODFs are expressed in units of multiples of random (MRD). MRD is a metric for how frequently a given texture component is present. A MRD value of 1 corresponds to a given texture component with a frequency equal to that of a random texture. A texture component with a MRD value greater than 1 has a frequency greater than that of the random texture. The greater the MRD value, the stronger the intensity of the specific texture component. A texture component with a MRD value less than 1 has a frequency less than expected of a random texture. ODFs were calculated in MTEX using the default settings.

Three Euler angles are necessary to fully describe a single orientation. Two different Euler angle systems are commonly used [60]. The Bunge Euler angles [73], φ_1, Φ, and φ_2, are used in this work. These angles transform the sample coordinate system into the crystal coordinate system when the correct order of rotations is followed [11, 73].

Euler space with axes φ_1, Φ, and φ_2 unambiguously describes any orientation. Assuming no crystal or sample symmetry, the Euler space bounds are the following:

$$0^\circ \leq \varphi_1, \varphi_2 \leq 360^\circ \tag{4.1}$$

and

$$0^\circ \leq \Phi \leq 180^\circ. \tag{4.2}$$

Crystal and specimen symmetry reduce the range of this fundamental region. φ_1 is affected by the sample symmetry. Monoclinic and orthotropic sample symmetry reduce the upper bound of φ_1 to 180° and 90°, respectively. Crystal symmetry affects Φ and φ_2. Conventionally, cubic symmetry is used to reduce the upper bounds of Φ and φ_2 to 90°. It should be noted that this convention for cubic crystal symmetry does not reduce the Euler space to its smallest fundamental region. Each orientation is actually repeated three times within this space for a cubic crystal. This convention is used because of the shape of the fundamental region for a cubic crystal is rather more complex than a simple cube in (φ_1, Φ, φ_2) space [11, 74].

The calculated ODFs were plotted in Euler space. The $\varphi_2 = 45^\circ$ Euler slice is particularly meaningful for rolled BCC sheet material [72]. This slice is

presented in Figure 4.1 below. Fiber textures that are present in the Euler slice are highlighted. The α- and γ-fibers are significant in this work. The α-fiber is the <110>||RD. It spans from the {001}<110> to {111}<110>. The γ-fiber is the <111>||STD. It traverses from {111}<110> to {111}<112> [45, 72].

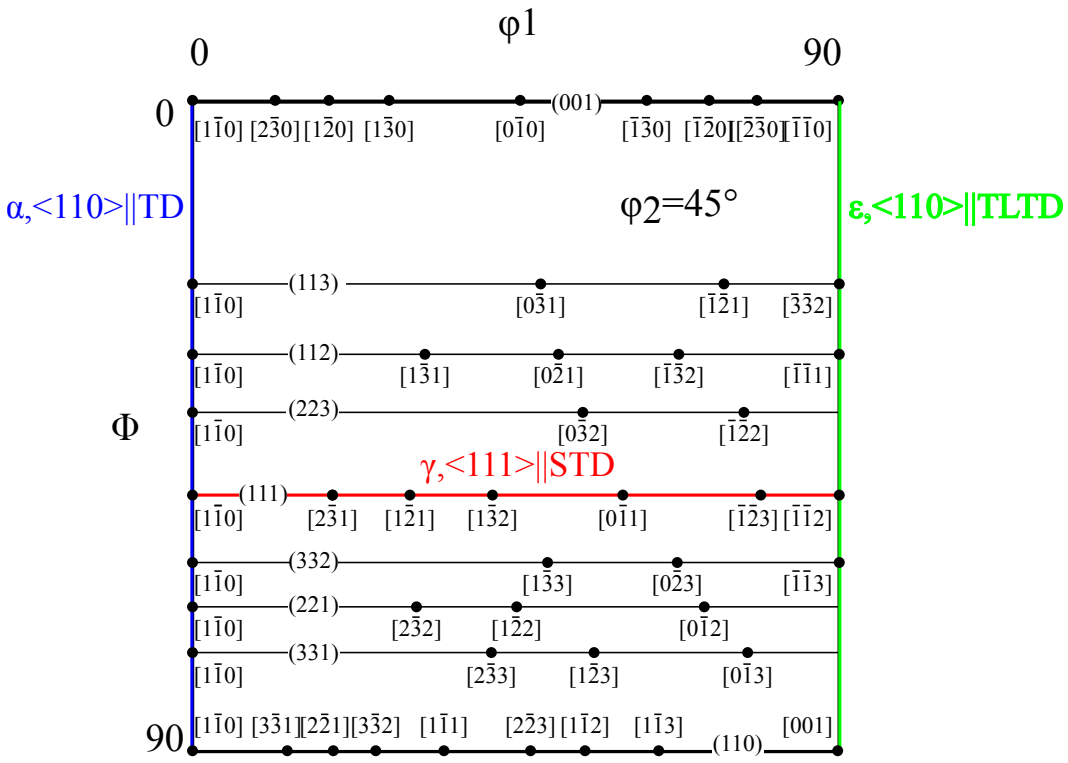

Figure 4.1: The $\varphi_2 = 45°$ Euler slice is shown with cubic crystal symmetry and orthotropic sample symmetry. Fiber textures present in this Euler slice are highlighted. This figure is based on work by Bunge in Ref. [73] and modifications by A. D. Rollett [75].

Conventionally in sheet materials, the notation to describe a texture component is {hkl}<uvw> where {hkl} is the crystallographic plane parallel to the plane of the sheet material and <uvw> is the crystallographic direction

parallel to the RD. In this work, the orientation of the TD was varied with respect RD. Texture interpretation was observed to be more meaningful when the <uvw> was expressed as the crystallographic direction parallel to the TD. Therefore, the texture component notation used in this work is {hkl}<uvw>, where {hkl} is the crystallographic plane normal parallel to the STD and <uvw> is the crystallographic direction parallel to the TD.

In order to isolate the effects of lattice rotation and DNGG, the ODFs of the textures from three different material states were calculated. These states were the microstructure after recrystallization, room-temperature tensile deformation, and high-temperature tensile deformation. The texture resulting from room-temperature tensile deformation is the combination of the recrystallized texture and lattice rotation during subsequent plastic deformation. The texture after high-temperature tensile deformation is the combination of the recrystallized texture, lattice rotation from plastic deformation, and the effect of DNGG. Although recovery occurs only at high temperature, the dislocation slip that causes lattice rotation will be similar for high and low temperatures.

The microtexture of each material state was determined experimentally using EBSD. It should be noted that the high-temperature tensile deformation occurred at the same temperature as recrystallization. The texture that resulted after room-temperature tensile deformation was also simulated using the VPSC software. The VPSC model used the recrystallized texture as its input texture and only simulates the lattice rotation effect. Therefore, the textures simulated by the VPSC software serve to verify that the lattice rotation effect

is being captured experimentally by room-temperature tensile deformation. A more in depth description of the VPSC simulation is provided in Section 4.4.

The lattice rotation and DNGG effects were then isolated. Seclusion of the lattice rotation effect was achieved by subtracting the ODF of the recrystallized texture from the ODF of the texture that resulted from room-temperature tensile deformation. Isolation of the DNGG effect was accomplished by subtracting the recrystallization texture and lattice rotation effect from the texture that resulted from high-temperature tensile deformation. This is equivalent to subtracting the ODF of the texture after room-temperature tensile deformation from the ODF of the texture after high-temperature tensile deformation. For the theoretical basis of this approach to be correct, the room- and high-temperature deformation must be to the same strain.

4.2.3 IPF/ ROD/ GOS maps

IPF, reference orientation deviation (ROD), and grain orientation spread (GOS) maps were produced. In order to calculate the ROD and GOS values, the pixels in an EBSD scan must be separated into individual grains. Grain boundaries were identified as boundaries between pixels with misorientations larger than 5°. A grain was required to consist of at least 5 pixels.

Maps of the inverse pole figure were produced as follows. The fundamental stereographic projection of the crystal coordinate frame is first color-coded. Each pixel in a scan is then colored depending on its crystal coordinates with respect to a specimen reference direction. Typically, IPF maps are

plotted with respect to the RD, LTD, and ND for the statically annealed specimens. The TD, TLTD, and STD are defined as the reference directions for the tensile specimens. These maps are useful for visualizing microstructure and information such as grain orientation and size. IPF maps superimposed with the identified grain boundaries were produced using Pedrazas' Mathematica script [65].

The ROD is the misorientation between the average orientation of the grain and the orientation of a pixel within the grain. A ROD value is calculated for each pixel in a scan [76]. Each pixel is assigned a color depending on its ROD value and plotted in map form. ROD maps are useful for identifying and visualizing individual subgrains. MTEX was used to produce the ROD maps with superimposed grain boundaries.

A single GOS value is calculated per grain. The GOS is the average misorientation between each pixel within a grain and the average orientation of the grain [76]. Each grain in a scan is assigned a color depending on its GOS value. The grain with its assigned color is then mapped. GOS maps visualize the relationship between different grains and their strain accumulation. These maps with grain boundaries superimposed were produced using MTEX.

4.2.4 Individual grain characteristics

For the recrystallized specimens and specimens deformed in uniaxial tension at elevated temperature, the following characteristics were measured for each grain: area, aspect ratio, GOS, and mean orientation. The grain's

location with respect to the boundary of the scan was also documented. The lineal intercept diameter, l, of the grain was calculated from the grain area, A, using the following equation provided in ASTM E112-13 [77]:

$$l = (\frac{\pi}{4} \times A)^{\frac{1}{2}}. \tag{4.3}$$

The goal was to analyze the characteristics of grains of similar orientation as a function of strain. Bunge previously used 62 orientations with low Miller indices to map out Euler space [73]; these 62 orientations were selected as reference orientations. An additional group, reference orientation number 63, was defined for grains that did not fit into any of the 62 reference orientations. A list of the 63 reference orientations are provided in Appendix B.

A set of criteria was defined to determine in which of the 62 reference orientations a grain fits. These criteria will now be discussed. A grain was considered to potentially match any reference orientation it had a disorientation of 15° or less with. A grain was allocated to reference orientation number 63 if the disorientation between the grain and each of the 62 reference orientations was larger than 15°. The reference orientation with the lowest disorientation was selected to represent the grain. The accuracy of the disorientation was estimated to be ± 1°. Additional reference orientations that were within this 1° disorientation tolerance were considered to be an equally good fit. Therefore a grain could potentially be represented by multiple reference orientations.

The disorientation uncertainty was estimated from a combination of

the uncertainty related to EBSD orientation indexing and specimen alignment in the SEM chamber. At its best, the angular accuracy of standard-resolution EBSD orientation indexing is ± 0.5° [78–80]. Noell performed an accuracy study on the EBSD system used in this work. A 250 μm × 250 μm scan with 8 × 8 binning was collected from a single crystal of Si that was strain free. An accuracy of ± 0.45° was measured for indexing [80]. In this study, EBSD data sets with scans larger than 250 μm × 250 μm were collected, which could negatively impact this accuracy. The data sets were collected with 4×4 binning, which could improve the accuracy. These specimens, especially the ones deformed in tension, are not strain free, which could adversely affect the uncertainty of indexing. An angular accuracy of ± 1° was used as a reasonably conservative estimate for the standard-resolution EBSD orientation indexing used in this work. Adjustments were made to correct for specimen misalignment in the SEM chamber. This process is described in Section 4.2.1. After making these adjustments, the mean standard error of specimen misalignment was calculated as ± 0.20° for 28 standard-resolution EBSD scans. The disorientation uncertainty, $\Delta_{Disorientation}$, was calculated using the propagation of uncertainty with the following equation

$$\Delta_{Disorientation} = \sqrt{(\Delta_{EBSD})^2 + (\Delta_{Alignment})^2}, \tag{4.4}$$

where Δ_{EBSD} is the uncertainty of standard-resolution EBSD orientation indexing and $\Delta_{Alignment}$ is the uncertainty related to the specimen alignment, post correction. Using the values for the uncertainties discussed above, the

disorientation uncertainty equals

$$\Delta_{Disorientation} = \sqrt{(1^\circ)^2 + (0.2^\circ)^2} = \pm 1.02^\circ \approx \pm 1^\circ. \tag{4.5}$$

This value likely overestimates the disorientation uncertainty. The mean orientation of the grain is the average of all the orientations measured within a grain. Assuming the accuracy of standard-resolution EBSD orientation indexing is random, the mean orientation reduces the uncertainty from orientation indexing. Thus, an orientation indexing error smaller than estimated is possible. Therefore, the estimated disorientation uncertainty of 1° is likely conservative.

Grains were allocated into the reference orientation group of which they best fit. For each reference orientation, the total area, area fraction, grain number, grain number fraction, and mean lineal intercept size with its 95% confidence interval were calculated. The changes of these characteristics as a function of strain were investigated. It should be noted that one grain contributes a count to each of its matching reference orientations.

The grains were further sorted based on their best fit into each of the following orientation categories. These categories are by direction parallel to the TD and plane normal parallel to the STD. For each category, the total area, area fraction, grain number, and grain number fraction were calculated. The relationship between these characteristics and strain was probed. It should be mentioned that for a given orientation category (i.e. direction||TD) a grain could be included in multiple groups. However, a grain could only be considered once in a single group (i.e. <110>||TD).

4.3 HR-EBSD

4.3.1 Background on HR-EBSD

The angular resultion of orientations indexed using standard-resolution EBSD is, at best, $\pm$ 0.5° [78–80]. The lower bound for subgrain misorientations, however, can be on the order of 0.001° [39]. The angular resolution of standard-resolution EBSD severely limits ones ability to characterize subgrains. To improve the accuracy of orientation measurements, an EBSD technique known as HR-EBSD can be used. The accuracy of HR-EBSD measurements is approximately $\pm$ 0.01° [79].

The HR-EBSD technique is based on the fact that strain distorts the crystal lattice, consequently altering the Kikuchi pattern. The distorted Kikuchi pattern is compared with a reference Kikuchi pattern that is ideally strain free. The shifts in regions of interest (ROIs) on the pattern are measured between the two patterns. Standard optimization techniques are then used to calculate the angular difference between these patterns. This process is known as cross-correlation and results in significant improvements in the accuracy of orientation measurements [79]. A more detailed description of this technique is beyond the scope of this work. The interested reader is directed to [79, 81, 82] for more information regarding this technique.

To acquire HR-EBSD data, the same equipment and approach is used as conventional EBSD with a few modifications. HR-EBSD is a post-processing technique and requires storage of the individual Kikuchi patterns produced during EBSD scanning. Since HR-EBSD involves looking for subpixel shifts

in the Kikuchi patterns, the Kikuchi patterns should be collected at their full resolution. Section 3.3.2 provides a description of the specific settings used in this study to collect HR-EBSD data.

4.3.2 Use of OpenXY

In this work, Kikuchi patterns within each grain were cross-correlated using OpenXY using a reference pattern from the same grain. The Kikuchi pattern with the highest image quality was selected as the reference pattern. Strain impacts the image quality. Therefore, the Kikuchi pattern with the highest image quality was likely to contain the least amount of strain. The settings used in OpenXY are detailed in Appendix C.

By using a reference pattern from within the same grain for cross-correlation, relative changes in misorientation are determined rather than a global orientation value. Because only relative misorientations were calculated, it was unnecessary to determine the exact camera projection settings. This also removed the need to determine the absolute pattern center. The effects of the following possible error sources were not considered: lens distortion, beam shift, lattice rotation, and pattern center uncertainty. The EBSD scans for HR-EBSD analysis were intentionally kept small, as mentioned previously, in order to minimize errors from beam shift.

4.3.3 Analysis of HR-EBSD data sets

The .ctf file output by OpenXY was corrected for specimen misalignments in the SEM chamber. These misalignments were specifically the result of the sample not being completely flat and parallel to the detector. The same correction technique as described in Section 4.2.1 was used.

MTEX was used to process all of the HR-EBSD data produced using OpenXY. Individual grains and grain boundaries were identified and segmented using the same requirements as specified for standard-resolution EBSD. To reiterate, a grain boundary was identified if the misorientation between two neighboring pixels was greater than 5°. An individual grain was required to be composed of at least 5 pixels. Analysis of HR-EBSD data focused on subgrains and strain accumulation. The HR-EBSD data were also used to measure individual grain characteristics and produce maps described previously for standard-resolution EBSD data.

4.4 Modeling texture changes from plastic deformation

4.4.1 Background and VPSC model

The VPSC model [70, 71] was used to simulate texture changes from plastic deformation. The VPSC model calculates for each grain its plastic response from slip, approximating its surroundings in the polycrystal as a viscoplastic medium. The model accomplishes this by treating the polycrystal as a homogeneous equivalent medium (HEM) and grains as embedded inhomogeneities. Each individual grain is analyzed with respect to the HEM. The

amount of plastic deformation that is accumulated by an individual grain is determined by the strength of its interaction with the HEM. The strain rate and stress in the grain and HEM are linearly related using an interaction equation. The model requires that the strain rate and stress match between the average of all the grains and the polycrystal [71].

The VPSC model has some limitations. It fails to take into account the effects of hardening. Large differences in properties between a grain and the HEM degrade VPSC predictions. The VPSC fails in the rate insensitive limit [71]. The interested reader is directed to [70] and [71] for a more detailed description of the VPSC model and its formulation.

4.4.2 Recrystallized texture input data

The VPSC model and code require an input file with information regarding the initial crystallographic texture of grains in the specimen. This entailed providing the Bunge Euler angles and volume fractions for individual grains within the microstructure. The VPSC manual recommends an initial input with at least 500 grains [70].

A VPSC .tex input file of the recrystallized Ti-IF steel microstructure was constructed from data for three standard-resolution EBSD scans. These scans were collected from a Ti-IF steel specimen that was statically annealed in a box furnace for 30 minutes at 850 °C. The procedure to produce this file will now be discussed.

The EBSD scans, corrected for specimen misalignment, were individ-

ually processed with Pedrazas' Mathematica script [65], which was slightly modified to output two files necessary for the VPSC model. One file contained the average grain orientation of each grain in Bunge Euler angles. The other file contained the number of pixels in each grain. If the grain was not fully contained within the scan, the pixel count was reported as 0. These files were input into a Mathematica [66] script written by the Author. This script performed the following actions. The number of pixels for each grain was converted into a volume fraction. The data from all of the files for each scan were consolidated into one single file. Grains situated on the boundary with respect to the scan were removed from the text file. This was necessary because the volume fraction cannot be measured for these boundary grains. A .tex input file for the VPSC simulation of the recrystallized microstructure was produced. This file contained 794 grains. Appendix D includes this .tex file and the other input files used by the VPSC simulation for this study.

4.4.3 Using the VPSC model for predictions

Tensile deformation at 25 °C (298 K) to a true strain of 0.1 or 0.2 was simulated in 20 steps using the VPSC model. The tensile axis was specified to be at 0°, 45°, and 90° with respect to the rolling direction. Up to three different slip systems could be active for the simulation. For singular slip of BCC materials, the {110}<111> slip system is activated. The {112}<111> slip system is added for double slip. The {123}<111> slip system was added when three slip systems were specified. For this dissertation, double slip was

specified with the {110}<111> and {112}<111> slip systems. Double slip was selected after comparing results from one, two, and three slip systems with an example simulation. Figures 4.2 and 4.3 demonstrates that there are only slight differences between the VPSC simulations using single and double slip. The VPSC simulations using double and triple slip are practically the same. When comparing the VPSC predictions with experimental data, there was no evidence that adding the third slip system provided any advantage. Therefore, the activation of two slip systems for modeling texture changes from plastic deformation was selected.

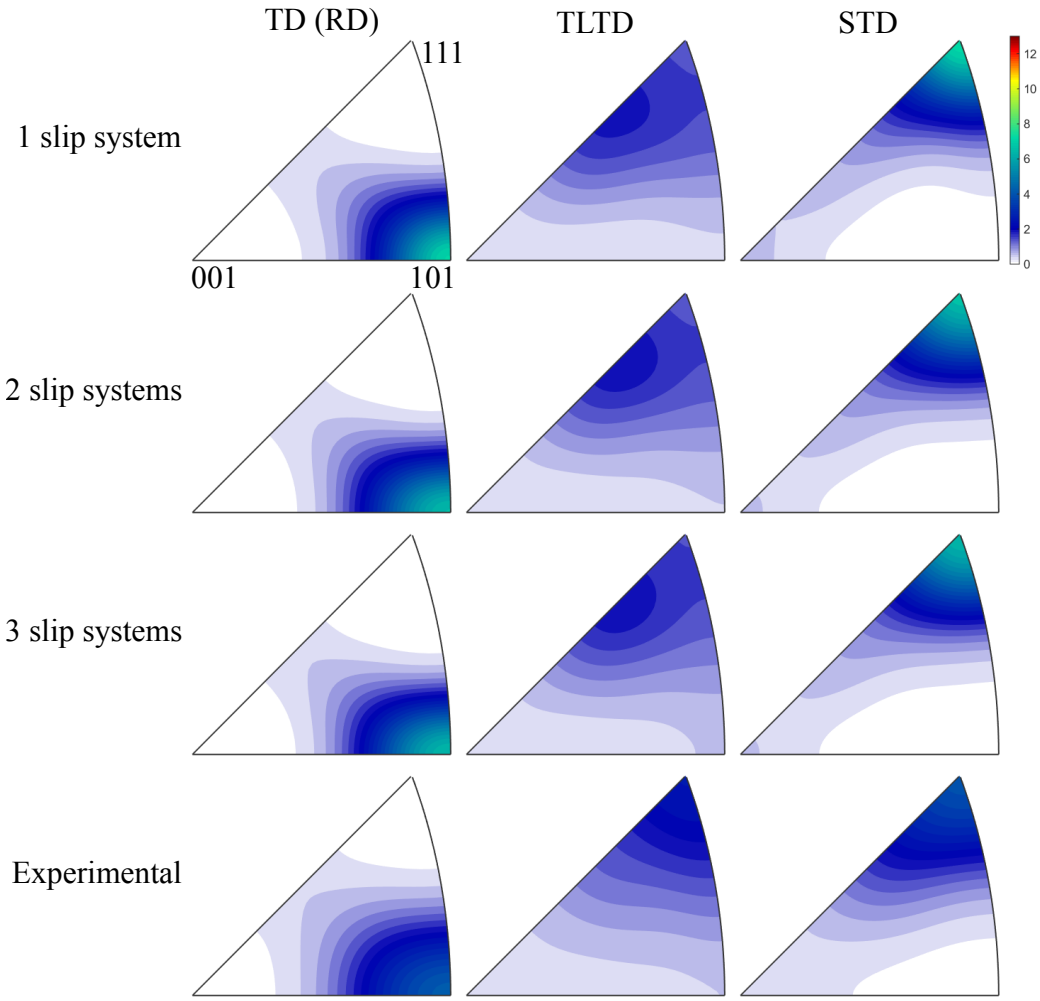

Figure 4.2: IPFs comparing the results from using one, two, and three slip systems with an example simulation. The simulation conditions are tensile deformation with the tensile axis parallel to the RD to a true strain of 0.2. IPFs of the experimental data from the microtexture of a specimen with the same deformation conditions are provided.

The simulated texture output by the VPSC model treats all grains equally. There is one data point per grain. This is considered grain number-

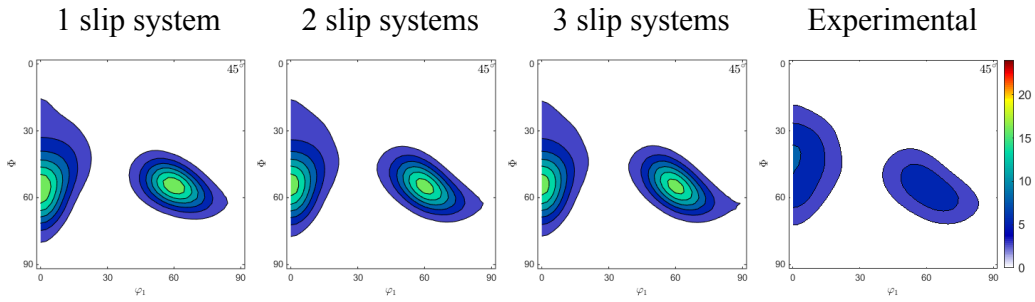

Figure 4.3: The $\varphi_2 = 45°$ Euler slices comparing the results from using one, two, and three slip systems with an example simulation. The simulation conditions are tensile deformation with the tensile axis parallel to the RD to a true strain of 0.2. The $\varphi_2 = 45°$ Euler slice of the experimental data from the microtexture of a specimen with the same deformation conditions are provided.

weighted data. EBSD data, however, take grain size into account. Larger grains have more data points than smaller grains, giving more weight to larger grains. This is considered volume-weighted data. In order to directly compare the VPSC simulated texture with experimental data, the VPSC simulation results were converted to a volume-weighted measure. An original Mathematica [66] script was written to carry out this conversion. An "intensity" value for each grain was calculated to determine its volume-weight. This intensity value was determined by dividing the volume fraction of a grain by the volume fraction of the smallest grain in the data file. This resulted in the smallest grain having an intensity value of 1. The intensity value was then multiplied by 5 and rounded to the nearest whole number. Multiplying the intensity value by 5 increased the variation from the floating point error. A text file containing the volume-weighted grains was generated by repeating each grain identity based on their calculated intensity.

4.4.4 Analysis of VPSC simulation results

The VPSC model only simulates the effect of lattice rotation on texture development. Therefore, the VPSC simulation results confirm that the lattice rotation effect is captured experimentally from room-temperature tensile test specimens. The volume-weighted form of the VPSC simulated texture data was imported into MTEX for analysis. ODFs were calculated using the default settings. The ODFs of the simulated and experimentally determined texture after room-temperature tensile deformation were compared.

Chapter 5

Results

5.1 Recrystallized material

5.1.1 Recrystallization Study

The goal of the recrystallization study was to characterize the microstructural evolution of the Ti-IF steel sheet material during static annealing through hardness measurements. Hardness is a measure of the material's resistance to deformation [61]. Dislocations in the grains of the highly-deformed, as-received sheet material resist additional deformation. Strain-free grains consume the highly-deformed microstructure during recrystallization. These strain-free grains are more susceptible to deformation. It is therefore expected for the hardness of the as-received material to be higher than the recrystallized material. Recrystallization would be marked by a rapid drop in hardness. The material is fully recrystallized at the bottom of this drop.

The Rockwell B hardness (HRB) values from the recrystallization study at 850 °C are presented *versus* strain in Figure 5.1. The top and bottom error bars correspond to the maximum and minimum hardness values measured for each specimen. The hardness varied sigmoidally with annealing time. Recrystallization began at approximately 8 seconds. The microstructure was fully

recrystallized by 11 seconds. During recrystallization, the hardness measurements varied most widely. This was because the microstructure was comprised of a mixture of the deformed and recrystallized microstructures. Higher hardness measurements would be recorded in a region of primarily deformed grains. A lower hardness value would be recorded in a region of primarily recrystallized grains. It should be noted that the Ti-IF steel sheet thickness is thinner than the minimum recommended by ASTM standard E18-17$^{\varepsilon 1}$ for the low hardness of the recrystallized material [61]. Therefore, interpretation of these data should be limited to only differences in hardness values.

5.1.2 Microstructure and microtexture

A Ti-IF steel specimen that was statically annealed for 30 minutes at 850 °C was imaged using BSE channeling contrast in an SEM. The three unique planes of this fully recrystallized specimen were imaged. These were (i) the RD-LTD plane in Figure 5.2, (ii) the RD-STD plane in Figure 5.3, and (iii) the LTD-STD plane in Figure 5.4. Both Figures 5.3 and 5.4 span the thickness of the sheet. From these BSE images, it is apparent that the microstructure of the recrystallized material is composed of equiaxed grains. Indications of banding are present in the RD-STD plane because the grains at the center of the specimen appear to be significantly larger than the rest of the grains in the microstructure.

EBSD data were collected for the three planes of the recrystallized Ti-IF steel specimen statically annealed for 30 minutes at 850 °C. These data are

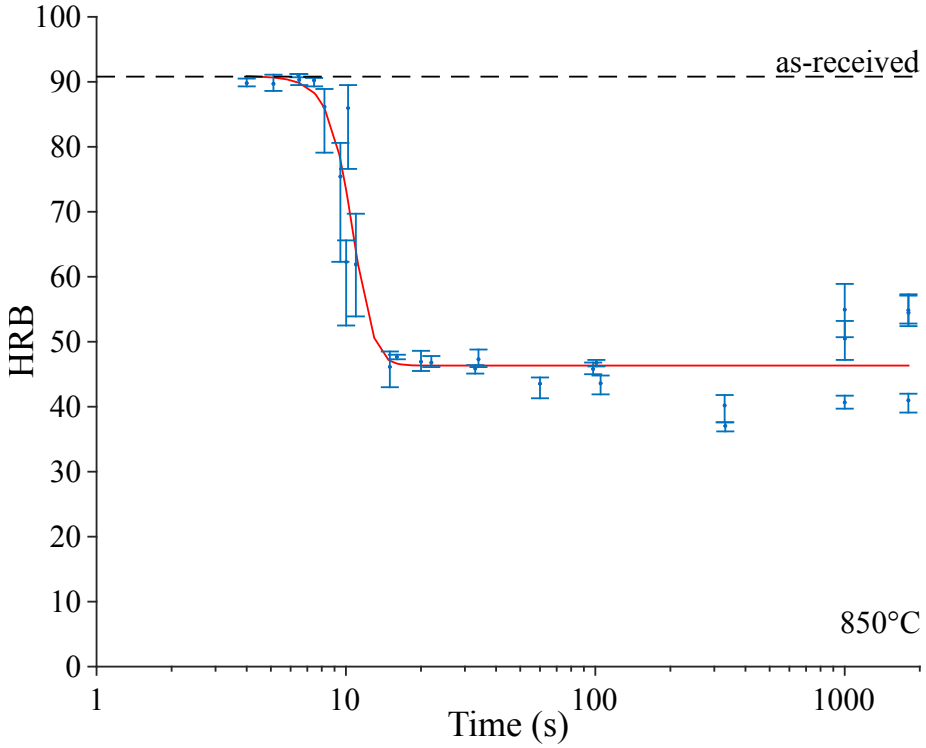

Figure 5.1: A plot of the Rockwell B hardness (HRB) is shown *versus* annealing time for Ti-IF steel specimens annealed at 850 °C using a salt pot. The scale on the x-axis is logarithmic.

presented as IPF maps with respect to both the RD and STD. A representative scan of the RD-LTD plane is presented in Figure 5.5, the RD-STD plane in Figure 5.6, and the LTD-STD plane in Figure 5.7. For both Figures 5.6 and 5.7, the specimen centerline is approximately at the horizontal center of the IPF map. From these maps, it is apparent that texture is uniform and consistent for all three planes. Figure 5.6 does not indicate any signs of banding in texture or grain size through the thickness of the material.

IPFs and φ_2=45° Euler slices from the EBSD data of the RD-LTD plane

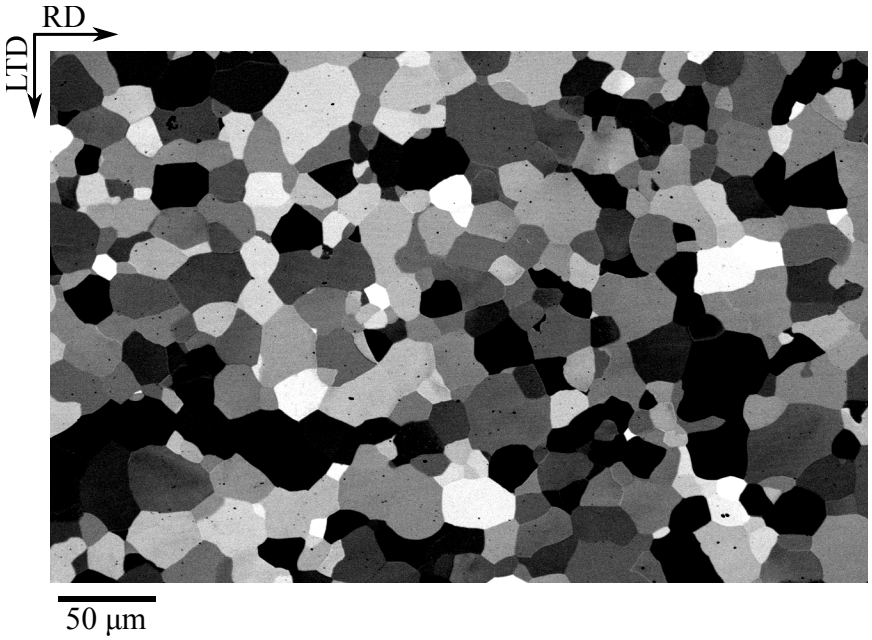

Figure 5.2: A BSE channeling contrast image of the RD-LTD plane of the Ti-IF steel annealed at 850 °C for 30 minutes is shown.

are presented in Figures 5.8 and 5.9, respectively. The initial recrystallized textures for the specimen TD at 0°, 90°, and 45° with respect to the RD are shown. For all three TD orientations, the initial recrystallized crystallographic texture with respect to the STD remains the same. Variations in the initial crystallographic texture were observed with respect to the TD and TLTD. This was consistent with expectations because the TD was only rotated in the RD-LTD plane, which does not affect the STD. The initial recrystallized textures were dominated by a γ-fiber for all three specimen tensile orientations. The γ-fiber was fairly uniform when the specimen TD was oriented at 0° and 90°. When the specimen TD was oriented at 0° with respect to the RD, the widest spread of the γ-fiber was at the intersection with the α-fiber. When the

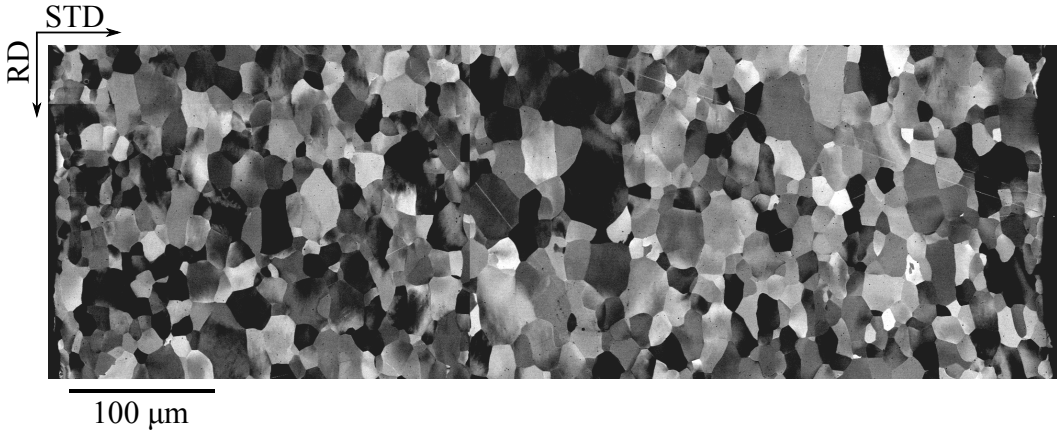

Figure 5.3: A BSE channeling contrast image of the RD-STD plane of the Ti-IF steel annealed at 850 °C for 30 minutes is shown. The image spans the thickness of the sheet.

specimen TD was oriented at 90° with respect to the RD, the widest spread of the γ-fiber was when it intersected with the ε-fiber. The initial recrystallized texture when the specimen TD was at 45° with respect to the RD was a γ-fiber with some peak strengthening of the $\{111\}\langle 110\rangle$ texture component.

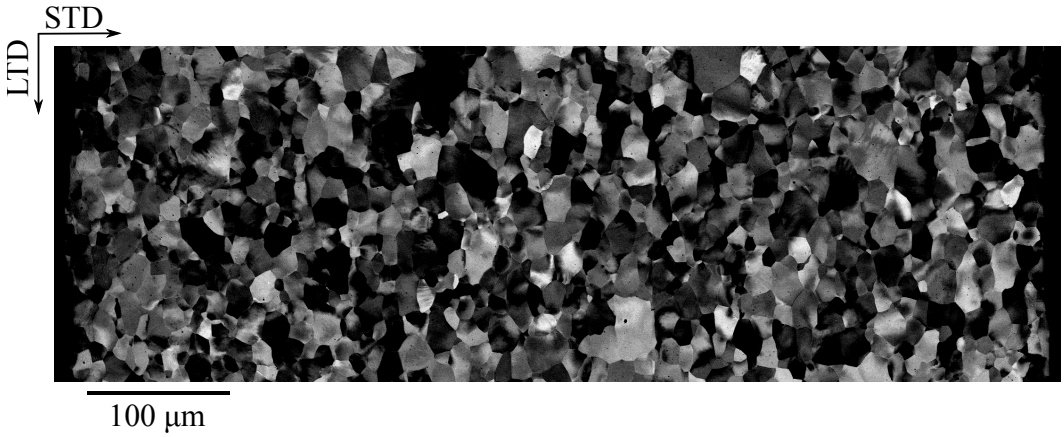

Figure 5.4: A BSE channeling contrast image of the LTD-STD plane of the Ti-IF steel annealed at 850 °C for 30 minutes is shown. The image spans the thickness of the sheet.

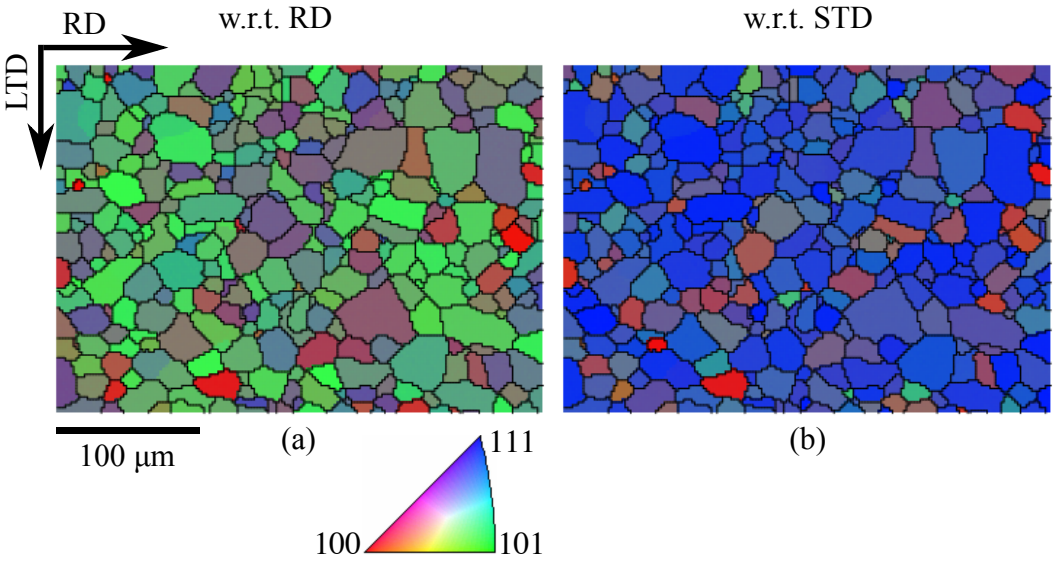

Figure 5.5: IPF maps of EBSD data from the initial recrystallized texture are shown with respect to the (a) RD and (b) STD. The RD-LTD plane is shown. The specimen was fully recrystallized for 30 minutes at 850 °C.

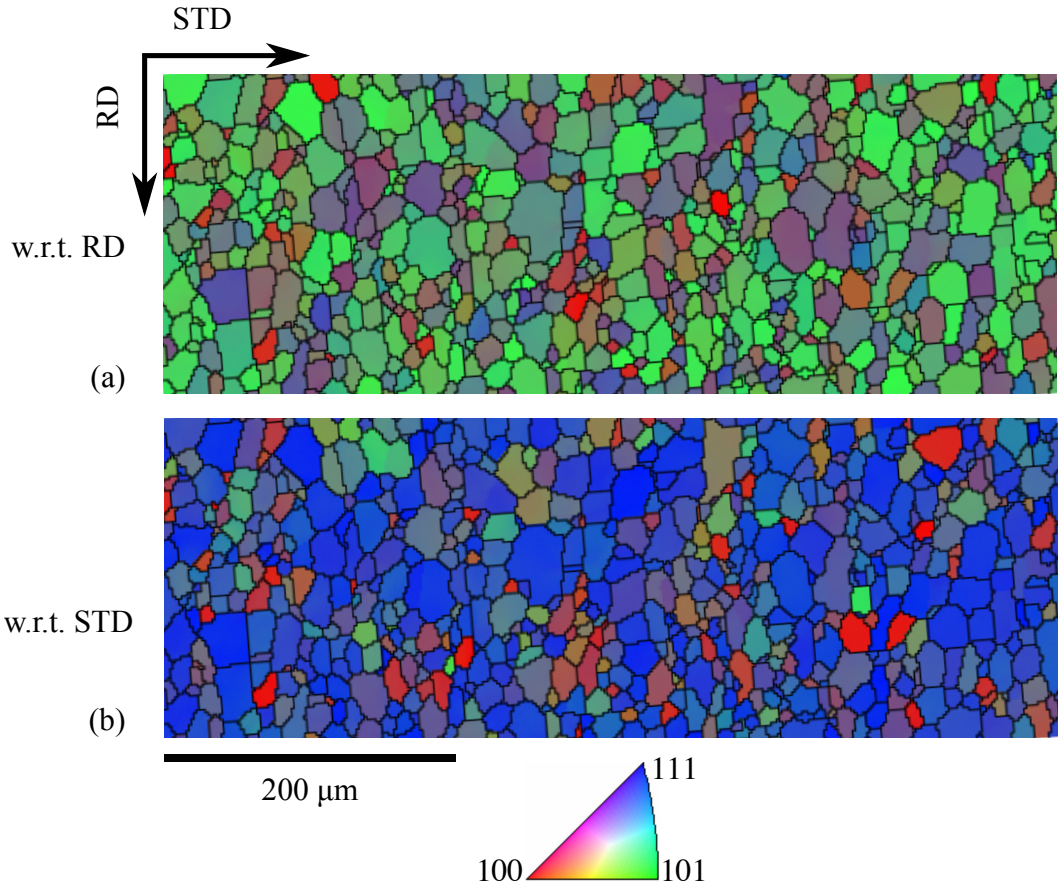

Figure 5.6: IPF maps of EBSD data of the initial recrystallized texture are shown with respect to the (a) RD and (b) STD. The RD-STD plane is shown. The specimen was fully recrystallized for 30 minutes at 850 °C. The centerline of the specimen is approximately at the horizontal center of the IPF map.

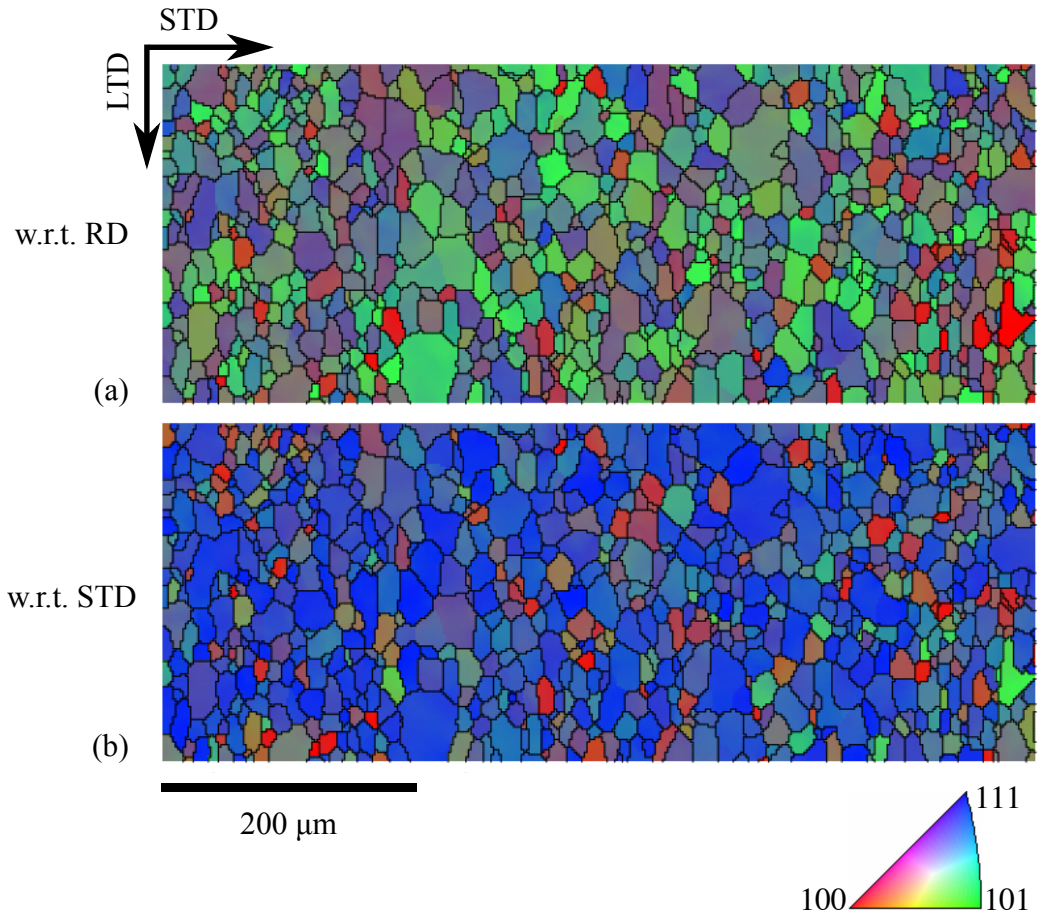

Figure 5.7: IPF maps of EBSD data of the initial recrystallized texture are shown with respect to the (a) RD and (b) STD. The LTD-STD plane is shown. The specimen was fully recrystallized for 30 minutes at 850 °C. The centerline of the specimen is approximately at the horizontal center of the IPF map.

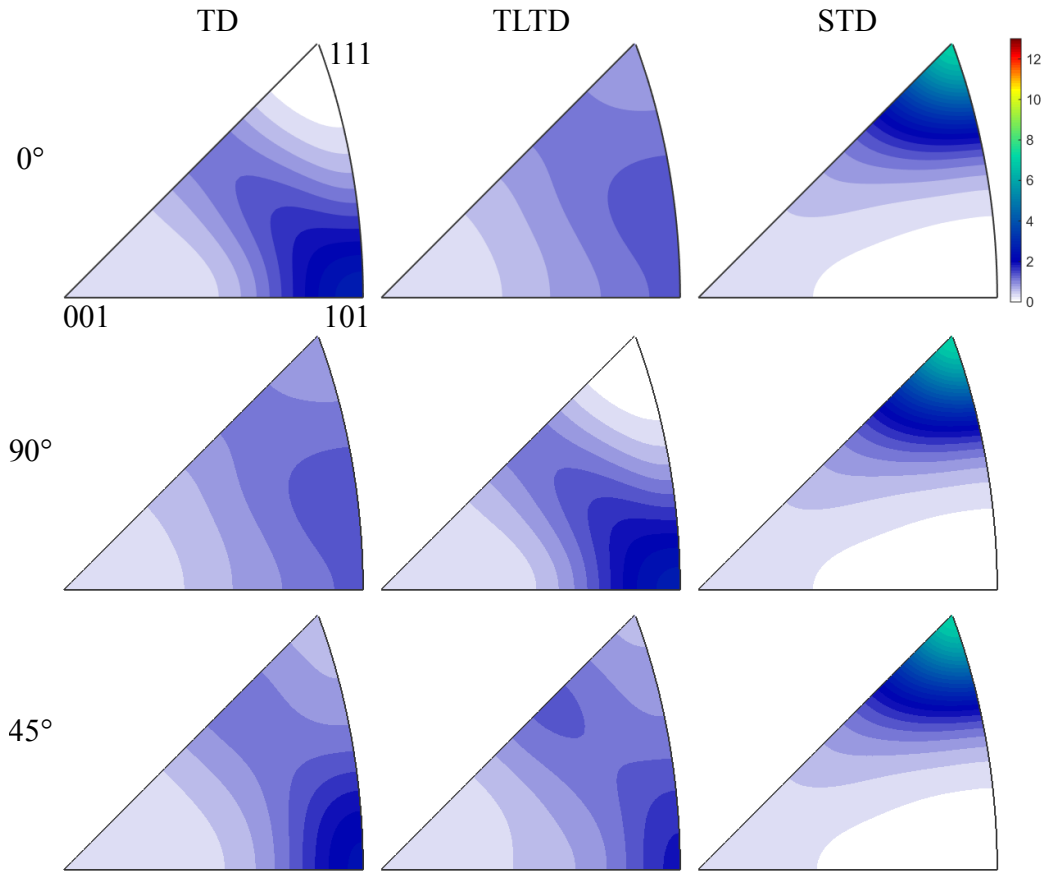

Figure 5.8: IPFs of EBSD data show the initial recrystallized textures with the specimen TD at 0°, 90°, and 45° with respect to the RD. This specimen was fully recrystallized for 30 minutes at 850 °C.

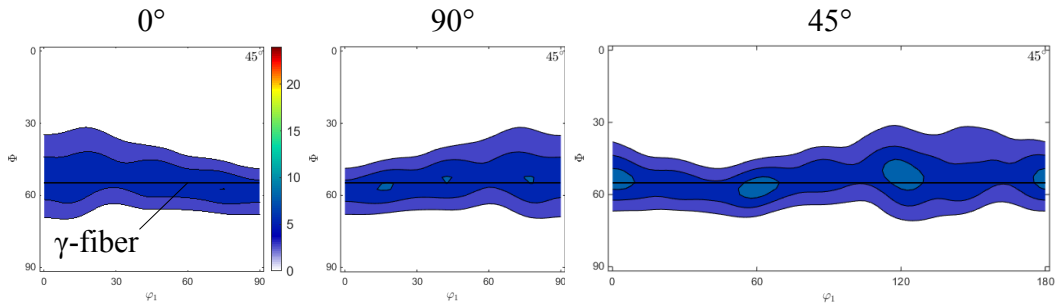

Figure 5.9: The φ_2=45° Euler slices of EBSD data show the initial recrystallized textures for the specimen TD at 0°, 90°, and 45° with respect to the RD. This specimen was fully recrystallized for 30 minutes at 850 °C.

5.2 Room-temperature tensile tests

5.2.1 Tensile test results

Ti-IF steel specimens for all three specimen tensile orientations were deformed in uniaxial tension at room temperature to true strains of 0.1 and 0.2. A plot of three representative true stress *versus* true strain curves are shown in Figure 5.10. These curves are typical for low-carbon steel. The yield point phenomenon occurred for all three tensile specimen orientations. The strengths were observed to vary slightly with specimen tensile orientation. The specimen with its TD at 45° with respect to the RD had the highest strength. The specimen with its TD oriented at 0° with respect to the RD had the lowest strength. Variations in strength with specimen tensile orientation were expected because of texture differences between the three specimen tensile orientations. Crosshead extension was used to determine strain because of problems with the extensometer slipping. The crosshead extension does not take into account grip slippage, which introduces inaccuracy into the calculation of strain. Score marks in the gauge region of the specimen were used to determine the specimen's final true strain. These calculated true strain values are provided in Table 5.1.

5.2.2 Microstructures and microtextures

Ti-IF steel specimens were imaged using BSE channeling contrast in an SEM. These specimens were orientated with the TD at 90° with respect to the RD and were deformed in uniaxial tension at room-temperature. The

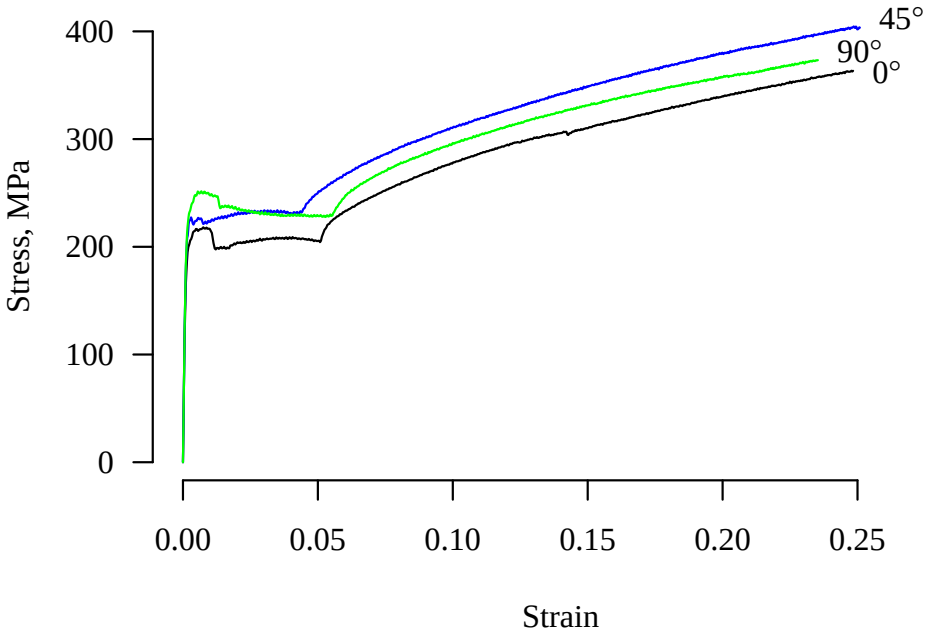

Figure 5.10: True stress-strain data are shown for the Ti-IF steel specimens deformed in uniaxial tension at room temperature.

specimens were deformed to a true strain of 0.1 and 0.2, and their resulting microstructures are shown in the top and bottom images of Figure 5.11, respectively. These images reveal microstructures that are extremely different from the initial recrystallized microstructure. With increasing strain the grains become more deformed and elongated. Figure 5.12 is a BSE image of a specimen with the specimen TD at 0° with respect to the RD deformed to a true strain of 0.2 at room-temperature. This image was taken at a higher

Table 5.1: The true strain of the specimens deformed at room temperature are listed. The true strain was calculated from score marks in the specimen gauge region.

specimen TD w.r.t RD	Intended strain	Measured strain
0°	0.1	0.128
0°	0.2	0.215
90°	0.1	0.115
90°	0.2	0.220
45°	0.1	0.118
45°	0.2	0.219

magnification compared to the images in Figure 5.11. Slip bands are clearly visible in the grains.

EBSD data were collected from specimens deformed in uniaxial tension at room-temperature to true strains of 0.1 or 0.2 for all three specimen tensile orientations. IPF maps of the EBSD data with respect to the TD and STD are presented in Figures 5.13 and 5.14, respectively. With increasing strain, the grains in the IPF maps become more elongated and contain deformation substructure represented as various color hues. This is indicative of a large amount of deformation in the grains, confirming the observations made from the BSE images. Two color changes are observed with increasing strain in the IPF maps with respect to the TD for all three orientations: (i) a significant increase in the number of green grains, and (ii) a decrease in grains of other colors, particularly red, blue, and purple grains. This represents an increase of grains orientated with the <110>||TD and a decrease of grains oriented

with the <100>, <111>, and <112>||TD. There did not appear to be any significant change in texture with increased strain in the IPF maps with respect to the STD.

Figures 5.15 and 5.16 present the EBSD data in the form of IPFs for specimens deformed to true strains of 0.1 and 0.2, respectively. From these figures, it is apparent that all three specimen tensile orientations produced a strengthening of the <110>||TD with increased strain. This texture evolution occurred at the expense of other orientations with respect to the TD. These observations are similar to those from the IPF maps in Figure 5.13. With increasing strain, a slight weakening of the {111} plane orientation with respect to the STD was also detected.

Figure 5.17 shows the φ_2=45° Euler slices from the EBSD data. Room-temperature uniaxial tension strengthens texture components within the α-fiber along the TD at the the expense of texture components from within the γ-fiber. The specific α-fiber texture components that were strengthened were observed to depend on the initial recrystallized texture. The widest range of α-fiber texture components was strengthened when the specimen TD was oriented at 0° with respect to the RD. The narrowest range of α-fiber texture components was strengthened when the specimen TD was orientated at 90° with respect to the RD. It is worth reiterating that the recrystallized γ-fiber had the largest overlap with the α-fiber when the specimen TD was oriented at 0° with respect to the RD. The smallest overlap was observed when the specimen TD was oriented at 90° with respect to the RD. This

indicates that room-temperature deformation strengthened the intensity of texture components within the α-fiber along the TD that intersected with the recrystallized γ-fiber.

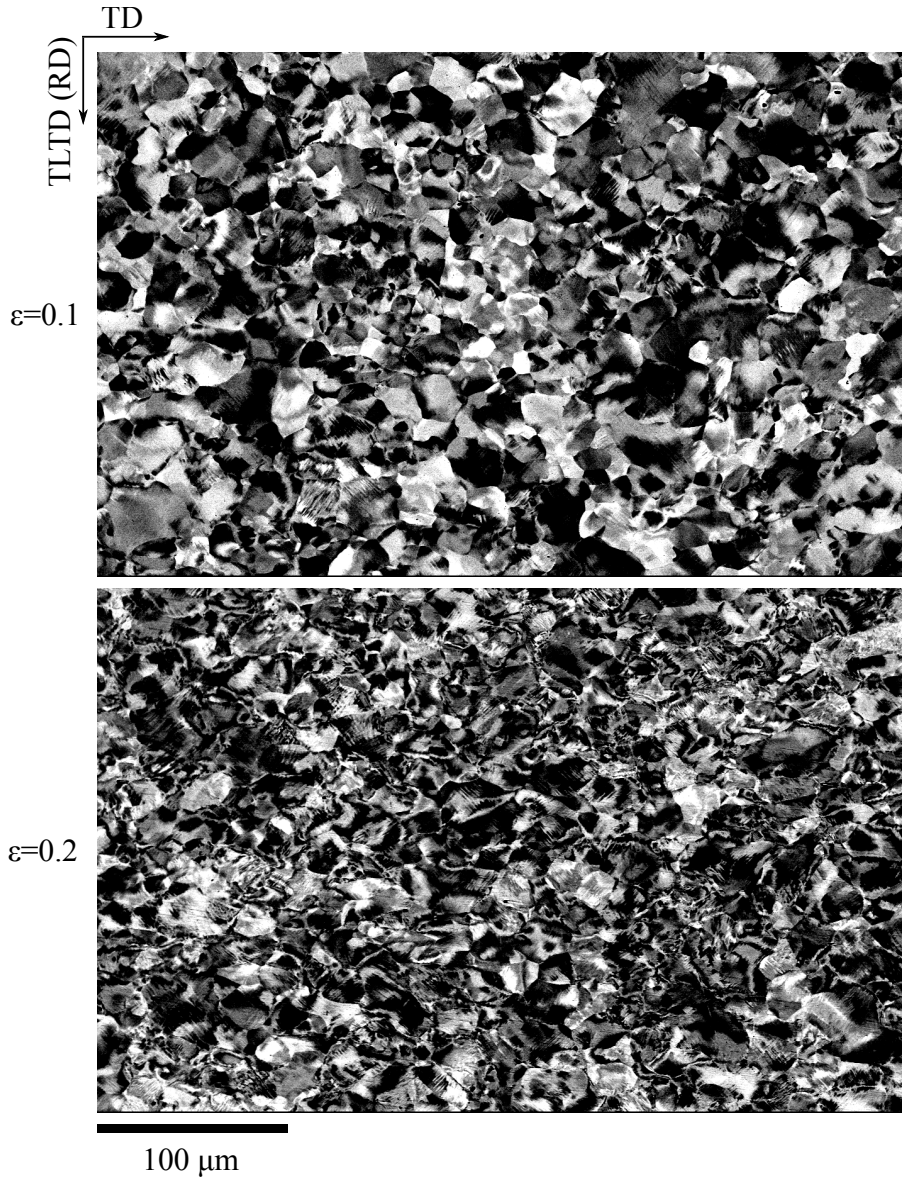

Figure 5.11: BSE channeling contrast images of the TD-TLTD plane of Ti-IF steel specimens deformed in uniaxial tension at room temperature are shown. The images on the top and bottom are from specimens deformed to true strains of 0.1 and 0.2, respectively. Both specimens were oriented with the specimen TD at 90° with respect to the RD. The scale bar on the bottom left applies to both images.

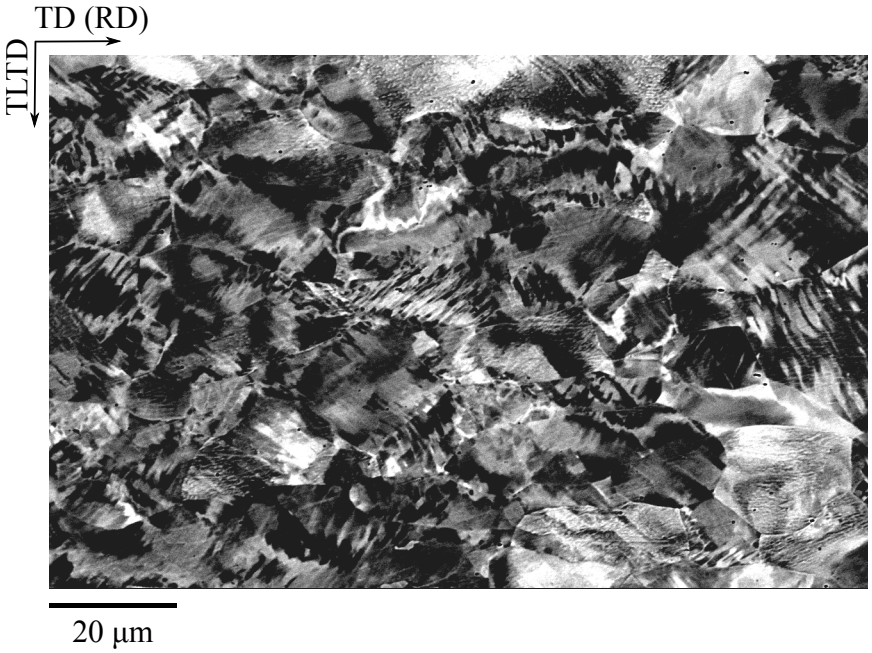

Figure 5.12: A BSE channeling contrast image is shown from the TD-TLTD plane of a Ti-IF steel specimen deformed in uniaxial tension at room-temperature. The specimen TD was oriented at 0° with respect to the RD. The specimen was deformed to a true strain of 0.2.

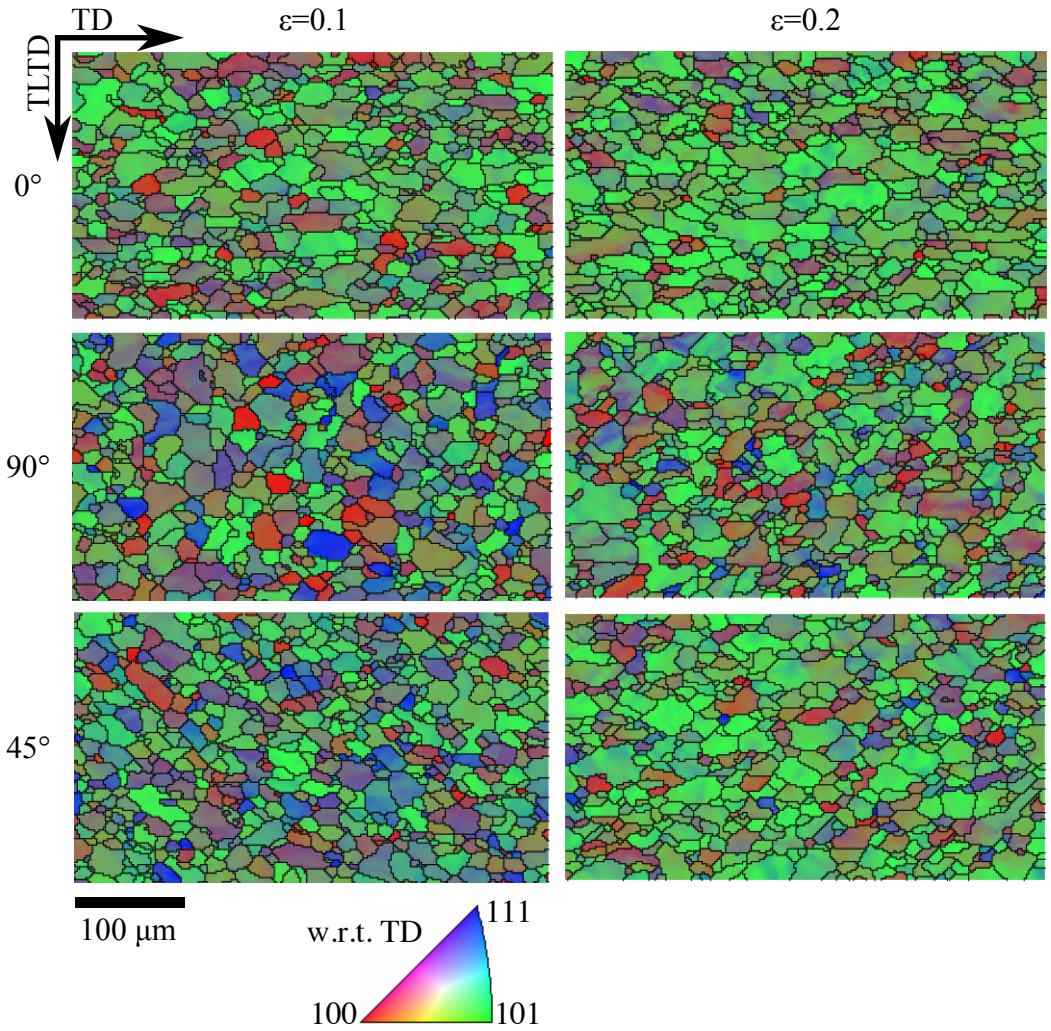

Figure 5.13: IPF maps of EBSD data from specimens deformed in uniaxial tension at room temperature are shown. The maps are with respect to the TD. The specimen TD was at 0°, 90°, and 45° with respect to the RD, as labeled for each row of images. The specimens were deformed to true strains of 0.1 and 0.2, as labeled in each column of images. The scale bar on the bottom left applies to all of the IPF maps.

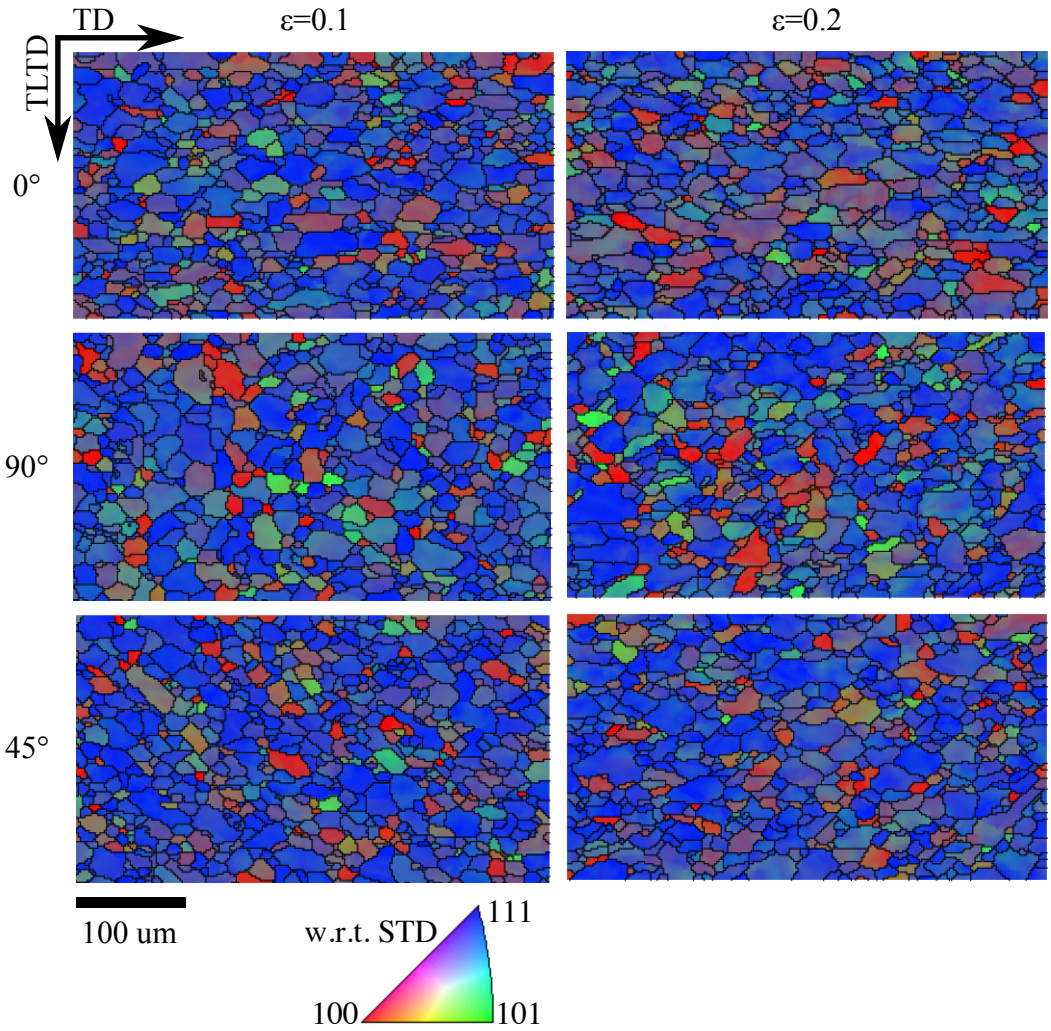

Figure 5.14: IPF maps of EBSD data from specimens deformed in uniaxial tension at room temperature are shown. The maps are with respect to the STD. The specimen TD was at 0°, 90°, and 45° with respect to the RD, as labeled for each row of images. The specimens were deformed to true strains of 0.1 and 0.2, as labeled in each column of images. The scale bar on the bottom left applies to all of the IPF maps.

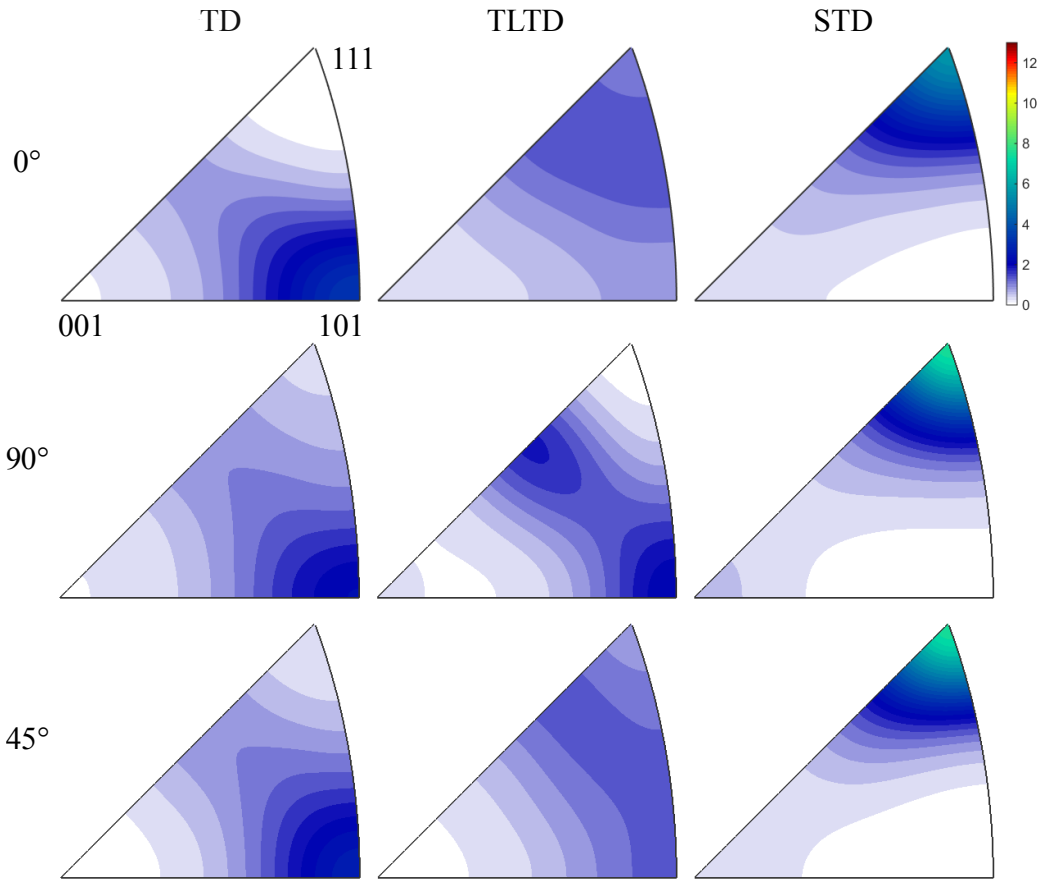

Figure 5.15: IPFs of EBSD data for specimens deformed at room temperature to a true strain of 0.1 are shown. The specimen TD was oriented at 0°, 90°, and 45° with respect to the RD, as labeled in each row.

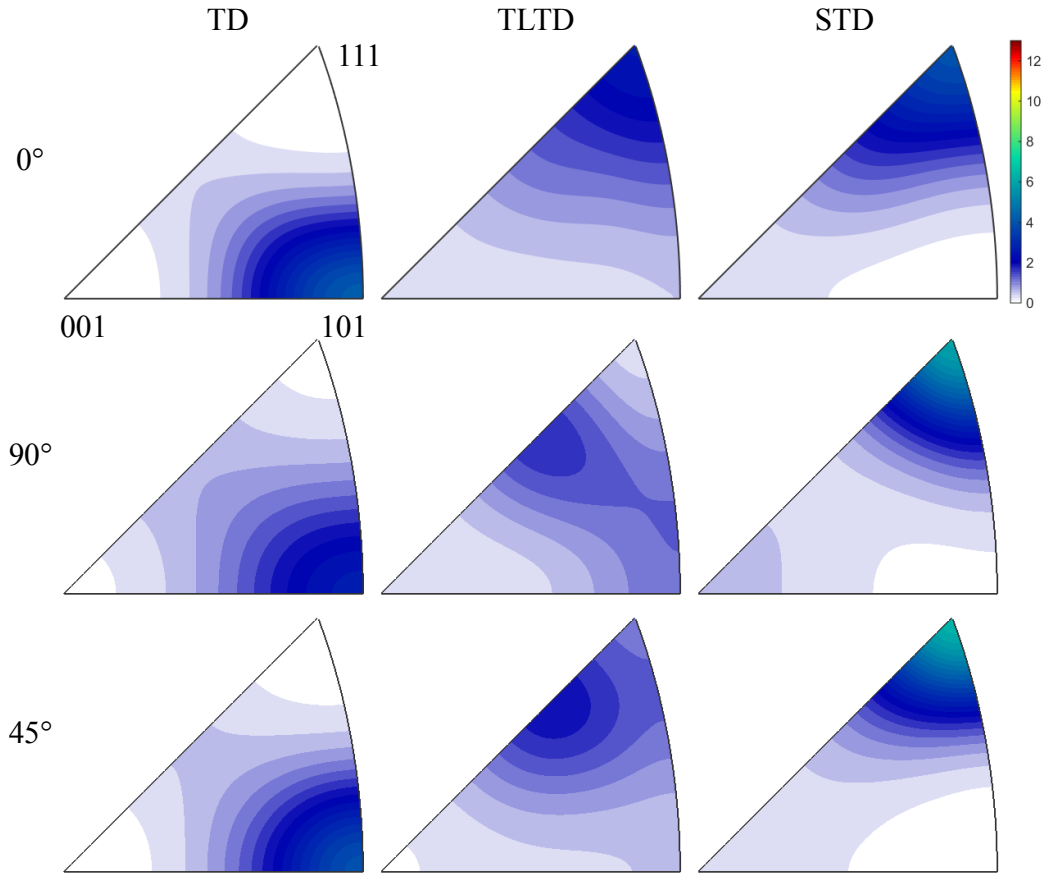

Figure 5.16: IPFs of EBSD data for specimens deformed at room temperature to a true strain of 0.2 are shown. The specimen TD was oriented at 0°, 90°, and 45° with respect to the RD, as labeled in each row.

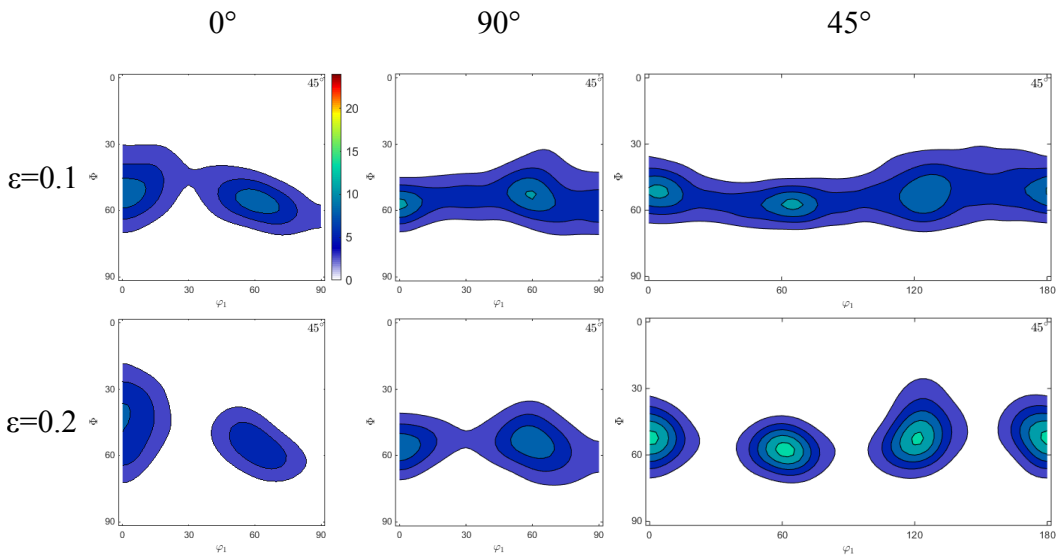

Figure 5.17: The φ_2=45° Euler slices of EBSD data are shown for specimens deformed at room-temperature to true strains of 0.1 and 0.2. The specimens were oriented with the TD at 0°, 90°, and 45° with respect to the RD, as labeled in each column.

5.3 High-temperature tensile tests

5.3.1 Tensile test results

Ti-IF steel specimens were deformed in uniaxial tension at 850 °C at a true-strain rate of 10^{-4} s^{-1} in air and in vacuum. The specimens were deformed to true strains of 0.1 and 0.2 for all three specimen tensile orientations. Two representative true stress *versus* true strain curves are shown in Figure 5.18. These specimens were deformed to a true strain of 0.2 in vacuum. The specimen tensile orientations were at 90° and 45° with respect to the RD. The steady-state flow stress was observed to vary slightly with specimen tensile orientation. The specimen with its TD oriented at 45° with respect to the RD had the highest steady-state flow stress (16.2 MPa). The specimen with its TD oriented at 0° with respect to the RD had the lowest steady-state flow stress (13.8 MPa) [13]. These differences in the steady-state flow stress among the three specimen orientations match the order in strengths measured at room temperature (See Section 5.2.1). Variations in steady-state flow stress among the three specimen tensile orientations were expected from their differences in texture. All specimens reached a steady-state flow stress well before a true strain of 0.1. No significant changes in flow stress were observed for either specimen during steady state. Therefore, there is no evidence that DAGG or DRX occurred during high-temperature uniaxial tension testing.

A Ti-IF steel specimen was deformed in uniaxial tension at 850 °C at a constant true-strain rate of 10^{-3} s^{-1} to a true strain of 0.2 in air. The specimen TD was oriented at 0° with respect to the RD. The axial force *versus*

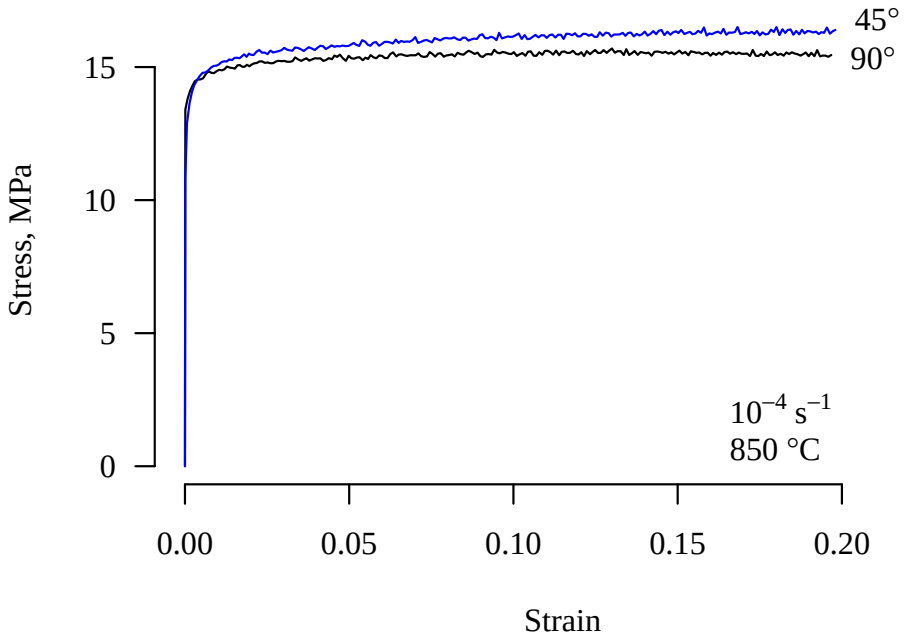

Figure 5.18: True stress-strain data are shown for the Ti-IF steel specimens deformed in uniaxial tension in vacuum at 850 °C at a constant true-strain rate of 10^{-4} s^{-1}.

axial displacement from this test is shown in Figure 5.19. Stress-strain curves could not be calculated because the specimen oxidized during testing. This prevented an accurate cross-sectional area from being measured. Fluctuations in the axial force that might indicate DRX were not observed.

A Ti-IF steel specimen was deformed in uniaxial tension at a constant true-strain rate of 10^{-5} s^{-1} to a true strain of 0.2 in vacuum. The specimen

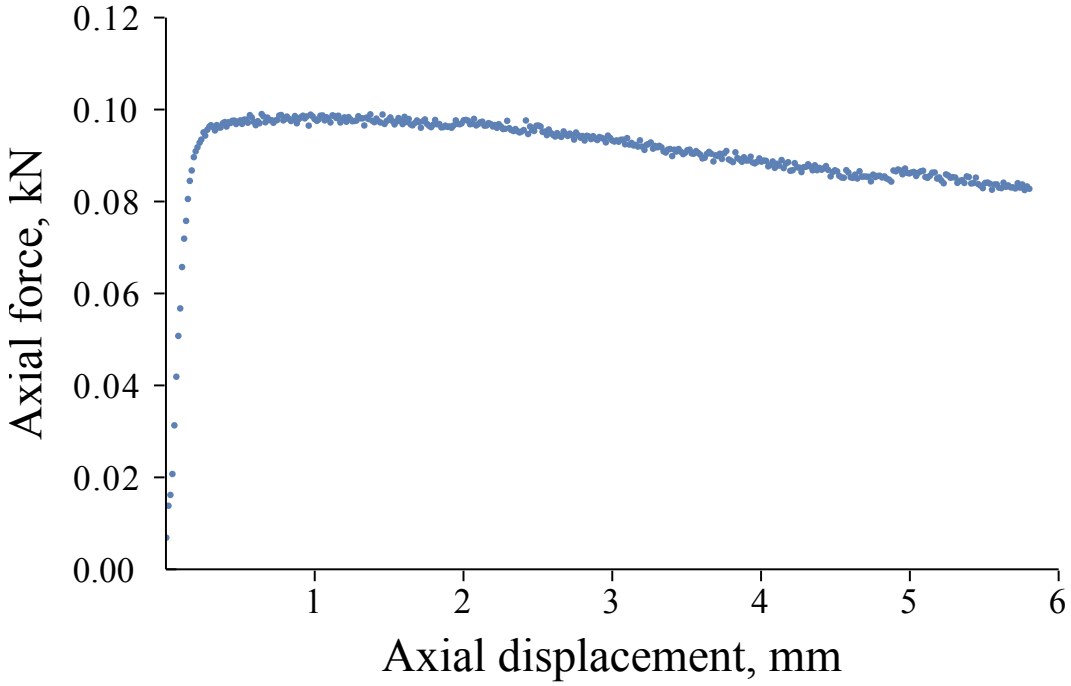

Figure 5.19: Axial force is plotted *versus* axial displacement for a a specimen deformed in uniaxial tension in air at 850 °C at a constant true-strain rate of 10^{-3} s^{-1} to a true strain of 0.2. The specimen TD was oriented at 0° with respect to the RD.

TD was oriented at 0° with respect to the RD. The true stress-strain curve is presented in Figure 5.20. No rapid drop in flow stress suggesting the occurrence of DAGG was observed.

5.3.2 Microstructures and microtextures

Ti-IF steel specimens deformed at elevated-temperature were imaged using BSE channeling contrast in an SEM. The specimens were deformed in uniaxial tension at 850 °C at a constant true-strain rate of 10^{-4} s^{-1} in air and water-quenched. Figure 5.21 shows the microstructures of specimens with the

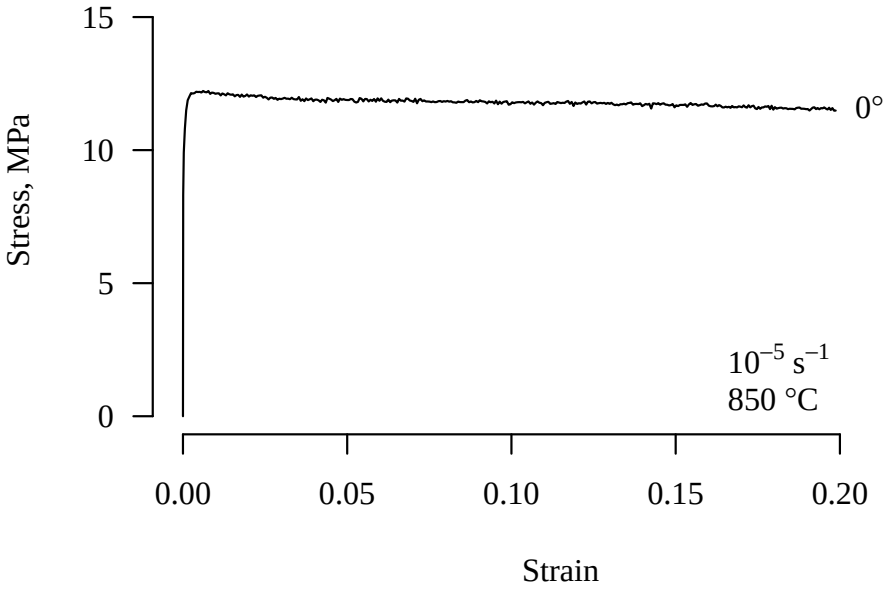

Figure 5.20: True stress-strain data are shown for the Ti-IF steel specimens deformed in uniaxial tension in vacuum at 850 °C at a constant true-strain rate of 10^{-5} s^{-1}. The specimen TD was oriented at 0° with respect to the RD.

specimen TD at 45° with respect to the RD tested to true strains of 0.1, top, and 0.2, bottom. The microstructures of both specimens were composed of equiaxed grains that were significantly less deformed than the microstructures after room-temperature deformation. Grain size was observed to increase with strain. Subgrains were visible in both microstructures.

The microstructure of the Ti-IF steel specimen deformed at a constant

true-strain rate of 10^{-3} s^{-1} with the specimen TD at 0° to the RD is shown by the BSE image in Figure 5.22. The specimen was tested in air and water-quenched. The microstructure was composed of large equiaxed grains that contained subgrains. This microstructure does not indicate the occurrence of DRX.

EBSD data were collected for the specimens deformed at 850 °C at a constant true-strain rate of 10^{-4} s^{-1}. These specimens were deformed to true strains of 0.1 or 0.2 for all three specimen tensile orientations. A representative EBSD scan for each deformation condition is presented in the form of IPF maps with respect to the TD, Figure 5.23, and STD, Figure 5.24. Like the BSE images, the microstructures were composed of equiaxed grains that increase in size with strain. When qualitatively comparing the texture between the specimens deformed to true strains of 0.1 and 0.2, there was no significant change in texture with respect to the TD or STD.

EBSD data from all the specimens tested at 850 °C and 10^{-4} s^{-1} (both in air and in vacuum) are presented as IPFs for true strains of 0.1, Figure 5.25, and 0.2, Figure 5.26. This presentation permits a quantitative examination of the texture evolution with high-temperature deformation. High-temperature deformation strengthened texture components ranging from the <110> to the <112>||TD at the expense of other texture components with respect to the TD. A strengthening of the <111>||STD was also observed. It should be noted that when the specimen TD was orientated at 45° with respect to the RD from a true strain of 0.1 to 0.2, the <111>||STD decreased slightly.

Figure 5.27 presents the EBSD data of Figures 5.25 and 5.26 in the form of φ_2=45° Euler slices. For all three specimen TD orientations, the texture consists of a γ-fiber with some peak strengthening of specific components from within the γ-fiber. This matches the observations made from the IPFs of Figures 5.25 and 5.26. There are some differences in texture between the three different specimen TD orientations. When the specimen TD was oriented at 0° with respect to the RD, the {111}<110> had the strongest intensity at a true strain of 0.1. With increased strain, other texture components from within the γ-fiber near the {111}<110> texture component strengthened. This texture evolution appeared to occur at the expense of the {111}<112> texture component from within the γ-fiber. When the specimen TD was at 90° with respect to the RD, strain was observed to increase the overall γ-fiber with the {111}<110> texture component significantly strengthened. No significant texture evolution was observed from a true strain of 0.1 to 0.2 when the specimen TD was at 45° with respect to the RD.

5.3.3 HR-EBSD data and substructure

HR-EBSD data were gathered from specimens deformed in uniaxial tension at 850 °C at a constant true-strain rate of 10^{-4} s^{-1} in air and water-quenched. The specimens were deformed to true strains of 0.1 or 0.2 for all three specimen tensile orientations. ROD maps from the EBSD and HR-EBSD data are presented. Figures 5.28 and 5.29 are from specimens with the TD at 0° with respect to the RD deformed to true strains of 0.1 and 0.2, respectively.

Figures 5.30 and 5.31 are from specimens with the TD at 90° with respect to the RD deformed to true strains of 0.1 and 0.2, respectively. Figures 5.32 and 5.33 present ROD maps from specimens with the TD at 45° with respect to the RD for true strains of 0.1 and 0.2, respectively. Subgrains are clearly visible in each of these maps. The HR-EBSD data was significantly less noisy than the standard EBSD data. This significantly improved identification of subgrains. In general there appeared to be more subgrains with increasing strain. Subgrain size depends on applied stress and not strain during steady-state deformation [7, 39, 40]. Since steady-state was reached by a strain of 0.1, this indicates that the subgrain boundary misorientation increased with strain, improving subgrain delineation in the EBSD data. The ROD maps demonstrate that HR-EBSD resolves many of the important features of subgrains that form during high-temperature tensile deformation.

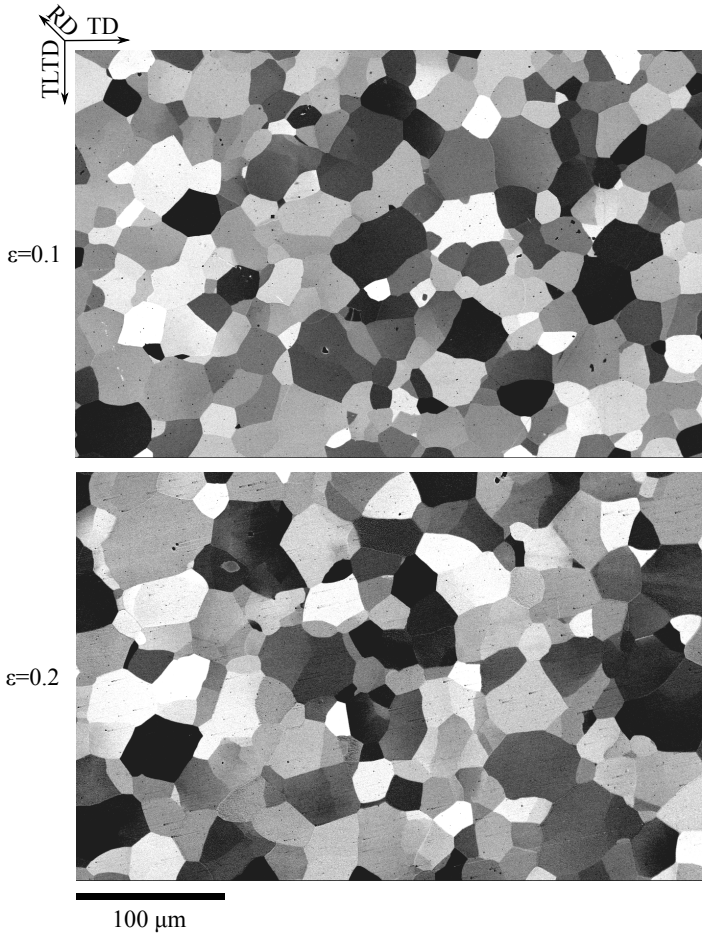

Figure 5.21: BSE channeling contrast images are shown from the TD-TLTD plane of Ti-IF steel specimens. The specimens were deformed in uniaxial tension at 850 °C at a constant true-strain rate of 10^{-4} s^{-1} and water-quenched. The images on the top and bottom are for specimens deformed to true strains of 0.1 and 0.2, respectively. Both specimens were oriented with the TD at 45° with respect to the RD. The scale bar on the bottom left applies to both images.

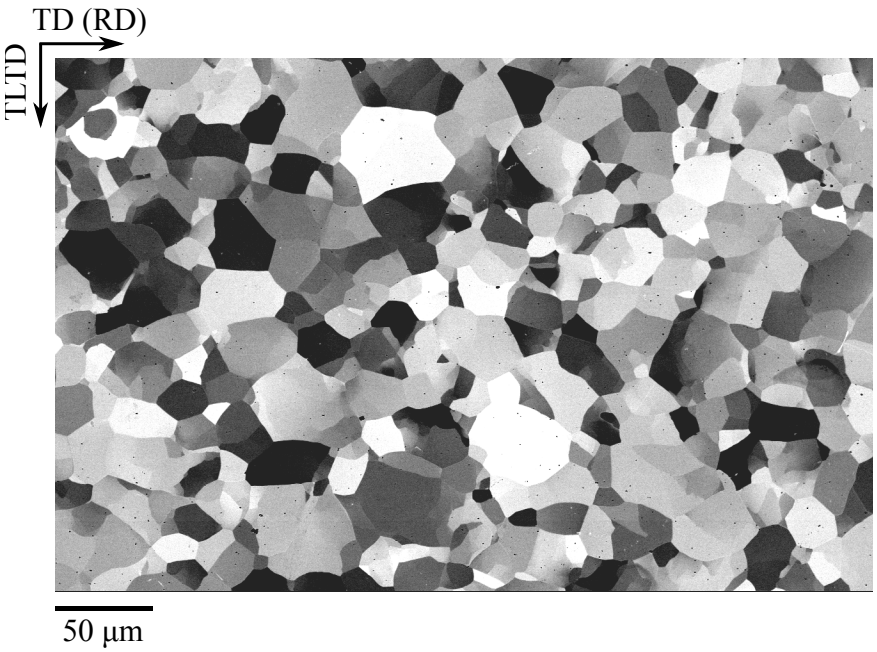

Figure 5.22: A BSE channeling contrast image is shown from the TD-TLTD plane of Ti-IF steel specimens. This specimen was deformed in uniaxial tension at 850 °C at a constant true-strain rate of 10^{-3} s^{-1} to a true strain of 0.2 and water-quenched. The specimen TD was oriented at 0° with respect to the RD.

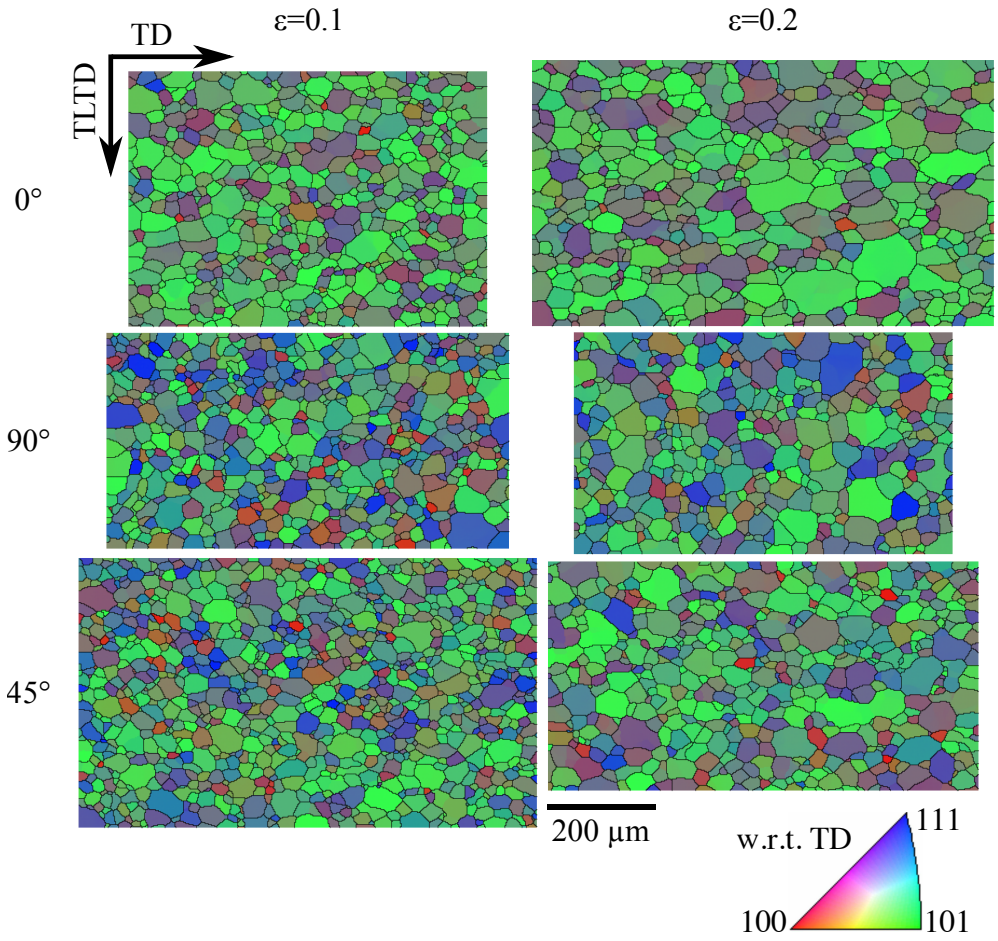

Figure 5.23: IPF maps of EBSD data are shown for the specimens tested in air at 850 °C at a constant true-strain rate of 10^{-4} s^{-1} and water-quenched. The maps are with respect to the TD. The specimen TD was at 0°, 90°, and 45° with respect to the RD, as labeled in each row. The specimens were deformed to true strains of 0.1 and 0.2, as labeled in each column. The scale bar on the bottom left applies to all of the IPF maps.

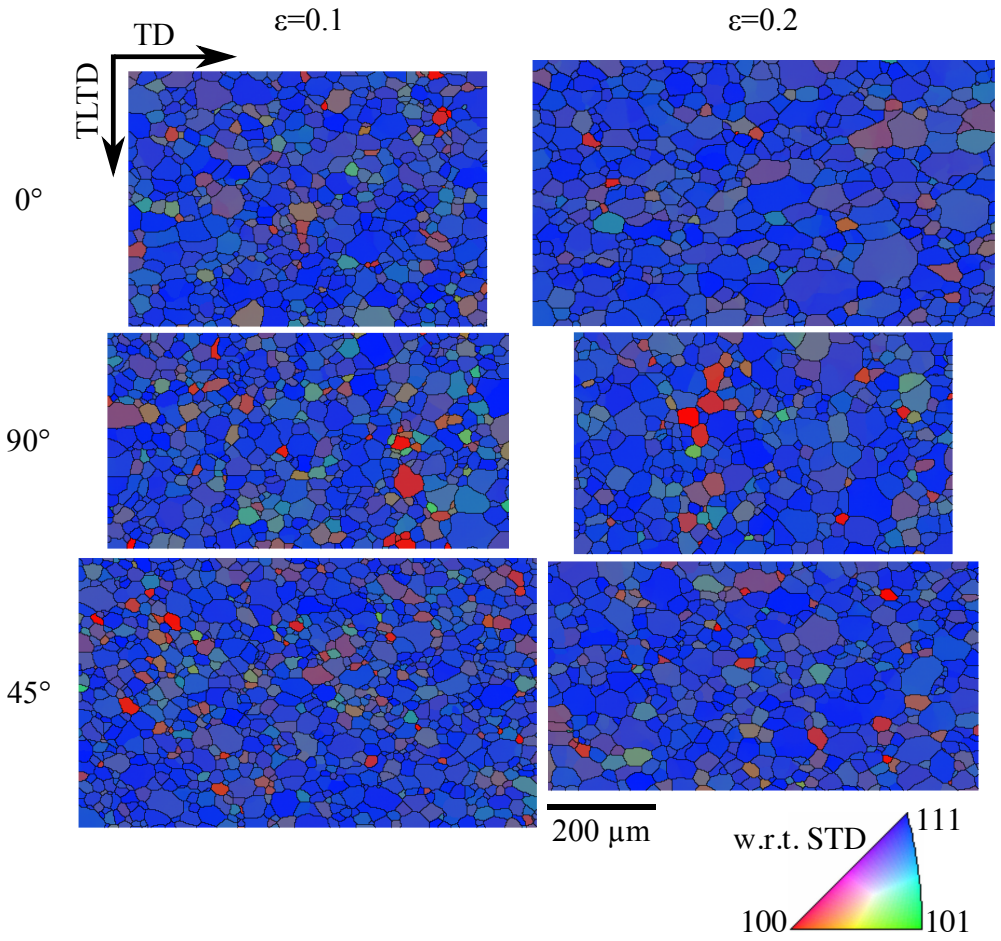

Figure 5.24: IPF maps of EBSD data are shown for the specimens tested in air at 850 °C at a constant true-strain rate of 10^{-4} s^{-1} and water-quenched. The maps are with respect to the STD. The specimen TD was at 0°, 90°, and 45° with respect to the RD, as labeled in each row. The specimens were deformed to true strains of 0.1 and 0.2, as labeled in each column. The scale bar on the bottom left applies to all of the IPF maps.

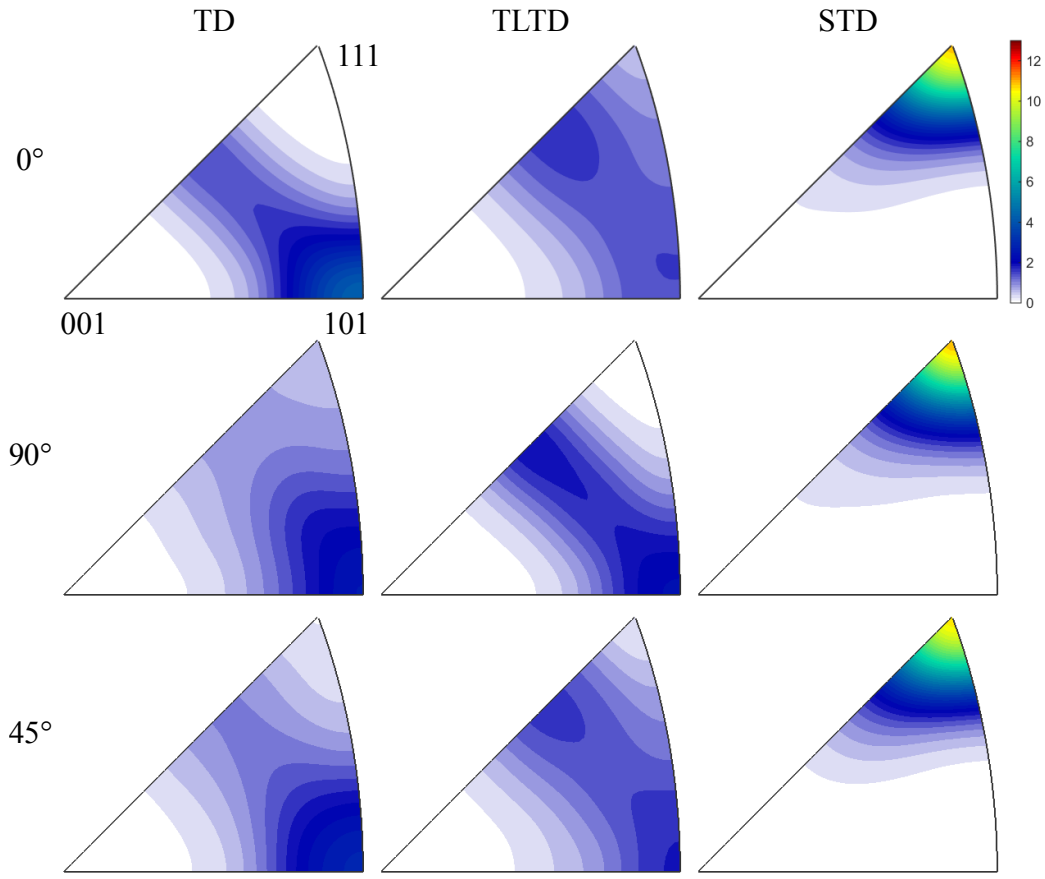

Figure 5.25: IPFs of EBSD data are shown for specimens deformed at 850 °C at a constant true strain of 10^{-4} s^{-1} to a true strain of 0.1. The specimen TD was oriented at 0°, 90°, and 45° with respect to the RD, as labeled in each row.

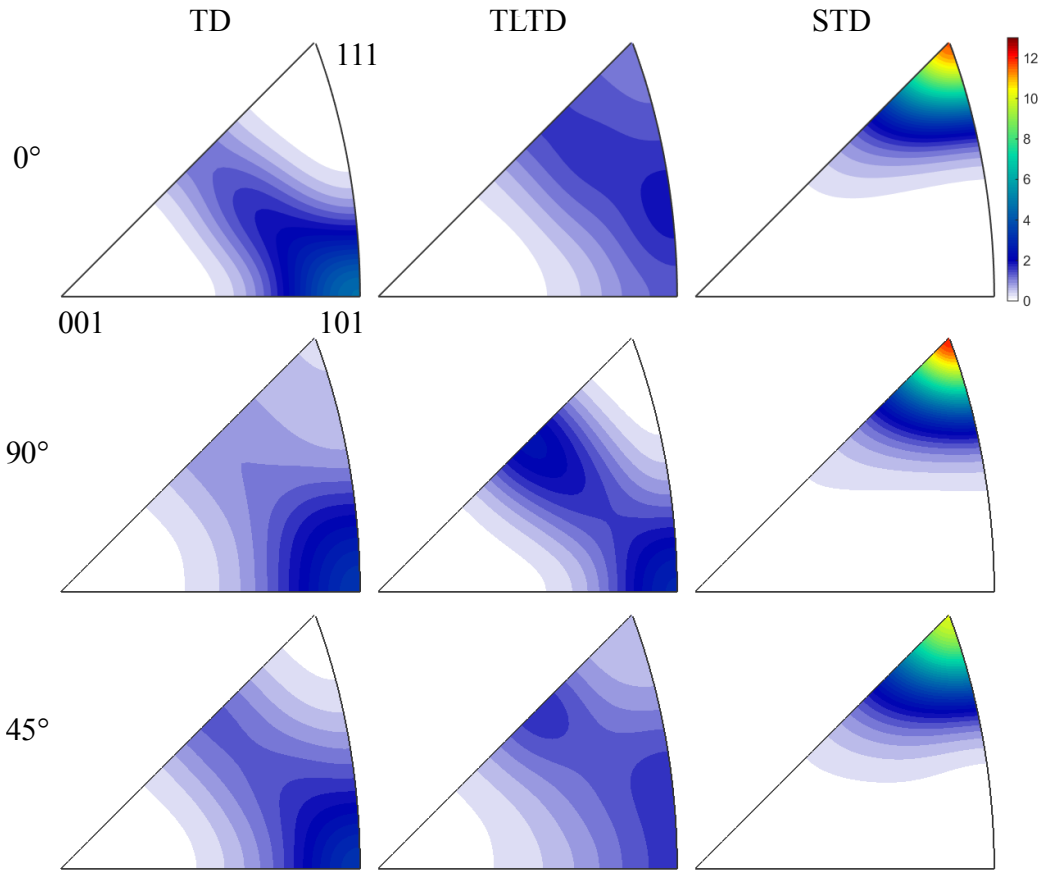

Figure 5.26: IPFs of EBSD data are shown for specimens deformed at 850 °C at a constant true strain of 10^{-4} s^{-1} to a true strain of 0.2. The specimen TD was oriented at 0°, 90°, and 45° with respect to the RD, as labeled in each row.

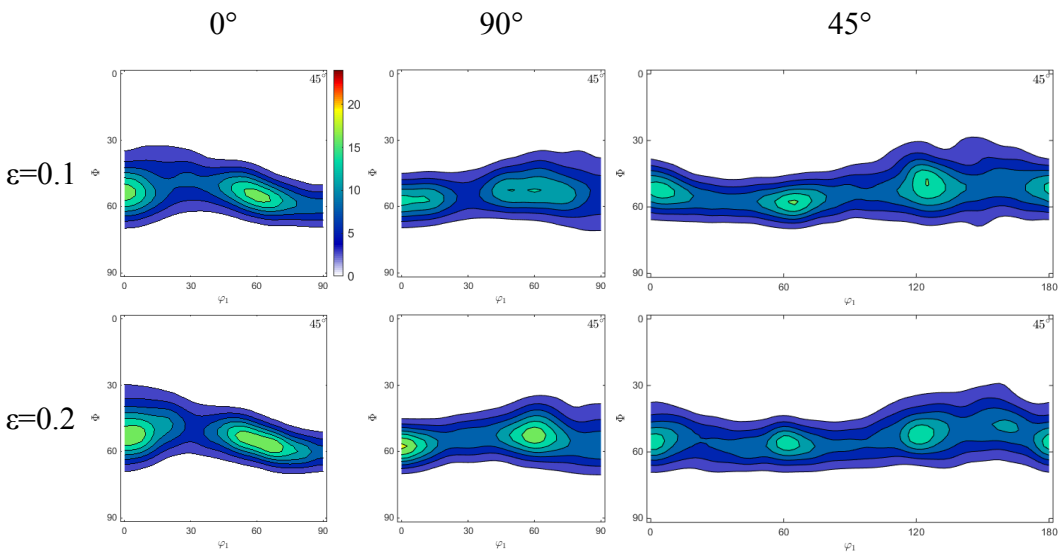

Figure 5.27: The φ_2=45° Euler slices of EBSD data are shown for specimens deformed in uniaxial tension at 850 °C at a constant true-strain rate of 10^{-4} s^{-1} to true strains of 0.1 and 0.2, as labeled in each row. The specimens were oriented with their TD at 0°, 90°, and 45° with respect to the RD, as labeled in each column.

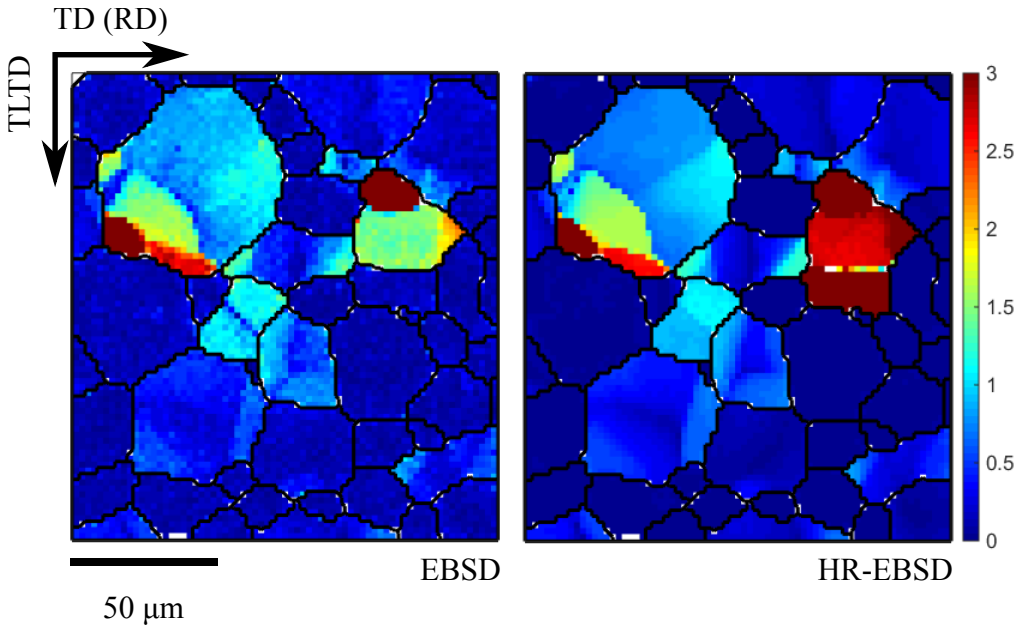

Figure 5.28: ROD maps are shown for a specimen deformed in uniaxial tension in air at 850 °C at a constant true-strain rate of 10^{-4} s^{-1} to a true strain of 0.1 and water-quenched. The specimen TD was oriented at 0° with respect to the RD. The map on the left was produced using standard-resolution EBSD data and the map on the right with HR-EBSD data.

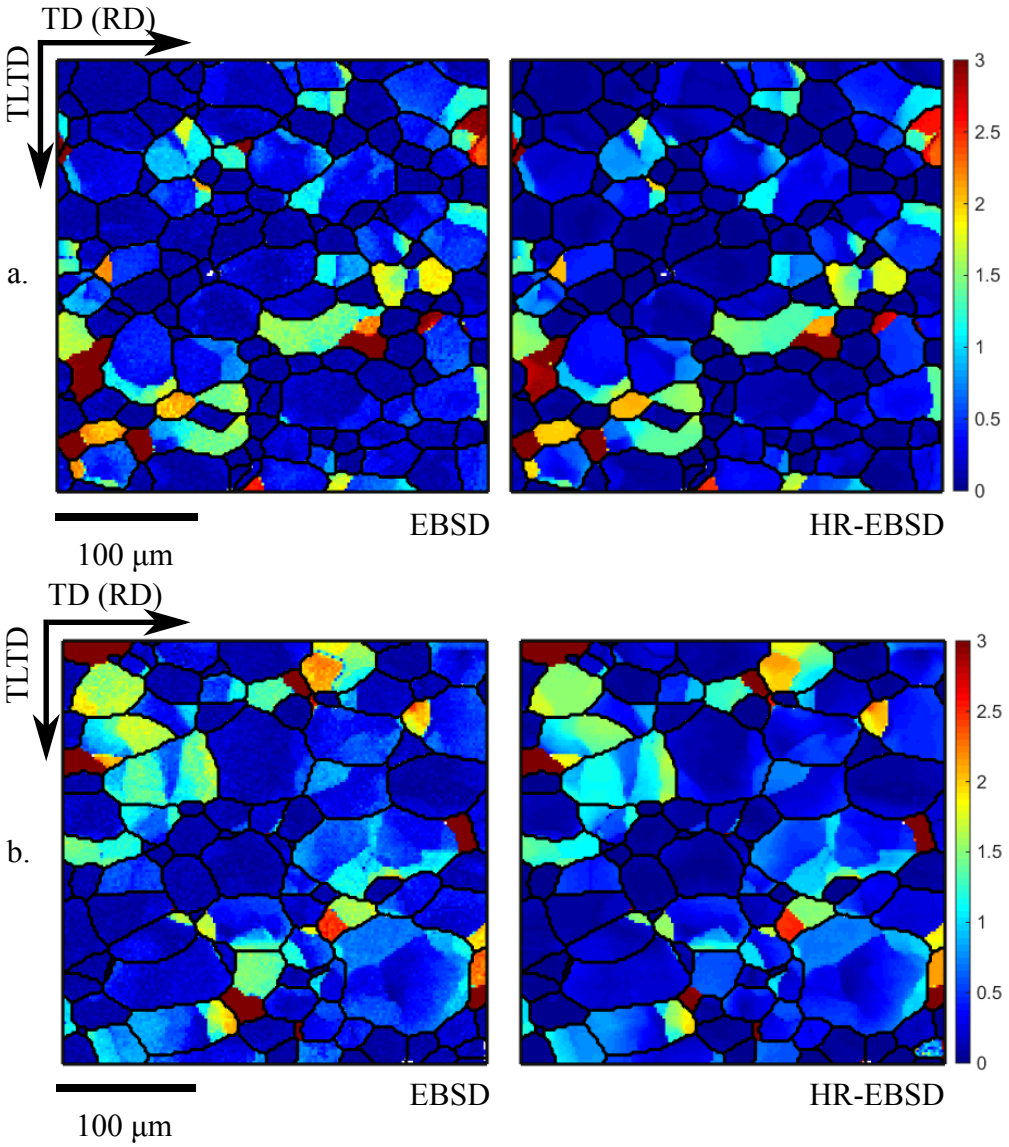

Figure 5.29: Figure 5.29 is continued on the next page.

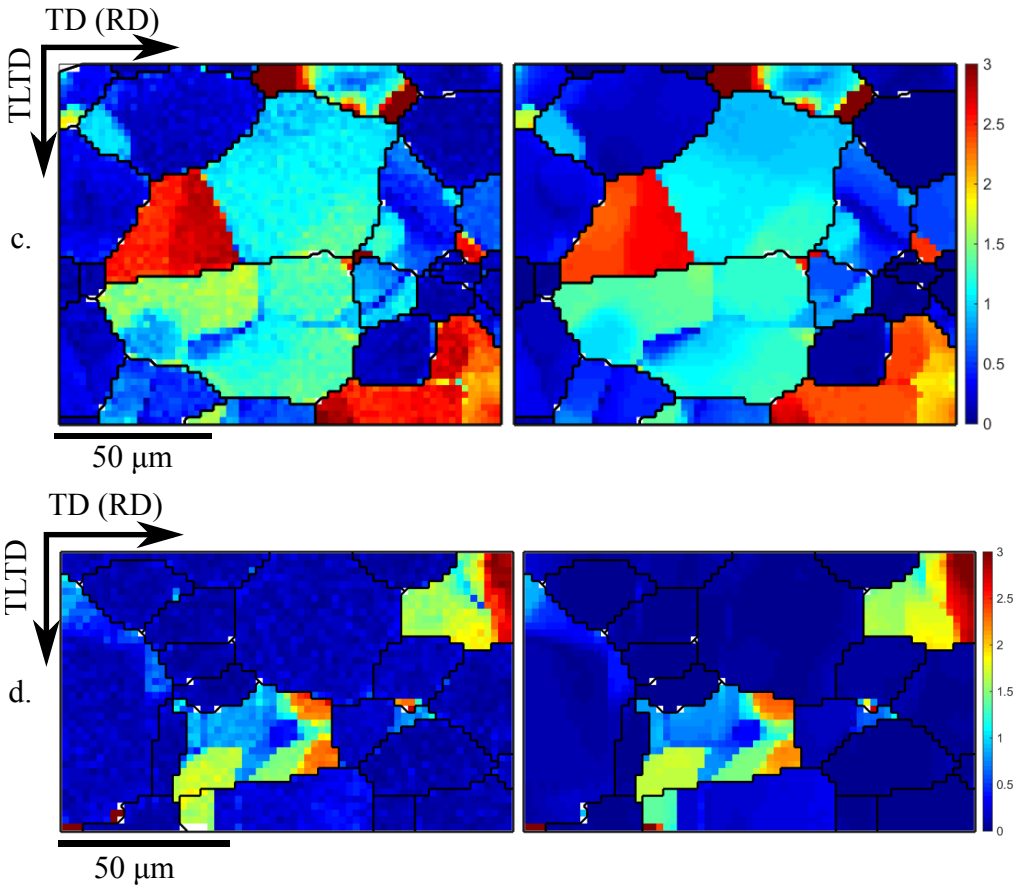

Figure 5.29: ROD maps are shown from different parts of a specimen deformed in uniaxial tension in air at 850 °C at a constant true-strain rate of 10^{-4} s^{-1} to a true strain of 0.2 and water-quenched. The specimen TD was oriented at 0° with respect to the RD. The maps on the left were produced using standard-resolution EBSD data and the maps on the right with HR-EBSD data. Each scale bar also applies to the ROD map on its right. The figure is a continuation from the previous page.

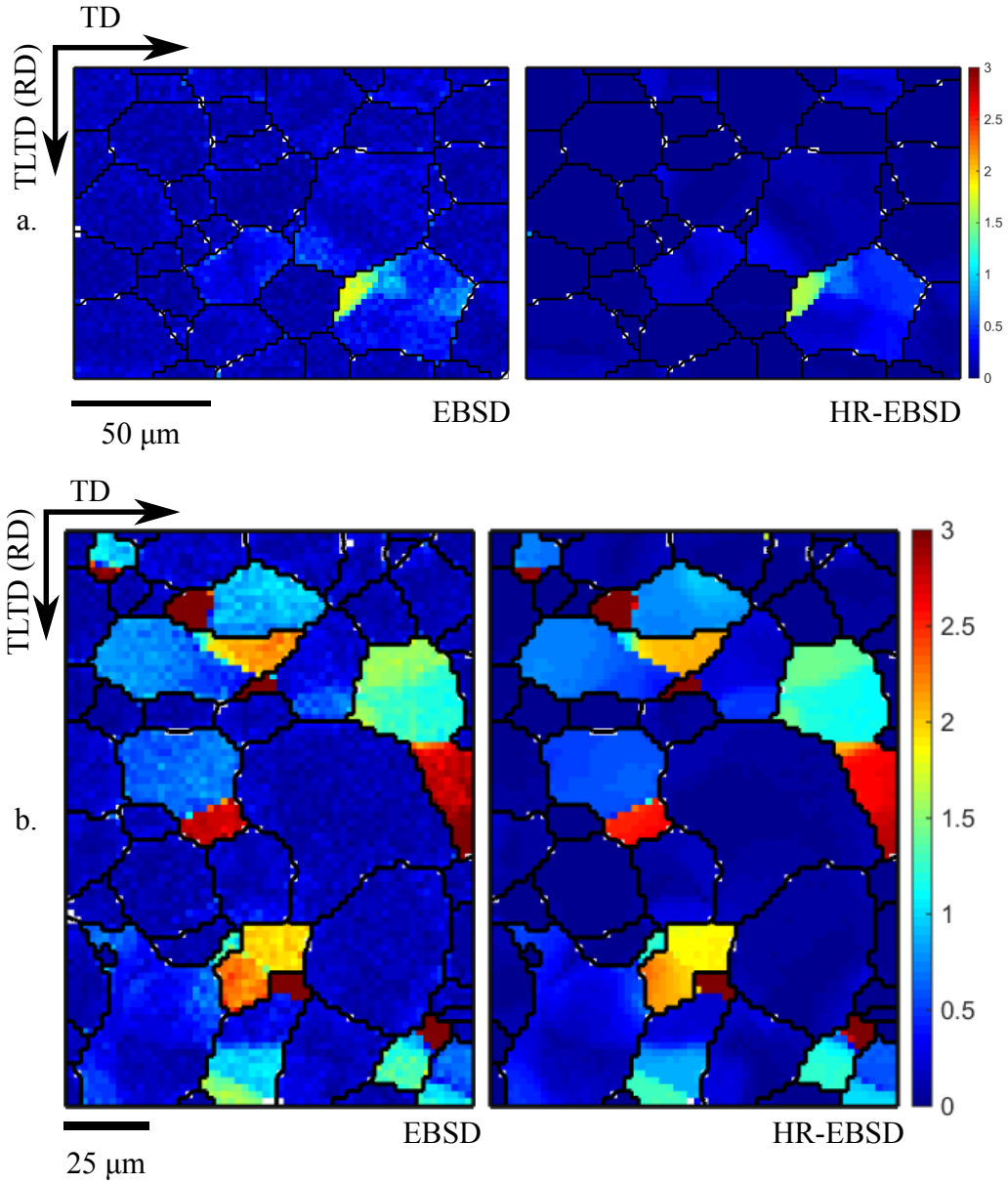

Figure 5.30: ROD maps are shown from different parts of a specimen deformed in uniaxial tension in air at 850 °C at a constant true-strain rate of 10^{-4} s^{-1} to a true strain of 0.1 and water-quenched. The specimen TD was oriented at 90° with respect to the RD. The maps on the left were produced using standard-resolution EBSD data and the maps on the right with HR-EBSD data. Each scale bar also applies to the ROD map on its right.

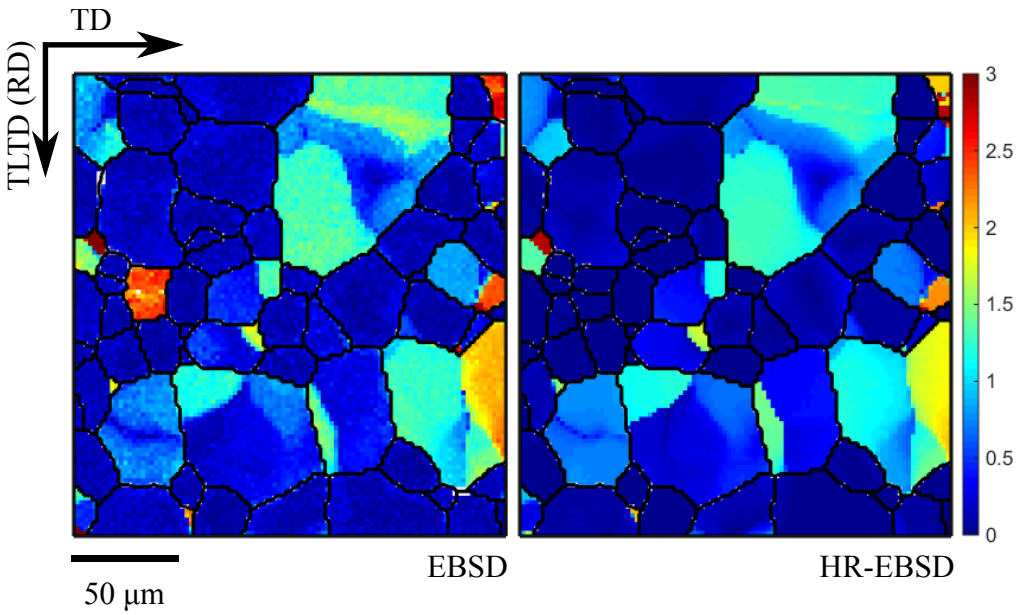

Figure 5.31: ROD maps are shown from a specimen deformed in uniaxial tension in air at 850 °C at a constant true-strain rate of 10^{-4} s^{-1} to a true strain of 0.2 and water-quenched. The specimen TD was oriented at 90° with respect to the RD. The map on the left was produced using standard-resolution EBSD data and the map on the right with HR-EBSD data.

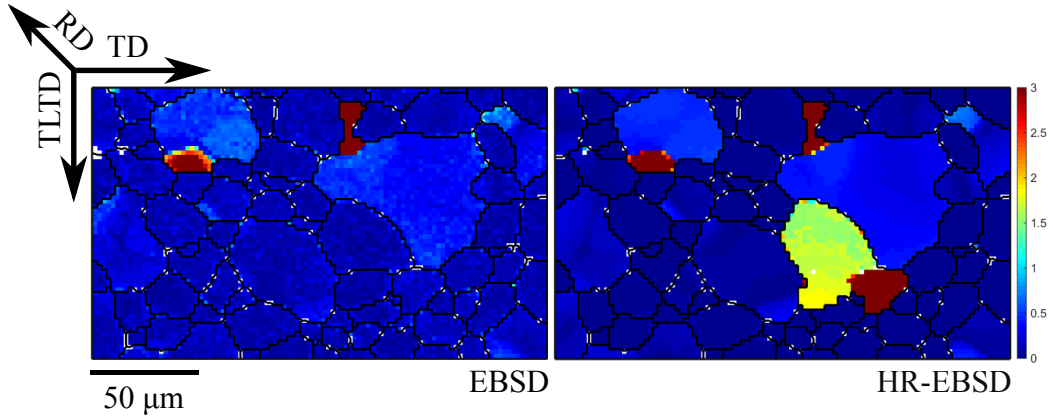

Figure 5.32: ROD maps are shown from a specimen deformed in uniaxial tension in air at 850 °C at a constant true-strain rate of 10^{-4} s^{-1} to a true strain of 0.1 and water-quenched. The specimen TD was oriented at 45° with respect to the RD. The map on the left was produced using standard-resolution EBSD data and the map on the right with HR-EBSD data.

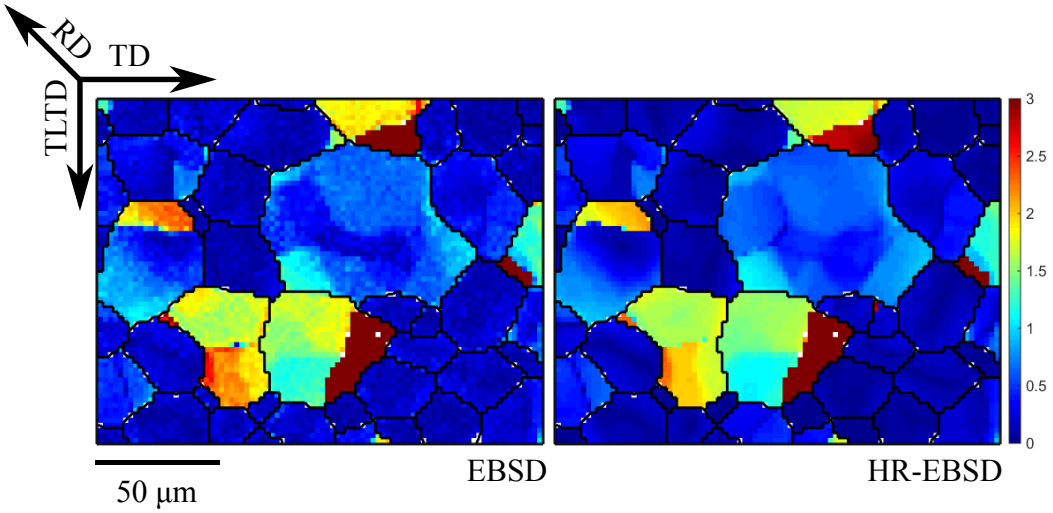

Figure 5.33: ROD maps are shown from a specimen deformed in uniaxial tension in air at 850 °C at a constant true-strain rate of 10^{-4} s^{-1} to a true strain of 0.2 and water-quenched. The specimen TD was oriented at 45° with respect to the RD. The map on the left was produced using standard-resolution EBSD data and the map on the right with HR-EBSD data.

5.4 Microstructural data for individual grains

For all three specimen tensile orientations, microstructural data were gathered for the following three conditions: (i) recrystallized, (ii) deformed at 850 °C at a constant true-strain rate of 10^{-4} s^{-1} to a true strain of 0.1, and (iii) deformed at 850 °C at a constant true-strain rate of 10^{-4} s^{-1} to a true strain of 0.2. Figures 5.34, 5.35, and 5.36 show the data gathered for individual grains as histograms of the grain number fraction *versus* the lineal intercept grain diameter for the specimen TD oriented at 0°, 90°, and 45° with respect to the RD. Each figure includes individual histograms of data for the following conditions: (i) recrystallized ($\varepsilon = 0$), (ii) deformed at elevated temperature to a true strain of 0.1 ($\varepsilon = 0.1$), and (iii) deformed at elevated temperature to a true strain of 0.2 ($\varepsilon = 0.2$). Grains situated on the boundaries of the EBSD scans were excluded from these histograms.

The grain size distribution of the recrystallized microstructure was observed to be lognormal. This is consistent with expectations. The mean lineal intercept grain diameter was observed to increase with strain for all three specimen tensile orientations. In general, a bimodal grain size distribution was observed for the specimens deformed at elevated temperature. This bimodal distribution consisted of the following: (i) a minor grouping of grains smaller than the mean recrystallized lineal intercept diameter and (ii) a much larger grouping of grains larger than the mean recrystallized lineal intercept diameter. Typical normal grain growth is expected from theory to simply shift the lognormal distribution to larger mean lineal intercept diameters [7].

The bimodal grain size distributions shown for the deformed specimens in Figures 5.34 through 5.36 deviate from this expectation for normal grain growth. While a majority of grains grew during tensile deformation, a small subset of grains did not grow or only grew slowly by comparison.

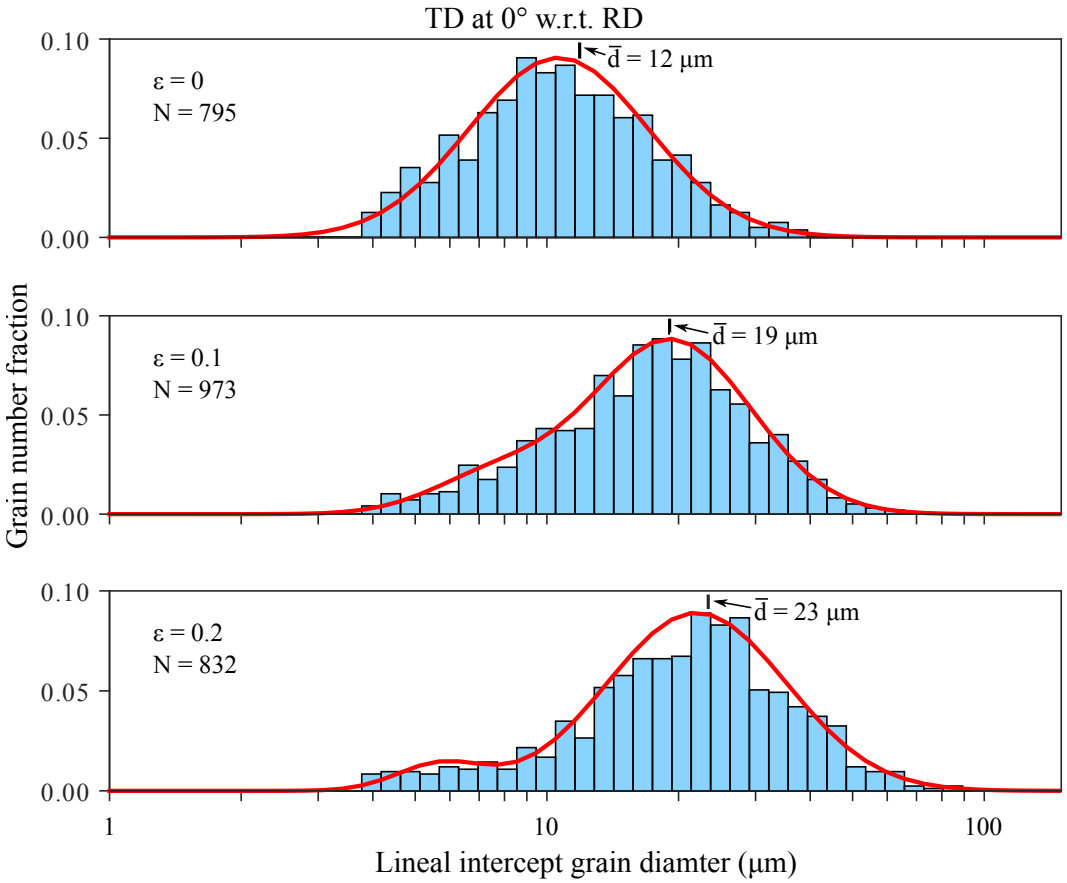

$\varepsilon = 0$		$\varepsilon = 0.1$			$\varepsilon = 0.2$		
μ (μm)	σ (μm)	μ (μm)	σ (μm)	w (%)	μ (μm)	σ (μm)	w (%)
11	2	8	1	14.6	6	1	6.8
		19	2	85.4	22	2	93.2

Figure 5.34: Histograms of the grain number fraction *versus* lineal intercept grain diameter are shown. The x-axis is on a logarithmic scale. The specimen TD was oriented at 0° with respect to the RD. The top histogram ($\varepsilon = 0$) is from a recrystallized specimen annealed at 850 °C for 30 minutes. The middle and bottom histograms are from specimens deformed in uniaxial tension at 850 °C at a constant true-strain rate of 10^{-4} s^{-1} to true strains of 0.1 and 0.2, respectively. Mean lineal intercept grain size ($\bar{d}$) is marked in each histogram. The mean (μ) and standard deviation (σ) are provided in the table for each grain size distribution. Bimodal grain size distributions have the mean, standard deviation, and weighted density (w) provided for each hump.

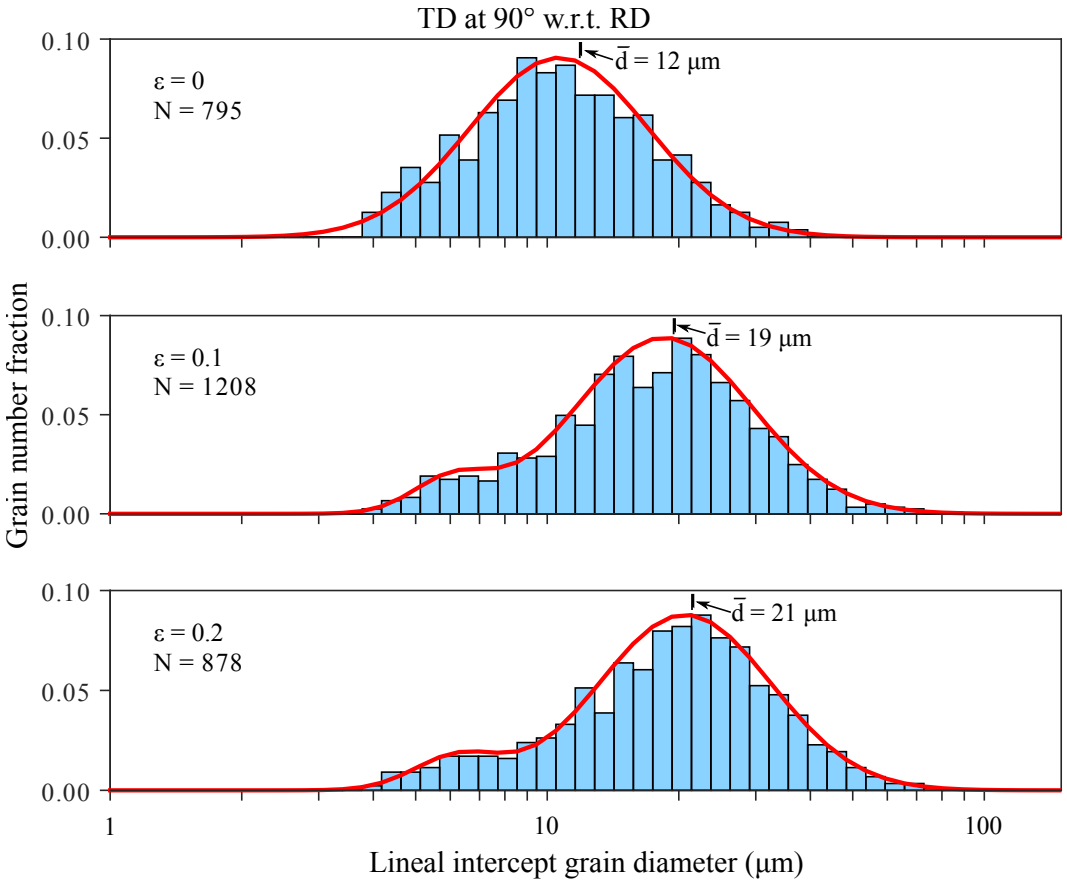

$\varepsilon = 0$		$\varepsilon = 0.1$			$\varepsilon = 0.2$		
μ (μm)	σ (μm)	μ (μm)	σ (μm)	w (%)	μ (μm)	σ (μm)	w (%)
11	2	6	1	7.6	6	1	8.6
		19	2	92.4	21	2	91.4

Figure 5.35: Histograms of the grain number fraction *versus* lineal intercept grain diameter are shown. The x-axis is on a logarithmic scale. The specimen TD was oriented at 90° with respect to the RD. The top histogram ($\varepsilon = 0$) is from a recrystallized specimen annealed at 850 °C for 30 minutes. The middle and bottom histograms are from specimens deformed in uniaxial tension at 850 °C at a constant true-strain rate of 10^{-4} s^{-1} to true strains of 0.1 and 0.2, respectively. Mean lineal intercept grain size ($\bar{d}$) is marked in each histogram. The mean (μ) and standard deviation (σ) are provided in the table for each grain size distribution. Bimodal grain size distributions have the mean, standard deviation, and weighted density (w) provided for each hump.

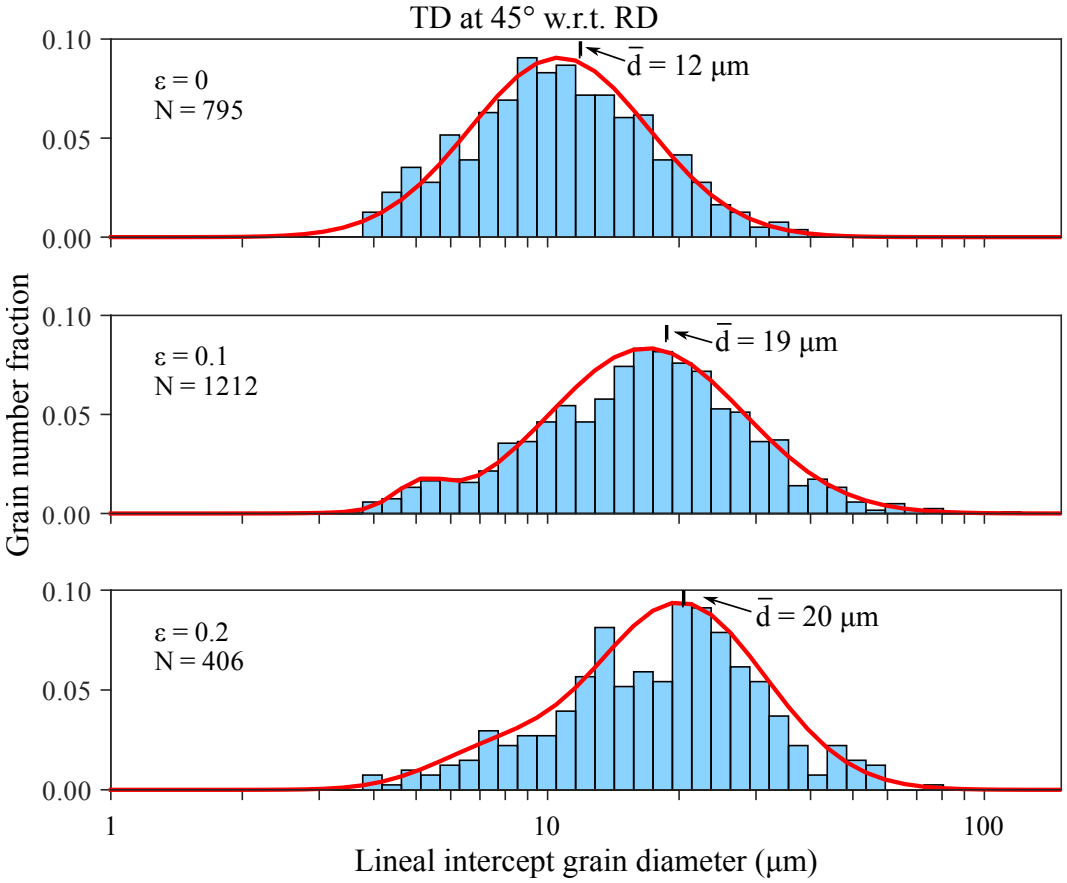

$\varepsilon = 0$		$\varepsilon = 0.1$			$\varepsilon = 0.2$		
μ (μm)	σ (μm)	μ (μm)	σ (μm)	w (%)	μ (μm)	σ (μm)	w (%)
11	2	5	1	3.7	7	1	12.0
		17	2	96.3	20	2	88.0

Figure 5.36: Histograms of the grain number fraction *versus* lineal intercept grain diameter are shown. The x-axis is on a logarithmic scale. The specimen TD was oriented at 45° with respect to the RD. The top histogram ($\varepsilon = 0$) is from a recrystallized specimen annealed at 850 °C for 30 minutes. The middle and bottom histograms are from specimens deformed in uniaxial tension at 850 °C at a constant true-strain rate of 10^{-4} s^{-1} to true strains of 0.1 and 0.2, respectively. Mean lineal intercept grain size ($\bar{d}$) is marked in each histogram. The mean (μ) and standard deviation (σ) are provided in the table for each grain size distribution. Bimodal grain size distributions have the mean, standard deviation, and weighted density (w) provided for each hump.

5.5 VPSC Predictions

Room-temperature uniaxial tensile deformation was simulated using the VPSC code for all three specimen tensile orientations. Figures 5.37 and 5.38 present the simulation results in the form of IPFs for deformation to true strains of 0.1 and 0.2, respectively. The VPSC simulation predicted the <110>||TD would strengthen with strain at the expense of other texture components. This is evident by comparison to the recrystallized texture shown in the IPFs of Figure 5.8. Slight differences in the texture with respect to the STD were predicted by the VPSC code depending on the initial recrystallized texture. When the specimen TD was oriented at 0° with respect to the RD, no significant changes with increasing strain were observed. A slight strengthening of the <100>||STD was observed for room-temperature deformation simulated to a true strain of 0.1 compared to the recrystallized texture. When the specimen TD was oriented at 90° with respect to the RD, a strengthening of the <111>||STD and <100>||STD was observed with a weakening of approximately the <112>||STD. When the specimen TD was oriented at 45° degrees with respect to the RD a strengthening of the <100>||STD and slight strengthening of the <111>||STD was observed.

Figure 5.39 shows the simulated room-temperature uniaxial tensile deformation predicted by the VPSC simulation in the form of φ_2=45° Euler slices. Room-temperature deformation was predicted for all three specimen tensile orientations to strengthen texture components from within the α-fiber, particularly the {111}<110>. See the reference orientation with the φ_2=45°

Euler space slice provided in Figure 4.1. The strengthening of the largest range of texture components from within the α-fiber was predicted when the specimen TD was oriented at 0° with respect to the RD. The texture for the specimen deformed with the specimen TD oriented at 90° with respect to the RD was predicted to have the smallest range of α-fiber texture components being strengthened. A strengthening of texture components with the <100>||STD were observed when the specimen TD was oriented at 90° and 45° with respect to the RD, e.g., see the top corners in the 90° case.

The room-temperature uniaxial tensile deformation textures predicted by the VPSC simulations shown in Figures 5.37-5.38 were very similar to the textures that were experimentally observed and shown in Figures 5.15-5.17. The textures predicted by the VPSC code, however, are significantly more intense. The strengthening of the <100>||STD predicted by the VPSC code when the TD was oriented at 90° and 45° with respect to the RD was generally not observed in experiments. A slight strengthening of the <100>||STD was possibly visible in the experimental data for the specimen TD oriented at 90° with respect to the RD, but at a much smaller intensity than predicted by the VPSC code.

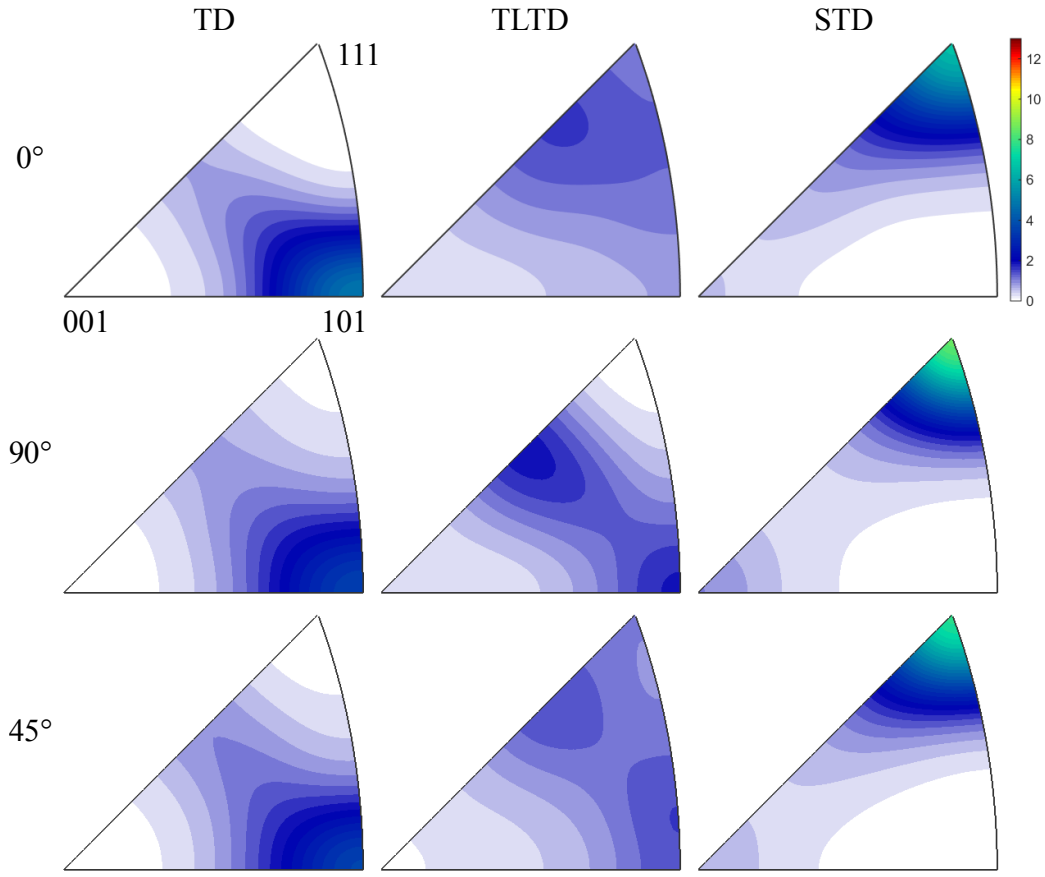

Figure 5.37: IPFs of simulated room-temperature uniaxial tensile deformation to a true strain of 0.1 predicted by the VPSC code are shown. The TD was oriented at 0°, 90°, and 45° with respect to the RD as labeled in each row.

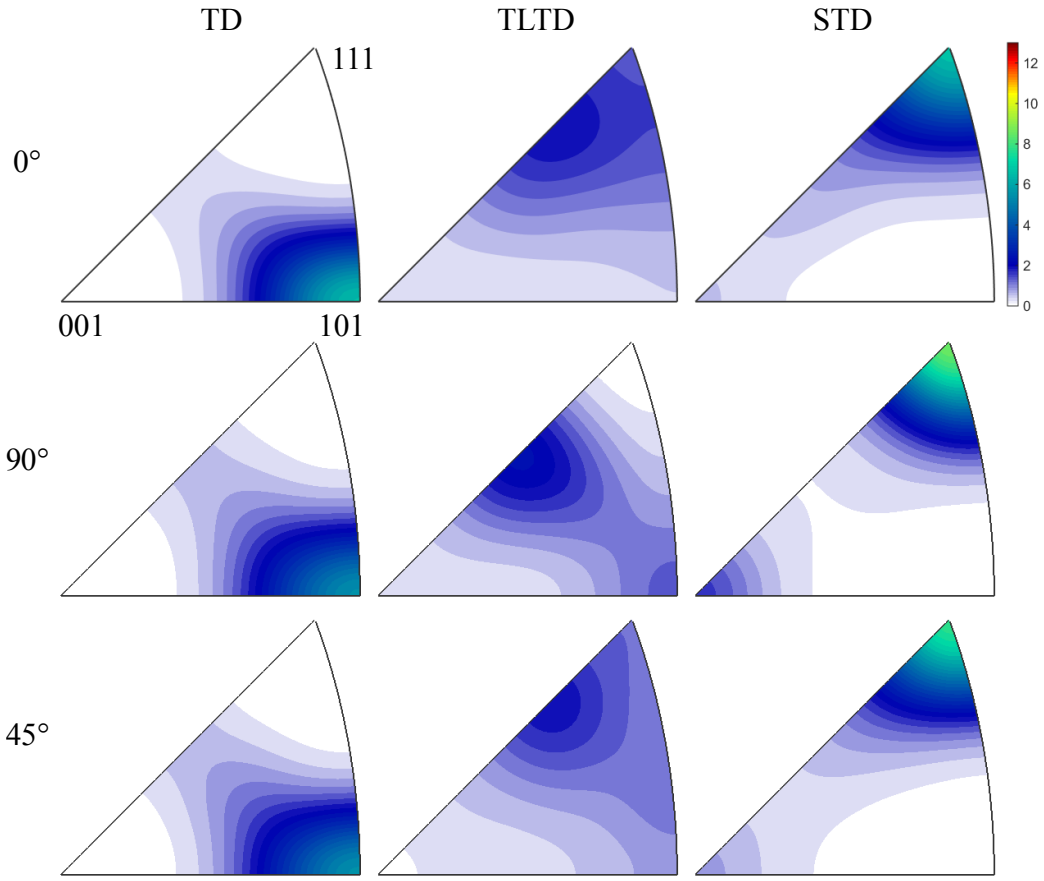

Figure 5.38: IPFs of simulated room-temperature uniaxial tensile deformation to a true strain of 0.2 predicted by the VPSC code are shown. The TD was oriented at 0°, 90°, and 45° with respect to the RD as labeled in each row.

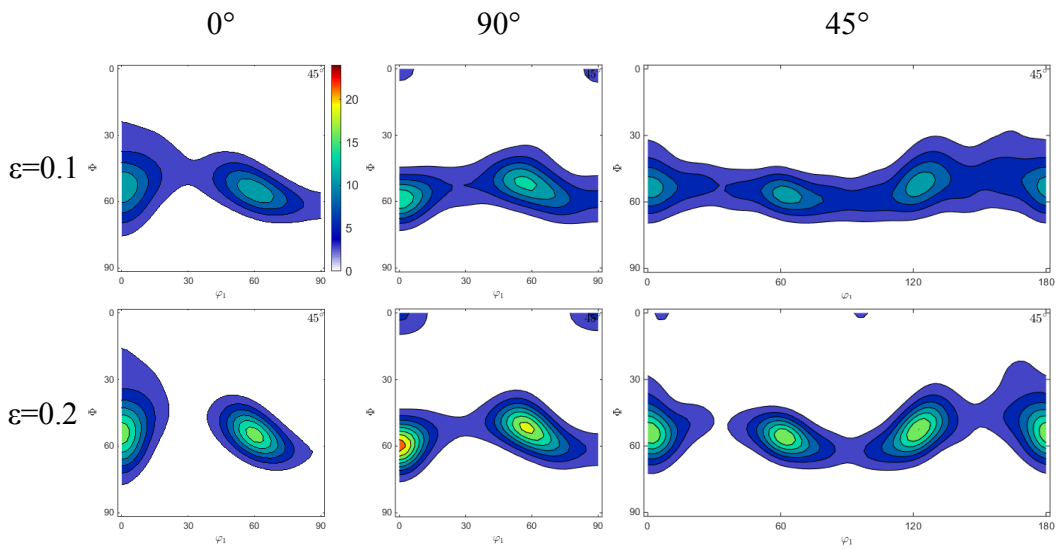

Figure 5.39: The φ_2=45° Euler slices of simulated room-temperature uniaxial tensile deformation to true strains 0.1 and 0.2 predicted by the VPSC code are shown. The TD was oriented at 0°, 90°, and 45° with respect to the RD as labeled in each column.

Chapter 6

Discussion

6.1 The effect of DNGG on grain size

The effect of DNGG on grain size was probed. This required comparing DNGG and SNGG. In order to investigate grain size evolution from DNGG, specimens were deformed at 850 °C at a constant true-strain rate of 10^{-4} s^{-1} in vacuum. Grain size was measured for specimens deformed to true strains of 0.1 and 0.2, which correspond to times at temperature of 80 and 100 minutes, respectively. The specimen TD was oriented at 0° with respect to the RD for both specimens. In order to investigate grain size evolution from SNGG, specimens were statically annealed at 850 °C. Grain size was measured for specimens annealed for 30, 100, and 480 minutes. Full recrystallization of the microstructure occurred within the first 30 minutes of annealing (see Section 5.1.1). A box furnace was used for the 30 and 480 minute anneals. The grip region of the specimen deformed to a true strain of 0.2 was used for the 100 minute static anneal. The grip region is not deformed during testing. Therefore, this region is only statically annealed during testing.

Specimen grain size was measured from BSE channeling contrast images of the specimen TD-TLTD (RD-LTD) plane. Grain size and its standard

error along the TD and TLTD were measured using the lineal intercept method [77]. The mean lineal intercept grain diameter was calculated from these directional grain size measurements. The uncertainty of the mean lineal intercept grain diameter was calculated using propagation of uncertainty of the standard error. The mean lineal intercept grain diameter ($\bar{d}$) as a function of time at temperature is shown in Figure 6.1.

The initial recrystallized grain size calculated after a 30 minute static anneal at 850 °C was 13 ± 1 μm. Figure 6.1 highlights drastic differences in grain size evolution between the specimens statically annealed and those deformed at 850 °C. The Ti-IF steel sheet material resists SNGG. This is evident from the following: (i) No change in grain size was observed between the specimens statically annealed for 30 and 100 minutes. (ii) The grain size was only slightly larger (21 ± 2 μm) for the specimen statically annealed for 480 minutes (8 hours). The Ti-IF steel sheet material, on the other hand, was susceptible to DNGG, which is evident from the following: (i) The grain size of the specimen deformed to a true strain of 0.1, which was at temperature for 80 minutes, was 19 ± 1 μm. This is effectively the same grain size as the specimen statically annealed for 480 minutes. (ii) The grains size for the specimen deformed to a true strain of 0.2, which was at temperature for 100 minutes, was 32 ± 3 μm. These data demonstrate that concurrent plastic deformation accelerated grain growth, leading to DNGG and larger grain sizes than were produced by static annealing alone.

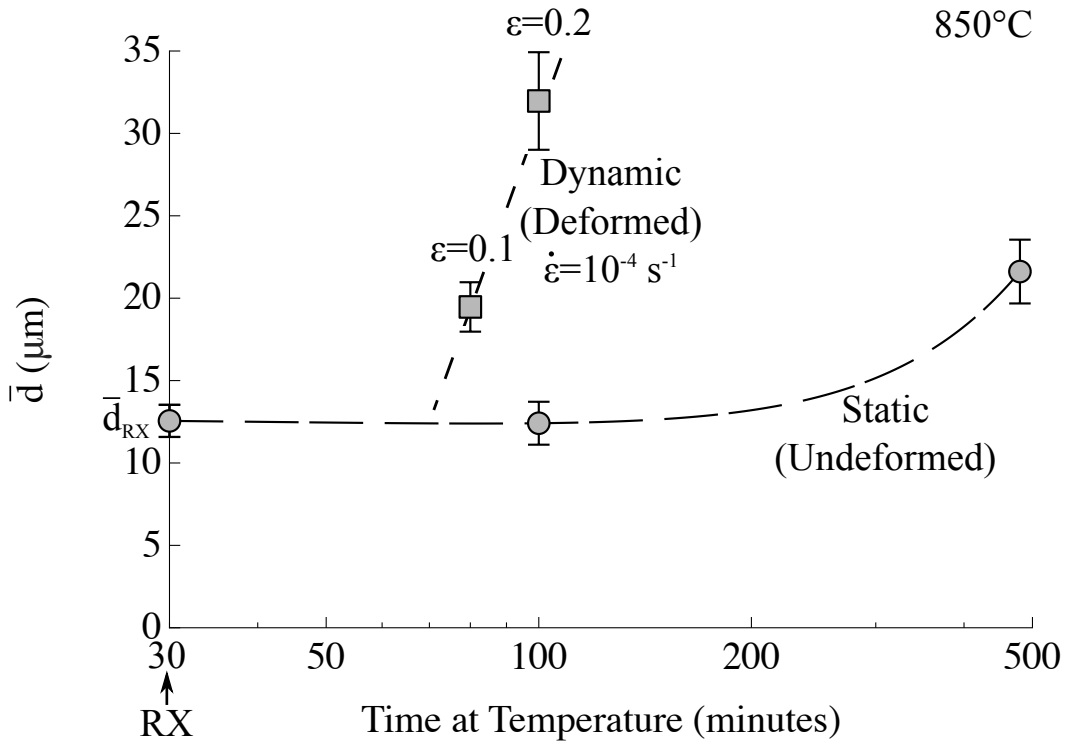

Figure 6.1: The mean lineal intercept grain diameter is shown *versus* annealing time for specimens statically annealed and deformed at 850 °C. Specimens were deformed in uniaxial tension at a constant true-strain rate of 10^{-4} s^{-1} to true strains of 0.1 and 0.2 in vacuum. The scale on the x-axis is logarithmic. Some data contributed by P. J. Noell.

6.2 The effect of DNGG on texture

The texture evolution from room-temperature tensile deformation predicted by the VPSC simulation was in general agreement with experimental observations. The VPSC code, however, predicted a much sharper texture compared to the experiments. The VPSC code only simulated the effect of lattice rotation during slip on texture evolution. Therefore, the VPSC simulations confirmed that the experimentally observed texture evolution from room-temperature deformation was the result of lattice rotation during slip. Consequently, it was hypothesized that the lattice rotation effect could be isolated from the effect of DNGG during high-temperature tensile deformation.

The lattice rotation effect was isolated by subtracting the ODF of the recrystallized texture from the ODF of the texture that resulted from room-temperature tensile deformation. Figure 6.2 shows the φ_2=45° Euler slices for the isolated lattice rotation effect. Lattice rotation was observed to strengthen the intensity of texture components within the α-fiber (along the TD) that intersected with the recrystallized γ-fiber. See the orientations and fiber components shown in the φ_2=45° Euler space slice of Figure 4.1 for reference. The strengthening of texture components from within the α-fiber occurred at the expense of texture components from within the γ-fiber.

The textures after uniaxial tension at 850 °C at a constant true-strain rate of 10^{-4} s^{-1}, shown in Figures 5.23-5.27, and at room-temperature, shown in Figures 5.13-5.17, were distinctly different. This suggests that there were specific changes to the texture during high-temperature tensile deformation

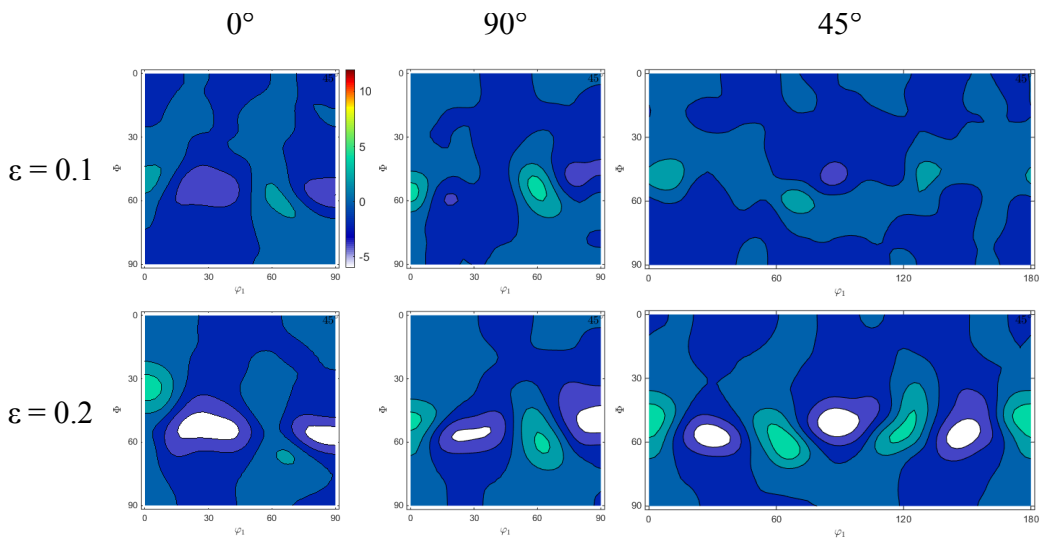

Figure 6.2: The φ_2=45° Euler slices of the isolated lattice rotation effect for true strains of 0.1 and 0.2, as labeled for each row, are shown. The specimen TD was oriented at 0°, 90°, and 45° with respect to the RD, as labeled in each column.

that are not attributable to lattice rotation, the only significant effect from room-temperature deformation. Neither the stress-strain curves, Figure 5.18, nor microstructures, Figures 5.21 and 5.23-5.24, indicated any signs of recrystallization during high-temperature tensile deformation. Therefore, the texture evolution during high-temperature tensile deformation was likely driven by DNGG, at least in part. This hypothesized DNGG effect was isolated by subtracting the ODF of the texture after room-temperature deformation from the ODF of the texture after high-temperature deformation. Figure 6.3 shows the φ_2=45° Euler slices of the isolated DNGG effect. DNGG was observed to preferentially grow grains from within the γ-fiber at the expense of grains within the α-fiber. The specific texture components that preferen-

tially grew depended on the initial recrystallized texture. Grains near the {111}<110> grew when the specimen TD was oriented at 0° with respect to the RD. The {111}<110> was the most preferred texture component for growth when the specimen TD was oriented at 90° with respect to the RD. Texture components within the γ-fiber that were not the {111}<110> components preferentially grew by DNGG when the specimen TD was oriented at 45° with respect to the RD.

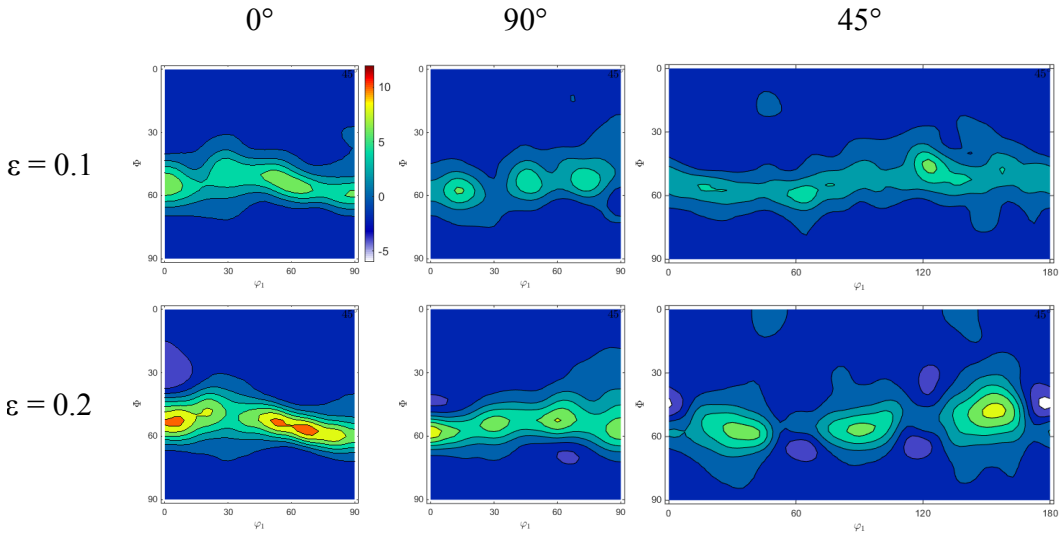

Figure 6.3: The φ_2=45° Euler slices of the isolated DNGG effect are shown for true strains of 0.1 and 0.2, as labeled for each row, at 850 °C and a constant true-strain rate of 10^{-4} s^{-1}. The specimen TD was oriented at 0°, 90°, and 45° with respect to the RD, as labeled in each column.

6.3 The effect of DNGG on individual grains

The previous section, 6.2, discussed the changes in crystallographic texture produced by DNGG. That discussion relied on texture measurements that did not consider grain size. This section discusses the segmented data for individual grains, which include their sizes and orientations. These data were used to categorize individual grains by crystallographic orientation. This section discusses the relationships between those orientation categories and change of grain area fraction, number fraction, and size (area per grain). The purpose of these comparisons is to determine if the growth of grains with specific orientations is responsible for the observed increases in the intensities of specific texture components; see Section 6.2. Likewise, it will be tested whether the decrease in specific texture components results from the disappearance of grains with corresponding orientation characteristics. Demonstrating these effects of grain growth will confirm that DNGG is responsible for the texture changes described in Section 6.2.

Measurements of individual grains were acquired from EBSD data as described in Section 4.2.4. These data include all three specimen tensile test orientations. Data are for three conditions: (i) recrystallized, (ii) deformed at 850 °C at a constant true-strain rate of 10^{-4} s^{-1} to a true strain of 0.1, and (iii) deformed at 850 °C at a constant true-strain rate of 10^{-4} s^{-1} to a true strain of 0.2. Each grain was assigned into the reference orientation(s) that fit it best. Grains situated on the boundaries of EBSD scans were excluded from analysis.

Grains were also categorized into two broader groups by: (i) crystallographic plane(s) parallel to the sheet plane and (ii) crystallographic direction(s) parallel to the TD. Grains were additionally grouped into one of three regions by the crystallographic plane parallel to the sheet plane. These were the {110}, {321}, and {111} regions of planes. Figure 6.4 illustrates the grouping of planes that constitute each of the three regions in the form of the standard triangle. A table listing the planes in each region is also included in Figure 6.4. Grains that did not match any of these categories (i.e., unidentified grains) were also analyzed.

The grain area fraction, grain number fraction, and area per grain were analyzed with respect to strain when the grains were categorized by (i) crystallographic plane and region of planes parallel to the sheet (Section 6.3.1), (ii) crystallographic direction parallel to the TD (Section 6.3.2), and (iii) reference orientation, which includes plane + direction (Section 6.3.3). In order to quantitatively characterize correlations of the grain area fraction, grain number fraction, and area per grain with strain, the slopes and correlation coefficients with strain were calculated. Slopes were calculated for the following ranges for each orientation type: (i) from $\varepsilon = 0$ to $\varepsilon = 0.1$, (ii) from $\varepsilon = 0.1$ to $\varepsilon = 0.2$, and (iii) from $\varepsilon = 0$ to $\varepsilon = 0.2$. Calculations were made for each specimen tensile orientation. The data from the three specimen tensile orientations were consolidated to compute the correlation coefficients. In other words, each correlation coefficient was calculated from nine data points; the three data points for the specimen TD orientated at 0°, 90°, and 45° with respect to the RD at

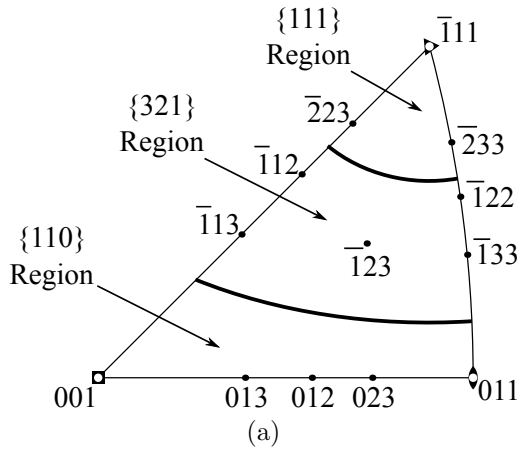

(a)

{1	1	0}	Region
{1	0	0}	
{3	1	0}	
{2	1	0}	
{3	2	0}	
{1	1	0}	

{3	2	1}	Region
{3	3	1}	
{3	2	1}	
{3	1	1}	
{2	2	1}	
{2	1	1}	

{1	1	1}	Region
{3	3	2}	
{3	2	2}	
{1	1	1}	

(b)

Figure 6.4: A depiction of the categorization of the three regions in (a) the standard triangle and (b) tabular form.

strains of 0, 0.1, and 0.2. This means that a single correlation coefficient was calculated for the TD oriented at 0°, 90°, and 45° with respect to the RD. A correlation coefficient was calculated for each orientation type. The correlation coefficient ranges from negative one to one. A correlation coefficient equal to zero indicates no linear correlation between the two variables. A correlation coefficient with an absolute value of one indicates perfect linear correlation. The data will have a positive slope if the correlation coefficient is positive, and a negative slope if the correlation coefficient is negative. Correlation coeffi-

cient magnitude between zero and one indicate how how well correlated are the data [83].

Caution must be taken when interpreting these data. This method of analysis was incapable of isolating the lattice rotation effect and differentiating it from the effect of DNGG. Therefore, increased grain area fractions and grain number fractions with strain could be attributable to lattice rotation during slip and/or DNGG. Lattice rotation strengthened the intensity of texture components within the α-fiber along the TD (see Section 6.2). This means that the lattice rotation effect must be taken into consideration when discussing the data with respect to the crystallographic directions along the TD and reference orientations.

6.3.1 Grains categorized by plane orientation

The data gathered for individual grains categorized by region of planes shown in Figure 6.4 are presented as histograms of the grain number fraction *versus* the lineal intercept grain diameter. Figures 6.5, 6.6, and 6.7 are for the TD oriented at 0°, 90°, and 45° with respect to the RD, respectively. For each specimen orientation, histograms are organized by the three regions of planes and the following three test conditions: (i) recrystallized ($\varepsilon = 0$), (ii) deformed at elevated temperature to a true strain of 0.1 ($\varepsilon = 0.1$), and (iii) deformed at elevated temperature to a true strain of 0.2 ($\varepsilon = 0.2$).

The histograms for the three specimen tensile orientations were very similar. The grain size distributions of the recrystallized microstructure for

each region of planes were lognormal. The grain number fraction of grains from the {110} region of planes decreased significantly with strain. The grain number fraction of grains from the {321} region of planes decreased slightly with strain. The grain number fraction of grains from the {111} region of planes increased significantly with strain. The mean lineal intercept grain diameter, noted in each figure, increased with strain for all three regions of planes. In general, grains from the {321} and {111} regions of planes had a bimodal grain size distribution for the specimens deformed at elevated temperature. The bimodal distribution consisted of the following: (i) a minor grouping of grains smaller than the mean lineal intercept recrystallized grain diameter, and (ii) a much larger grouping of grains larger than the mean lineal intercept recrystallized grain diameter. As stated in Section 5.4, this bimodal distribution implied that a majority of grains grew during tensile deformation, and a small subset of grains did not grow or only grew slowly by comparison. The observations from the histograms suggest that DNGG preferentially grew grains from the {111} region of planes at the expense of grains from the {110} and {321} regions of planes.

For all three specimen tensile orientations, the grain area fraction, grain number fraction, and area per grain were calculated for each region of planes at each test condition. The grain area fraction, grain number fraction, and area per grain are shown as functions of strain in Figures 6.8, 6.9, and 6.10. The grain area fraction, grain number fraction, and area per grain for grains that did not match any of the regions of planes (i.e. unidentified grains) were

also calculated. Unidentified grains are represented by pink circles. Data points with a grain count of less than 1% of the total number of non-boundary grains in the data set were excluded from analysis. This excluded all of the unidentified grains with the exception of the recrystallized specimen with the TD at 45° with respect to the RD, ε=0. Because this left only one data point for the unidentified grains, unidentified grains were not further characterized. The slopes and correlation coefficients with strain were calculated for data presented in Figures 6.8-6.10 and are provided in Appendix E.

Figure 6.8 shows that the grain area fraction increased with strain for grains belonging to the {111} region of planes. A decrease in grain area fraction with strain was observed for grains belonging to the {110} and {321} regions of planes. These observations were consistent for all three specimen tensile orientations. This consistency was quantified using the correlation coefficient. For all three regions of planes, the absolute value of the correlation coefficient was greater than 0.85 (see Appendix E). This suggests that the grain area fraction is strongly correlated with strain for all three specimen test orientations.

Figure 6.9 shows that the number fraction of grains belonging to the {111} region of planes increased with strain. The grain number fraction decreased with strain for grains belonging to the {321} and {110} regions of planes. The correlation coefficient of the grain number fraction as a function of strain was calculated to be greater than the absolute value of 0.85 for all three regions of planes (see Appendix E). This is a strong correlation. The

trends in the grain number fraction as a function of strain, Figure 6.9, are very similar to those of the grain area fraction as a function of strain, Figure 6.8. As mentioned in Section 6.2, recrystallization did not occur during or after elevated-temperature deformation. Thus, new grains were not created. Therefore, grains from the {111} region of planes must be consuming grains from the other regions of planes.

The area per grain, a measure of grain size, is shown as a function of strain in Figure 6.10. The area per grain increased with strain for all three regions of planes. This does not necessarily mean that all grains were growing. The average area per grain could increase by the dissappearance of small grains consumed during the growth of grains from another orientation category. The correlation coefficient of the area per grain with strain was greater than 0.9 for each region of planes. This indicates a very strong correlation. The {111} region of planes for all three specimen orientations was observed to have the steepest overall slope (from $\varepsilon = 0$ to $\varepsilon = 0.2$). The average overall slope of the {111} region of planes for all three tensile specimen orientations was calculated to be 2825 μm^2

Figures 6.5 through 6.10 strongly suggest that grains from the {111} region of planes are favored for DNGG. The individual planes that make up each region of planes were identified to investigate a more detailed relationship between orientation and growth. For all three specimen tensile orientations, the grain area fraction, grain number fraction, and area per grain for individual planes were calculated. Figures 6.11, 6.12, and 6.13 show these respective

values as functions of strain. Data points with a grain count less than 1% the total number of non-boundary grains were excluded. The calculated slopes and correlation coefficients for the data of Figures 6.11-6.13 are provided in Appendix E.

From the grain area fraction *versus* strain data categorized by individual plane orientations, Figure 6.11, the following general observations were made for all three specimen tensile orientations. The {111}, {332}, and {322} were the only planes with a positive correlation coefficient for the grain area fraction with strain. These were the planes that constituted the {111} region of planes. The {111} plane orientation had the highest correlation coefficient at 0.92, followed by the {332} at 0.79, and finally the {322} at 0.25. These correlation coefficients suggest the following. The area fraction of grains with the {111} plane orientation was similar for all three specimen tensile orientations and increased with strain. The area fraction of grains with the {332} plane orientation increased with strain but with slight variation between the three specimen tensile orientations. The weak positive correlation coefficient calculated for grains with the {322} plane orientation could have two possible implications: (i) the area fraction of grains with the {322} plane orientation did not change consistently with strain, or (ii) the area fraction of grains with the {322} orientation was different between the three specimen tensile orientations. The data of Figure 6.11 present evidence for both these possibilities. The area fractions of grains with the {111} plane orientation were the largest at each strain for all three specimen tensile orientations. The general order of

fastest to slowest increase in grain area fraction with strain were the {111}, {332}, and {322} plane orientations. All other plane orientations had a negative correlation coefficient between grain area fraction and strain. Many of these correlation coefficients were less than -0.8. Of the plane orientations with negative correlation coefficients, the {211} had the largest grain area fraction; note that the {211} plane orientation is near the {111} region of planes (see Figure 6.4).

Three differences were observed for the grain area fraction *versus* strain by plane orientation between the three specimen tensile orientations. (i) The plane orientation with the largest overall slope (from $\varepsilon = 0$ to $\varepsilon = 0.2$) depended on specimen orientation. When the TD was oriented at 0° with respect to the RD, the {111} plane orientation had the fastest growing grain area fraction, followed closely by the {332} plane orientation. When the TD was oriented at 90° with respect to the RD, the {332} plane orientation had the fastest growing grain area fraction, followed by the {111} plane orientation. When the TD was oriented at 45° with respect to the RD, the {111} plane orientation had the fastest growing grain area fraction by far. (ii) There were differences in the change of the grain area fraction with strain for the {322} plane orientations between the three specimen tensile orientations. The grain area fraction of the {322} plane orientation increased with strain when the TD was oriented at 0° with respect to the RD. The grain area fraction of the {322} plane orientation increased only slightly when the TD was oriented at 90° with respect to the RD. The grain area fraction decreased slightly with strain when

the TD was oriented at 45° with respect to the RD. (iii) Another difference observed between the three specimen tensile orientations was that the grain area fraction of the {211} plane orientation decreased with strain when the TD was orientated at 0° or 90° with respect to the RD. However, when the TD was oriented at 45° with respect to the RD, the grain area fraction of the {211} plane orientation increased slightly with strain.

The grain number fraction was categorized by individual plane orientation as a function of strain for all three specimen tensile orientations and is shown in Figure 6.12. A positive correlation coefficient of the grain number fraction with increasing strain was observed only for the {111}, {332}, and {322} plane orientations. These were the planes that comprised the {111} region of planes. Their correlation coefficients with strain were 0.95 for the {111} plane orientation, 0.90 for the {332} plane orientation, and 0.42 for the {322} plane orientations, including all specimen tensile orientations. This indicates that the grain number fractions increased with strain for the {111} and {332} plane orientations. The data presented in Figure 6.12 indicate that this behavior is similar between the three specimen tensile orientations. The grain number fractions of {322} plane orientations for specimens oriented with the TD at 90° or 45° with respect to the RD increased from a strain of 0 to 0.1 and decreased from 0.1 to 0.2. This behavior likely caused the weak correlation coefficient for the {322} plane orientation. For all three specimen tensile orientations, the overall slope (from $\varepsilon = 0$ to $\varepsilon = 0.2$) for the grain number fraction with strain was greatest for the {111} plane orientation, followed by

the {332}, and trailed by the {322}. The correlation coefficients for grain number fraction with strain were negative for all other plane orientations, i.e. planes other than the {111}, {332}, and {322}. The grain number fraction for the {111} plane orientation was the largest at each strain for every specimen tensile orientation. Of the plane orientations with decreasing grain number fractions, the {211}, in general, had the largest grain number fraction.

The trends in the grain number fraction as a function of strain categorized by plane orientation, Figure 6.12, were very similar to those of the grain area fraction as a function of strain, Figure 6.11. Because new grains were not being created, grains orientated with the {111}, {332}, and {322} planes parallel to the sheet must be consuming grains of other orientations. Grains with the {111} plane orientation followed by the {332} were the most favored for growth.

The area per grain is plotted against strain and categorized by plane orientation in Figure 6.13. With increased strain, the average area per grain increased for all plane orientations. The overall slopes (from $\varepsilon = 0$ to $\varepsilon = 0.2$) of the area per grain with strain for the individual plane orientations were observed to vary between the three specimen tensile orientations. Of the {111}, {332}, and {322} plane orientations, the plane with the largest increase in area per grain depended on specimen tensile orientation.

The plane orientations with the largest increase in area per grain were often those with a grain area fraction and grain number fraction that decreased with strain. Many of these plane orientations are comprised only of a small

number of grains. Thus, it is difficult to draw firm conclusions from these sparse data. Nevertheless, these trends are consistent with the consumption of the smallest grains from these orientations. This is evident in the histograms of the {110} region of planes in Figures 6.5-6.7. The number fraction of grains belonging to the {110} region of planes decreased significantly with strain. The vast majority of grains from the {110} region of planes that remained after high-temperature tensile deformation were larger than the mean recrystallized grain size of the {110} region of planes. This is consistent for all three specimen tensile orientations. The consumption of the smallest grains is consistent with theory (see Section 1.2.2). Small grains have a high grain boundary curvature which results in a large driving pressure for consumption. The consumption of small grains with orientations that are unfavored for growth increases the average area per grain for that group of grains, even when none from that group grow. It should be noted that some grains from the {110} region of planes were larger after high-temperature tensile deformation than their largest recrystallized counterparts. This likely means that these grains did grow during high-temperature tensile deformation. These observations also apply to grains from the {321} region of planes.

From Figures 6.5 through 6.13, it is apparent that DNGG grew grains with specific planes parallel to the plane of the sheet at the expense of other grain orientations. The planes most favored for DNGG were those that comprise the {111} region of planes. All planes that comprise the {111} region of planes are not equally favored for growth, however. Grains with a {111}

plane orientation are the most favored for growth, followed by the {332} plane orientation.

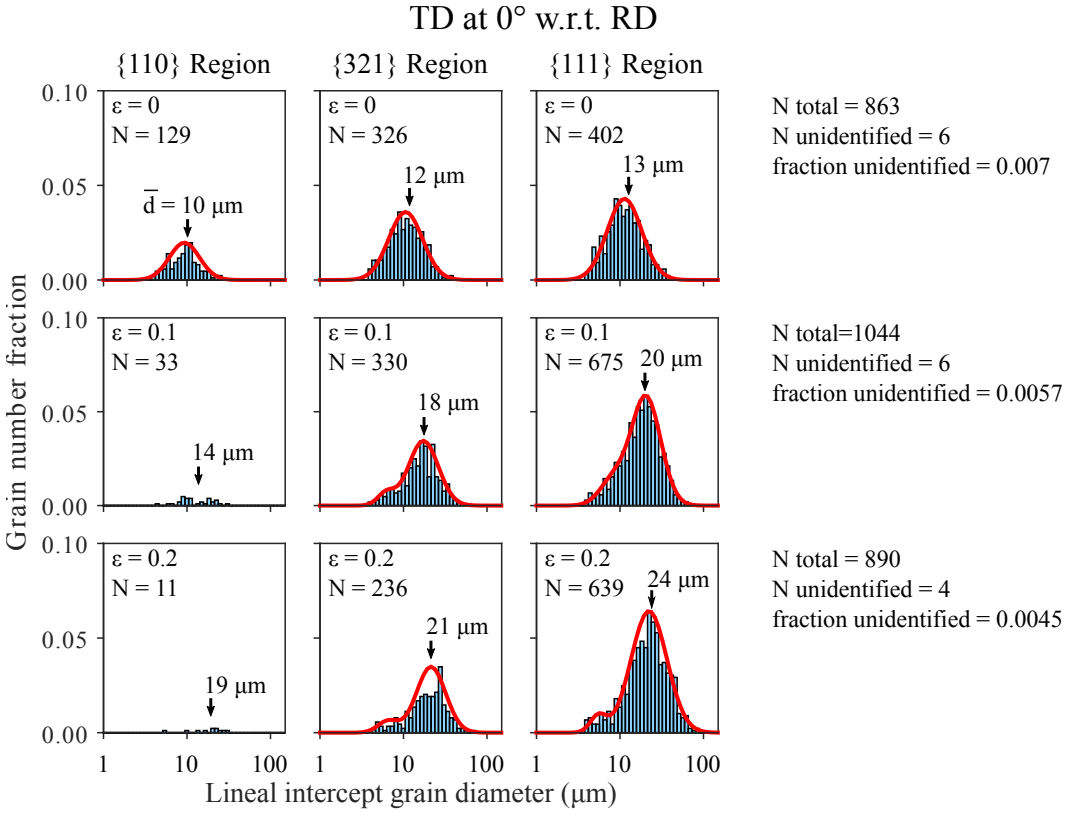

	{110} Region		{321} Region			{111} Region		
	μ (μm)	σ (μm)	μ (μm)	σ (μm)	w (%)	μ (μm)	σ (μm)	w (%)
$\varepsilon = 0$	9	2	11	2	-	11	2	-
$\varepsilon = 0.1$	-	-	6	1	10.0	8	1	17.6
	-	-	17	2	90.0	20	2	82.4
$\varepsilon = 0.2$	-	-	7	1	11.1	6	1	5.8
	-	-	21	1	88.9	22	2	94.2

Figure 6.5: Histograms are shown of the grain number fraction *versus* lineal intercept grain diameter for the {110}, {321}, and {111} regions of planes, as labeled in each column, for strains of 0, 0.1, and 0.2, as labeled in each row. The TD was oriented at 0° with respect to the RD. Mean lineal intercept grain size ($\bar{d}$) is marked in each histogram. The mean (μ) and standard deviation (σ) are provided in the table for each grain size distribution. Bimodal grain size distributions have the mean, standard deviation, and weighted density (w) provided for each hump.

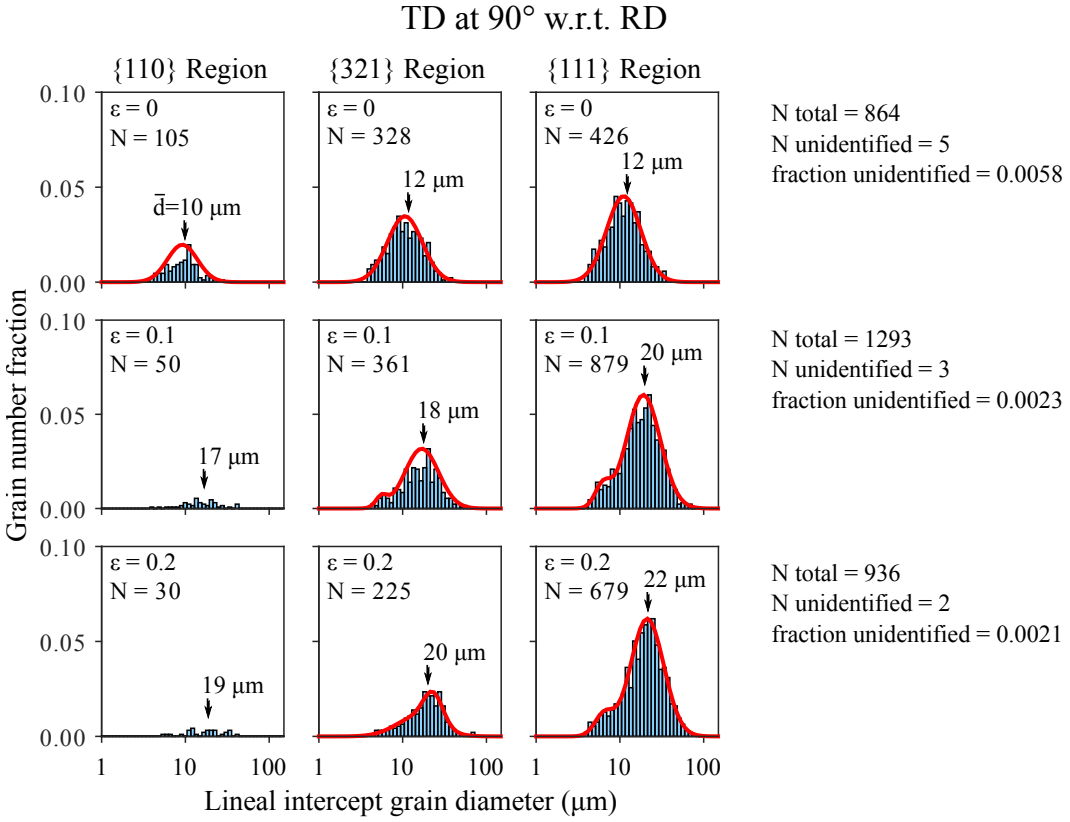

	{110} Region		{321} Region			{111} Region		
	μ (μm)	σ (μm)	μ (μm)	σ (μm)	w (%)	μ (μm)	σ (μm)	w (%)
$\varepsilon = 0$	9	2	11	2	-	11	2	-
$\varepsilon = 0.1$	-	-	6	1	5.8	6	1	8.1
	-	-	17	2	94.2	19	2	91.9
$\varepsilon = 0.2$	-	-	15	2	5.8	6	1	9.5
	-	-	23	1	94.2	21	2	90.5

Figure 6.6: Histograms are shown of the grain number fraction *versus* lineal intercept grain diameter for the {110}, {321}, and {111} region of planes, as labeled in each column, for strains of 0, 0.1, and 0.2, as labeled in each row. The TD was oriented at 90° with respect to the RD. Mean lineal intercept grain size ($\bar{d}$) is marked in each histogram. The mean (μ) and standard deviation (σ) are provided in the table for each grain size distribution. Bimodal grain size distributions have the mean, standard deviation, and weighted density (w) provided for each hump.

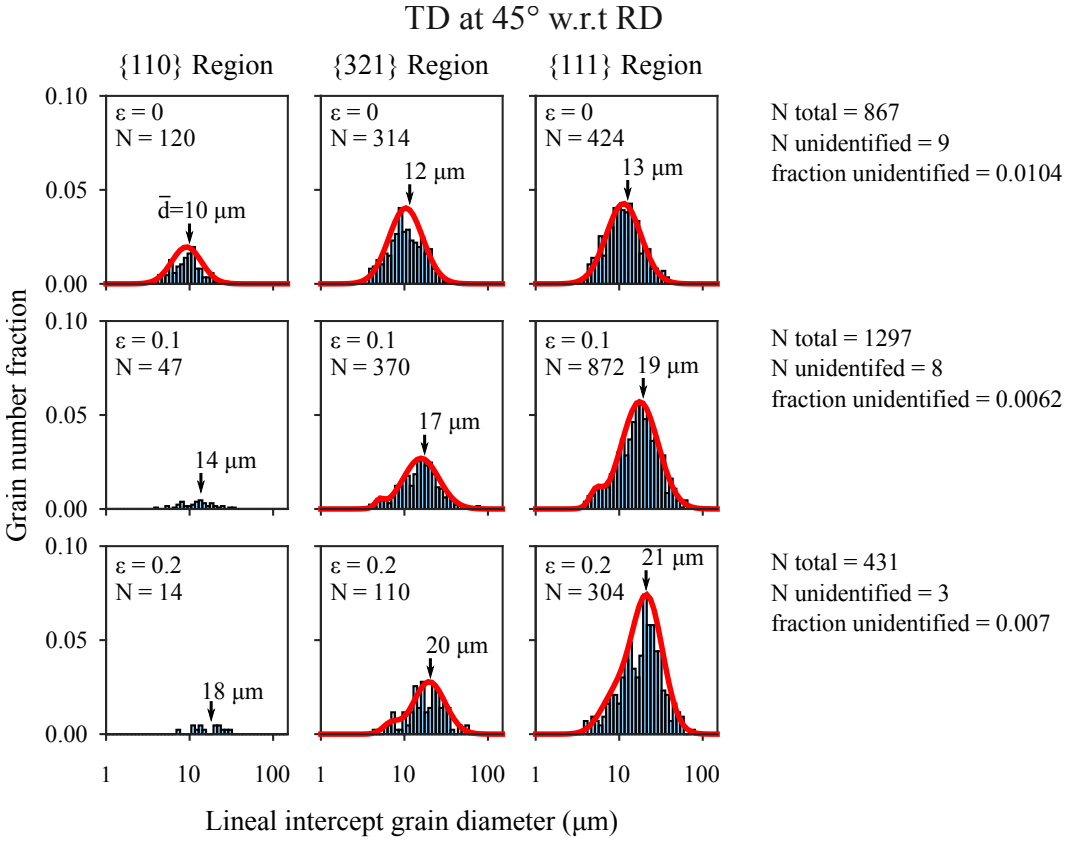

	{110} Region		{321} Region			{111} Region		
	μ (μm)	σ (μm)	μ (μm)	σ (μm)	w (%)	μ (μm)	σ (μm)	w (%)
$\varepsilon = 0$	9	2	10	2	-	11	2	-
$\varepsilon = 0.1$	-	-	5	1	3.4	5	1	4.7
	-	-	16	2	96.6	18	2	95.3
$\varepsilon = 0.2$	-	-	7	1	9.0	9	1	18.2
	-	-	20	2	91.0	21	2	81.8

Figure 6.7: Histograms are shown of the grain number fraction *versus* lineal intercept grain diameter for the {110}, {321}, and {111} region of planes, as labeled in each column, for strains of 0, 0.1, and 0.2, as labeled in each row. The TD was oriented at 45° with respect to the RD. Mean lineal intercept grain size ($\bar{d}$) is marked in each histogram. The mean (μ) and standard deviation (σ) are provided in the table for each grain size distribution. Bimodal grain size distributions have the mean, standard deviation, and weighted density (w) provided for each hump.

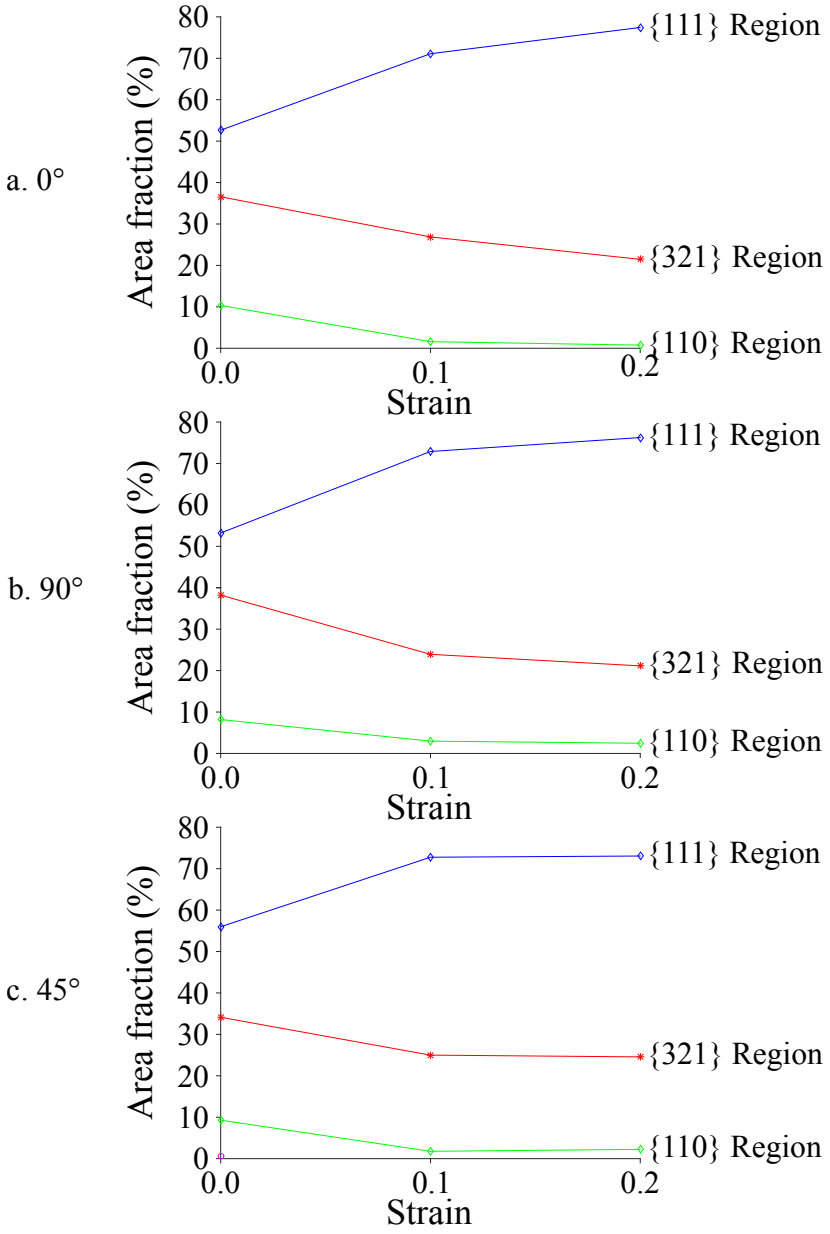

Figure 6.8: Plots of the grain area fraction *versus* strain categorized by region of planes are shown when the specimen TD is orientated at (a) 0°, (b) 90°, and (c) 45° with respect to the RD. Unidentified grains are represented by a pink circle. Data points with a grain count of less than 1% of the total number of non-boundary grains for each data set were excluded. Only the specimen with its TD at 45° with respect to the RD at a strain of 0 had unidentified grains exceeding the 1% threshold.

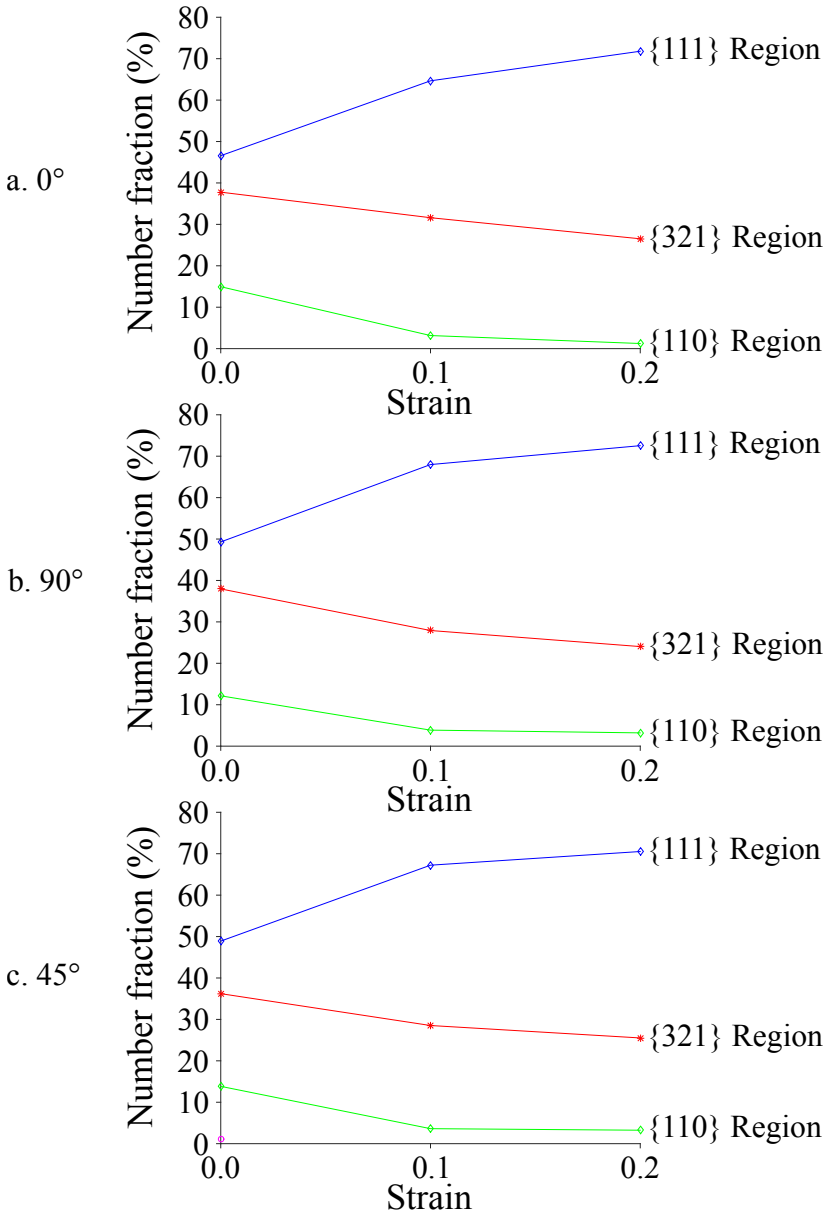

Figure 6.9: Plots of the grain number fraction *versus* strain categorized by region of planes are shown when the specimen TD is orientated at (a) 0°, (b) 90°, and (c) 45° with respect to the RD. Unidentified grains are represented by a pink circle. Data points with a grain count of less than 1% of the total number of non-boundary grains for each data set were excluded. Only the specimen with its TD at 45° with respect to the RD at a strain of 0 had unidentified grains exceeding the 1% threshold.

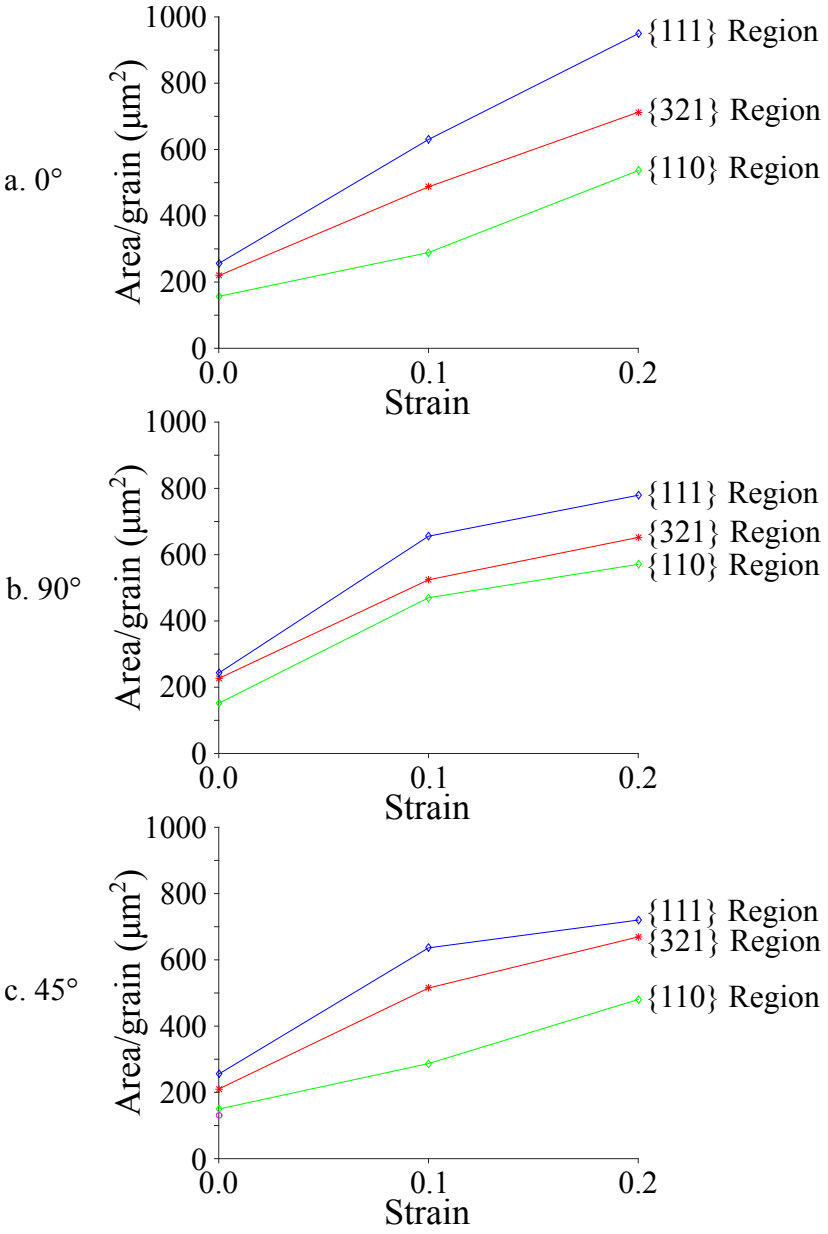

Figure 6.10: Plots of the area per grain *versus* strain categorized by region of planes are shown when the specimen TD is orientated at (a) 0°, (b) 90°, and (c) 45° with respect to the RD. Unidentified grains are represented by a pink circle. Data points with a grain count of less than 1% of the total number of non-boundary grains for each data set were excluded. Only the specimen with its TD at 45° with respect to the RD at a strain of 0 had unidentified grains exceeding the 1% threshold.

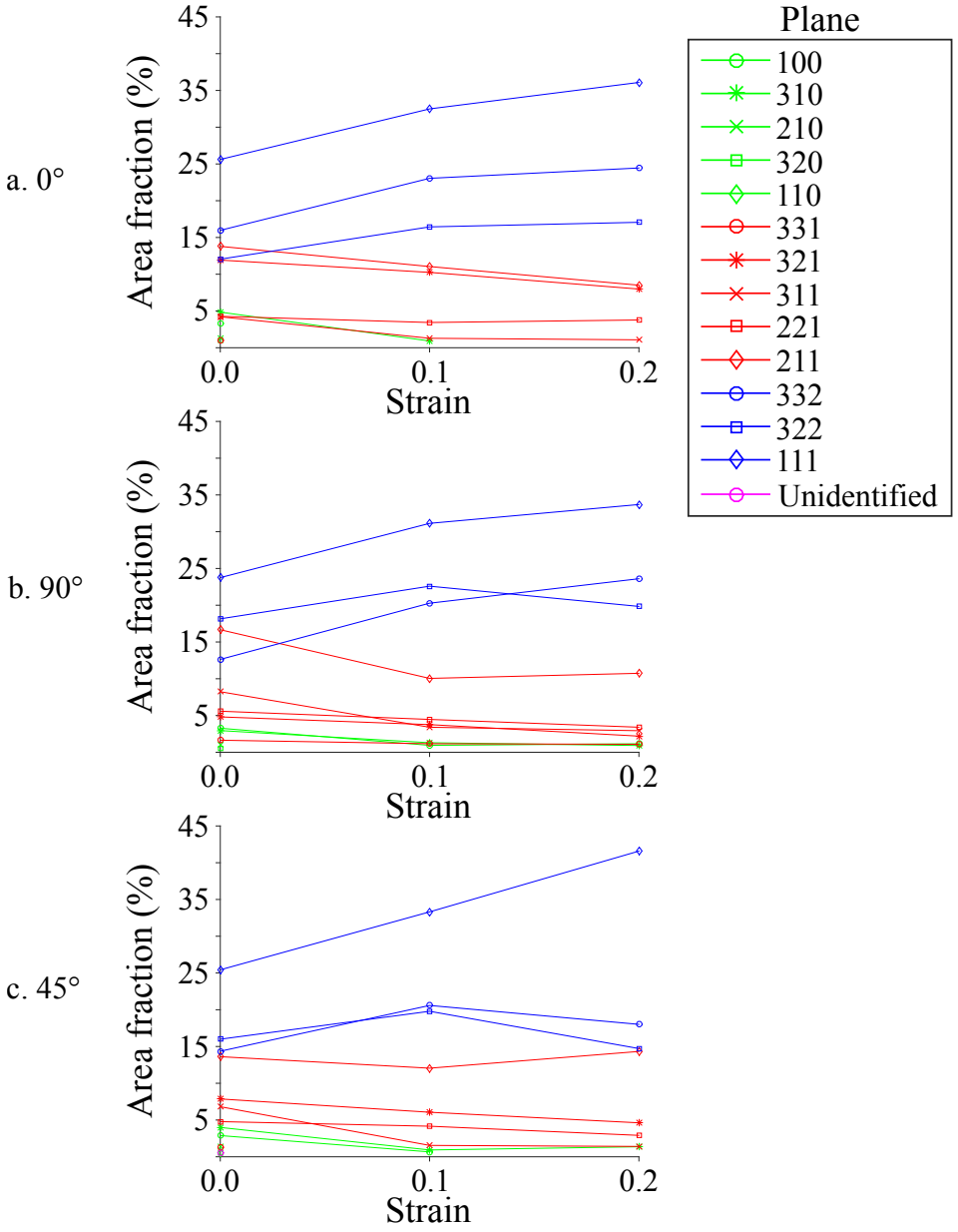

Figure 6.11: Plots of the grain area fraction *versus* strain are shown categorized by crystallographic plane parallel to the sheet plane. Specimen tensile orientations are with the TD at (a) 0°, (b) 90°, and (c) 45° with respect to the RD. Data points with a grain count of less than 1% of the total number of non-boundary grains were excluded. The colors of the individual planes match the colors of the region of planes used in previous figures.

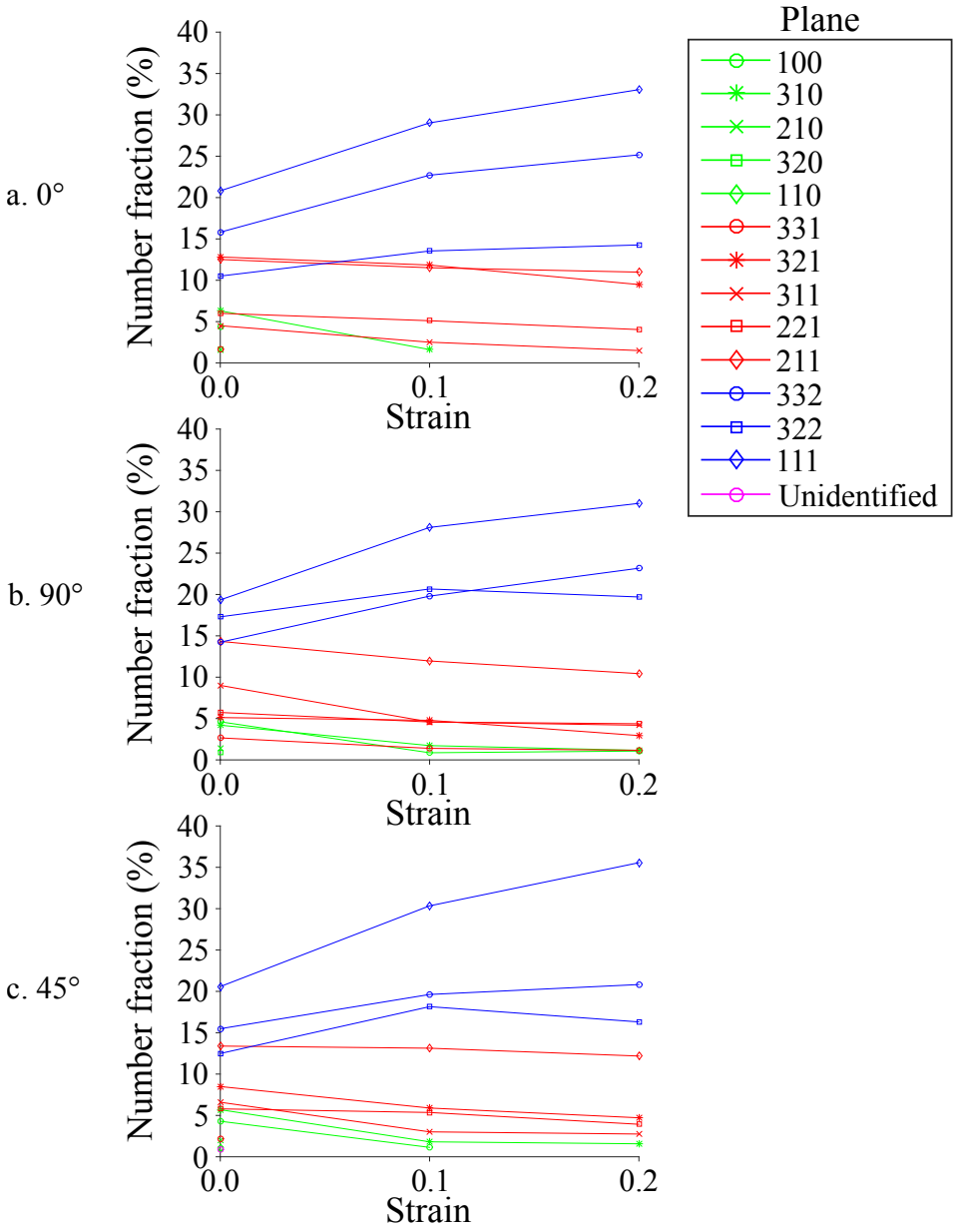

Figure 6.12: Plots of the grain number fraction *versus* strain are shown categorized by crystallographic plane parallel to the sheet plane. Specimen tensile orientations are with the TD at (a) 0°, (b) 90°, and (c) 45° with respect to the RD. Data points with a grain count of less than 1% of the total number of non-boundary grains were excluded. The colors of the individual planes match the colors of the region of planes used in previous figures.

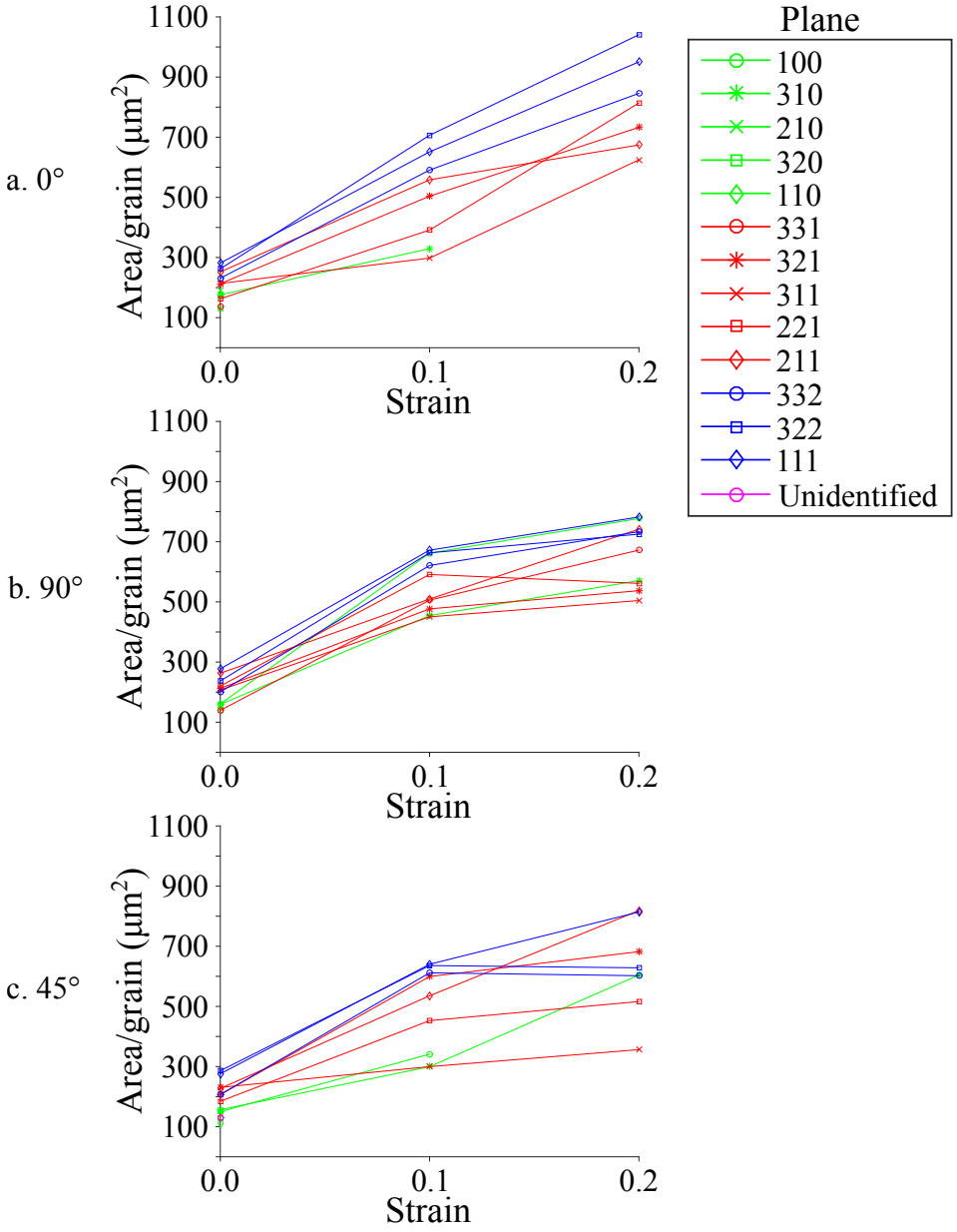

Figure 6.13: Plots of the area per grain *versus* strain are shown categorized by crystallographic plane parallel to the sheet plane. Specimen tensile orientations are with the TD at (a) 0°, (b) 90°, and (c) 45° with respect to the RD. Data points with a grain count of less than 1% of the total number of non-boundary grains were excluded. The colors of the individual planes match the colors of the region of planes used in previous figures.

6.3.2 Grains categorized by crystallographic direction along the TD

The grain area fraction, grain number fraction, and area per grain for individual crystallographic directions along the TD were calculated for each of the three specimen tensile orientations. Figures 6.14, 6.15, and 6.16 show these respective values as functions of strain. Data points with a grain count of less than 1% the total number of non-boundary grains were excluded. The calculated slopes and correlation coefficients with strain for the data in Figures 6.14-6.16 are provided in Appendix E. Caution must be taken when interpreting these data. This method of analysis was incapable of isolating the lattice rotation effect and differentiating it from the effect of DNGG. Therefore, increased grain area fractions and grain number fractions with strain could be attributable to lattice rotation during slip and/or DNGG. Lattice rotation strengthened the intensity of texture components within the α-fiber along the TD (see Section 6.2). This means that the lattice rotation effect must be taken into consideration when discussing the data with respect to crystallographic directions along the TD. These data were probed for any sensitivity of changes with strain to grain crystallographic orientation with respect to the specimen TD. None were observed. The analyses that demonstrate this insensitivity of grain area fraction, grain number fraction, and area per grain with strain to grain crystallographic orientation along the specimen TD are described in the following.

The grain area fraction *versus* strain, Figure 6.14, and grain number

fraction *versus* strain, Figure 6.15, show no dependence on a grain's crystallographic direction along the TD. The correlation coefficients (calculated per grain crystallographic direction along the TD) of the grain area fraction and grain number fraction as functions of strain were in general weak ($< |0.8|$). This could indicate some combination of the following three possibilites: (i) The grain area fraction and grain number fraction categorized by crystallographic direction along the TD were independent of strain. (ii) The grain area fraction and grain number fraction were nonlinearly dependent on strain. (iii) The behavior of the three specimen tensile orientations are contradictory, cancelling each other out in the correlation. The data in Figures 6.14 and 6.15 present evidence for (i) and (iii). The grain area fraction and grain number fraction data vary significantly between the three specimen tensile orientations. Altering the tensile specimen orientation with respect to the RD changes the initial recrystallized texture. This is likely contributing to the variation in grain area fraction and grain number fraction for specific grain orientations along the TD as specimen tensile orientation changes. Note that changes to the specimen TD with respect to the RD do not change the crystallographic planes parallel to the sheet plane, i.e., the plane orientations are invarient with specimen tensile orientation changes within the sheet.

In general, there are not clear trends evident between grain area fraction and grain number fraction with strain in Figures 6.14 and 6.15. Many of the grain area fractions and grain number fractions categorized by crystallographic direction along the TD do not change with strain. Others were observed to

increase from a strain of 0 to 0.1 and then decrease from a strain of 0.1 to 0.2 or vice versa. The crystallographic direction along the TD with the largest overall slope with strain (from $\varepsilon = 0$ to $\varepsilon = 0.2$) for the grain area fraction and grain number fraction depended on specimen tensile orientation. When the TD was oriented at 0° with respect to the RD, the largest increase in grain area fraction was the <110>||TD trailed by the <320>||TD. Grains from the <320>||TD followed closely by the <110>||TD had the largest increase in grain number fraction. When the TD was oriented at 90° with respect to the RD, the largest increase in grain area fraction was the <110>||TD followed by the <320>||TD. Grains from the <110>||TD followed closely by the <320>||TD had the largest increase in grain number fraction. When the TD was oriented at 45° with respect to the RD, the largest increase in grain area fraction was the <321>||TD followed by the <320>||TD. Grains from the <110>||TD followed by the <321>||TD had the largest increase in grain number fraction. This discussion was limited to the top two crystallographic directions along the TD for each specimen tensile orientation. From these data, it is apparent that there are not any strong trends. However, the <110>||TD and the <320>||TD were in general the fastest growing orientations. It should be noted the <110>||TD is the α-fiber and strengthened by lattice rotation during slip.

The area per grain is plotted against strain and categorized by crystallographic direction along the TD in Figure 6.16. With increased strain, the overall average area per grain (from $\varepsilon = 0$ to $\varepsilon = 0.2$) increased for all crys-

tallographic directions along the TD. A decrease in the area per grain from a strain of 0.1 to 0.2 was observed for some of the crystallographic directions along the TD. In general, the correlation coefficient of the area per grain with strain for each crystallographic direction along the TD was positive and strong (> 0.8). The overall slopes (from $\varepsilon = 0$ to $\varepsilon = 0.2$) of the area per grain with strain were observed to vary between the three specimen tensile orientations. When the TD was oriented at 0° with respect to the RD, grains from the <110>||TD had the largest increase in area per grain. When the TD was oriented at 90° with respect to the RD, grains from the <111>||TD had the largest increase in area per grain. When the TD was oriented at 45° with respect to the RD, grains from the <311>||TD had the largest increase in area per grain.

The crystallographic direction along the TD of a grain alone was not observed to significantly influence growth by DNGG. The <110>||TD and <320>||TD appear to be the most favored for growth. The <110>||TD is strengthened by lattice rotation during slip. The <320>||TD is near the <110>||TD, which may also be strengthened by lattice rotation during slip.

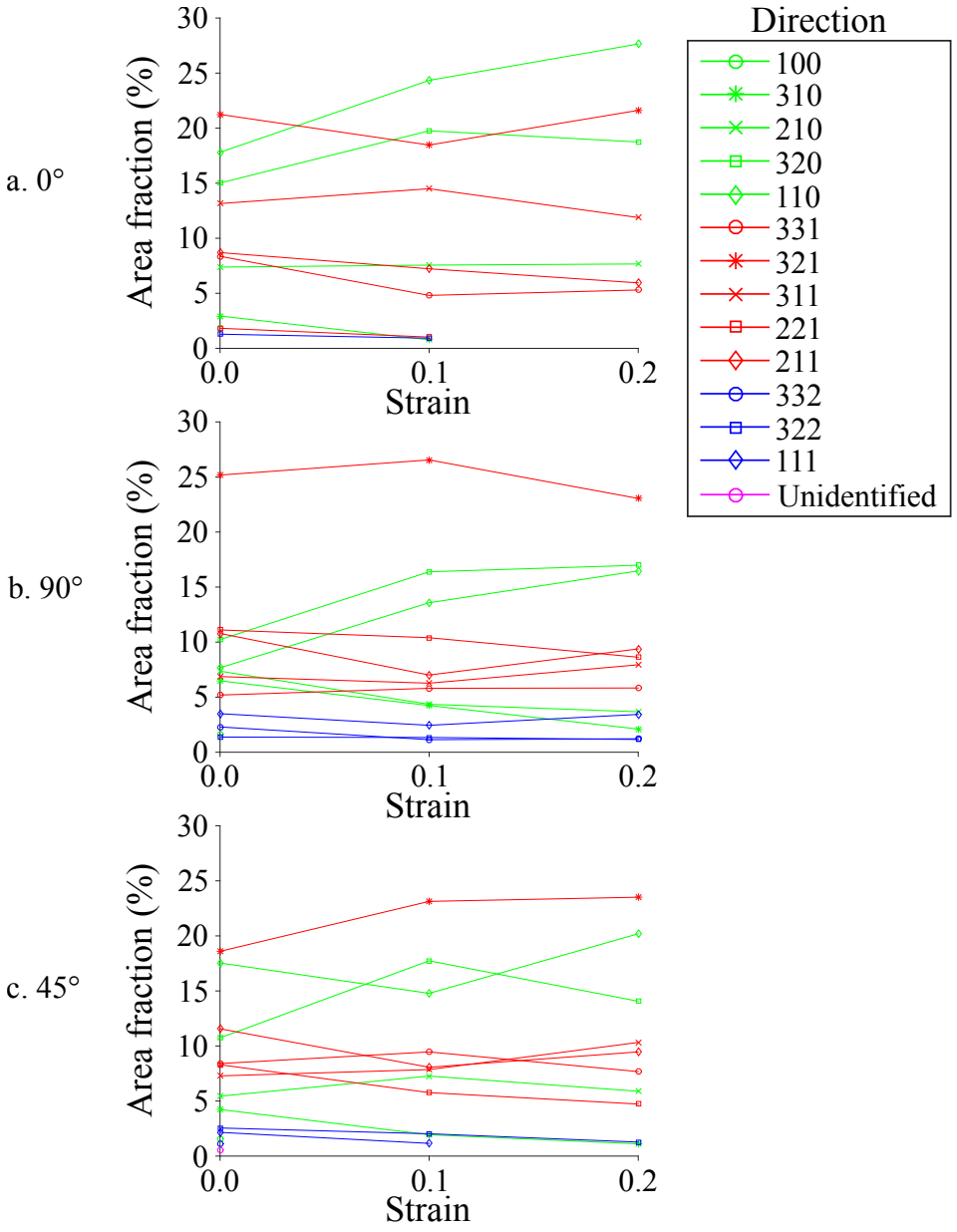

Figure 6.14: Plots of the grain area fraction *versus* strain are shown categorized by crystallographic direction along the TD. Specimen tensile orientations are with the TD at (a) 0°, (b) 90°, and (c) 45° with respect to the RD. Data points with a grain count of less than 1% of the total number of non-boundary grains were excluded.

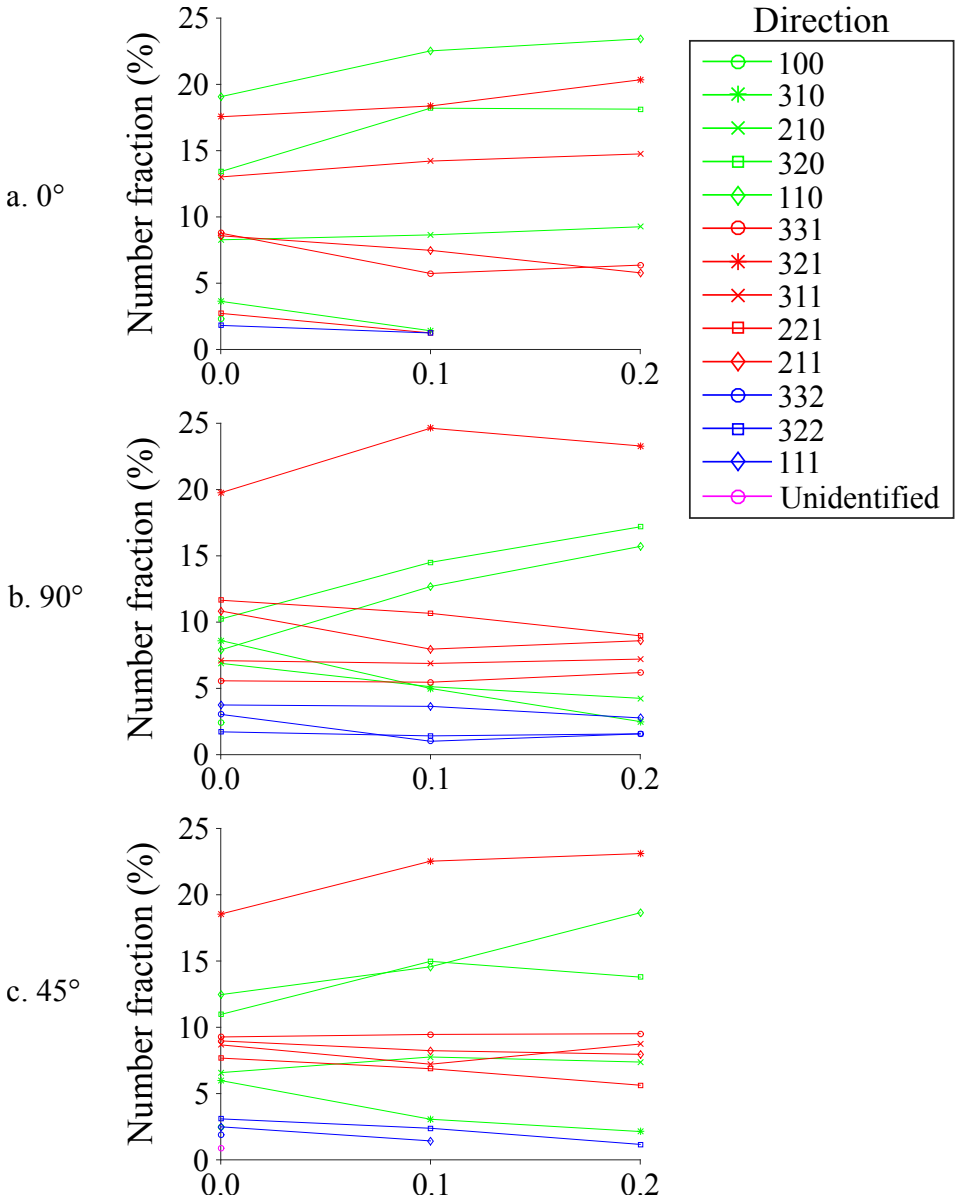

Figure 6.15: Plots of the grain number fraction *versus* strain are shown categorized by crystallographic direction along the TD. Specimen tensile orientations are with the TD at (a) 0°, (b) 90°, and (c) 45° with respect to the RD. Data points with a grain count of less than 1% of the total number of non-boundary grains were excluded.

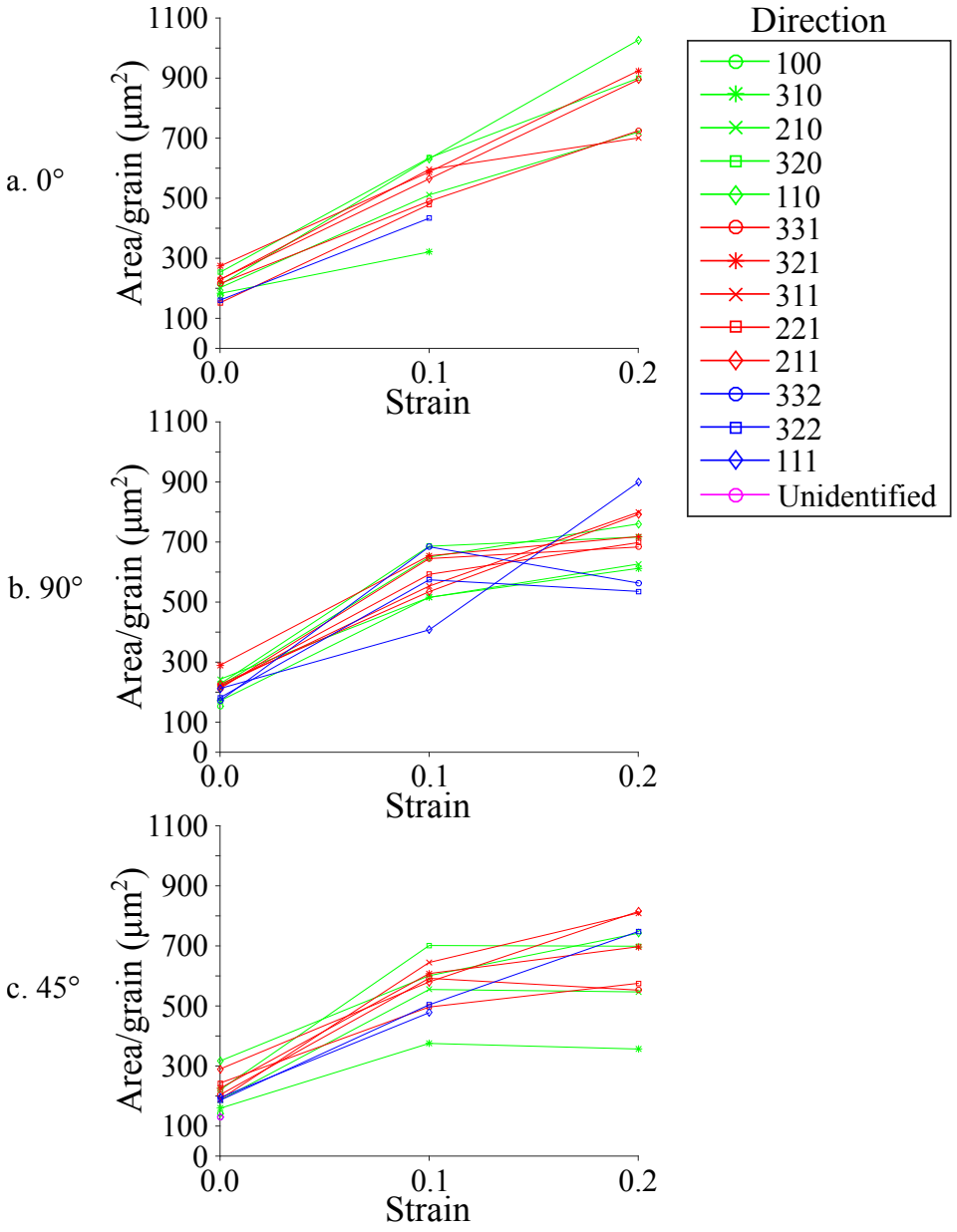

Figure 6.16: Plots of the area per grain *versus* strain are shown categorized by crystallographic direction along the TD. Specimen tensile orientations are with the TD at (a) 0°, (b) 90°, and (c) 45° with respect to the RD. Data points with a grain count of less than 1% of the total number of non-boundary grains were excluded.

6.3.3 Grains categorized by reference orientation (plane + direction)

The grain area fraction, grain number fraction, and area per grain for individual crystallographic reference orientations (see Section 4.2.4) were calculated for each of the three specimen tensile orientations. The calculated slopes and correlation coefficients for these data as functions of strain are provided in Appendix E. Caution must be taken when interpreting these data. This method of analysis was incapable of isolating the lattice rotation effect and differentiating it from the effect of DNGG. Therefore, increased grain area fractions and grain number fractions with strain could be attributable to lattice rotation during slip and/or DNGG. Lattice rotation strengthened the intensity of texture components within the α-fiber along the TD (see Section 6.2). This means that the lattice rotation effect must be taken into consideration when discussing the data with respect to reference orientations.

A large number of the reference orientations had a grain count of less than 1% of the total number of non-boundary grains at strains of 0, 0.1, or 0.2. A list of these scarce reference orientations for each specimen tensile orientation is provided in Appendix F. The combined grain area fractions of these scarce reference orientations are presented as functions of strain for each specimen tensile orientation in Figure 6.17. In the recrystallized condition, the combined grain area fraction of these scarce reference orientations was between 15% and 25%. The grain area fraction of these scarce reference orientations was observed to drop significantly with strain. After uniaxial tensile deforma-

tion at 850 °C at a constant true-strain rate of 10^{-4} s^{-1} to a true strain of 0.2, the combined grain area fraction of these reference orientations was between approximately 3% and 10%. These scarce reference orientations were uncommon in the recrystallized state ($\varepsilon = 0$) of all specimen tensile orientations, although several individual orientations each comprised over 1% of the total number of non-boundary grains. However, the number of grains among these scarce reference orientations rapidly decreased with strain, as demonstrated by Figure 6.17. This suggests that grains from these scarce reference orientations were consumed by the growth of grains from other orientations. Because grains from these scarce reference orientations were small in number, particularly as strain increased, statistical analysis of their influence was difficult, but any influence from them was likely small. For these reasons, the scarce reference orientations listed in Appendix F were excluded from further analysis. This excluded all reference orientations from the {110} region of planes, all of which were part of this scarce group.

Figures 6.18-6.20 show grain area fractions as functions of strain for each specimen tensile orientation categorized by reference orientation. The data in these figures show the following general trends. Only the {111}<110> texture component had a positive correlation coefficient with strain of greater than 0.8. This indicates that the grain area fraction of grains with the {111}<110> texture component had a direct dependence on strain. This dependency was similar for all three specimen tensile orientations. The vast majority of grains with reference orientations that belonged to the {321} region of planes had a

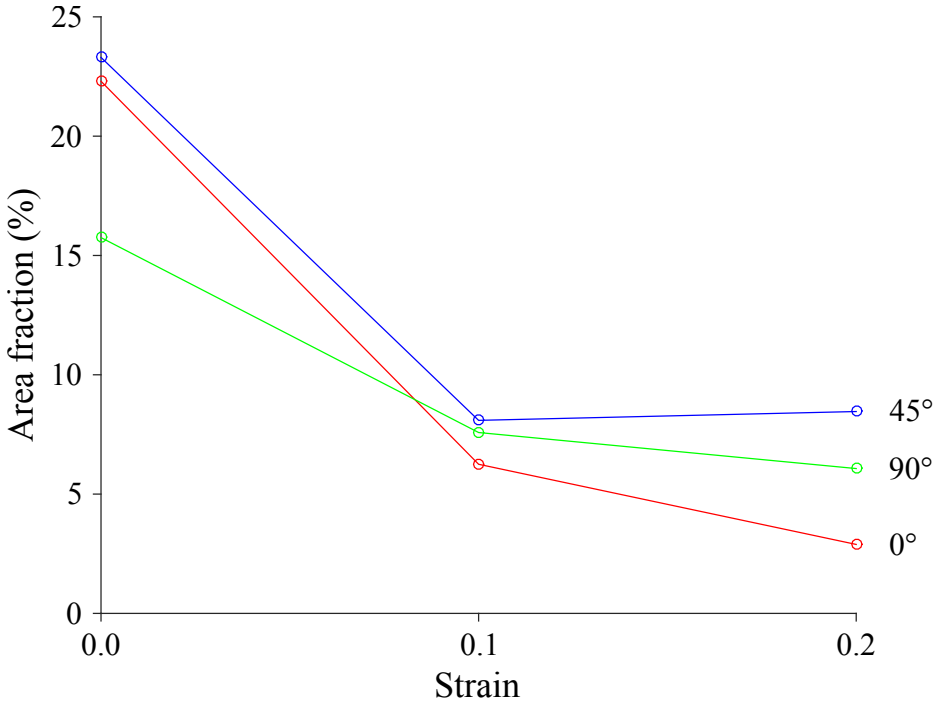

Figure 6.17: A plot of the total grain area fraction of scarce reference orientations *versus* strain for the three specimen tensile orientations is shown. The total grain area fraction is comprised of the summation of all reference orientations with a grain count of less than 1% of the total number of non-boundary grains at strains of 0, 0.1, or 0.2.

negative overall slope with strain (from $\varepsilon = 0$ to $\varepsilon = 0.2$). Meanwhile, the vast majority of grains with reference orientations that belonged to the {111} region of planes had a positive overall slope with strain (from $\varepsilon = 0$ to $\varepsilon = 0.2$). The {322}<221> was the only texture component from the {111} region of planes with a negative overall slope with strain (from $\varepsilon = 0$ to $\varepsilon = 0.2$) for all three specimen tensile orientations. Its correlation coefficient with strain, however, was only -0.15. The {111}<110> texture component had the highest overall grain area fraction slope with strain (from $\varepsilon = 0$ to $\varepsilon = 0.2$) for

all three specimen tensile orientations. The {332}<320> texture component followed closely behind when the specimen TD was oriented at 0° with respect to the RD. The {111}<321> texture component followed closely behind when the specimen TD was oriented at 45° with respect to the RD. These three reference orientations presented the greatest changes in grain area fraction with strain. It should be noted that the {111}<110> texture component is part of the α-fiber that is strengthened by lattice rotation during tensile deformation.

Figures 6.21-6.23 show grain number fractions as functions of strain for each specimen tensile orientation. The following general trends are evident from these data. The {111}<110> and {111}<321> texture components were the only reference orientations with positive correlation coefficients with strain of greater than 0.8. This indicates that these texture components are well correlated with strain for all three specimen tensile orientations. The majority of reference orientations from the {321} region of planes had a negative overall slope with strain (from $\varepsilon = 0$ to $\varepsilon = 0.2$). The majority of reference orientations from the {111} region of planes had a positive overall slope with strain (from $\varepsilon = 0$ to $\varepsilon = 0.2$). The {322}<221> texture component was the only reference orientation from the {111} region of planes that had a negative overall slope with strain for all three specimen tensile orientations. The correlation coefficient of the {322}<221> texture component with strain was extremely weak at only -0.12. The texture components with the largest overall grain number fraction slope with strain (from $\varepsilon = 0$ to $\varepsilon = 0.2$) varied with specimen tensile orientation. When the specimen TD was ori-

ented at 0° with respect to the RD, the {111}<321> texture component had the largest overall slope with strain (from $\varepsilon = 0$ to $\varepsilon = 0.2$) followed closely by the {332}<320> and {111}<110> texture components. When the TD was oriented at 90° with respect to the RD, the {111}<110> texture component had the largest overall slope with strain (from $\varepsilon = 0$ to $\varepsilon = 0.2$) followed closely by the {111}<321> texture component. When the TD was oriented at 45° with respect to the RD, the {111}<321> texture component had the largest overall slope with strain (from $\varepsilon = 0$ to $\varepsilon = 0.2$) followed closely by the {111}<110> texture component. It should be noted that the {111}<110> texture component is part of the α-fiber that is strengthened by lattice rotation during tensile deformation.

Among all the specimen tensile orientations, 14 unique reference orientations out of the 63 total have grain area fractions and grain number fractions that increased with strain. Only 6 of these have grain area fractions and grain number fractions that increased with strain for all three specimen tensile orientations. These 14 unique reference orientations are grouped by specimen tensile orientation in Tables 6.1-6.3. Values are provided in these tables only if the grain area fraction and grain number fraction had a positive overall slope with strain (from $\varepsilon = 0$ to $\varepsilon = 0.2$) for the specified specimen tensile orientation. The 6 reference orientations that appeared for all three specimen tensile orientations are emphasized with an asterisk. These 6 reference orientations belong to the {111} region of planes. All three of the reference orientations containing a {111} plane are included in these 6. The fastest

growing reference orientations varied with specimen tensile orientation. New grains were not created during or after elevated-temperature tensile deformation. Therefore, these reference orientations must be strengthened by either lattice rotation during slip and/or by DNGG.

Table 6.1: Reference orientations with a positive overall slope with strain (from $\varepsilon = 0$ to $\varepsilon = 0.2$) for both the grain area fraction and grain number fraction are shown. The specimen TD is oriented at 0° with respect to the RD. The overall slopes of the grain area fraction and grain number fraction are provided.

ID	{h k l}	<u v w>	area fraction slope	number fraction slope
37	{3 2 1}	<2 1 0>	4.68	5.97
44	{2 2 1}	<2 1 0>	11.31	9.41
48	{2 1 1}	<2 1 0>	N/A	N/A
51	{2 1 1}	<1 1 0>	4.45	5.14
52	{2 1 1}	<1 1 0>	N/A	N/A
53*	{3 3 2}	<3 2 0>	30.54	28.82
54	{3 3 2}	<3 3 1>	N/A	N/A
55	{3 3 2}	<1 1 0>	N/A	N/A
56*	{3 3 2}	<3 1 1>	12.44	20.83
57*	{3 2 2}	<3 2 0>	3.83	7.18
59	{3 2 2}	<1 1 0>	23.46	15.71
60*	{1 1 1}	<1 1 0>	33.93	27.39
61*	{1 1 1}	<3 2 1>	17.71	32.27
62*	{1 1 1}	<2 1 1>	0.51	1.96

* Reference orientations with a positive overall slope with strain for both the grain area fraction and grain number fraction for all three specimen tensile orientations.

The area per grain is plotted as a function of strain and categorized by reference orientation in Figures 6.24-6.26 for each specimen tensile orienta-

Table 6.2: Reference orientations with a positive overall slope with strain (from $\varepsilon = 0$ to $\varepsilon = 0.2$) for both the grain area fraction and grain number fraction are shown. The specimen TD is oriented at 90° with respect to the RD. The overall slopes of the grain area fraction and grain number fraction are provided.

ID	{h k l}	<u v w>	area fraction slope	number fraction slope
37	{3 2 1 }	<2 1 0>	N/A	N/A
44	{2 2 1}	<2 1 0>	N/A	N/A
48	{2 1 1}	<2 1 0>	N/A	N/A
51	{2 1 1}	<1 1 0>	N/A	N/A
52	{2 1 1}	<3 1 1>	N/A	N/A
53*	{3 3 2}	<3 2 0>	18.84	15.35
54	{3 3 2}	<3 3 1>	6.75	6.39
55	{3 3 2}	<1 1 0>	18.19	16.27
56*	{3 3 2}	<3 1 1>	12.10	7.15
57*	{3 2 2}	<3 2 0>	17.64	21.20
59	{3 2 2}	<1 1 0>	N/A	N/A
60*	{1 1 1}	<1 1 0>	34.28	32.14
61*	{1 1 1}	<3 2 1>	9.68	27.60
62*	{1 1 1}	<2 1 1>	6.70	1.62

* Reference orientations with a positive overall slope with strain for both the grain area fraction and grain number fraction for all three specimen tensile orientations.

tion. With increased strain, the overall area per grain (from $\varepsilon = 0$ to $\varepsilon = 0.2$) increased for all reference orientations. The area per grain for some of the reference orientations was observed to decrease or stay approximately the same from a strain of 0.1 to 0.2. The reference orientations whose area per grain remained approximately the same from a strain of 0.1 to 0.2 belonged primarily to the {111} region of planes. This was especially prominent when

Table 6.3: Reference orientations with a positive overall slope with strain (from $\varepsilon = 0$ to $\varepsilon = 0.2$) for both the grain area fraction and grain number fraction are shown. The specimen TD is oriented at 45° with respect to the RD. The overall slopes of the grain area fraction and grain number fraction are provided.

ID	{h k l}	<u v w>	area fraction slope	number fraction slope
37	{3 2 1}	<2 1 0>	N/A	N/A
44	{2 2 1}	<2 1 0>	N/A	N/A
48	{2 1 1}	<2 1 0>	0.43	3.20
51	{2 1 1}	<1 1 0>	N/A	N/A
52	{2 1 1}	<3 1 1>	10.61	0.27
53*	{3 3 2}	<3 2 0>	10.98	9.26
54	{3 3 2}	<3 3 1>	1.40	10.14
55	{3 3 2}	<1 1 0>	N/A	N/A
56*	{3 3 2}	<3 1 1>	12.70	7.49
57*	{3 2 2}	<3 2 0>	8.77	10.71
59	{3 2 2}	<1 1 0>	N/A	N/A
60*	{1 1 1}	<1 1 0>	31.21	29.58
61*	{1 1 1}	<3 2 1>	29.96	33.6
62*	{1 1 1}	<2 1 1>	13.68	10.24

* Reference orientations with a positive overall slope with strain for both the grain area fraction and grain number fraction for all three specimen tensile orientations.

the TD was oriented at 45° with respect to the RD. The reference orientations with the highest overall area per grain slope with strain (from $\varepsilon = 0$ to $\varepsilon = 0.2$) depended on the specimen tensile orientation. The {322}<110> texture component followed closely by the {332}<110> texture component were the highest when the TD was oriented at 0° with respect to the RD. The {211}<111> texture component followed closely by the {111}<211> texture

component were the highest when the TD was oriented at 90° with respect to the RD. The {211}<311> texture component followed by the {111}<211> and {332}<311> texture components were the highest when the TD was oriented at 45° with respect to the RD. Some of these reference orientations had positive overall slopes with strain (from $\varepsilon = 0$ to $\varepsilon = 0.2$) for both the grain number fraction and grain area fraction. An example was the {322}<110> texture component for the specimen TD oriented at 0° with respect to the RD. Thus, it is likely that these grains grew at the expense of others, which resulted in their increased area per grain. The other reference orientations did not have positive overall slopes with strain (from $\varepsilon = 0$ to $\varepsilon = 0.2$) for both the grain number fraction and grain area fraction. An example was the {332}<110> texture component for the specimen TD oriented at 0° with respect to the RD. Grains of these orientations were likely consumed. An increase in the area per grain for these orientations was primarily caused by the consumption of small grains from these orientations.

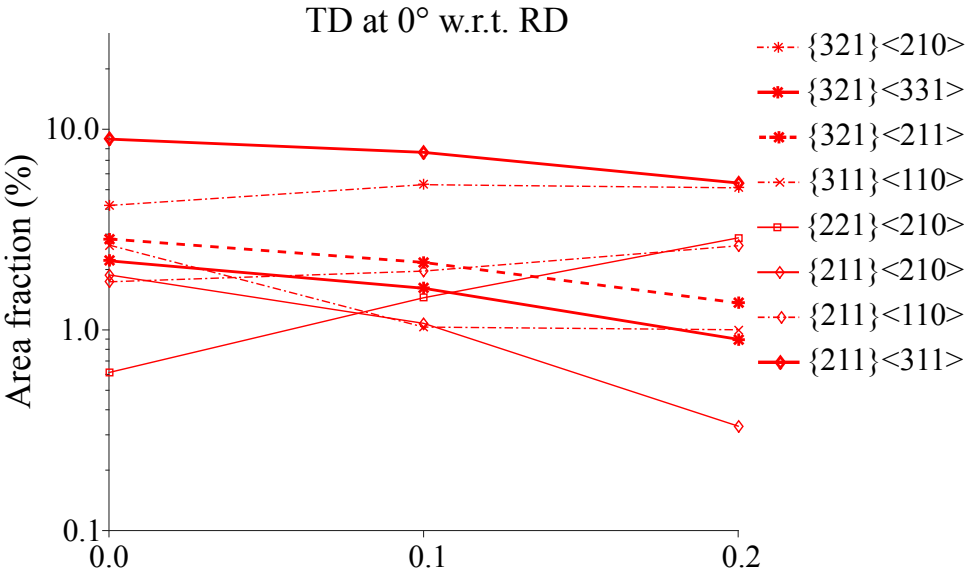

a. {321} Region

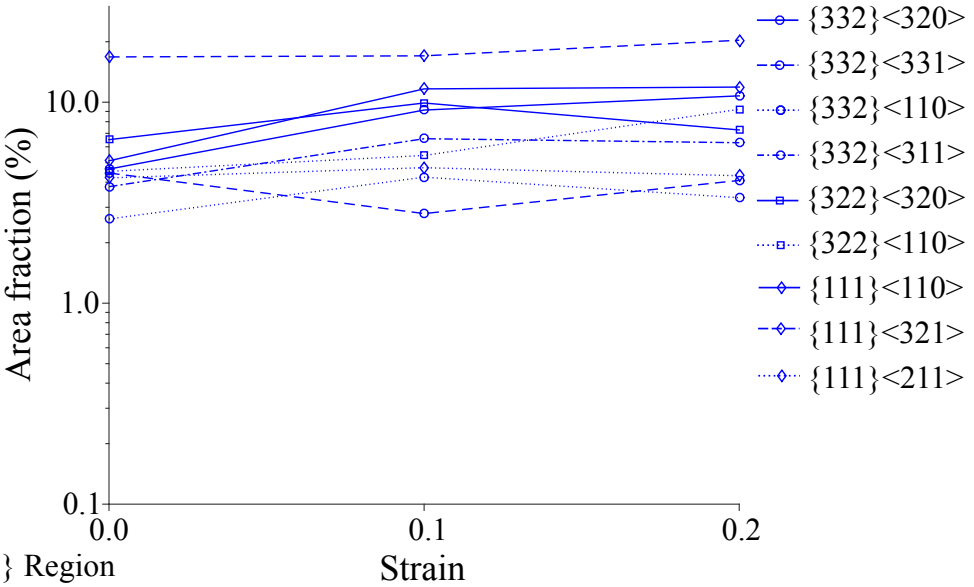

b. {111} Region

Figure 6.18: Plots of the grain area fraction *versus* strain are shown categorized by reference orientation. The plots are comprised of data with grains from (a) the {321} region of planes and (b) the {111} region of planes. The specimen tensile direction is oriented at 0° with respect to the RD. The scale on the y-axis is logarithmic. Reference orientations with a grain count of less than 1% of the total number of non-boundary grains at strains of 0, 0.1, or 0.2 were excluded.

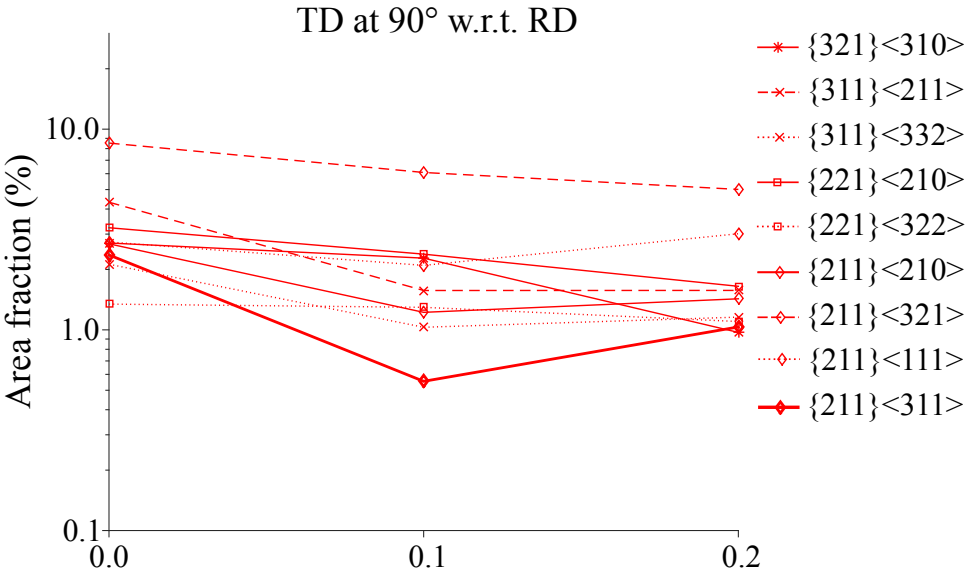

a. {321} Region

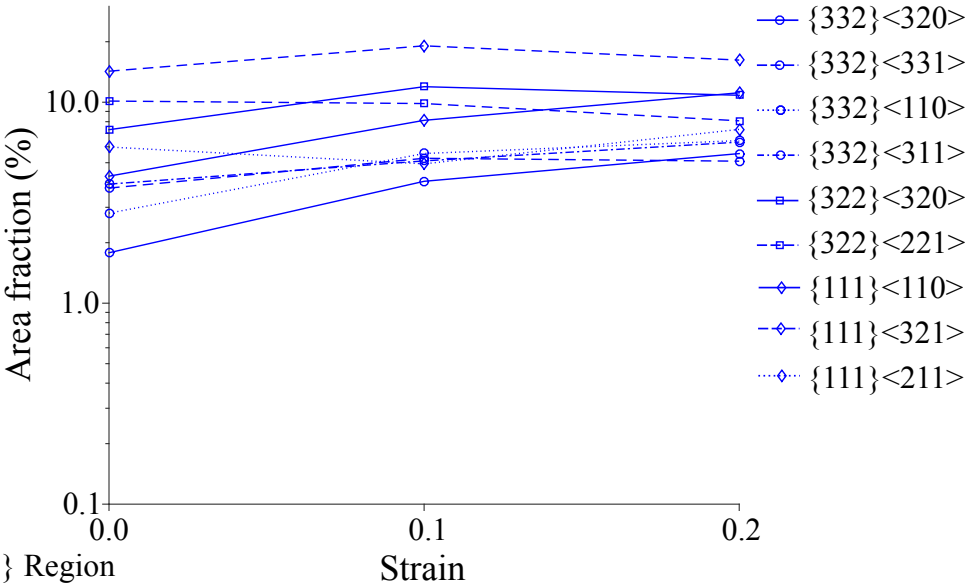

b. {111} Region

Figure 6.19: Plots of the grain area fraction *versus* strain are shown categorized by reference orientation. The plots are comprised of data with grains from (a) the {321} region of planes and (b) the {111} region of planes. The specimen tensile direction is oriented at 90° with respect to the RD. The scale on the y-axis is logarithmic. Reference orientations with a grain count of less than 1% of the total number of non-boundary grains at strains of 0, 0.1, or 0.2 were excluded.

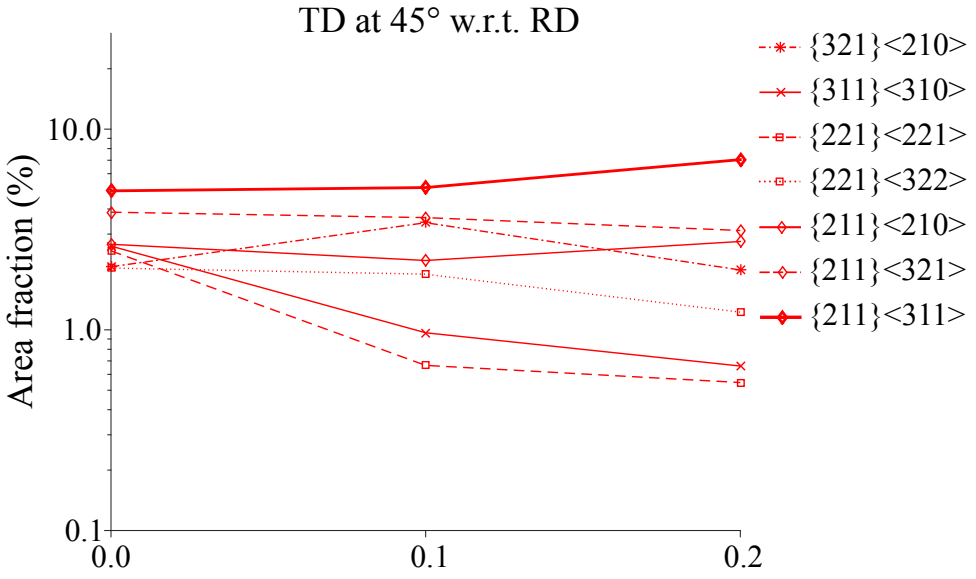

a. {321} Region

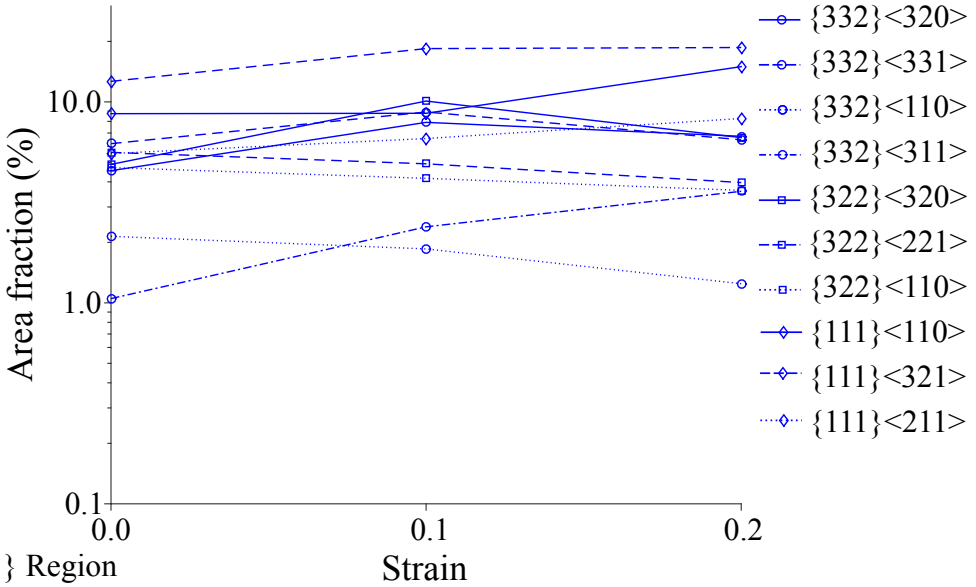

b. {111} Region

Figure 6.20: Plots of the grain area fraction *versus* strain are shown categorized by reference orientation. The plots are comprised of data with grains from (a) the {321} region of planes and (b) the {111} region of planes. The specimen tensile direction is oriented at 45° with respect to the RD. The scale on the y-axis is logarithmic. Reference orientations with a grain count of less than 1% of the total number of non-boundary grains at strains of 0, 0.1, or 0.2 were excluded.

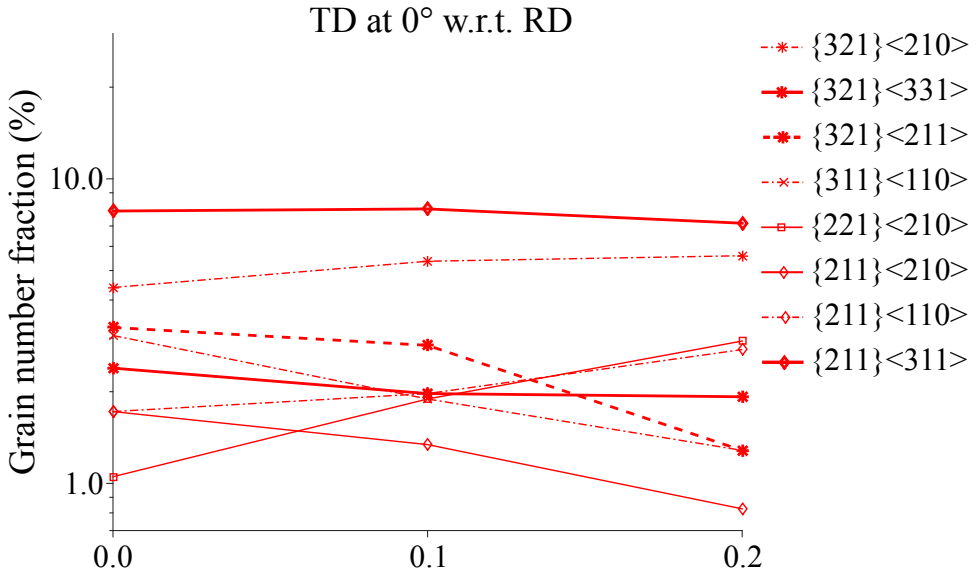

a. {321} Region

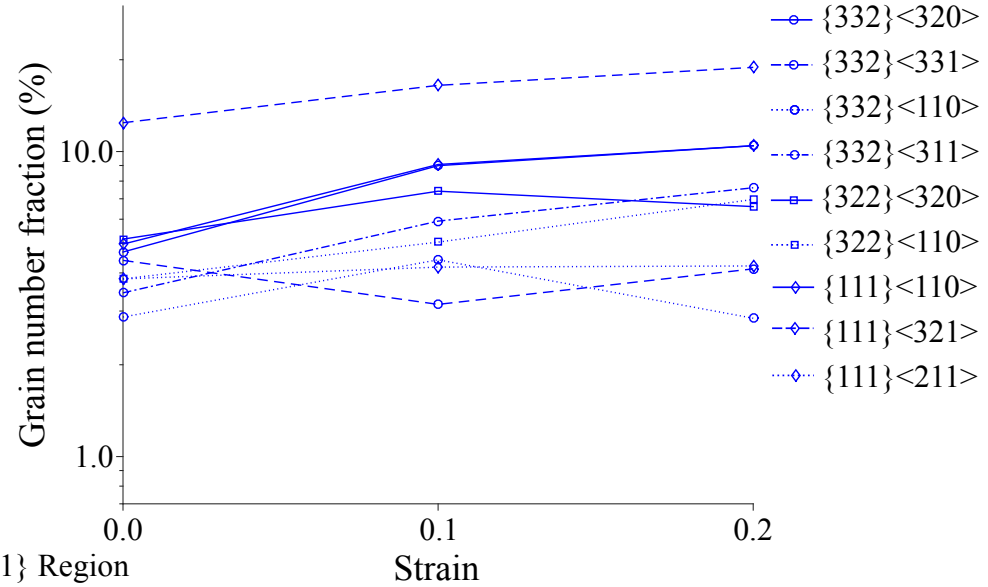

b. {111} Region

Figure 6.21: Plots of the grain number fraction *versus* strain are shown categorized by reference orientation. The plots are comprised of data with grains from (a) the {321} region of planes and (b) the {111} region of planes. The specimen tensile direction is oriented at 0° with respect to the RD. The scale on the y-axis is logarithmic. Reference orientations with a grain count of less than 1% of the total number of non-boundary grains at strains of 0, 0.1, or 0.2 were excluded.

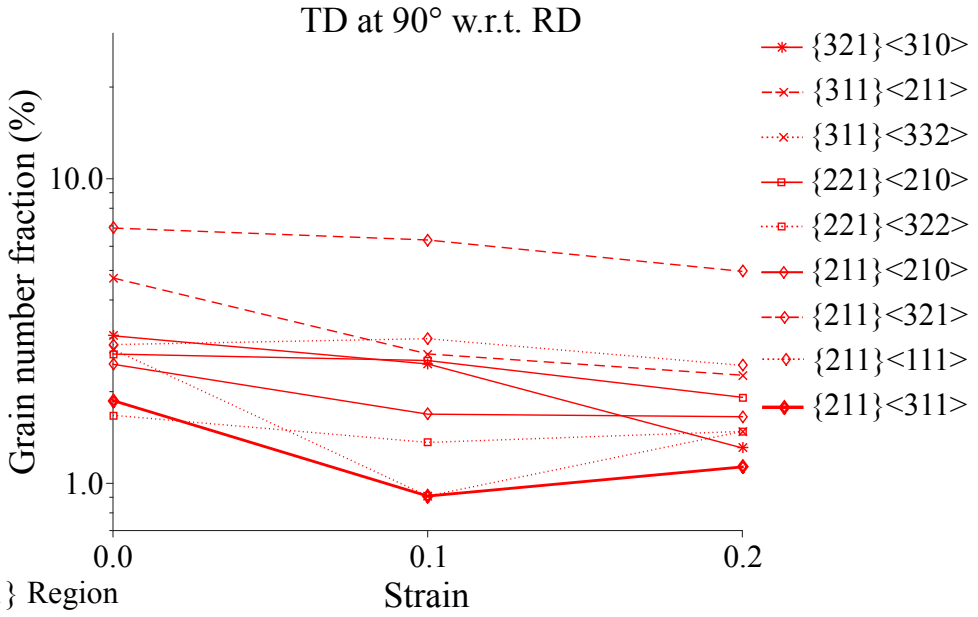

a. {321} Region

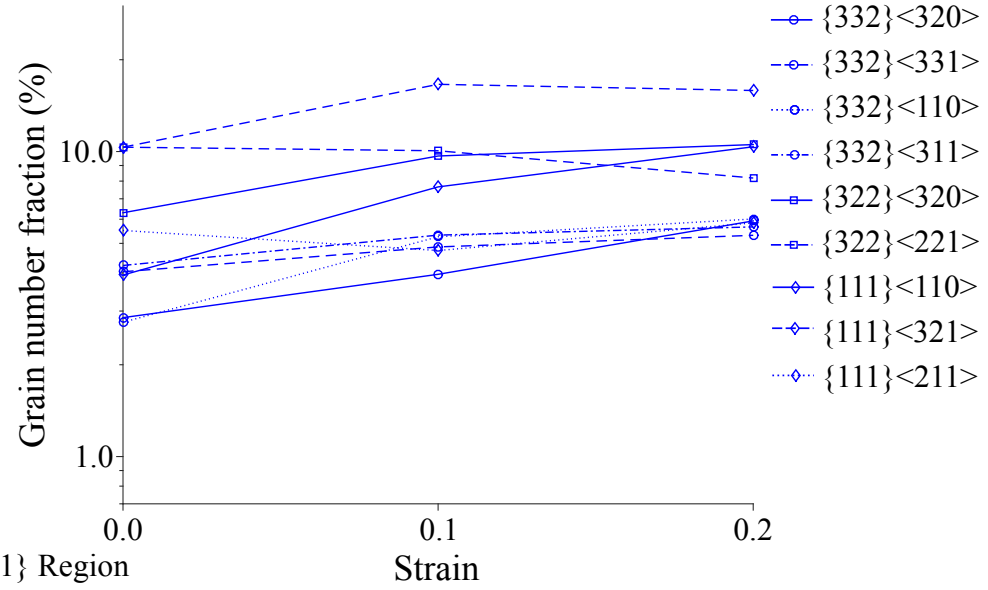

b. {111} Region

Figure 6.22: Plots of the grain number fraction *versus* strain are shown categorized by reference orientation. The plots are comprised of data with grains from (a) the {321} region of planes and (b) the {111} region of planes. The specimen tensile direction is oriented at 90° with respect to the RD. The scale on the y-axis is logarithmic. Reference orientations with a grain count of less than 1% of the total number of non-boundary grains at strains of 0, 0.1, or 0.2 were excluded.

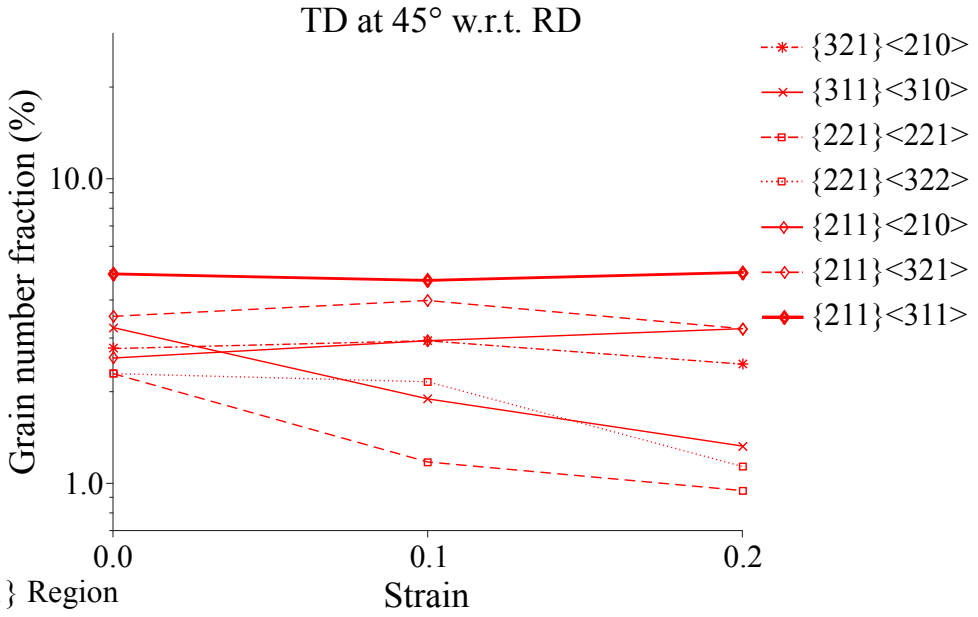

a. {321} Region

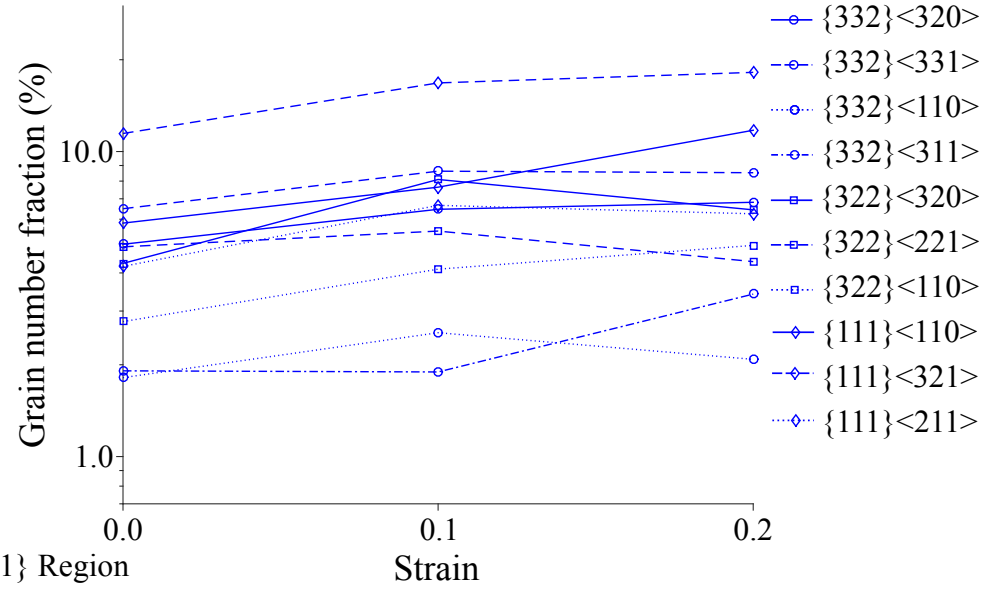

b. {111} Region

Figure 6.23: Plots of the grain number fraction *versus* strain are shown categorized by reference orientation. The plots are comprised of data with grains from (a) the {321} region of planes and (b) the {111} region of planes. The specimen tensile direction is oriented at 45° with respect to the RD. The scale on the y-axis is logarithmic. Reference orientations with a grain count of less than 1% of the total number of non-boundary grains at strains of 0, 0.1, or 0.2 were excluded.

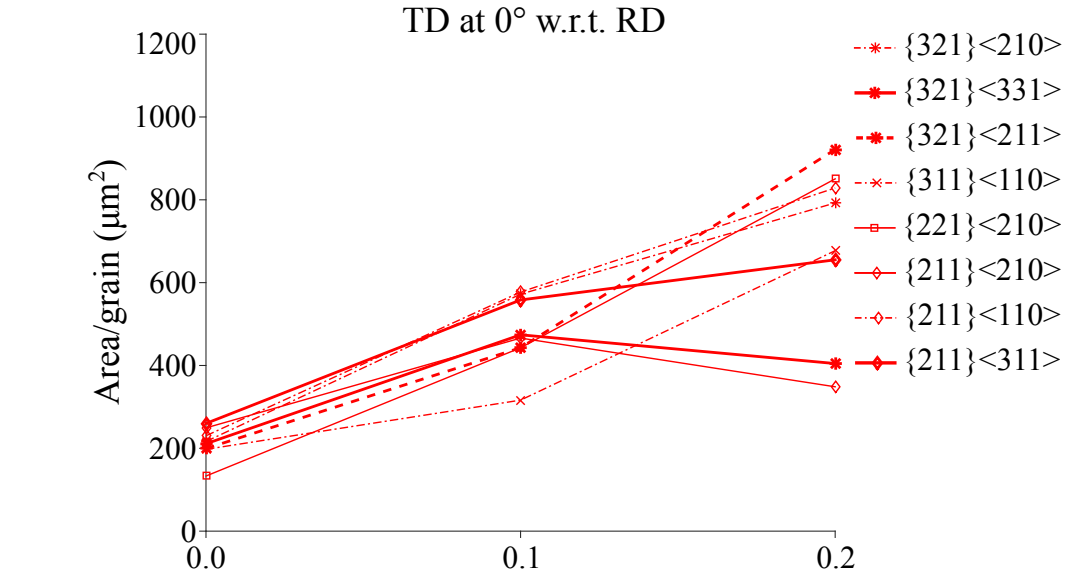

a. {321} Region

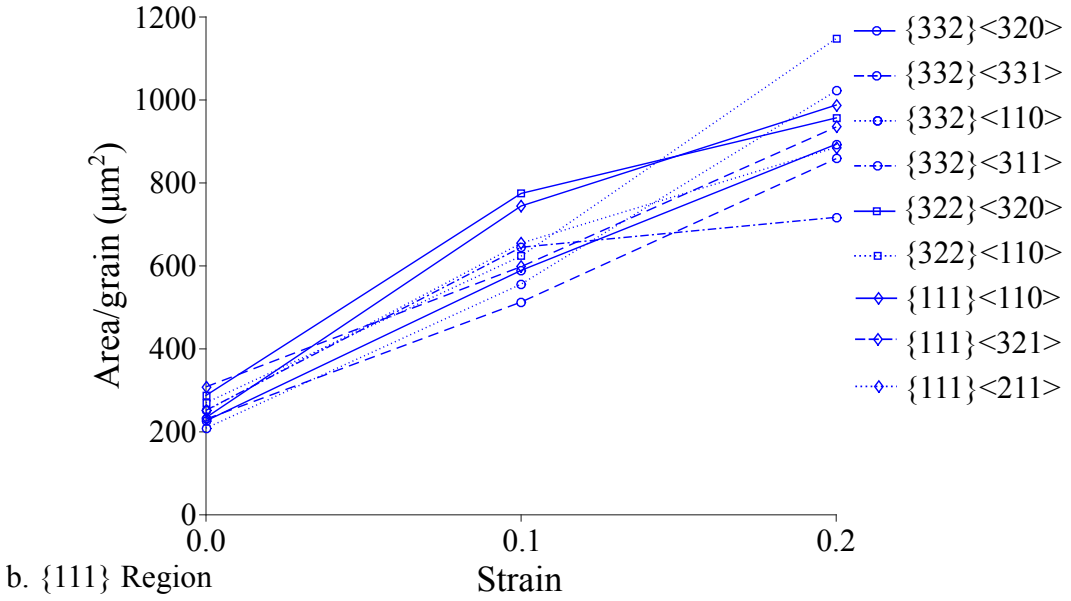

b. {111} Region

Figure 6.24: Plots of the area per grain *versus* strain are shown categorized by reference orientation. The plots are comprised of data with grains from (a) the {321} region of planes and (b) the {111} region of planes. The specimen tensile direction is oriented at 0° with respect to the RD. Reference orientations with a grain count of less than 1% of the total number of non-boundary grains at strains of 0, 0.1, or 0.2 were excluded.

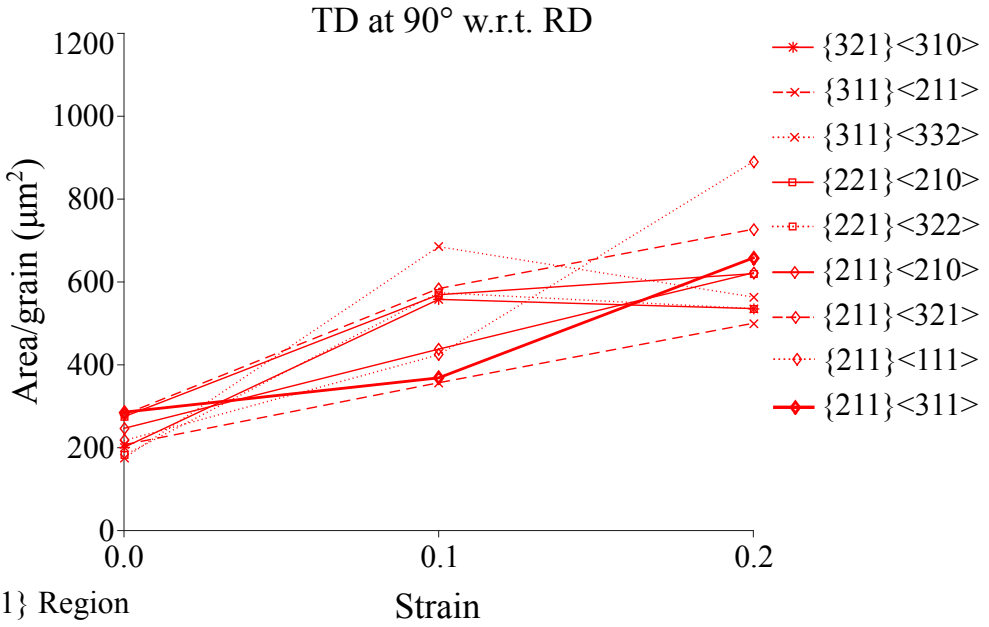

a. {321} Region

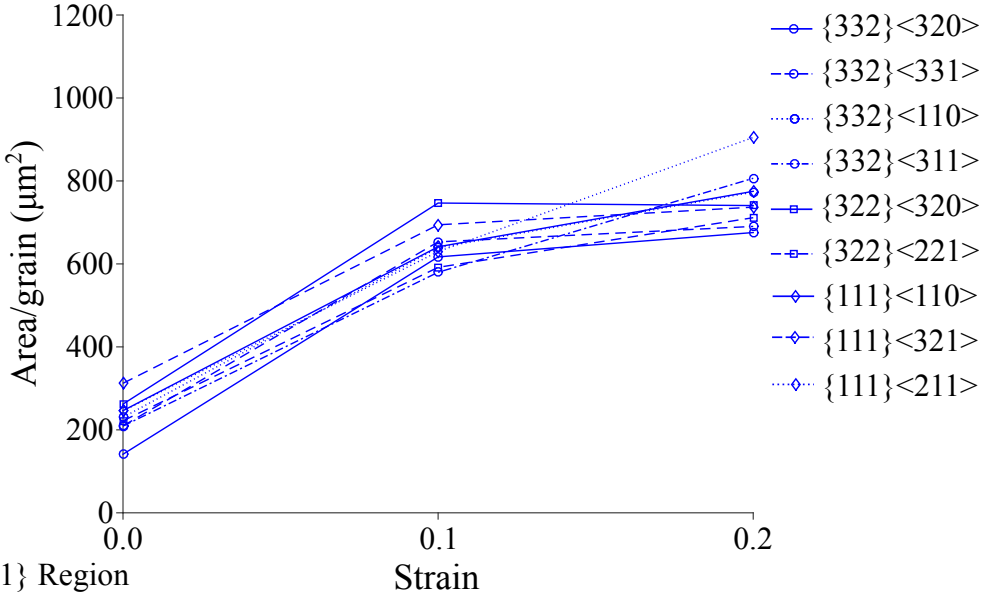

b. {111} Region

Figure 6.25: Plots of the area per grain *versus* strain are shown categorized by reference orientation. The plots are comprised of data with grains from (a) the {321} region of planes and (b) the {111} region of planes. The specimen tensile direction is oriented at 90° with respect to the RD. Reference orientations with a grain count of less than 1% of the total number of non-boundary grains at strains of 0, 0.1, or 0.2 were excluded.

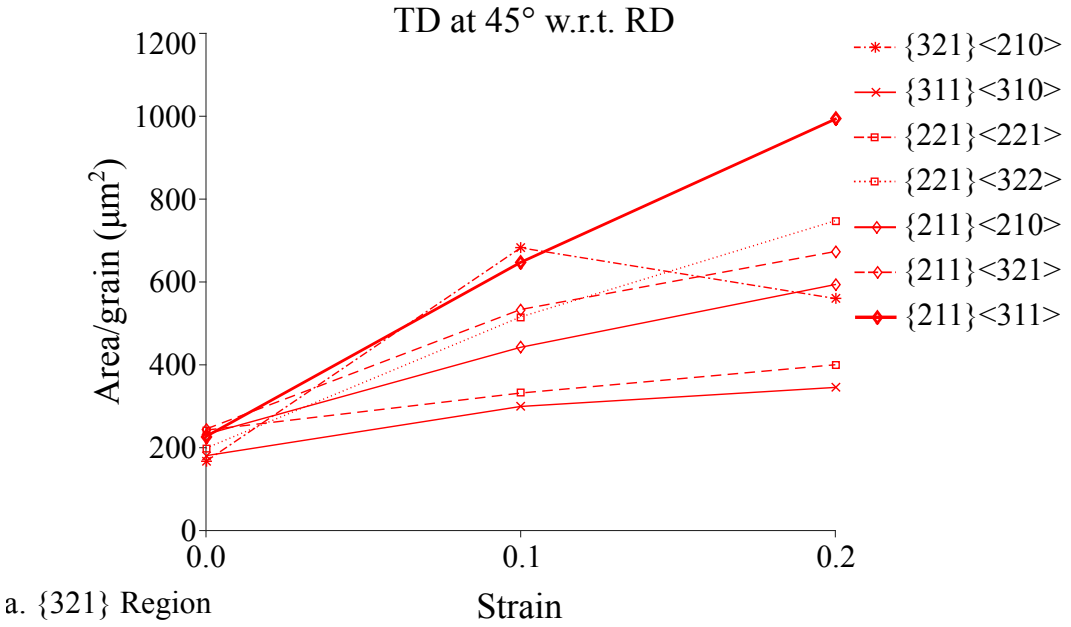

a. {321} Region

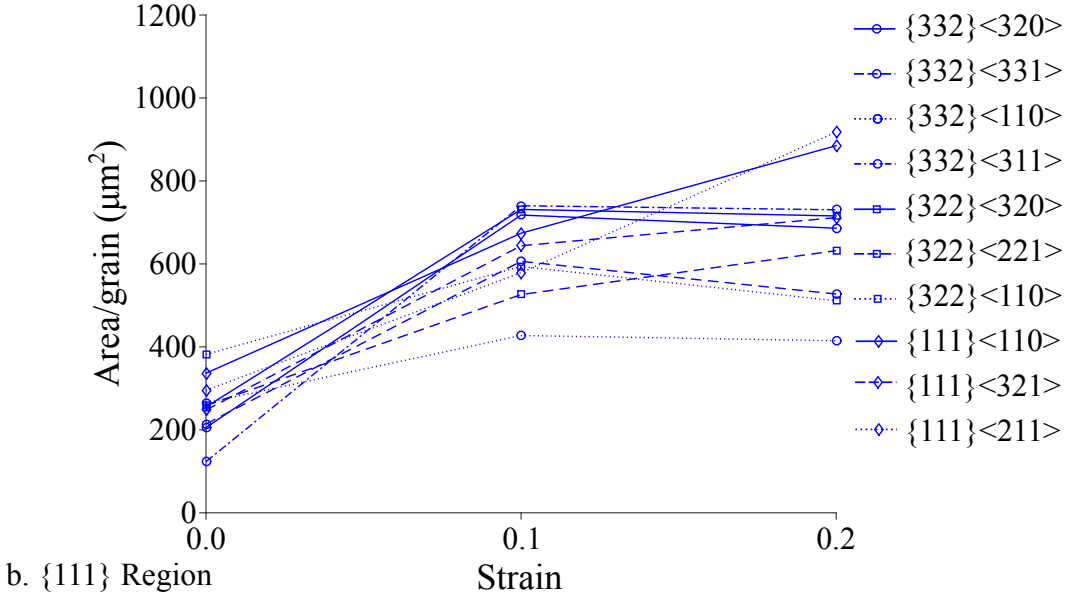

b. {111} Region

Figure 6.26: Plots of the area per grain *versus* strain are shown categorized by reference orientation. The plots are comprised of data with grains from (a) the {321} region of planes and (b) the {111} region of planes. The specimen tensile direction is oriented at 45° with respect to the RD. Reference orientations with a grain count of less than 1% of the total number of non-boundary grains at strains of 0, 0.1, or 0.2 were excluded.

From Figures 6.18-6.26 and Tables 6.1-6.3, it is apparent that DNGG grew grains with specific orientations at the expense of grains from other orientations. Grains that preferentially grew by DNGG were observed to be from orientations with specific crystallographic planes parallel to the plane of the sheet material. Grains oriented with their {111}, {332}, or {322} planes parallel to the plane of the sheet material were preferred for growth. Among grains with these plane orientations, a specific subset of orientations were most preferred for growth. The reference orientations most favored for growth varied with the specimen tensile orientation. A more detailed connection between DNGG and specific reference orientations, however, could not be determined from the trends analyzed in this study.

6.4 Comparison of analysis methods

Two analysis methodologies were used to investigate DNGG and its mechanisms. The first analysis method discussed the changes in crystallographic texture produced by DNGG, Section 6.2. This analysis method relied on texture measurements that did not consider grain size. The effects of lattice rotation and DNGG were isolated by determining the texture of three states: (i) undeformed (recrystallized), (ii) deformed at room temperature, and (iii) deformed at high temperature. The second analysis method segmented EBSD data by individual grains, which included determining individual grain sizes and orientations, Section 6.3. These segmented data were used to categorize individual grains by crystallographic orientation. This method analyzed the

relationships between orientation categories and change in grain area fraction, number fraction, and size with strain. A statistical analysis was performed to identify the characteristics of grains that are preferred for growth. The lattice rotation effect could not be isolated in this second analysis. Therefore, caution must be taken when interpreting these data. To properly interpret these data, lattice rotation must be considered. It is useful to remember that the first analysis method used orientation data for crystallographic textures to calculate continuous ODFs, but the second analysis method categorized these data into a finite number of discrete reference orientations. The different strengths and weaknesses between these two analysis methods arise in part because of the fundamental difference between continuous and discrete analyses.

The findings from the two analysis methods complemented each other to provide a thorough investigation of DNGG and its mechanisms. The first analysis method identified texture changes that occurred during high-temperature tensile deformation that were not attributable to lattice rotation. DNGG is hypothesized to be causing this effect because there was not any evidence of recrystallization during or after high-temperature deformation. The lattice rotation effect was also successfully isolated using the first analysis method. This methodology did not characterize individual grains, which prevented verification that specific grain orientations grew by DNGG. The second analysis method probed the relationships between orientation categories and changes in grain area faction, number fraction, and size with strain. A statistical analysis identified the characteristics of grains that were preferred for growth in order to

investigate DNGG and its mechanisms. To properly interpret these data, however, the isolated lattice rotation effect determined by the first analysis method was necessary. Some examples of this were when the specimen TD was oriented at 45° with respect to the RD. The first analysis method isolated the effects of lattice rotation and DNGG on texture. Lattice rotation strengthened texture components from within the α-fiber, including the {111}<110> texture component. DNGG strengthened texture components from within the γ-fiber. The {111}<211> texture component was the most favored for DNGG, while that the {111}<110> texture component was least favored for DNGG. The second analysis method indicated that {111}<110> grains grew during high-temperature tensile deformation. This was determined by an increased grain area fraction, number fraction, and size with strain. Without the observations from the first analysis method, the strengthening of the {111}<110> texture component during high-temperature deformation could erroneously be attributed to DNGG alone. Instead, the strengthening of the {111}<110> texture component should be attributed partly to lattice rotation during slip. The second analysis method, however, showed that the {111}<211> texture component had a grain area fraction and grain number fraction that increased with strain. The {111}<211> texture component was also observed to have one of the fastest growing mean grain sizes (area per grain) with strain. This confirmed that DNGG grew grains of the {111}<211> texture component during high-temperature tensile deformation and is the likely cause of this increased texture component demonstrated in the ODFs. These examples demonstrate

the complementary nature of the two analysis methods.

6.5 Subgrains

Subgrains were observed to occur in grains during high-temperature deformation and concurrently with DNGG (see Sections 5.3). Subgrains may be one of the intrinsic characteristic(s) that provided a growth advantage to the grains preferred for DNGG. This growth advantage may come from two possible mechanisms: (i) stored energy or (ii) interfacial tension forces from subgrains on the grain boundary (see Section 1.2.5.3).

HR-EBSD data were gathered from specimens deformed at elevated temperature to improve the angular-resolution of orientation indexing. HR-EBSD resolved subgrains and associated hot-deformation substructure thought important to DNGG. The HR-EBSD technique significantly improved the identification of subgrains compared to standard-resolution EBSD. This is because of the improved angular-resolution of the crystallographic orientations indexed by HR-EBSD and consequent reduction of noise. This is the first known demonstration of HR-EBSD for this application.

6.6 Mechanisms of DNGG

This dissertation investigated DNGG and its mechanisms. It is hypothesized that the grains preferred for DNGG possess one or more intrinsic characteristics that provide a growth advantage. Two theories were presented

in the literature regarding the advantage of grains favored for normal grain growth. These were growth controlled by (i) boundary character and (ii) strain accumulation. The characteristics of DNGG observed in this work did not conform to either of these theories. The discordance between observations of DNGG and these theories will now be discussed.

The theory of growth controlled by boundary character is based on the dependence of grain boundary mobility on the character of the grain boundary, particularly its disorientation. Lücke reported that a 27°<110> misorientation had the highest mobility in single crystal growth selection experiments for a Fe-3%Si (BCC) alloy. In polycrystalline low-carbon steel, microstructural evolution during recrystallization was reported to be the result of growth controlled by boundary character. This was based on an approximate 35°<110> misorientation between the {111}<112> γ-fiber and the {112}<110> α-fiber components; see Section 1.2.5.1. Growth controlled by boundary character, as reported by Lücke, was not observed in this study. This was particularly evident when the specimen TD was oriented at 0° with respect to the RD. Lattice rotation strengthened texture components from within the α-fiber, which included the {112}<110> (Figure 6.2). DNGG strengthened texture components from within the γ-fiber at the expense of texture components from the α-fiber, including the {112}<110> (Figure 6.3). Within the γ-fiber, however, texture components near the {111}<110> had the highest intensity, while the {111}<112> had the lowest intensity. Furthermore, the intensity of the {111}<112> attributed to DNGG remained constant between a strain of

0.1 and 0.2. However, the {110}<112> had a drop in intensity between 0.1 and 0.2, which indicated further consumption of these grains. Instead, DNGG strengthened the {111}<110> and {111}<132> texture components from a strain of 0.1 to 0.2. This suggests that growth of the {111}<112> was not directly dependent on consumption of the {112}<110>, disproving Lücke's theory. A link between other forms of boundary character and a growth advantage for DNGG was not probed.

Growth controlled by strain accumulation was reported by Fukutomi. He theorized that the preferred grain orientation for growth is one having stability during deformation and a low Taylor factor; see Section 1.2.5.2. The Ti-IF steel grains preferred for DNGG in this study did not possess these characteristics. This was obvious from the following: (i) Texture components strengthened by DNGG were weakened by lattice rotation; see Section 6.2. Therefore, grains favored for DNGG were not necessarily stable during deformation. (ii) The Taylor factor depends on the crystallographic direction along the TD. However, the crystallographic direction along the TD of a grain alone was not observed to significantly influence growth by DNGG. (iii) The <110>||TD has one of the highest Taylor factors [65]. Yet, the {111}<110> texture component was the most favored for DNGG when the specimen TD was oriented at 0° and 90° with respect to the RD. This indicates that strain accumulation as theorized by Fukutomi is not providing the growth advantage for DNGG observed in this dissertation.

Grains that preferentially grew by DNGG were observed to be from

orientations with specific crystallographic planes parallel to the plane of the sheet material. Grains oriented with the {111}, {332}, or {322} planes parallel with the plane of the sheet material were preferred for growth. Among grains with these planes parallel to the sheet plane, a specific subset of orientations were most preferred for growth. The reference orientation most favored for growth varied with specimen tensile orientation. The additional intrinsic characteristic(s) possessed by these grains most favored for DNGG remain unknown.

Chapter 7

Conclusions

The following conclusions were drawn from this work:

1. Concurrent plastic deformation accelerated grain growth, leading to DNGG and larger grains sizes than were produced by static annealing alone.

2. Hot tensile deformation produced a distinctly different texture than did room-temperature deformation. This was because the texture evolved at elevated temperature was produced by a combination of lattice rotation during slip and DNGG instead of lattice rotation alone.

3. Lattice rotation strengthened the intensity of texture components within the α-fiber (along the TD) that intersected with the recrystallized γ-fiber.

4. Two analysis methodologies were used to investigate DNGG and its mechanisms. The findings from the two analysis methods complemented each other.

5. DNGG preferentially grew grains of specific orientations at the expense of other orientations. Some characteristics of these orientations were determined.

6. Grains that preferentially grew by DNGG were observed to be from orientations with specific crystallographic planes parallel to the plane of the sheet material. Grains oriented with their {111}, {332}, or {322} planes parallel with the plane of the sheet material were preferred for growth.

7. Grain orientation relative to the TD alone was not observed to influence growth by DNGG.

8. Among grains oriented with a {111}, {332}, or {322} plane parallel to the sheet plane, a specific subset of orientations were most preferred for growth. The reference orientations most favored for growth varied with specimen tensile orientation. A more detailed connection between DNGG and specific reference orientations, however, could not be determined from the trends analyzed in this study.

9. The data obtained for grain size distributions during DNGG deviated from the lognormal distribution typically expected and observed for the recrystallized material. DNGG produced a bimodal distribution that suggested two groupings for grains, one group that grew during DNGG and another much smaller group that either did not grow or that grew only slowly by comparison.

10. Subgrains were observed to occur in grains during hot deformation and concurrently with DNGG.

11. HR-EBSD resolved subgrains and associated hot deformation substructure thought important to DNGG. This is the first know demonstration of HR-EBSD for this application.

Chapter 8

Suggestions for Future Work

This dissertation collected many different forms of data in order to investigate DNGG and its mechanisms. While significant contributions have been made, there are many aspects of DNGG left unexplored. Further analysis on DNGG could be conducted by further mining the data collected for this dissertation without requiring any additional experiments. Some suggested avenues for further data analysis are the following:

1. The relationship between grain boundary character and grains that are favored for DNGG could be analyzed.

2. Subgrains in the HR-EBSD data could be segmented and characterized in order to investigate the relationship between subgrains and DNGG.

3. The grain orientation spread (GOS) measurement from HR-EBSD data could be used to probe the relationship between DNGG and grain deformation substructure.

4. The contribution of lattice rotation during hot deformation to grain data categorized by reference orientation might be better isolated by further

analysis. Such analysis may aid identification of specific mechanisms responsible for DNGG.

Besides additional mining of the available data, the following avenue of research is recommended. The relationship between DNGG and DAGG could be probed further. This may involve identifying the mechanisms for both types of grain growth and determining if they are related. It would be ideal to identify a material in which both DNGG and DAGG occur. It would also be extremely beneficial to identify a material or an improved test setup that would allow rapid specimen quenching immediately after DAGG to better preserve microstructure.

Appendices

Appendix A

Test profiles for elevated temperature tensile testing in air

Table A.1: The .blk test profile used for tension tests with the MTS TestSuite Multipurpose Elite version 2.2.1 software at elevated temperature in air at a constant true strain rate of 10^{-4} s^{-1}

FileType= Block-Arbitrary
Date=11_11_2016
Description= 10e-4
Channels= 1

Channel(1)=20 KIP Axial
Max=32.0000 mm
Min=-10.0000 mm
Shape= Ramp

Rate mm/Sec	Level1 mm
0.0025654	0.1
0.0025754	0.2
0.0025854	0.3
0.0025954	0.4
0.0026054	0.5
0.0026154	0.6
0.0026254	0.7
0.0026354	0.8
0.0026454	0.9
0.0026554	1

Continued on next page

0.0026654	1.1
0.0026754	1.2
0.0026854	1.3
0.0026954	1.4
0.0027054	1.5
0.0027154	1.6
0.0027254	1.7
0.0027354	1.8
0.0027454	1.9
0.0027554	2
0.0027654	2.1
0.0027754	2.2
0.0027854	2.3
0.0027954	2.4
0.0028054	2.5
0.0028154	2.6
0.0028254	2.7
0.0028354	2.8
0.0028454	2.9
0.0028554	3
0.0028654	3.1
0.0028754	3.2
0.0028854	3.3
0.0028954	3.4
0.0029054	3.5
0.0029154	3.6
0.0029254	3.7
0.0029354	3.8
0.0029454	3.9
0.0029554	4
0.0029654	4.1
0.0029754	4.2
0.0029854	4.3
0.0029954	4.4
0.0030054	4.5
0.0030154	4.6

Continued on next page

0.0030254	4.7
0.0030354	4.8
0.0030454	4.9
0.0030554	5
0.0030654	5.1
0.0030754	5.2
0.0030854	5.3
0.0030954	5.4
0.0031054	5.5
0.0031154	5.6
0.0031254	5.7
0.0031354	5.8
0.0031454	5.9
0.0031554	6
0.0031654	6.1
0.0031754	6.2
0.0031854	6.3
0.0031954	6.4
0.0032054	6.5
0.0032154	6.6
0.0032254	6.7
0.0032354	6.8
0.0032454	6.9
0.0032554	7
0.0032654	7.1
0.0032754	7.2
0.0032854	7.3
0.0032954	7.4
0.0033054	7.5
0.0033154	7.6
0.0033254	7.7
0.0033354	7.8
0.0033454	7.9
0.0033554	8
0.0033654	8.1
0.0033754	8.2

Continued on next page

0.0033854	8.3
0.0033954	8.4
0.0034054	8.5
0.0034154	8.6
0.0034254	8.7
0.0034354	8.8
0.0034454	8.9
0.0034554	9
0.0034654	9.1
0.0034754	9.2
0.0034854	9.3
0.0034954	9.4
0.0035054	9.5
0.0035154	9.6
0.0035254	9.7
0.0035354	9.8
0.0035454	9.9
0.0035554	10
0.0035654	10.1
0.0035754	10.2
0.0035854	10.3
0.0035954	10.4
0.0036054	10.5
0.0036154	10.6
0.0036254	10.7
0.0036354	10.8
0.0036454	10.9
0.0036554	11
0.0036654	11.1
0.0036754	11.2
0.0036854	11.3
0.0036954	11.4
0.0037054	11.5
0.0037154	11.6
0.0037254	11.7
0.0037354	11.8

Continued on next page

0.0037454	11.9
0.0037554	12
0.0037654	12.1
0.0037754	12.2
0.0037854	12.3
0.0037954	12.4
0.0038054	12.5
0.0038154	12.6
0.0038254	12.7
0.0038354	12.8
0.0038454	12.9
0.0038554	13
0.0038654	13.1
0.0038754	13.2
0.0038854	13.3
0.0038954	13.4
0.0039054	13.5
0.0039154	13.6
0.0039254	13.7
0.0039354	13.8
0.0039454	13.9
0.0039554	14
0.0039654	14.1
0.0039754	14.2
0.0039854	14.3
0.0039954	14.4
0.0040054	14.5
0.0040154	14.6
0.0040254	14.7
0.0040354	14.8
0.0040454	14.9
0.0040554	15
0.0040654	15.1
0.0040754	15.2
0.0040854	15.3
0.0040954	15.4

Continued on next page

0.0041054	15.5
0.0041154	15.6
0.0041254	15.7
0.0041354	15.8
0.0041454	15.9
0.0041554	16
0.0041654	16.1
0.0041754	16.2
0.0041854	16.3
0.0041954	16.4
0.0042054	16.5
0.0042154	16.6
0.0042254	16.7
0.0042354	16.8
0.0042454	16.9
0.0042554	17
0.0042654	17.1
0.0042754	17.2
0.0042854	17.3
0.0042954	17.4
0.0043054	17.5
0.0043154	17.6
0.0043254	17.7
0.0043354	17.8
0.0043454	17.9
0.0043554	18
0.0043654	18.1
0.0043754	18.2
0.0043854	18.3
0.0043954	18.4
0.0044054	18.5
0.0044154	18.6
0.0044254	18.7
0.0044354	18.8
0.0044454	18.9
0.0044554	19

Continued on next page

0.0044654	19.1
0.0044754	19.2
0.0044854	19.3
0.0044954	19.4
0.0045054	19.5
0.0045154	19.6
0.0045254	19.7
0.0045354	19.8
0.0045454	19.9
0.0045554	20
0.0045654	20.1
0.0045754	20.2
0.0045854	20.3
0.0045954	20.4
0.0046054	20.5
0.0046154	20.6
0.0046254	20.7
0.0046354	20.8
0.0046454	20.9
0.0046554	21
0.0046654	21.1
0.0046754	21.2
0.0046854	21.3
0.0046954	21.4
0.0047054	21.5
0.0047154	21.6
0.0047254	21.7
0.0047354	21.8
0.0047454	21.9
0.0047554	22
0.0047654	22.1
0.0047754	22.2
0.0047854	22.3
0.0047954	22.4
0.0048054	22.5
0.0048154	22.6

Continued on next page

0.0048254	22.7
0.0048354	22.8
0.0048454	22.9
0.0048554	23
0.0048654	23.1
0.0048754	23.2
0.0048854	23.3
0.0048954	23.4
0.0049054	23.5
0.0049154	23.6
0.0049254	23.7
0.0049354	23.8
0.0049454	23.9
0.0049554	24
0.0049654	24.1
0.0049754	24.2
0.0049854	24.3
0.0049954	24.4
0.0050054	24.5
0.0050154	24.6
0.0050254	24.7
0.0050354	24.8
0.0050454	24.9
0.0050554	25
0.0050654	25.1
0.0050754	25.2
0.0050854	25.3
0.0050954	25.4
0.0051054	25.5
0.0051154	25.6
0.0051254	25.7
0.0051354	25.8
0.0051454	25.9
0.0051554	26
0.0051654	26.1
0.0051754	26.2

Continued on next page

0.0051854	26.3
0.0051954	26.4
0.0052054	26.5
0.0052154	26.6
0.0052254	26.7
0.0052354	26.8
0.0052454	26.9
0.0052554	27
0.0052654	27.1
0.0052754	27.2
0.0052854	27.3
0.0052954	27.4
0.0053054	27.5
0.0053154	27.6
0.0053254	27.7
0.0053354	27.8
0.0053454	27.9
0.0053554	28
0.0053654	28.1
0.0053754	28.2
0.0053854	28.3
0.0053954	28.4
0.0054054	28.5
0.0054154	28.6
0.0054254	28.7
0.0054354	28.8
0.0054454	28.9
0.0054554	29
0.0054654	29.1
0.0054754	29.2
0.0054854	29.3
0.0054954	29.4
0.0055054	29.5
0.0055154	29.6
0.0055254	29.7
0.0055354	29.8

Continued on next page

0.0055454	29.9
0.0055554	30
0.0055654	30.1
0.0055754	30.2
0.0055854	30.3
0.0055954	30.4
0.0056054	30.5
0.0056154	30.6
0.0056254	30.7
0.0056354	30.8
0.0056454	30.9
0.0056554	31
0.0056654	31.1
0.0056754	31.2
0.0056854	31.3
0.0056954	31.4
0.0057054	31.5

Table A.2: The .blk test profile used for tension tests with the MTS **x** software at elevated temperature in air at a constant true strain rate of 10^{-3} s^{-1}

FileType= Block-Arbitrary
Date=07_26_2017
Description= 10e-3
Channels= 1

Channel(1)=20 KIP Axial
Max=20.0000 mm
Min=-1.0000 mm
Shape= Ramp

Rate mm/Sec	Level1 mm
0.025652	0
0.025652	0.1
0.025752	0.2
0.025852	0.3
0.025952	0.4
0.026052	0.5
0.026152	0.6
0.026252	0.7
0.026352	0.8
0.026452	0.9
0.026552	1
0.026652	1.1
0.026752	1.2
0.026852	1.3
0.026952	1.4
0.027052	1.5
0.027152	1.6
0.027252	1.7
0.027352	1.8
0.027452	1.9
0.027552	2

Continued on next page

0.027652	2.1
0.027752	2.2
0.027852	2.3
0.027952	2.4
0.028052	2.5
0.028152	2.6
0.028252	2.7
0.028352	2.8
0.028452	2.9
0.028552	3
0.028652	3.1
0.028752	3.2
0.028852	3.3
0.028952	3.4
0.029052	3.5
0.029152	3.6
0.029252	3.7
0.029352	3.8
0.029452	3.9
0.029552	4
0.029652	4.1
0.029752	4.2
0.029852	4.3
0.029952	4.4
0.030052	4.5
0.030152	4.6
0.030252	4.7
0.030352	4.8
0.030452	4.9
0.030552	5
0.030652	5.1
0.030752	5.2
0.030852	5.3
0.030952	5.4
0.031052	5.5
0.031152	5.6

Continued on next page

0.031252	5.7
0.031352	5.8
0.031452	5.9
0.031552	6
0.031652	6.1
0.031752	6.2
0.031852	6.3
0.031952	6.4
0.032052	6.5
0.032152	6.6
0.032252	6.7
0.032352	6.8
0.032452	6.9
0.032552	7
0.032652	7.1
0.032752	7.2
0.032852	7.3
0.032952	7.4
0.033052	7.5
0.033152	7.6
0.033252	7.7
0.033352	7.8
0.033452	7.9
0.033552	8
0.033652	8.1
0.033752	8.2
0.033852	8.3
0.033952	8.4
0.034052	8.5
0.034152	8.6
0.034252	8.7
0.034352	8.8
0.034452	8.9
0.034552	9
0.034652	9.1
0.034752	9.2

Continued on next page

0.034852	9.3
0.034952	9.4
0.035052	9.5
0.035152	9.6
0.035252	9.7
0.035352	9.8
0.035452	9.9
0.035552	10
0.035652	10.1
0.035752	10.2
0.035852	10.3
0.035952	10.4
0.036052	10.5
0.036152	10.6
0.036252	10.7
0.036352	10.8
0.036452	10.9
0.036552	11
0.036652	11.1
0.036752	11.2
0.036852	11.3
0.036952	11.4
0.037052	11.5
0.037152	11.6
0.037252	11.7
0.037352	11.8
0.037452	11.9
0.037552	12
0.037652	12.1
0.037752	12.2
0.037852	12.3
0.037952	12.4
0.038052	12.5
0.038152	12.6
0.038252	12.7
0.038352	12.8

Continued on next page

0.038452	12.9
0.038552	13
0.038652	13.1
0.038752	13.2
0.038852	13.3
0.038952	13.4
0.039052	13.5
0.039152	13.6
0.039252	13.7
0.039352	13.8
0.039452	13.9
0.039552	14
0.039652	14.1
0.039752	14.2
0.039852	14.3
0.039952	14.4
0.040052	14.5
0.040152	14.6
0.040252	14.7
0.040352	14.8
0.040452	14.9
0.040552	15
0.040652	15.1
0.040752	15.2
0.040852	15.3
0.040952	15.4
0.041052	15.5
0.041152	15.6
0.041252	15.7
0.041352	15.8
0.041452	15.9
0.041552	16
0.041652	16.1
0.041752	16.2
0.041852	16.3
0.041952	16.4

Continued on next page

0.042052	16.5
0.042152	16.6
0.042252	16.7
0.042352	16.8
0.042452	16.9
0.042552	17
0.042652	17.1
0.042752	17.2
0.042852	17.3
0.042952	17.4
0.043052	17.5
0.043152	17.6
0.043252	17.7
0.043352	17.8
0.043452	17.9
0.043552	18
0.043652	18.1
0.043752	18.2
0.043852	18.3
0.043952	18.4
0.044052	18.5
0.044152	18.6
0.044252	18.7
0.044352	18.8
0.044452	18.9
0.044552	19
0.044652	19.1
0.044752	19.2
0.044852	19.3
0.044952	19.4
0.045052	19.5
0.045152	19.6
0.045252	19.7
0.045352	19.8
0.045452	19.9
0.045552	20

Continued on next page

0.045652	20.1
0.045752	20.2
0.045852	20.3
0.045952	20.4
0.046052	20.5
0.046152	20.6
0.046252	20.7
0.046352	20.8
0.046452	20.9
0.046552	21
0.046652	21.1
0.046752	21.2
0.046852	21.3
0.046952	21.4
0.047052	21.5
0.047152	21.6
0.047252	21.7
0.047352	21.8
0.047452	21.9
0.047552	22
0.047652	22.1
0.047752	22.2
0.047852	22.3
0.047952	22.4
0.048052	22.5
0.048152	22.6
0.048252	22.7
0.048352	22.8
0.048452	22.9
0.048552	23
0.048652	23.1
0.048752	23.2
0.048852	23.3
0.048952	23.4
0.049052	23.5
0.049152	23.6

Continued on next page

0.049252	23.7
0.049352	23.8
0.049452	23.9
0.049552	24
0.049652	24.1
0.049752	24.2
0.049852	24.3
0.049952	24.4
0.050052	24.5
0.050152	24.6
0.050252	24.7
0.050352	24.8
0.050452	24.9
0.050552	25
0.050652	25.1
0.050752	25.2
0.050852	25.3
0.050952	25.4
0.051052	25.5
0.051152	25.6
0.051252	25.7
0.051352	25.8
0.051452	25.9
0.051552	26
0.051652	26.1
0.051752	26.2
0.051852	26.3
0.051952	26.4
0.052052	26.5
0.052152	26.6
0.052252	26.7
0.052352	26.8
0.052452	26.9
0.052552	27
0.052652	27.1
0.052752	27.2

Continued on next page

0.052852	27.3
0.052952	27.4
0.053052	27.5
0.053152	27.6
0.053252	27.7
0.053352	27.8
0.053452	27.9
0.053552	28
0.053652	28.1
0.053752	28.2
0.053852	28.3
0.053952	28.4
0.054052	28.5
0.054152	28.6
0.054252	28.7
0.054352	28.8
0.054452	28.9
0.054552	29
0.054652	29.1
0.054752	29.2
0.054852	29.3
0.054952	29.4
0.055052	29.5
0.055152	29.6
0.055252	29.7
0.055352	29.8
0.055452	29.9
0.055552	30
0.055652	30.1
0.055752	30.2
0.055852	30.3
0.055952	30.4
0.056052	30.5
0.056152	30.6
0.056252	30.7
0.056352	30.8

Continued on next page

0.056452	30.9
0.056552	31
0.056652	31.1
0.056752	31.2
0.056852	31.3
0.056952	31.4
0.057052	31.5

Appendix B

Reference Orientations

Table B.1: This list provides the reference orientations into which the grains were separated. Reference orientations are listed by ID# and {hkl}<uvw> orientations.

ID	h	k	l	u	v	w
1	1	0	0	1	0	0
2	1	0	0	3	1	0
3	1	0	0	2	1	0
4	1	0	0	3	2	0
5	1	0	0	1	1	0
6	3	1	0	1	0	0
7	3	1	0	3	3	1
8	3	1	0	3	2	1
9	3	1	0	3	1	1
10	3	1	0	3	1	0
11	2	1	0	1	0	0
12	2	1	0	3	2	1
13	2	1	0	2	2	1
14	2	1	0	2	1	1
15	2	1	0	2	1	0
16	3	2	0	1	0	0
17	3	2	0	3	3	2
18	3	2	0	3	2	2
19	3	2	0	3	2	1
20	3	2	0	3	2	0
21	1	1	0	1	0	0
22	1	1	0	3	1	1
23	1	1	0	2	1	1

Continued on next page

ID	h	k	l	u	v	w
24	1	1	0	3	2	2
25	1	1	0	1	1	1
26	1	1	0	3	3	2
27	1	1	0	2	2	1
28	1	1	0	3	3	1
29	1	1	0	1	1	0
30	3	3	1	3	1	0
31	3	3	1	3	2	1
32	3	3	1	3	3	2
33	3	3	1	1	1	0
34	3	2	1	3	1	0
35	3	2	1	1	1	1
36	3	2	1	3	2	0
37	3	2	1	2	1	0
38	3	2	1	3	3	1
39	3	2	1	2	1	1
40	3	1	1	3	1	0
41	3	1	1	2	1	1
42	3	1	1	3	3	2
43	3	1	1	1	1	0
44	2	2	1	2	1	0
45	2	2	1	2	2	1
46	2	2	1	3	2	2
47	2	2	1	1	1	0
48	2	1	1	2	1	0
49	2	1	1	3	2	1
50	2	1	1	1	1	1
51	2	1	1	1	1	0
52	2	1	1	3	1	1
53	3	3	2	3	2	0
54	3	3	2	3	3	1
55	3	3	2	1	1	0
56	3	3	2	3	1	1
57	3	2	2	3	2	0
58	3	2	2	2	2	1

Continued on next page

ID	h	k	l	u	v	w
59	3	2	2	1	1	0
60	1	1	1	1	1	0
61	1	1	1	3	2	1
62	1	1	1	2	1	1
63*	0	0	0	0	0	0

* ID# for orientations not matching any of the above.

Appendix C

OpenXY Settings

The following settings were used in OpenXY [69] to perform the cross-correlation analysis. These settings are listed by the GUI window in which they are located.

1. **MainGUI**
    - Scan type: Square
    - Material: Scan File
    - Processors: 3
2. **ROI Settings**
    - ROI Size (% of Total): 25
    - Number of ROI's: 48
    - ROI Style: Grid
    - ROI Filtering: 2, 50, 1, 1
    - Image Filter Type: Standard
    - Image Filter Values: 9, 90, 0, 0

3. **Advanced Settings**

   - Calculate Strain: Checked
   - Reference Image Type: Real-Grain Ref
   - Ref Image Index: not an option
   - Standard Deviation: 2
   - Misorientation Tol (Degrees): 5
   - Real Reference Selection: IQ > Fit > CI
   - Grain ID Method: not an option
   - Minimum grain size: 5
   - Calculate Dislocation Density: checked
   - GND Method: Full Cross-Correlation
   - Number of Points to Skip: 0
   - IQ Cutoff: 0
   - Split Dislocation Density: Not Checked
   - Enable Profiler: Not Checked

4. **Microscope Settings**

   - Accel. Voltage (keV): 20
   - Sample Tilt (deg): 70
   - Sample Azimuthal (deg): 0

- Camera Elevation (deg): 10
- Camera Azimuthal (deg): 0
- Screen Size (Microns/pixel): 25

5. **Pattern Center Calibration**

   - New Pattern Center: Tiff
   - New Pattern Center: Strain Minimization with naïve plane fit. The values from the Tiff pattern center were used at the input. The strain minimization was chosen to include one point per grain with a high image quality over the entire scan. Occasionally a grain could be missed. I also excluded some of the boundary grains that were mostly cut off. If there were very apparent subgrains in a grain, a reference point would sometimes be placed in each subgrain.

Appendix D

VPSC Input Files

```
1                         number of elements (nelem)
1                         number of phases (nph)
1.0  0.0                  relative vol. fract. of phases (wph(i))
*INFORMATION ABOUT PHASE #1
0   0   25                   grain shape contrl, fragmentn, crit
aspect ratio
1.0  1.0  1.0                initial ellipsoid ratios (dummy if
ishape=4)
0.0  0.0  0.0                init Eul ang ellips axes (dummy if
ishape=3,4)
* name and path of texture file (filetext)
tifsteel.tex
* name and path of single crystal file (filecrys)
FE.sx
* name and path of grain shape file (dummy if ishape=0) (fileaxes)
shape1.100
*PRECISION SETTINGS FOR CONVERGENCE PROCEDURES (default values)
0.001 0.001 0.001 0.001    errs,errd,errm,errso
100 100 25     itmax:   max # of iter, external, internal and SO loops
0  2 10 2   irsvar & xrsini,xrsfin,xrstep (dummy if irsvar=0)
1              ibcinv (0: don't use <Bc>**-1, 1: use <Bc>**-1 in SC
eq)
*INPUT/OUTPUT SETTINGS FOR THE RUN (default is zero)
0              irecover:read grain states from POSTMORT.IN (1) or not
(0)?
0              isave:   write grain states in POSTMORT.OUT at step
'isave'?
0              icubcomp:calculate fcc rolling components?
0              nwrite (frequency of texture downloads)
*MODELING CONDITIONS FOR THE RUN
0              ihardlaw (0:Voce, 1:MTS, 2:composite grain)
1              iratesens (0:rate insensitive, 1:rate sensitive)
1              interaction (0:FC,1:affine,2:secant,
3:neff=10,4:tangent,5:SO)
1  1  1        iupdate: update orient, grain shape, hardening
0              nneigh (0 for no neighbors, 1 for pairs, etc.)
0              iflu (0: don't calc, 1: calc fluctuations)
*NUMBER OF PROCESSES (COMBINATION OF UNIFORM OR VARIABLE
LOAD,PCYS,LANKFORD)
3
*IVGVAR AND PATH\NAME OF FILE OR STRESS SUBSPACE OR ANGULAR INCREMENT
0         ivgvar=0 will run a monotonic strain path
tension_x0_298
2         ivgvar=2 will calculate PCYS at the end
1 2             -->   section of stress space
3         ivgvar=3 will calculate Lankford coefficients at the end
10              -->   angular increment for tensile probing
```

Figure D.1: The "vpsc7_x0.in" file used in this work to run a VPSC simulation. This file can be easily modified to simulate the 45° and 90° tensile orientations.

```
  20   3   0.005    298.          nsteps  ictrl  eqincr  temp
* boundary conditions
    1       1       1           iudot    |    flag for vel.grad.
    1       1       1                    |    (0:unknown-1:known)
    1       1       1                    |
                                         |
    1.0     0.      0.          udot     |    vel.grad
    0.     -0.5     0.                   |
    0.      0.     -0.5                  |
                                         |
    0       0       0           iscau    |    flag for Cauchy
            0       0                    |
                    0                    |
                                         |
    0.      0.      0.          scauchy  |    Cauchy stress
            0.      0.                   |
                    0.                  @
```

Figure D.2: The "tension_x0_298" input file used in this work for tensile strain parallel to the RD for a true strain of 0.1 in 20 steps. For a true strain of 0.2 the 0.005 value in the top row in the third column should be changed to 0.01.

```
  20   3   0.005    298.          nsteps  ictrl  eqincr  temp
* boundary conditions
    1       1       1           iudot    |    flag for vel.grad.
    1       1       1                    |    (0:unknown-1:known)
    1       1       1                    |
                                         |
   -0.5     0.      0.          udot     |    vel.grad
    0.      1.0     0.                   |
    0.      0.      -0.5                  |
                                         |
    0       0       0           iscau    |    flag for Cauchy
            0       0                    |
                    0                    |
                                         |
    0.      0.      0.          scauchy  |    Cauchy stress
            0.      0.                   |
                    0.                  @
```

Figure D.3: The "tension_x90_298" input file used in this work for tensile strain perpendicular to the RD for a true strain of 0.1 in 20 steps. For a true strain of 0.2 the 0.005 value in the top row in the third column should be changed to 0.01.

```
  20   3   0.005    298.          nsteps  ictrl  eqincr  temp
* boundary conditions
    1       1       1           iudot    |    flag for vel.grad.
    1       1       1                    |    (0:unknown-1:known)
    1       1       1                    |
                                         |
    0.25    0.75    0.          udot     |    vel.grad
    0.75    0.25    0.                   |
    0.      0.     -0.5                  |
                                         |
    0       0       0           iscau    |    flag for Cauchy
            0       0                    |
                    0                    |
                                         |
    0.      0.      0.          scauchy  |    Cauchy stress
            0.      0.                   |
                    0.                  @
```

Figure D.4: The "tension_x45_298" input file for tensile strain oriented at + 45° with respect to the RD for a true strain of 0.1 in 20 steps. For a true strain of 0.2 the 0.005 value in the top row in the third column should be changed to 0.01.

Table D.1: The "tifsteel.tex" input file from the recrystallized Ti-IF steel microstructure.

"Ti-IF Steel 850 °C anneal for 30 min. on 7/19/2016"			
Data collected on 8/10/2016, 9/28/2016, and 2/13/2017			
"x = RD, y = LTD, z = STD 2 μm step size 4 $\times$ 4 binning"			
B	794		
89.9	49.8	46.6	0.000882692
212	54.8	44.6	0.000339497
176.3	38.7	36.8	0.002625444
334.8	43.9	45.8	0.001018491
195.2	41.9	48.2	0.000611095
193.8	51.6	55.1	0.001357988
27.5	42.2	38.1	0.000135799
169	19.8	2.8	0.001109024
140.6	6.7	44.3	0.002964941
184.1	42.4	36	0.002987574
30.6	51.5	41.6	0.001244823
95	44	73.7	0.001403255
346.1	39.5	38.6	0.002014349
231.1	40.7	35	0.000588462
244.8	43.9	13.7	0.000248965
202	42.3	46.9	0.000860059
180.4	44.4	44.3	0.001674852
79.2	51.6	36	0.007174705
154.9	54	42.7	0.002625444
358.3	44.5	41.5	0.000860059
45.1	50.5	43.5	0.004707693
16.4	46.8	46.2	0.003802367
149.2	24.3	47.4	0.001652219
312	47	45.8	0.00036213
350.1	49.6	42.4	0.000565828
12.1	47.5	51.8	0.001969083
209.9	35.7	57.6	0.001901184
354.7	21.2	38.8	0.001629586
287.7	46.4	66.2	0.002150148

Continued on next page

49.4	47.6	42.2	0.003394971
157	51	48.7	0.003915533
207.9	31.4	52	0.003304438
194.3	51.7	55.6	0.004662427
29.4	35.2	49.4	0.002082249
201.9	50.1	44.8	0.001720119
8.3	47.6	49.7	0.001720119
120	51.9	51.2	0.00115429
333	41	38.4	0.000565828
159.4	34.3	42.8	0.000656361
193.8	3.5	43.3	0.000656361
4.2	34.1	31.4	0.00346287
93	20.8	76.8	0.000113166
186.7	38.1	47.4	0.007242605
196.6	44.5	46.3	0.001606953
137.5	42.2	49.3	0.001176923
114.7	48.8	59	0.000769527
203.7	40.6	50.4	0.009664351
311.7	40	51.7	0.000837426
187.1	28.3	63.6	0.000158432
206.6	54.6	45.2	0.002851776
202.2	34	39.5	0.00316864
111.7	39.8	49.7	0.000520562
180.5	37.2	38.2	0.002829142
16	40	37.8	0.001697485
126.9	46.2	53.8	0.001788018
139.4	53.6	46.4	0.001765385
190.2	17.8	35.9	0.001923817
32.6	37.8	45.1	0.001539053
201.7	42	52.6	0.000271598
210.4	54.1	45.5	0.000746894
336.2	40.9	44	0.000113166
5.9	34.2	53.7	0.000248965
9	25.6	41.3	0.001403255
210.2	20.4	42.6	0.001674852
319.5	13.6	66	0.001335355

Continued on next page

134.5	50.9	30.8	0.001425888
230.3	45.7	41.9	0.002150148
39.5	38.6	46.2	0.001063758
328.6	20.2	56.7	0.001539053
63.3	41.9	14.9	0.000905326
196.5	44.6	46.4	0.000158432
306	49.8	46	0.00346287
204.5	50.1	42.2	0.000769527
178.1	42.2	51.3	0.004979291
127.2	44.6	60.2	0.003078107
136.2	48.8	52.8	0.00079216
56.1	50.6	41.4	0.001380622
196.7	44.6	46.4	0.000271598
14.8	24.2	42.8	0.003123373
69.1	52.2	44.7	0.000678994
35.8	39.1	36.8	0.000475296
106.9	49	39	0.001131657
16.1	26.7	45.8	0.00079216
236.5	45.1	53	0.003055474
145.5	29.1	39.4	0.002195415
291	48.9	43	0.004707693
2.3	11.3	20.6	0.000181065
316.9	48.5	48.4	0.003485503
0.5	23.8	42.8	0.000248965
155.2	43.9	46.7	0.000927959
356.8	48.1	44	0.000158432
185.1	42	46.9	0.000927959
138.4	42.5	54	0.00115429
106.8	45.1	58.9	0.001086391
7.4	47.6	43.1	0.00079216
168.2	44	42.8	0.002602811
298.4	45	37.8	0.00079216
37.1	20.8	29.5	0.003960799
175.7	54.2	41.7	0.002263314
200.8	46.1	39	0.001312722
201.2	50.2	55.9	0.001901184

Continued on next page

114.9	53.2	47	0.002421746
165.2	21.2	56.8	0.000543195
239	53.1	48.7	0.00079216
171	51.7	40.3	0.000271598
52.6	52	44.1	0.00122219
21.6	28.7	44.5	0.000588462
186.6	53.1	52.5	0.002919675
338.1	25.7	61.3	0.000656361
318.4	41.7	53	0.002014349
352.3	47.2	43.8	0.001652219
52.8	48.4	35.5	0.001674852
186.1	42.6	55.5	0.000407397
333.1	45.8	43.6	0.002829142
199.4	56.4	46.1	0.000294231
283	45.7	44.2	0.00115429
300.8	44.2	45.4	0.000814793
14.4	14.3	75.9	0.001901184
40.3	29.8	62.5	0.001674852
171.4	29.7	54.6	0.000339497
186.5	38.6	44.3	0.00043003
302.5	45.4	52.5	0.001290089
329	43.5	54.1	0.001267456
155.1	23.6	37.1	0.00237648
185.2	54.9	48.3	0.004526628
294.6	45.3	47.2	0.000339497
38.2	33.2	30.5	0.004549261
313.3	45.1	65.4	0.000113166
210.5	20.3	29.6	0.002467012
207.1	52.1	53.5	0.00043003
59.2	52.8	41.4	0.000475296
240.1	51.6	46.7	0.001109024
15.3	42.6	43.9	0.000316864
58.9	47.7	37.5	0.003191273
2.6	45.5	48.1	0.000135799
75.6	41.1	25.3	0.001855917
67.4	52.9	42	0.000995858

Continued on next page

344.1	18.8	51.4	0.000135799
150	42	36.7	0.000656361
302.2	43.6	64.3	0.000497929
74.6	46.2	31.3	0.001018491
21.8	26	60.9	0.000271598
2.9	48.5	41.9	0.00432293
56	15.7	33.7	0.001380622
329.2	41.5	41.8	0.001652219
25.1	51.2	43.3	0.000543195
328.2	40.1	42	0.000905326
337.5	48.3	47.5	0.000543195
132.7	56.3	45.1	0.004979291
249	39.9	33	0.002172781
325.5	46.6	45	0.000520562
323.7	18.1	64	0.00079216
180.2	56.9	45.7	0.003576036
40.1	27.4	27.6	0.000339497
233.8	49.1	61.5	0.000950592
270.4	45.6	70	0.000588462
146.6	54.7	40.7	0.010049114
151.2	55.9	45.1	0.000995858
244.9	34.3	23.5	0.000565828
10.3	40.3	54.3	0.003191273
193.3	52.4	52.9	0.00273861
44.2	46.1	32	0.00036213
311.4	33.1	47	0.001290089
2.1	35.3	51.5	0.002036983
218.1	49.3	46.3	0.003281805
235.8	45.9	38.4	0.002353847
281.5	41	57	0.002353847
185.3	52.1	43.1	0.00072426
125.5	45	54.3	0.008419528
15.4	34	38.1	0.000339497
145.1	47.8	45.3	0.000611095
2.8	48.4	42	0.000271598
349.7	12.2	9.2	0.000294231

Continued on next page

223.8	38.7	46.4	0.000181065
127.3	51.5	36.7	0.001199556
335.2	44.7	43	0.003417604
215	48.2	42.2	0.001629586
201.7	36.7	46	0.000814793
269.6	47.4	34.3	0.000588462
2.8	48.4	42	0.00043003
159	24.2	48.7	0.000565828
174.3	14.2	27	0.00043003
292.1	41.7	62.8	0.00122219
323.1	46.3	41.4	0.008193196
220.8	32.2	46.9	0.003372338
136.4	55.1	41.1	0.002942308
128.1	45.4	50.9	0.00072426
125.3	56.9	44.8	0.007650001
326.5	39.3	41.9	0.000633728
69.6	50.1	39.8	0.00079216
342.4	46.8	51.6	0.00158432
102.9	53.5	44.4	0.000520562
204.5	41.7	44.7	0.001335355
181.4	48.8	39.9	0.000497929
156.7	43.9	41.4	0.001267456
95	50	30.1	0.001063758
221.6	46.3	44	0.001720119
345.6	41.1	52.3	0.000611095
7.3	48	36.3	0.00115429
292	41.8	62.9	0.002014349
143.8	52.9	35.6	0.001380622
343.7	41	39.4	0.002331213
194.5	9.7	35.4	0.000181065
31.6	47	47.2	0.001878551
143.7	51.2	34.3	0.000995858
319.1	45.7	43.5	0.000746894
98.7	52.7	49.2	0.000565828
218	52.5	40.4	0.000226331
185.2	13	35.9	0.002625444

Continued on next page

208.2	42.8	45.9	0.001041124
277.9	52.2	44.4	0.000271598
149.7	45.6	44.4	0.001380622
209.7	45	45.1	0.002874409
16.1	30.4	44.2	0.005205622
19.6	27.9	48.9	0.002851776
40.4	34.2	34.6	0.000113166
221.6	44.1	37.7	0.00122219
248.5	49.5	59.5	0.00115429
125.7	43.5	53.5	0.001493787
345.5	48.8	46.2	0.001765385
293.3	45	56.6	0.000611095
123.5	44.4	53.5	0.000950592
116	35.9	72.8	0.001018491
247.3	41.8	44	0.001403255
105.7	39.9	71.9	0.000814793
145	34.4	57.3	0.00230858
190.1	27.6	37.9	0.000678994
218.3	42.5	25.9	0.002942308
220.2	50.9	55.1	0.000339497
17.8	37.4	47.6	0.003191273
256.9	38.1	39.4	0.003078107
170.8	48.2	40.7	0.001109024
56	39.7	34.4	0.00079216
208.3	49.4	56.3	0.001878551
199.3	25.8	25.2	0.001629586
55.2	40.9	24.6	0.000339497
184.1	38.2	50.4	0.000543195
193.8	32.2	32.1	0.000633728
259.1	53.4	46.7	0.000927959
152.2	42.5	59.4	0.00072426
225.4	41.9	15.3	0.00036213
141.5	42.8	41	0.001086391
358.3	16.2	6.1	0.000203698
265.6	42.8	22	0.000135799
249.3	53	45.1	0.00036213

Continued on next page

165	40.7	53.2	0.001539053
318.5	15	63.6	0.000746894
96.2	44.3	60	0.000181065
233	44.6	43.6	0.003394971
278.7	48.4	57.7	0.000181065
162.2	25.2	44.7	0.001991716
283.4	15.5	81.9	0.002489645
345.8	8.6	6.3	0.000769527
181.4	47.3	45.4	0.005590385
66.9	49.6	45.1	0.00072426
292.1	52.8	46.2	0.000181065
207.5	25.7	30.4	0.000203698
123.8	53.5	41.6	0.000565828
21.3	43.8	36.6	0.001448521
211.9	27.5	41.4	0.00115429
178.9	41.5	49.6	0.00043003
180.6	53.1	40.7	0.001697485
268.5	43.2	10.3	0.000656361
203.9	12.1	27.6	0.000181065
336.1	18.6	47.2	0.000203698
169.8	47.8	39.6	0.00072426
212.5	4.1	83.5	0.001357988
294	50.6	48.7	0.006948374
227.5	52.4	50.3	0.002150148
192	43	48.2	0.00036213
227.9	50.6	47.7	0.001855917
180.1	42.6	37.5	0.000611095
308.4	48	51.6	0.005567752
44.1	53.1	42.3	0.001788018
266.3	34.7	80.2	0.001199556
210.3	9.3	9.8	0.000927959
9.8	24.9	63	0.001244823
182.5	47	38.6	0.001425888
120.6	47.4	56.9	0.000543195
136.6	47.8	42.3	0.001018491
192.2	27.4	56.5	0.002489645

Continued on next page

122.3	49.7	56.6	0.000860059
51	15.2	11.1	0.000452663
242.6	43.2	42.2	0.000611095
273.7	42.9	74.6	0.000158432
160.6	54.9	45.2	0.000633728
184.3	42.2	39.9	0.003847634
326.3	50.1	42.1	0.000520562
73.4	50.1	53.2	0.00461716
214.8	50.5	50.1	0.002331213
0.7	52.6	44.6	0.004028699
70.5	40.6	20.1	0.00043003
224.7	21	36.5	0.000248965
53.6	47.2	50.9	0.000271598
189.6	46.5	42.1	0.004119231
253.1	53.5	44.9	0.003508137
23.6	46.5	48.5	0.001063758
197.2	44.5	46.9	0.002014349
60.3	50.7	41.7	0.002218048
185.5	52.2	51.3	0.001335355
359.9	25.2	43.8	0.000950592
316.4	53.3	43.5	0.000339497
59.3	53.9	44	0.000543195
26.9	19.7	26.8	0.000248965
244.7	39.9	34.8	0.001629586
215.1	51.9	44.8	0.000452663
188.7	37.2	42.7	0.000226331
195.4	43.9	52.9	0.000226331
175	48.8	38.9	0.001493787
314.4	50.1	41.2	0.00079216
308.3	52.5	47.5	0.001312722
229.9	39.9	41.1	0.000882692
329.4	42.4	50.8	0.002806509
9	43.9	43.9	0.000271598
159.3	28.9	59.1	0.000158432
314.8	44.4	37.5	0.000882692
81.5	16.1	7.1	0.000452663

Continued on next page

147.4	48	44.7	0.001425888
174.1	50.5	39.5	0.000135799
320.6	8.5	44.8	0.00043003
6.6	12.7	44.2	0.00504719
201.7	43.6	38.3	0.001855917
128.6	50.3	54.5	0.000475296
333.3	39.5	54.3	0.000497929
36	26.8	38.4	0.002263314
323.2	51.2	44.8	0.001629586
183.1	32.3	38.3	0.000656361
267.4	8	65.7	0.001561687
143.5	48.3	53.5	0.000814793
190.7	42.9	41.5	0.000927959
156	42.9	48.5	0.000633728
9.1	45.2	44.2	0.000384763
189.1	46.9	48.2	0.000565828
157.5	9.6	44.2	0.000226331
137.1	42.1	56	0.000543195
20.7	46	45.6	0.000950592
138.9	35.3	40.1	0.000407397
1.4	34.5	39.8	0.003440237
210	45.4	47.1	0.001357988
181.3	45.7	52.4	0.000701627
251	33.1	14.4	0.000678994
76.4	52.8	47.3	0.002421746
196.6	32.8	84	0.000746894
149.6	20.3	53.7	0.000158432
123.2	53.6	43.4	0.001561687
20.2	50.2	47.4	0.001199556
130.9	47.1	55.9	0.001176923
149.5	20.3	53.8	0.001267456
152.8	51.3	45.4	0.00043003
201	47.5	56.3	0.000181065
18.6	50.1	43	0.003553403
157	9.5	44.7	0.000113166
243.7	48.9	51.8	0.00237648

Continued on next page

142.2	47.4	43.9	0.000203698
99.5	28.4	79.3	0.000452663
35.8	19.9	18.9	0.000475296
359.7	34.9	56.6	0.000678994
40.1	26.2	30.9	0.001606953
22	42.2	43.6	0.001041124
35.7	19.8	19.1	0.000882692
48	36.2	23.9	0.000565828
250.4	37.1	8.2	0.00072426
125.7	48.4	51.1	0.000158432
188.7	54.9	45.8	0.001290089
40.3	16.8	35.8	0.000769527
51.5	27.3	13.5	0.004277663
6.1	41	55.2	0.001041124
222.2	39.2	39.2	0.00122219
34.3	44.6	34.6	0.000882692
303.8	44.4	48.5	0.001878551
318.1	50.4	46.4	0.000973225
237	43.8	33.3	0.000384763
295.7	30.7	84.1	0.000248965
300.6	48.4	51.2	0.000814793
144	39.5	46.6	0.000135799
194.6	49.7	50.7	0.001493787
29.3	16.9	65.3	0.000611095
188.4	30.8	33.9	0.000339497
205.2	33	27.1	0.001720119
149.7	20.2	53.6	0.000520562
88.7	44.5	4.2	0.000973225
207.9	49.3	58.6	0.00072426
59.1	51.7	50.8	0.001267456
14.1	44	46.7	0.003779734
134.2	7.7	354.3	0.00346287
214.9	50.9	48.6	0.000135799
160.4	48.2	34.8	0.000181065
200.7	49.8	45.7	0.00036213
195.6	44.3	78.4	0.001629586

Continued on next page

67	52.2	50.1	0.001810651
197.7	49.3	42.2	0.000520562
352.9	4	16.6	0.000927959
152.2	50.2	38.9	0.000452663
73.8	41.5	15.2	0.000543195
137.3	34.3	42.3	0.000339497
190	53.5	47.8	0.001493787
10.9	33.5	41	0.000769527
332.7	9.2	44.5	0.000407397
139.4	35.6	44.9	0.001969083
341.2	41.8	43.2	0.002783876
55.5	41.5	24.2	0.00072426
34.4	7.7	2.4	0.001312722
356.5	26.1	47.6	0.002602811
87.5	44.1	33.2	0.001131657
85.6	18.2	26.2	0.000565828
129.6	50.3	44.7	0.001969083
212.5	9	22.1	0.000905326
187.8	23.2	35.8	0.000113166
63.9	45.4	27	0.000113166
157.4	31.2	56.2	0.003078107
189.6	38.4	53.4	0.001109024
324.2	51.2	38.5	0.002512278
128.8	52.7	43.2	0.001923817
215.5	29.9	50	0.001041124
244.2	49.7	38.2	0.000769527
187.6	23.1	36	0.000520562
191	21.1	43.1	0.000882692
27	50.1	37.8	0.000497929
177.4	43.6	42.7	0.001561687
137.1	34.4	42.5	0.000339497
43.6	49.5	45.1	0.001086391
5.6	5.5	41	0.001176923
197	49.1	46.6	0.000158432
167.3	35	89.5	0.001267456
80.5	38.6	29.4	0.000497929

Continued on next page

221.2	36.4	34.4	0.000294231
341.5	40.6	57.7	0.00043003
171.4	35.3	39.7	0.002240681
349	51.2	42.4	0.005069823
240.8	44.5	44.2	0.000384763
146.7	41.8	12.6	0.000611095
161.6	35.9	49.5	0.005228255
174	47	40.5	0.003213906
343.5	49.3	49.2	0.000226331
181	36.2	40.3	0.000520562
137.8	19.1	49.8	0.000384763
0.2	10.8	48.6	0.000271598
61.4	51.7	40.2	0.000882692
155.2	19.5	50.3	0.000384763
63.7	33	35.5	0.004639794
198.2	20.3	58.3	0.002919675
334.4	29.5	50	0.00158432
337.7	21.3	54.6	0.000226331
60.8	49.9	39	0.000113166
208.3	50.1	48	0.003938166
120.3	46.6	31.2	0.001063758
146.7	40.9	55.2	0.000294231
352.4	10.5	19.8	0.000158432
202.8	46.8	46	0.000520562
236.9	46.4	31.4	0.000882692
48.5	40.3	45.3	0.001290089
255	40.2	19.5	0.000814793
206.6	35	45.5	0.000248965
108.6	42.2	49.1	0.001991716
206.5	34.8	32.8	0.001244823
207.6	53.5	48.1	0.000226331
112.2	45.4	66.2	0.00036213
185.9	29.7	55.4	0.000452663
354.1	46.9	39	0.001991716
205.1	43.6	57.8	0.000543195
244.9	30.8	26.8	0.004141865

Continued on next page

62.1	43.9	47.5	0.001425888
171.8	34.9	82.6	0.000611095
332.9	52.5	49	0.002897042
145.8	43.2	41.4	0.000769527
188.8	46.7	54.7	0.00036213
153	32.5	47.7	0.004413462
326.1	43.6	50.5	0.000701627
34.5	51.1	41.7	0.000746894
352.3	24.7	28.3	0.000565828
168.4	41.5	38.4	0.000316864
18.9	42	54.6	0.002127515
159.8	48.9	53.2	0.001855917
230.5	45.8	34.7	0.002829142
175.8	42.4	49.8	0.000226331
72.1	40.2	21.5	0.00036213
338.7	39.7	49.2	0.000973225
353.9	9.7	61.5	0.00043003
201.7	53.4	46	0.000678994
31	41.5	37.5	0.002489645
229.9	48.8	44.5	0.000294231
40.4	52.3	42.8	0.00043003
41.1	22.5	22.9	0.00194645
245.8	44.4	26.5	0.000407397
206.6	44.2	38.2	0.002059616
229.9	40.7	25.2	0.000226331
70.8	52.5	46.1	0.005273521
181.6	42.2	39.5	0.000452663
222.9	46.4	40.9	0.001403255
150.3	25.4	42.9	0.002218048
124.1	36.7	67.4	0.000475296
176.8	52.8	47.6	0.001335355
91.9	15.9	62.9	0.001788018
126.5	53.3	47.3	0.000158432
238.3	10.5	23.1	0.001086391
171	30.4	26.7	0.000588462
225.3	23.5	41.4	0.001991716

Continued on next page

207.9	45	46.3	0.000543195
134.6	15.9	61.4	0.000656361
172.9	36.5	35.6	0.000135799
58.1	24.9	4.2	0.000837426
252.7	11	31.6	0.001403255
317.7	40.3	50.2	0.008826924
159.9	42.5	39.1	0.010614942
28.4	8.2	57.1	0.000905326
358.1	17.9	43.2	0.001629586
322.5	37.8	60.5	0.001357988
64.2	52	45.1	0.000497929
351.7	11.5	57.8	0.002195415
288.3	32.3	73	0.001290089
73.2	43.9	14.9	0.001244823
147.2	17.4	40.7	0.004481362
294.5	44.3	56.2	0.001267456
26.2	52.3	39.9	0.005228255
314.5	41	38.1	0.003213906
232.5	44.8	34.5	0.002127515
157.6	53.1	44.6	0.001109024
18	49.5	44.5	0.006178847
186.8	50	42.7	0.000271598
330.7	54.1	45.6	0.000588462
350	37.9	50.6	0.000520562
70.5	49.7	35	0.001335355
315.2	50.3	40.4	0.001267456
21.1	32.5	50.7	0.00036213
123.3	49.1	56.3	0.002444379
166.4	6.4	79.3	0.000226331
129	55	44.8	0.00036213
185.1	44.7	38.3	0.000633728
189.2	33.5	64	0.000475296
23.1	42.2	39.1	0.000203698
157.6	13.3	56.8	0.001176923
33.3	41.5	33.6	0.001742752
296	42.6	56.8	0.001312722

Continued on next page

341.2	32.9	60	0.000701627
183.9	39.3	32.1	0.000520562
150.8	38.5	47.6	0.000135799
233.1	44.7	33.8	0.000113166
358	45.1	45.1	0.001403255
117.8	31.5	71.7	0.001561687
128.4	30.8	59.9	0.000769527
184.7	51.4	54	0.000882692
336.8	31.9	44.7	0.000384763
247.7	14.6	85.7	0.000611095
240.1	12.8	14.8	0.000135799
124.5	49.1	39.6	0.000226331
150.2	46.8	46.2	0.000158432
131.4	42.9	56.3	0.000113166
138.3	19.1	72.3	0.000860059
178.5	52	43.8	0.000520562
359.9	48.6	41.9	0.000316864
327.9	23	74.2	0.000927959
321.3	48	39.1	0.002851776
333.5	33	12.5	0.000339497
190.5	46.1	61.8	0.000226331
64.3	31.2	13.4	0.000678994
342.2	15.3	69.3	0.000339497
163.8	37.4	46.2	0.002285947
326.9	38.1	70.1	0.000950592
346.5	43	51.7	0.000113166
357.6	48.1	38.1	0.000611095
134.1	48	57.2	0.001244823
203.3	34.2	40.9	0.00115429
154.4	41	44	0.000475296
122.3	26.5	75.2	0.000746894
308.2	46	53.4	0.002919675
124.2	40.2	51.1	0.00346287
177.5	15.6	53.7	0.000995858
334.6	48.7	48.2	0.000158432
158.5	9	28.1	0.000407397

Continued on next page

15.3	32.8	33.2	0.000769527
111	48.9	57.8	0.000475296
181.3	33.5	45.1	0.000769527
323.3	48.1	48.5	0.000271598
264.4	46.6	33.1	0.00043003
21.6	48.4	44.2	0.000248965
178.9	46.8	44.6	0.002218048
3.1	48.2	39.1	0.000565828
136.8	44	49.5	0.000633728
293.6	11.5	79.3	0.00043003
236	45.1	41.7	0.000746894
89.4	52.9	34.7	0.00079216
268.5	42.3	26.1	0.000611095
29.7	48.9	40.3	0.00036213
2.5	32.7	40.9	0.001561687
298.5	16.7	62.7	0.00072426
184.8	50.8	35.2	0.000248965
350.6	6.9	31.6	0.000656361
275.8	33	18.8	0.000497929
52.9	53.2	41.4	0.000814793
42.4	33.1	52.2	0.000339497
280.7	39.8	8	0.000475296
171.2	5.9	41.3	0.001041124
89.8	34.1	5.1	0.000226331
343.9	38.9	52	0.000158432
344.3	27	53.5	0.000475296
44.7	45.2	32.9	0.000203698
110.7	49.4	27.3	0.000339497
290.2	47.9	49.4	0.00115429
233.8	49.3	47.1	0.001742752
70.8	48.4	36.8	0.001244823
174	28.5	55.8	0.000407397
69.5	44.2	33.3	0.00072426
147.4	49.7	37.4	0.000384763
55.4	45.4	31.6	0.000656361
156.7	47	48.7	0.000294231

Continued on next page

172.2	36.6	27.5	0.001357988
204.1	43.9	50.5	0.000814793
307.8	41.4	51.2	0.000271598
34.2	36.5	45.2	0.000407397
150.2	16.1	28.7	0.000860059
155.3	53.1	48.9	0.000181065
96.9	51.2	50.3	0.000905326
144	39.2	59.6	0.001471154
41.3	51.2	45.2	0.001290089
22.2	40.5	55.2	0.000135799
190.1	10.7	58.1	0.000520562
316.4	44.2	53.6	0.000837426
180.4	46	46	0.000384763
155.5	51.6	35.8	0.000294231
293.4	47.6	52.9	0.000746894
241.5	44.4	34.5	0.001290089
288.1	40.4	75.5	0.000407397
193.4	52.4	39.5	0.000226331
311	42	59.9	0.000226331
291.5	11.3	60.2	0.000497929
65.6	38.5	13	0.000611095
202	45.8	38.7	0.000158432
129.4	46.3	56.5	0.000678994
325	38.8	52.2	0.00079216
24.9	47.6	49.7	0.001493787
86.1	53.7	39.1	0.001606953
211	49.9	48.8	0.001290089
182.6	15.5	95.4	0.000248965
269.2	22.2	86.5	0.000407397
346.4	45.4	37	0.001018491
340.8	30.4	45.1	0.000497929
168.5	35.9	45.4	0.000158432
134.6	50.4	49.5	0.000135799
198.5	26.5	10.6	0.000543195
183.8	40.6	17.3	0.000905326
180.9	23.7	36.5	0.002059616

Continued on next page

95.4	46.1	58.8	0.001109024
75.3	52.7	38.5	0.002218048
160.2	51.2	44.4	0.00237648
3.3	21.7	65.9	0.000656361
18.8	38.5	45	0.000927959
217.4	41.9	37	0.000973225
149.5	16.4	41.6	0.000611095
205.2	21.3	91.5	0.000678994
192.2	39.4	45.2	0.000837426
174.5	47.8	41	0.000497929
0.5	29.9	33.1	0.000316864
67	45.8	54.7	0.001312722
6.3	47.5	52	0.000384763
28.6	10.8	58.3	0.00115429
199.8	54.3	46	0.000407397
293.8	7.4	72.2	0.000611095
205.6	33.3	36.4	0.000950592
150.2	48.5	37.9	0.00036213
209.4	10.7	31.6	0.000746894
250.3	18.4	84.5	0.000203698
17.7	46.6	52	0.000452663
171	46.7	50.3	0.001833284
12.8	47.4	45.1	0.001629586
17.6	44	41.3	0.000203698
86.4	55.3	41.5	0.00043003
194.8	40.4	51.2	0.000497929
183.3	56	46.5	0.000339497
36.1	32.5	49.7	0.000475296
182.9	54.2	45.2	0.001561687
359.1	25.3	38.6	0.00036213
164.9	10.2	54.7	0.000860059
243.2	10.3	101.2	0.000226331
2.9	38.1	41.2	0.000226331
181	25	38.6	0.000181065
12.8	3.1	26.9	0.000113166
243.4	39.1	29.4	0.003236539

Continued on next page

227.5	49.6	39.7	0.000452663
178.6	12.6	49	0.000543195
223.5	52.4	42.4	0.001742752
183.2	56	46.6	0.000203698
198.3	54.3	50.3	0.00230858
156	36.3	42	0.001018491
219.2	32.1	13.1	0.00072426
128.7	15.3	10.9	0.000203698
159.8	49.9	52.9	0.000135799
187	7.6	61.7	0.001176923
110.4	47.6	64.3	0.000339497
186.7	34.4	56	0.000181065
198.7	24.5	40.7	0.000181065
36.7	44.9	43.2	0.000905326
164.5	17.7	12.1	0.000746894
62.8	7.5	346.1	0.000543195
165.7	51.4	55.2	0.00079216
127.4	54.2	41.2	0.000611095
178.1	41	51.6	0.000203698
184.2	54.4	43.9	0.000181065
145.8	46	47.8	0.000475296
347.6	34.2	38.2	0.002919675
16.3	6.8	33.2	0.000860059
137.6	54.9	38.9	0.00814793
336	49.8	42.8	0.000565828
133.2	53.7	51.8	0.000656361
142.4	50.4	26.6	0.000203698
358.6	46.7	54.9	0.00072426
131.8	51.4	46.9	0.002059616
145.8	36.7	51	0.000294231
168.8	31.9	52.8	0.001018491
197.6	47	46.4	0.000294231
219	52	53.4	0.002104882
288.2	48.3	52.8	0.000316864
156.6	40.4	42.2	0.002195415
297.5	44.3	42.7	0.000203698

Continued on next page

7.6	23.7	81.8	0.000746894
206.6	47.9	54.7	0.001855917
340.4	29.7	57.3	0.000271598
19.7	50.4	38.2	0.000611095
224.6	47.6	69.6	0.000475296
4.4	23.4	44.3	0.000565828
25.8	44	34.1	0.000294231
0.8	26.5	35.3	0.001788018
155.8	47	55.2	0.000656361
341.6	47.8	51.5	0.000226331
12.5	40.6	51.9	0.001041124
342.7	32.9	39.6	0.000384763
116.2	55.6	40.8	0.002104882
35.6	49.2	46	0.002806509
124.4	27.7	58.3	0.000294231
121.6	35.1	73.6	0.000520562
172.8	48	49.2	0.000633728
185.5	52	43.2	0.000452663
117	53.5	32.2	0.000656361
225.7	49	43.2	0.007898966
165.9	54	44.8	0.000565828
333.1	26.3	23.5	0.00079216
299.6	49.7	44.8	0.000497929
65.6	43.2	33.1	0.001041124
169.7	48.4	45	0.000475296
308.7	16	35.5	0.00043003
134.3	22.9	65.9	0.000339497
116.5	52.3	50	0.000226331
349.6	44.1	51.3	0.000678994
165.9	23.3	56.1	0.000497929
177.3	43.3	46.6	0.000543195
207.3	53.5	55	0.001041124
273.7	4.2	45.1	0.000226331
141.5	32.3	58.7	0.000203698
344.4	47.9	39.9	0.000950592
184	27.8	35.8	0.000543195

Continued on next page

193.8	42.6	53.3	0.001901184
102.6	42.8	43	0.000113166
215.3	54.4	49.3	0.000611095
99.9	53.1	42.8	0.000905326
210	52.6	46.7	0.002580178
215.8	46.5	38.8	0.000294231
3.8	49.4	45.3	0.000995858
162.9	47.4	25.8	0.000294231
44.5	12.9	5.5	0.000203698
178.1	41.6	29.1	0.000746894
198.7	49.8	30.3	0.001131657
324.8	1.8	74	0.000248965
299.7	43.4	57.9	0.00072426
183.6	39.6	53.8	0.000248965
348	38	42.5	0.000565828
182.2	49	48.5	0.000294231
0.1	21.3	5.9	0.000271598
11.4	46.1	45	0.000905326
18.5	29.4	38.6	0.000927959
327.2	42.3	49.7	0.00072426
192.8	50.8	51.5	0.000475296
208.8	49.1	35.5	0.000837426
353.7	43.5	40	0.000611095
245.3	52.3	45.1	0.001063758
179.7	17.6	27.6	0.000158432
183	47.3	30.3	0.00079216
77.7	27.9	29	0.000384763
185.4	51.2	48.5	0.000701627
271.9	31.9	5.6	0.000882692
158.6	19.7	69.2	0.000407397
73	50.5	37.8	0.001176923
193.4	47.8	47.9	0.000588462
291.1	36.8	91.2	0.000248965
235.4	47.1	41.2	0.000860059
313.3	38.6	53.8	0.000113166
5.5	35.8	37.7	0.000248965

Continued on next page

117.6	6.6	14.6	0.000339497
160.2	48.3	43	0.000384763
234.3	50	42.3	0.000248965
329.3	32.3	48.9	0.000475296
166.5	54.2	50.1	0.000294231
335.8	48.8	47.8	0.001425888
176.1	44.2	35.1	0.000497929
303.1	14.6	68.5	0.000158432
300.1	47.1	48.7	0.00036213

```
Iron ELASTIC CONSTANTS AND 'NO-HARDENING' PARAMETERS
CUBIC             crysym
   1.   1.   1.    90.   90.   90.   unit cell axes and angles
Elastic stiffness for Fe at 300K [GPa] (Simmons and Huang)
 233.0   135.0   135.0   000.0   000.0   000.0
 135.0   233.0   135.0   000.0   000.0   000.0
 135.0   135.0   233.0   000.0   000.0   000.0
 000.0   000.0   000.0   117.0   000.0   000.0
 000.0   000.0   000.0   000.0   117.0   000.0
 000.0   000.0   000.0   000.0   000.0   117.0
*Thermal expansion coefficients (single crystal in crystal axis):
  0.0e-6   0.0e-6   0.0e-6   0.0e0   0.0e0   0.0e0
INFORMATION ABOUT SLIP AND TWIN SYSTEMS
   3              nmodesx (total # of modes listed in the file)
   3              nmodes  (# of modes to be used in the calculation)
   1 2 3              mode(i) (label of the modes to be used)
   {110}<111> SLIP
  1   12   20    1                    modex,nsmx,nrsx,isensex
  0.0   0    0.   0.                   twshx,isectw,thres1,thres2
  2.   0.0     0.0    0.0     0.  0.
tau0,tau1,thet0,thet1 ,hpfac,hgnd
         1.0    1.0    1.0            hlatex
    0    1    1     1    1   -1       slip (n-b)
    1    0    1     1    1   -1
    1   -1    0     1    1   -1
    0    1   -1     1   -1   -1
    1    0    1     1   -1   -1
    1    1    0     1   -1   -1
    0    1    1     1   -1    1
    1    0   -1     1   -1    1
    1    1    0     1   -1    1
    0    1   -1     1    1    1
    1    0   -1     1    1    1
    1   -1    0     1    1    1
   {112}<111> SLIP
  2   12   20    1                    modex,nsmx,nrsx,isensex
  0.0   0    0.   0.                   twshx,isectw,thres1,thres2
  2.0   0.0   0.000  0.000    0.  0.
tau0,tau1,thet0,thet1 ,hpfac,hgnd
         1.0    1.0    1.0            hlatex
   -2    1   -1    -1   -1    1       slip (n-b)
    1   -2   -1    -1   -1    1
    1    1    2    -1   -1    1
   -2   -1   -1    -1    1    1
    1    2   -1    -1    1    1
    1   -1    2    -1    1    1
    2    1   -1     1   -1    1
   -1   -2   -1     1   -1    1
   -1    1    2     1   -1    1
    2   -1   -1     1    1    1
```

Figure D.5: The beginning of the "Fe.sx" input file. The rest of the file is provided in Figure D.6. Three slip systems are activated in this file. To select the number of slip systems, the following changes should be made. The number before "nmodes" should be changed to the desired number of active slip systems. The numbers prior to "mode(i)" specify which specific slip systems should be active.

```
  -1    2   -1     1    1    1
  -1   -1    2     1    1    1
  {123}<111> SLIP
  3   24   20    1                    modex,nsmx,nrsx,isensex
  0.0   0    0.   0.                   twshx,isectw,thres1,thres2
  2.0   0.0   0.000  0.000    0.  0.
tau0,tau1,thet0,thet1 ,hpfac,hgnd
         1.0    1.0    1.0            hlatex
   1    2    3     1    1   -1        slip (n-b)
  -1    3    2     1    1   -1
   2    1    3     1    1   -1
  -2    3    1     1    1   -1
   3   -1    2     1    1   -1
   3   -2    1     1    1   -1
  -1    2   -3     1   -1   -1
   1    3   -2     1   -1   -1
   2   -1    3     1   -1   -1
   2    3   -1     1   -1   -1
   3    1    2     1   -1   -1
   3    2    1     1   -1   -1
   1   -2   -3     1   -1    1
   1    3    2     1   -1    1
   2   -1   -3     1   -1    1
   2    3    1     1   -1    1
   3    1   -2     1   -1    1
   3    2   -1     1   -1    1
   1    2   -3     1    1    1
   1   -3    2     1    1    1
   2    1   -3     1    1    1
   2   -3    1     1    1    1
  -3    1    2     1    1    1
  -3    2    1     1    1    1
```

Figure D.6: The "Fe.sx" input file continued from Figure D.5.

Appendix E

Slopes and correlation coefficients calculated by orientation category

E.1 Slopes and correlation coefficients by region of planes

Table E.1: The slopes of the grain area fraction as a function of strain are presented from (i) $\varepsilon = 0$ to $\varepsilon = 0.1$, (ii) $\varepsilon = 0.1$ to $\varepsilon = 0.2$, and (iii) $\varepsilon = 0$ to $\varepsilon = 0.2$ by region of planes for each specimen test orientation.

Region	0°			90°			45°		
{hkl}	i	ii	iii	i	ii	iii	i	ii	iii
{110}	-88	-8	-48	-52	-5	-29	-75	5	-35
{321}	-97	-54	-76	-143	-28	-85	-91	-4	-48
{111}	185	63	124	197	34	115	168	3	85
Unidentified	0	-1	0	-2	-1	-1	-1	-3	-2

Table E.2: The slopes of the grain number fraction as a function of strain are presented from (i) $\varepsilon = 0$ to $\varepsilon = 0.1$, (ii) $\varepsilon = 0.1$ to $\varepsilon = 0.2$, and (iii) $\varepsilon = 0$ to $\varepsilon = 0.2$ by region of planes for each specimen test orientation.

Region	0°			90°			45°		
{hkl}	i	ii	iii	i	ii	iii	i	ii	iii
{110}	-118	-19	-69	-83	-7	-45	-102	-4	-53
{321}	-62	-51	-56	-100	-39	-70	-77	-30	-53
{111}	181	71	126	187	46	116	183	33	108
Unidentified	-1	-1	-1	-3	0	-2	-4	1	-2

Table E.3: The slopes of the area per grain as a function of strain are presented from (i) $\varepsilon = 0$ to $\varepsilon = 0.1$, (ii) $\varepsilon = 0.1$ to $\varepsilon = 0.2$, and (iii) $\varepsilon = 0$ to $\varepsilon = 0.2$ by region of planes for each specimen test orientation.

Region	0°			90°			45°		
{hkl}	i	ii	iii	i	ii	iii	i	ii	iii
{110}	1322	2474	1898	3186	1009	2097	1373	1935	1654
{321}	2681	2252	2466	2977	1279	2128	3048	1542	2295
{111}	3742	3193	3467	4130	1236	2683	3808	839	2323
Unidentified	2789	2529	2659	3962	-614	1674	3255	-3193	31

Table E.4: The correlation coefficients are given by region of planes for the grain area fraction, number fraction, and area per grain as functions of strain.

{hkl} Region	Area fraction	Number fraction	Area per grain
{110} Region	-0.86	-0.89	0.94
{321} Region	-0.92	-0.96	0.98
{111} Region	0.92	0.94	0.95
Unidentified	-0.71	-0.55	0.60

E.2 Slopes and correlation coefficients by plane orientation

Table E.5: The slopes of the grain area fraction as a function of strain are presented from (i) $\varepsilon = 0$ to $\varepsilon = 0.1$, (ii) $\varepsilon = 0.1$ to $\varepsilon = 0.2$, and (iii) $\varepsilon = 0$ to $\varepsilon = 0.2$ by plane orientation for each specimen test orientation.

Plane	0°			90°			45°		
{hkl}	i	ii	iii	i	ii	iii	i	ii	iii
{100}	-30	-2	-16	-23	2	-11	-22	-4	-13
{310}	-39	-5	-22	-17	-4	-10	-31	4	-13
{210}	-13	0	-7	-6	-2	-4	-13	2	-6
{320}	-9	-1	-5	-3	-2	-2	-4	-1	-3
{110}	-3	1	-1	-4	0	-2	-5	0	-3
{331}	-7	-2	-4	-5	-1	-3	-10	1	-4
{321}	-17	-23	-20	-11	-16	-13	-18	-14	-16
{311}	-29	-2	-16	-48	-5	-27	-53	-1	-27
{221}	-8	3	-2	-11	-11	-11	-6	-12	-9
{211}	-27	-25	-26	-66	7	-30	-16	23	4
{332}	71	14	42	76	33	55	62	-26	18
{322}	44	6	25	44	-28	8	38	-51	-6
{111}	69	36	52	74	26	50	79	83	81
Unidentified	0	-1	0	-1	-1	-1	-1	-3	-2

Table E.6: The slopes of the grain number fraction as a function of strain are presented from (i) $\varepsilon = 0$ to $\varepsilon = 0.1$, (ii) $\varepsilon = 0.1$ to $\varepsilon = 0.2$, and (iii) $\varepsilon = 0$ to $\varepsilon = 0.2$ by plane orientation for each specimen test orientation.

Plane	0°			90°			45°		
{hkl}	i	ii	iii	i	ii	iii	i	ii	iii
{100}	-37	-4	-20	-37	2	-18	-32	-4	-18
{310}	-47	-11	-29	-25	-6	-15	-39	-2	-21
{210}	-14	-2	-8	-6	-4	-5	-18	2	-8
{320}	-15	-2	-9	-5	-3	-4	-7	-3	-5
{110}	-7	1	-3	-5	-1	-3	-11	0	-5
{331}	-12	-4	-8	-13	-2	-8	-17	-1	-9
{321}	-10	-24	-17	-3	-18	-11	-26	-12	-19
{311}	-20	-10	-15	-44	-4	-24	-36	-3	-19
{221}	-9	-11	-10	-11	-2	-7	-4	-14	-9
{211}	-10	-5	-8	-24	-15	-20	-3	-9	-6
{332}	69	25	47	56	34	45	41	12	27
{322}	30	7	19	34	-10	12	57	-18	19
{111}	82	40	61	88	29	58	98	52	75
Unidentified	-1	-1	-1	-3	0	-2	-4	1	-2

Table E.7: The slopes of the area per grain as a function of strain are presented from (i) $\varepsilon = 0$ to $\varepsilon = 0.1$, (ii) $\varepsilon = 0.1$ to $\varepsilon = 0.2$, and (iii) $\varepsilon = 0$ to $\varepsilon = 0.2$ by plane orientation for each specimen test orientation. The slopes have units of μm^2.

Plane	0°			90°			45°		
{hkl}	i	ii	iii	i	ii	iii	i	ii	iii
{100}	712	617	664	5019	1149	3084	1913	-653	630
{310}	1537	2599	2068	2955	1164	2060	1431	3047	2239
{210}	-802	NaN	NaN	1571	310	941	78	2366	1222
{320}	1488	NaN	NaN	2376	-61	1158	1867	NaN	NaN
{110}	NaN	NaN	5168	1338	NaN	NaN	NaN	NaN	NaN
{331}	2331	7763	5047	3664	1666	2665	1670	4056	2863
{321}	2910	2289	2599	2644	605	1625	3926	826	2376
{311}	843	3267	2055	2437	542	1489	691	566	628
{221}	2285	4224	3254	3710	-295	1708	2683	635	1659
{211}	3062	1159	2110	2467	2321	2394	3082	2835	2958
{332}	3597	2551	3074	4205	1123	2664	4046	-96	1975
{322}	4442	3342	3892	4261	621	2441	3498	-74	1712
{111}	3698	2992	3345	3945	1104	2524	3643	1737	2690
Unidentified	2789	2529	2659	3962	-614	1674	3255	-3193	31

Table E.8: The correlation coefficients are given by plane orientation for the grain area fraction, number fraction, and area per grain as functions of strain.

{hkl} Plane	Area fraction	Number fraction	Area per grain
{100}	-0.85	-0.88	0.56
{310}	-0.83	-0.89	0.97
{210}	-0.84	-0.85	NaN
{320}	-0.87	-0.87	NaN
{110}	-0.79	-0.81	NaN
{331}	-0.63	-0.80	0.90
{321}	-0.45	-0.39	0.93
{311}	-0.78	-0.73	0.83
{221}	-0.81	-0.95	0.88
{211}	-0.60	-0.78	-0.93
{332}	0.79	0.90	0.92
{322}	0.25	0.42	0.87
{111}	0.92	0.95	0.97
Unidentifiied	-0.72	-0.57	0.60

E.3 Slopes and correlation coefficients by crystallographic direction along the TD

Table E.9: The slopes of the grain area fraction as a function of strain are presented from (i) $\varepsilon = 0$ to $\varepsilon = 0.1$, (ii) $\varepsilon = 0.1$ to $\varepsilon = 0.2$, and (iii) $\varepsilon = 0$ to $\varepsilon = 0.2$ by crystallographic direction along the TD for each specimen test orientation.

Direction	0°			90°			45°		
<uvw>||TD	i	ii	iii	i	ii	iii	i	ii	iii
<100>	-17	0	-9	-13	-3	-8	-14	2	-6
<310>	-22	-4	-13	-22	-21	-22	-23	-8	-16
<210>	2	1	1	-30	-7	-18	18	-14	2
<320>	47	-10	19	62	6	34	70	-37	17
<110>	65	33	49	59	29	44	-28	54	13
<331>	-36	5	-15	6	0	3	11	-18	-4
<321>	-28	31	2	14	-35	-11	45	4	25
<311>	13	-26	-6	-6	17	5	6	25	15
<221>	-8	-7	-7	-7	-18	-12	-25	-10	-18
<211>	-15	-13	-14	-38	24	-7	-35	14	-10
<332>	0	-1	0	-12	1	-5	-9	-1	-5
<322>	-4	-8	-6	0	-2	-1	-5	-8	-6
<111>	1	-1	0	-11	10	0	-10	0	-5
Unidentified	0	-1	0	-1	-1	-1	-1	-3	-2

Table E.10: The slopes of the grain number fraction as a function of strain are presented from (i) $\varepsilon = 0$ to $\varepsilon = 0.1$, (ii) $\varepsilon = 0.1$ to $\varepsilon = 0.2$, and (iii) $\varepsilon = 0$ to $\varepsilon = 0.2$ by crystallographic direction along the TD for each specimen test orientation.

Direction	0°			90°			45°		
<uvw>||TD	i	ii	iii	i	ii	iii	i	ii	iii
<100>	-21	-2	-11	-16	-8	-12	-19	0	-10
<310>	-22	-7	-15	-36	-25	-31	-29	-9	-19
<210>	4	6	5	-18	-9	-13	12	-4	4
<320>	48	-1	24	43	27	35	40	-12	14
<110>	35	9	22	48	30	39	21	41	31
<331>	-30	6	-12	-1	7	3	2	1	1
<321>	8	20	14	49	-13	18	40	6	23
<311>	12	5	9	-2	3	1	-15	15	0
<221>	-15	-8	-11	-10	-17	-13	-8	-12	-10
<211>	-11	-17	-14	-29	6	-11	-7	-3	-5
<332>	-1	-1	-1	-20	6	-7	-16	-1	-9
<322>	-6	-10	-8	-3	2	-1	-7	-12	-10
<111>	1	-1	0	-1	-9	-5	-11	-8	-10
Unidentified	-1	-1	-1	-3	0	-2	-4	0	-2

Table E.11: The slopes of the area per grain as a function of strain are presented from (i) $\varepsilon = 0$ to $\varepsilon = 0.1$, (ii) $\varepsilon = 0.1$ to $\varepsilon = 0.2$, and (iii) $\varepsilon = 0$ to $\varepsilon = 0.2$ by crystallographic direction along the TD for each specimen test orientation. The slopes have units of μm^2.

Direction	0°			90°			45°		
<uvw>||TD	i	ii	iii	i	ii	iii	i	ii	iii
<100>	756	4963	2860	713	NaN	NaN	404	3000	1702
<310>	1382	1281	1331	3446	964	2205	2161	-187	987
<210>	3090	2092	2591	2724	1112	1918	3687	-80	1803
<320>	3809	2652	3231	4585	310	2448	4809	-23	2393
<110>	4201	3948	4075	4292	1105	2699	2841	1415	2128
<331>	2744	2346	2545	4329	387	2358	3881	-393	1744
<321>	3135	3368	3252	3647	635	2141	3822	893	2358
<311>	3673	1046	2359	3330	2459	2894	4559	1648	3104
<221>	3276	1320	2298	3756	1059	2407	2533	788	1660
<211>	3350	3297	3323	3084	2572	2828	2901	2345	2623
<332>	2670	NaN	NaN	5124	-1206	1959	2083	-967	558
<322>	2728	-346	1191	3926	-385	1770	3182	2439	2811
<111>	NaN	NaN	NaN	1952	4914	3433	2829	8996	5912
Unidentified	2789	2529	2659	3962	-614	1674	3255	-3193	31

Table E.12: The correlation coefficients are given by crystallographic direction along the TD for the grain area fraction, grain number fraction, and area per grain as functions of strain.

<uvw>||TD	Area fraction	Number fraction	Area per grain
<100>	-0.86	-0.91	NaN
<310>	-0.73	-0.75	0.82
<210>	-0.28	-0.08	0.93
<320>	0.60	0.72	0.91
<110>	0.52	0.52	0.94
<331>	-0.26	-0.12	0.90
<321>	0.17	0.62	0.94
<311>	0.14	0.08	0.96
<221>	-0.27	-0.25	-0.84
<211>	-0.50	-0.65	0.99
<332>	-0.40	-0.46	NaN
<322>	-0.57	-0.66	0.82
<111>	-0.11	-0.27	NaN
Unidentified	-0.72	-0.57	0.60

E.4 Slopes and correlation coefficients by reference orientation (plane + direction)

Table E.13: The slopes of the grain area fraction as a function of strain are presented from (i) $\varepsilon = 0$ to $\varepsilon = 0.1$, (ii) $\varepsilon = 0.1$ to $\varepsilon = 0.2$, and (iii) $\varepsilon = 0$ to $\varepsilon = 0.2$ by reference orientation for each specimen test orientation.

Reference Orientation		0°			90°			45°		
ID	{hkl}<uvw>	i	ii	iii	i	ii	iii	i	ii	iii
1	{100}<100>	-7	0	-3	-7	0	-4	-10	1	-4
2	{100}<310>	-3	-1	-2	-3	1	-1	-3	-4	-3
3	{100}<210>	-4	0	-2	-1	-2	-2	0	-3	-2
4	{100}<320>	-13	0	-6	-10	3	-4	-7	0	-3
5	{100}<110>	-11	-1	-6	-8	-1	-4	-5	0	-2

Continued on next page

Reference Orientation		0°			90°			45°		
ID	{hkl}<uvw>	i	ii	iii	i	ii	iii	i	ii	iii
6	{310}<100>	-8	0	-4	-5	-1	-3	-5	1	-2
7	{310}<331>	-8	-3	-5	-8	1	-3	-9	-1	-5
8	{310}<321>	-10	-3	-7	-5	2	-2	-4	3	-1
9	{310}<311>	-11	0	-6	-1	-2	-1	-7	3	-2
10	{310}<310>	-5	0	-3	-2	-3	-3	-6	-1	-3
11	{210}<100>	-1	0	0	1	-1	0	-1	0	-1
12	{210}<321>	-1	0	0	-6	1	-2	-5	2	-2
13	{210}<221>	-1	0	0	-1	0	0	-1	0	-1
14	{210}<211>	-9	0	-5	0	0	0	-4	0	-2
15	{210}<210>	-1	0	0	1	-1	0	0	0	0
16	{320}<100>	-1	-1	-1	-1	-1	-1	-1	0	0
17	{320}<332>	-1	0	0	0	0	0	0	-1	0
18	{320}<322>	0	0	0	0	0	0	-2	-1	-1
19	{320}<321>	-6	0	-3	-2	-1	-1	0	-1	0
20	{320}<320>	-1	0	-1	0	1	0	-1	0	0
21	{110}<100>	0	0	0	-1	0	-1	0	0	0
22	{110}<311>	0	0	0	0	0	0	-1	0	-1
23	{110}<211>	0	0	0	0	0	0	-2	0	-1
24	{110}<322>	0	0	0	0	0	0	-1	0	-1
25	{110}<111>	0	0	0	0	0	0	0	0	0
26	{110}<332>	0	0	0	0	0	0	-1	0	0
27	{110}<221>	-1	0	-1	-1	0	0	0	0	0
28	{110}<331>	-2	1	0	-2	0	-1	-1	0	0
29	{110}<110>	-1	0	-1	0	0	0	0	0	0
30	{331}<310>	-2	0	-1	-4	-1	-2	-1	0	-1
31	{331}<321>	-1	0	-1	0	-1	0	-2	2	0
32	{331}<332>	0	-1	0	0	-1	0	-4	0	-2
33	{331}<110>	-4	-1	-2	-1	2	0	-2	0	-1
34	{321}<310>	0	-1	-1	-4	-13	-9	0	-1	0
35	{321}<111>	1	-1	0	-2	-3	-3	-8	0	-4
36	{321}<320>	-17	-2	-9	2	2	2	4	-3	0
37	{321}<210>	11	-2	5	-6	1	-2	14	-14	0
38	{321}<331>	-6	-7	-7	0	0	0	-10	15	2
39	{321}<211>	-7	-8	-7	1	-2	-1	-17	-6	-11
40	{311}<310>	-10	-2	-6	-9	-6	-8	-16	-3	-10
41	{311}<211>	-2	0	-1	-28	0	-14	-21	3	-9
42	{311}<332>	0	0	0	-11	1	-5	-3	0	-2

Continued on next page

Reference Orientation		0°			90°			45°		
ID	{hkl}<uvw>	i	ii	iii	i	ii	iii	i	ii	iii
43	{311}<110>	-16	0	-8	0	0	0	-10	-1	-5
44	{221}<210>	8	14	11	-8	-7	-8	8	-1	3
45	{221}<221>	-9	-1	-5	-4	1	-2	-18	-1	-10
46	{221}<322>	-3	-7	-5	0	-2	-1	-1	-7	-4
47	{221}<110>	-3	-3	-3	2	-2	0	-2	-3	-2
48	{211}<210>	-8	-7	-8	-15	2	-6	-5	5	0
49	{211}<321>	-7	-1	-4	-24	-11	-18	-2	-5	-4
50	{211}<111>	0	0	0	-6	9	1	0	1	0
51	{211}<110>	2	7	4	0	0	0	-6	4	-1
52	{211}<311>	-13	-23	-18	-18	5	-7	2	19	11
53	{332}<320>	45	16	31	23	15	19	34	-12	11
54	{332}<331>	-17	13	-2	15	-2	7	27	-24	1
55	{332}<110>	16	-9	4	28	9	18	-3	-6	-4
56	{332}<311>	28	-3	12	12	12	12	13	12	13
57	{322}<320>	34	-26	4	46	-11	18	52	-35	9
58	{322}<221>	3	-6	-1	-3	-18	-10	-7	-10	-8
59	{322}<110>	9	38	23	3	1	2	-5	-5	-5
60	{111}<110>	65	2	34	38	30	34	0	62	31
61	{111}<321>	2	33	18	48	-29	10	58	2	30
62	{111}<211>	5	-4	1	-11	24	7	10	17	14
63	Unidentified	0	-1	0	-1	-1	-1	-1	-3	-2

Table E.14: The slopes of the grain number fraction as a function of strain are presented from (i) $\varepsilon = 0$ to $\varepsilon = 0.1$, (ii) $\varepsilon = 0.1$ to $\varepsilon = 0.2$, and (iii) $\varepsilon = 0$ to $\varepsilon = 0.2$ by reference orientation for each specimen test orientation.

Reference Orientation		0°			90°			45°		
ID	{hkl}<uvw>	i	ii	iii	i	ii	iii	i	ii	iii
1	{100}<100>	-9	0	-4	-8	-1	-4	-13	1	-6
2	{100}<310>	-7	-3	-5	-10	2	-4	-8	-3	-5
3	{100}<210>	-7	-2	-4	-5	-1	-3	-3	-4	-3
4	{100}<320>	-10	1	-5	-10	0	-5	-9	1	-4

Continued on next page

Reference Orientation		0°			90°			45°		
ID	{hkl}<uvw>	i	ii	iii	i	ii	iii	i	ii	iii
5	{100}<110>	-12	-2	-7	-11	-1	-6	-6	0	-3
6	{310}<100>	-9	-1	-5	-7	-2	-4	-6	-1	-4
7	{310}<331>	-7	-4	-5	-8	1	-3	-13	-1	-7
8	{310}<321>	-11	-5	-8	-2	1	-1	-7	4	-1
9	{310}<311>	-17	-1	-9	-4	-3	-3	-9	-2	-5
10	{310}<310>	-7	0	-3	-6	-3	-4	-4	-1	-3
11	{210}<100>	-2	0	-1	3	-5	-1	-2	0	-1
12	{210}<321>	-1	-1	-1	-7	2	-2	-8	1	-4
13	{210}<221>	0	-1	0	-1	0	0	-4	2	-1
14	{210}<211>	-8	-1	-4	-1	0	-1	-3	-1	-2
15	{210}<210>	-2	0	-1	0	-1	0	0	0	0
16	{320}<100>	-1	-1	-1	-1	-3	-2	-1	0	0
17	{320}<332>	-1	0	0	0	0	0	-1	-1	-1
18	{320}<322>	0	-1	0	0	0	0	-3	-1	-2
19	{320}<321>	-11	0	-5	-3	-1	-2	0	-1	0
20	{320}<320>	-3	0	-1	0	2	1	-1	0	0
21	{110}<100>	0	0	0	-1	-1	-1	0	0	0
22	{110}<311>	-1	0	0	-1	0	0	-3	0	-1
23	{110}<211>	0	0	0	0	0	0	-3	0	-1
24	{110}<322>	0	0	0	0	0	0	-2	0	-1
25	{110}<111>	0	0	0	0	0	0	-1	0	0
26	{110}<332>	0	0	0	-1	0	0	-2	0	-1
27	{110}<221>	-3	0	-1	-1	0	0	0	0	0
28	{110}<331>	-4	1	-1	-2	0	-1	-2	0	-1
29	{110}<110>	-2	0	-1	0	0	0	0	0	0
30	{331}<310>	-1	-2	-1	-11	-5	-8	-2	0	-1
31	{331}<321>	-2	0	-1	1	1	1	-4	-1	-3
32	{331}<332>	0	-1	0	0	-1	0	-8	1	-4
33	{331}<110>	-8	-1	-5	-1	3	1	-1	-1	-1
34	{321}<310>	-2	1	0	-6	-12	-9	-2	1	-1
35	{321}<111>	1	-1	0	4	-8	-2	-8	-3	-5
36	{321}<320>	-9	-8	-9	3	2	3	6	-7	0
37	{321}<210>	10	2	6	-4	2	-1	2	-5	-2
38	{321}<331>	-4	0	-2	0	0	0	-9	8	-1
39	{321}<211>	-4	-16	-10	1	-2	0	-14	-3	-8
40	{311}<310>	-5	-4	-4	-5	-7	-6	-14	-6	-10
41	{311}<211>	-2	0	-1	-21	-4	-12	-13	6	-3

Continued on next page

Reference Orientation		0°			90°			45°		
ID	{hkl}<uvw>	i	ii	iii	i	ii	iii	i	ii	iii
42	{311}<332>	0	0	0	-18	6	-6	-4	-1	-2
43	{311}<110>	-12	-6	-9	0	0	0	-5	-3	-4
44	{221}<210>	8	10	9	-1	-6	-4	7	3	5
45	{221}<221>	-8	-2	-5	-7	2	-2	-11	-2	-7
46	{221}<322>	-5	-8	-7	-3	1	-1	-1	-10	-6
47	{221}<110>	-2	-11	-6	-1	1	0	0	-5	-2
48	{211}<210>	-4	-5	-4	-8	0	-4	4	3	3
49	{211}<321>	-8	1	-3	-6	-13	-10	5	-8	-2
50	{211}<111>	0	0	0	1	-5	-2	0	-5	-2
51	{211}<110>	3	8	5	0	0	0	-4	-3	-3
52	{211}<311>	1	-8	-3	-10	2	-4	-2	3	0
53	{332}<320>	43	15	29	11	20	15	15	4	9
54	{332}<331>	-12	10	-1	8	4	6	21	-1	10
55	{332}<110>	15	-16	0	25	8	16	7	-5	1
56	{332}<311>	25	17	21	11	3	7	0	15	7
57	{322}<320>	23	-8	7	34	9	21	38	-17	11
58	{322}<221>	-3	-4	-3	-3	-19	-11	6	-11	-3
59	{322}<110>	12	19	16	5	1	3	13	8	11
60	{111}<110>	41	14	27	37	27	32	18	41	30
61	{111}<321>	41	24	32	63	-8	28	53	14	34
62	{111}<211>	4	0	2	-8	11	2	25	-4	10
63	Unidentified	-1	-1	-1	-3	0	-2	-3	0	-1

Table E.15: The slopes of the area per grain as a function of strain are presented from (i) $\varepsilon = 0$ to $\varepsilon = 0.1$, (ii) $\varepsilon = 0.1$ to $\varepsilon = 0.2$, and (iii) $\varepsilon = 0$ to $\varepsilon = 0.2$ by reference orientation for each specimen test orientation. The slopes have units of μm^2.

Reference Orientation		0°			90°			45°		
ID	{hkl}<uvw>	i	ii	iii	i	ii	iii	i	ii	iii
1	{100}<100>	NaN	NaN	NaN	-645	NaN	NaN	25	2229	1127
2	{100}<310>	1108	NaN	NaN	7986	-1689	3148	3906	-3334	286
3	{100}<210>	-174	NaN	NaN	4672	-305	2183	3461	NaN	NaN

Continued on next page

Reference Orientation		0°			90°			45°		
ID	{hkl}<uvw>	i	ii	iii	i	ii	iii	i	ii	iii
4	{100}<320>	-494	1232	369	1857	6194	4025	-162	81	-41
5	{100}<110>	1677	NaN	NaN	4000	NaN	NaN	NaN	NaN	NaN
6	{310}<100>	-311	5889	2789	244	NaN	NaN	603	4805	2704
7	{310}<331>	1318	-2153	-417	3237	718	1977	1190	NaN	NaN
8	{310}<321>	1714	2998	2356	-1885	3634	875	1227	1255	1241
9	{310}<311>	2037	3490	2763	4347	3881	4114	1691	5099	3395
10	{310}<310>	NaN	NaN	NaN	4080	-21	2030	1409	1635	1522
11	{210}<100>	NaN	NaN	NaN	1064	NaN	NaN	NaN	NaN	NaN
12	{210}<321>	-595	NaN	NaN	1964	-70	947	-183	5340	2579
13	{210}<221>	-455	NaN	NaN	NaN	NaN	NaN	NaN	NaN	311
14	{210}<211>	-1011	NaN	NaN	3865	-2950	458	-210	NaN	NaN
15	{210}<210>	NaN	NaN	NaN	4845	NaN	NaN	NaN	NaN	NaN
16	{320}<100>	2610	NaN	NaN	1803	NaN	NaN	NaN	NaN	NaN
17	{320}<332>	NaN	NaN	NaN	NaN	NaN	NaN	1850	NaN	NaN
18	{320}<322>	712	NaN	NaN	NaN	NaN	NaN	1713	NaN	NaN
19	{320}<321>	NaN	NaN	NaN	3145	-3037	54	3685	NaN	NaN
20	{320}<320>	NaN	NaN	NaN	NaN	NaN	NaN	NaN	NaN	NaN
21	{110}<100>	NaN	NaN	NaN	1398	NaN	NaN	NaN	NaN	NaN
22	{110}<311>	NaN	NaN	NaN	NaN	NaN	NaN	NaN	NaN	NaN
23	{110}<211>	NaN	NaN	NaN	NaN	NaN	NaN	NaN	NaN	NaN
24	{110}<322>	NaN	NaN	NaN	NaN	NaN	NaN	NaN	NaN	NaN
25	{110}<111>	NaN	NaN	NaN	NaN	NaN	NaN	NaN	NaN	NaN
26	{110}<332>	NaN	NaN	NaN	NaN	NaN	NaN	NaN	NaN	NaN
27	{110}<221>	NaN	NaN	NaN	NaN	NaN	NaN	NaN	NaN	NaN
28	{110}<331>	NaN	NaN	5234	NaN	NaN	NaN	NaN	NaN	NaN
29	{110}<110>	NaN	NaN	NaN	NaN	NaN	NaN	NaN	NaN	NaN
30	{331}<310>	-841	NaN	NaN	3339	4360	3849	NaN	NaN	NaN
31	{331}<321>	NaN	NaN	NaN	3896	-1933	982	1864	8839	5352
32	{331}<332>	3050	NaN	NaN	5028	NaN	NaN	3275	-2095	590
33	{331}<110>	4160	5987	5074	NaN	NaN	1015	-2253	NaN	NaN
34	{321}<310>	4881	-1639	1621	3572	-223	1675	4321	-1504	1408
35	{321}<111>	NaN	NaN	NaN	1049	2757	1903	2117	3680	2899
36	{321}<320>	484	5443	2964	2646	795	1721	2304	4048	3176
37	{321}<210>	3557	2203	2880	1705	453	1079	5153	-1224	1965
38	{321}<331>	2630	-694	968	NaN	NaN	NaN	1276	6727	4001
39	{321}<211>	2435	4786	3610	3721	NaN	NaN	6816	-4488	1164
40	{311}<310>	-293	227	-33	2055	-1657	199	1188	460	824
41	{311}<211>	NaN	NaN	NaN	1497	1436	1467	829	26	428
42	{311}<332>	NaN	NaN	NaN	5110	-1217	1946	873	NaN	NaN
43	{311}<110>	1188	3609	2398	NaN	NaN	NaN	-1658	NaN	NaN
44	{221}<210>	3097	4078	3587	2946	508	1727	3825	-770	1527
45	{221}<221>	1026	7030	4028	3175	-321	1427	896	683	789

Continued on next page

Reference Orientation		0°			90°			45°		
ID	{hkl}<uvw>	i	ii	iii	i	ii	iii	i	ii	iii
46	{221}<322>	2887	-571	1158	3926	-385	1770	3167	2323	2745
47	{221}<110>	1587	4848	3217	6990	-3537	1726	1044	NaN	NaN
48	{211}<210>	2168	-1176	496	1913	1842	1877	2100	1515	1808
49	{211}<321>	9806	-9775	16	3043	1431	2237	2886	1400	2143
50	{211}<111>	NaN	NaN	NaN	2071	4664	3367	3510	10024	6767
51	{211}<110>	3470	2513	2991	NaN	NaN	NaN	191	8480	4335
52	{211}<311>	2982	970	1976	829	2895	1862	4204	3458	3831
53	{332}<320>	3627	3041	3334	4757	587	2672	5123	-317	2403
54	{332}<331>	2823	3457	3140	4436	373	2404	3920	-788	1566
55	{332}<110>	3471	4662	4066	4086	1340	2713	1623	-126	749
56	{332}<311>	3931	722	2327	3707	2266	2987	6168	-97	3036
57	{322}<320>	4869	1820	3345	4846	-61	2393	4762	-158	2302
58	{322}<221>	4753	-726	2013	3700	1197	2449	2676	1059	1868
59	{322}<110>	3536	5245	4390	NaN	1658	NaN	2119	-828	646
60	{111}<110>	5099	2433	3766	3950	1338	2644	3374	2111	2742
61	{111}<321>	2898	3367	3132	3820	426	2123	3960	677	2318
62	{111}<211>	4041	2311	3176	3841	2752	3297	2833	3391	3112
63	Unidentified	2789	2529	2659	3962	-614	1674	3255	-3193	31

Table E.16: The correlation coefficients are given by reference orientation for the grain area fraction, grain number fraction, and area per grain as functions of strain.

ID	{ h k l }<u v w >	Area fraction	Number fraction	Area per grain
1	{100}<100>	-0.80	-0.78	NaN
2	{100}<310>	-0.79	-0.90	NaN
3	{100}<210>	-0.73	-0.88	NaN
4	{100}<320>	-0.74	-0.82	0.45
5	{100}<110>	-0.82	-0.83	NaN
6	{310}<100>	-0.80	-0.91	NaN
7	{310}<331>	-0.85	-0.86	NaN
8	{310}<321>	-0.58	-0.56	0.72
9	{310}<311>	-0.66	-0.80	0.94
10	{310}<310>	-0.86	-0.87	NaN

Continued on next page

ID	{ h k l }<u v w >	Area fraction	Number fraction	Area per grain
11	{210}<100>	-0.66	-0.53	NaN
12	{210}<321>	-0.55	-0.60	NaN
13	{210}<221>	-0.72	-0.45	NaN
14	{210}<211>	-0.67	-0.71	NaN
15	{210}<210>	-0.37	-0.57	NaN
16	{320}<100>	-0.77	-0.70	NaN
17	{320}<332>	-0.59	-0.57	NaN
18	{320}<322>	-0.47	-0.54	NaN
19	{320}<321>	-0.66	-0.65	NaN
20	{320}<320>	-0.29	-0.30	NaN
21	{110}<100>	-0.43	-0.43	NaN
22	{110}<311>	-0.68	-0.72	NaN
23	{110}<211>	-0.43	-0.43	NaN
24	{110}<322>	-0.43	-0.43	NaN
25	{110}<111>	-0.43	-0.43	NaN
26	{110}<332>	-0.62	-0.62	NaN
27	{110}<221>	-0.63	-0.57	NaN
28	{110}<331>	-0.55	-0.73	NaN
29	{110}<110>	-0.43	-0.43	NaN
30	{331}<310>	-0.29	-0.43	NaN
31	{331}<321>	-0.14	-0.39	NaN
32	{331}<332>	-0.49	-0.47	NaN
33	{331}<110>	-0.52	-0.44	NaN
34	{321}<310>	-0.29	-0.27	0.67
35	{321}<111>	-0.45	-0.39	NaN
36	{321}<320>	-0.32	-0.31	0.91
37	{321}<210>	0.03	0.04	0.80
38	{321}<331>	-0.15	-0.09	NaN
39	{321}<211>	-0.50	-0.43	NaN
40	{311}<310>	-0.81	-0.62	0.38
41	{311}<211>	-0.48	-0.31	NaN
42	{311}<332>	-0.25	-0.27	NaN
43	{311}<110>	-0.43	-0.34	NaN
44	{221}<210>	0.20	0.41	0.84
45	{221}<221>	-0.63	-0.62	0.71

Continued on next page

ID	{ h k l }<u v w >	Area fraction	Number fraction	Area per grain
46	{221}<322>	-0.55	-0.65	0.81
47	{221}<110>	-0.43	-0.38	NaN
48	{211}<210>	-0.46	-0.19	0.82
49	{211}<321>	-0.26	-0.17	0.39
50	{211}<111>	0.05	-0.10	NaN
51	{211}<110>	0.10	0.05	NaN
52	{211}<311>	-0.13	-0.07	0.88
53	{332}<320>	0.62	0.64	0.91
54	{332}<331>	0.10	0.22	0.88
55	{332}<110>	0.29	0.34	0.80
56	{332}<311>	0.56	0.53	0.91
57	{322}<320>	0.37	0.56	0.88
58	{322}<221>	-0.15	-0.12	0.87
59	{322}<110>	0.20	0.35	NaN
60	{111}<110>	0.84	0.96	0.95
61	{111}<321>	0.68	0.88	0.93
62	{111}<211>	0.43	0.39	0.99
63	Unidentified	-0.70	-0.56	0.60

Appendix F

Scarce reference orientations

Table F.1: Scarce reference orientations with a grain count of less than 1% of the total number of nonboundary grains at a strain of 0, 0.1, or 0.2 are shown. The specimen TD was oriented at 0° with respect to the RD.

ID	{hkl}<uvw>
1	{100}<100>
2	{100}<310>
3	{100}<210>
4	{100}<320>
5	{100}<110>
6	{310}<100>
7	{310}<331>
8	{310}<321>
9	{310}<311>
10	{310}<310>
11	{210}<100>
12	{210}<321>
13	{210}<221>
14	{210}<211>
15	{210}<210>
16	{320}<100>
17	{320}<332>
18	{320}<322>
19	{320}<321>
20	{320}<320>
22	{110}<311>
27	{110}<221>
28	{110}<331>

Continued on next page

ID	{hkl}<uvw>
29	{110}<110>
30	{331}<310>
31	{331}<321>
32	{331}<332>
33	{331}<110>
34	{321}<310>
35	{321}<111>
36	{321}<320>
40	{311}<310>
41	{311}<211>
45	{221}<221>
46	{221}<322>
47	{221}<110>
49	{211}<321>
58	{322}<221>
63	Unidentified

Table F.2: Scarce reference orientations with a grain count of less than 1% of the total number of nonboundary grains at a strain of 0, 0.1, or 0.2 are shown. The specimen TD was oriented at 90° with respect to the RD.

ID	{hkl}<uvw>
1	{100}<100>
2	{100}<310>
3	{100}<210>
4	{100}<320>
5	{100}<110>
6	{310}<100>
7	{310}<331>
8	{310}<321>
9	{310}<311>

Continued on next page

ID	{hkl}<uvw>
10	{310}<310>
11	{210}<100>
12	{210}<321>
13	{210}<221>
14	{210}<211>
15	{210}<210>
16	{320}<100>
19	{320}<321>
20	{320}<320>
21	{110}<100>
22	{110}<311>
26	{110}<332>
27	{110}<221>
28	{110}<331>
30	{331}<310>
31	{331}<321>
32	{331}<332>
33	{331}<110>
35	{321}<111>
36	{321}<320>
37	{321}<210>
39	{321}<211>
40	{311}<310>
45	{221}<221>
47	{221}<110>
59	{322}<110>
63	Unidentified

Table F.3: Scarce reference orientations with a grain count of less than 1% of the total number of nonboundary grains at a strain of 0, 0.1, or 0.2 are shown. The specimen TD was oriented at 45° with respect to the RD.

ID	{hkl}<uvw>
1	{100}<100>
2	{100}<310>
3	{100}<210>
4	{100}<320>
5	{100}<110>
6	{310}<100>
7	{310}<331>
8	{310}<321>
9	{310}<311>
10	{310}<310>
11	{210}<100>
12	{210}<321>
13	{210}<221>
14	{210}<211>
16	{320}<100>
17	{320}<332>
18	{320}<322>
19	{320}<321>
20	{320}<320>
22	{110}<311>
23	{110}<211>
24	{110}<322>
25	{110}<111>
26	{110}<332>
28	{110}<331>
30	{331}<310>
31	{331}<321>
32	{331}<332>
33	{331}<110>
34	{321}<310>
35	{321}<111>

Continued on next page

ID	{hkl}<uvw>
36	{321}<320>
38	{321}<331>
39	{321}<211>
41	{311}<211>
42	{311}<332>
43	{311}<110>
44	{221}<210>
47	{221}<110>
50	{211}<111>
51	{211}<110>
63	Unidentifed

Bibliography

[1] T. Ukena. Effect of applied stress during annealing on the texture of cold rolled steel sheet. *CAMP-ISIJ*, 8:593, 1995.

[2] J. Ciulik and E. M. Taleff. Dynamic abnormal grain growth: A new method to produce single crystals. *Scripta Materialia*, 61(9):895–898, 2009.

[3] D. L. Worthington, N. A. Pedrazas, P. J. Noell, and E. M. Taleff. Dynamic abnormal grain growth in molybdenum. *Metallurgical and Materials Transactions A*, 44(11):5025–5038, 2013.

[4] N. A. Pedrazas, T. E. Buchheit, E. A. Holm, and E. M. Taleff. Dynamic abnormal grain growth in tantalum. *Materials Science and Engineering: A*, 610:76–84, 2014.

[5] P. J. Noell and E. M. Taleff. Dynamic abnormal grain growth in refractory metals. *JOM*, 67(11):2642–2645, 2015.

[6] P. J. Noell, D. L. Worthington, and E. M. Taleff. The initiation and propagation of dynamic abnormal grain growth in molybdenum. *Metallurgical and Materials Transactions A*, 46(12):5708–5718, 2015.

[7] F. J. Humphreys and M. Hatherly. *Recrystallization and related annealing phenomena*. Elsevier, 2004.

[8] G. Gottstein and L. S. Shvindlerman. *Grain boundary migration in metals: thermodynamics, kinetics, applications*. CRC Press, 2009.

[9] P. Lejcek. *Grain boundary segregation in metals*, volume 136. Springer Science & Business Media, 2010.

[10] D. M. Saylor, B. S. El-Dasher, B. L. Adams, and G. S. Rohrer. Measuring the five-parameter grain-boundary distribution from observations of planar sections. *Metallurgical and Materials Transactions A*, 35(7):1981–1989, 2004.

[11] V. Randle and O. Engler. *Introduction to texture analysis: macrotexture, microtexture, and orientation mapping*. CRC press, 2014.

[12] J. G. Byrne. *Recovery, recrystallization, and grain growth*. The Macmillan Company, 1965.

[13] P. J. Noell. *The Influence of High-Temperature Tensile Deformation on Microstructure Evolution in Select BCC Metals*. PhD thesis, The University of Texas at Austin, 2015.

[14] P. H. X. Thành. *Microstructure Evolution in Alpha Iron during High Temperature Tensile Deformation*. PhD thesis, University of California, Davis, 2012.

[15] G. Ibe and K. Lücke. Growth selection during recrystallization of single crystals. *Recrystallization, grain growth, and textures: papers presented*

at a seminar of the American Society for Metals, October 16 and 17, 1965, pages 434–447, 1966.

[16] P. A. Beck. Annealing of cold worked metals. *Advances in Physics*, 3(11):245–324, 7 1954.

[17] H. Yoshida, B. Liebmann, and K. Lücke. Orientation of recrystallized grains in strained aluminum single crystals. *Acta Metallurgica*, 7(1):51–56, 1959.

[18] K. Lücke. The orientation dependence of grain boundary motion and the formation of recrystallization textures. *Canadian Metallurgical Quarterly*, 13(1):261–274, 1974.

[19] C. D. Graham Jr. and R. W. Cahn. Grain growth rates and orientation relationships in the recrystallization of aluminum single crystals. *Trans. Met. Soc. AIME*, 206(517–521), 1956.

[20] K. Lücke, R. Rixen, and F. W. Rosenbaum. On the theory of grain boundary motion. *The Nature and Behavior of Grain Boundaries*, pages 245–283, 1972.

[21] K. Lücke and R. Rixen. Orientation relationships in the recrystallization of polycrystalline, hexagonal metals. *Metallurgical Transactions*, 1(1):259–266, 1970.

[22] P. A. Beck. Notes on the theory of annealing textures. *Acta Metallurgica*, 1(2):230–234, 1953.

[23] M. Hölscher, D. Raabe, and K. Lücke. Rolling and recrystallization textures of BCC steels. *Steel Research International*, 62(12):567–575, 1991.

[24] N. Mizui and K. Lücke. Recrystallization texture formation in an ultra-low C Ti-added steel with 1.5% Si. *Texture and Microstructures*, 14–18:685–690, 1991.

[25] D. Raabe and K. Lücke. Annealing textures of BCC metals. *Scripta Metallurgica et Materialia*, 27(11):1533–1538, 1992.

[26] D. Raabe and K. Lücke. Rolling and annealing textures of BCC metals. *Materials Science Forum*, 157–162:597–610, 1994.

[27] E. Lindh, W. B. Hutchinson, and P. S. Bate. Texture evolution during recrystallisation of ultra-low carbon steel. *Materials Science Forum*, 157–162:997–1002, 1994.

[28] K. Okayasu and H. Fukutomi. Texture formation during high temperature deformation of Al-3mass% Mg solid solution. *Materials Science Forum*, 495–497:579–584, 2005.

[29] K. Okayasu, H. Takekoshi, and H. Fukutomi. Influence of grain boundary migration on {001} texture formation in Al-3 mass% Mg based alloys during high temperature compression deformation. *Materials Transactions*, 48(8):2002–2007, 2007.

[30] K. Okayasu, M. Sakakibara, and H. Fukutomi. Effect of deformation constraints on the texture formation in Al-5mass% Mg solid solution at high temperatures. *Materials Processing and Texture: Ceramic Transcations*, pages 679–685, 2009.

[31] K. Okayasu, H. Takekoshi, M. Sakakibara, and H. Fukutomi. Effect of Mg concentration on texture formation in Al-Mg alloys during high temperature compression. *Applications of Texture Analysis: Ceramic Transactions*, pages 507–513, 2009.

[32] H.-M. Jeong, K. Okayasu, and H. Fukutomi. {001} texture map of AA5182 aluminum alloy for high temperature uniaxial compression. *Materials Transactions*, 51(12):2162–2167, 2010.

[33] Y. Onuki, K. Okayasu, and H. Fukutomi. Formation of {001} fiber texture in Fe-3mass% Si alloy during uniaxial compression deformation at elevated temperatures. *ISIJ International*, 51(9):1564–1565, 2011.

[34] K. Okayasu, S. Takahata, and H. Fukutomi. Formation process of {001} texture in Al-Cu solid solution during high temperature compression deformation. *Materials Science Forum*, 702–703:336–339, 2012.

[35] Y. Onuki, K. Okayasu, and H. Fukutomi. Texture development in ferritic steels during high temperature uniaxial compression deformation. *Materials Science Forum*, 702–703:810–813, 2012.

[36] H.-M. Jeong, K. Okayasu, and H. Fukutomi. Texture formation by the compression deformation of AA5182 aluminum alloy at high temperatures. *Materials Science Forum*, 715–716:918–923, 2012.

[37] Y. Onuki, R. Hongo, K. Okayasu, and H. Fukutomi. Texture development in Fe–3.0 mass% Si during high-temperature deformation: Examination of the preferential dynamic grain growth mechanism. *Acta Materialia*, 61:1294–1302, 2013.

[38] K.-H. Kim, K. Okayasu, and H. Fukutomi. Influence of the initial texture on texture formation of high temperature deformation in AZ80 magnesium alloy. *Materials Transactions*, 56(1):17–22, 2015.

[39] J.-P. Poirier. *Creep of crystals: high-temperature deformation processes in metals, ceramics and minerals*. Cambridge University Press, 1985.

[40] O. D. Sherby and P. M. Burke. Mechanical behavior of crystalline solids at elevated temperature. *Progress in Materials Science*, 13:323–390, 1968.

[41] J. H. Driver, M.-C. Theyssier, and CI. Maurice. Electron backscattered diffraction microtexture studies on hot deformed aluminium crystals. *Materials Science and Technology*, 12(10):851–858, 1996.

[42] A. Bardal, I. Lindseth, H. E. Vatne, and E. Nes. Dislocation densities, subgrain sizes and sub-boundary misorientations within the different texture components of hot deformed AlMgMn. In *Proc. 16th Risø Int. Symp. on Mater. Sci.: Microstructural and crystallographic aspects of*

recrystallization, N. Hansen, D. Juul Jensen, Y. L. Liu, and B. Ralph, eds., Risø national laboratory, Roskilde, pages 261–266, 1995.

[43] O. D. Sherby, R. H. Klundt, and A. K. Miller. Flow stress, subgrain size, and subgrain stability at elevated temperature. *Metallurgical Transactions A*, 8(6):843–850, 1977.

[44] I. Samajdar, P. Ratchev, B. Verlinden, and E. Aernoudt. Hot working of AA1050—relating the microstructural and textural developments. *Acta Materialia*, 49(10):1759–1769, 2001.

[45] R. K. Ray, J. J. Jonas, and R. E. Hook. Cold rolling and annealing textures in low carbon and extra low carbon steels. *International Materials Reviews*, 39(4):129–172, 1994.

[46] J. A. Schey. *Introduction to Manufacturing Processes*. The McGraw-Hill Companies, Inc., 2000.

[47] Z. X. Guo. *The deformation and processing of structural materials*. Elsevier, 2005.

[48] G. Krauss. *Steels: processing, structure, and performance*. ASM International, 2015.

[49] W. D. Callister, Jr. and D. G. Rethwisch. *Materials Science and Engineering An Introduction*. John Wiley & Sons. Inc.–New York, USA, eigth edition, 2010.

[50] G. Glover and C. M. Sellars. Recovery and recrystallization during high temperature deformation of α-iron. *Metallurgical Transactions*, 4(3):765–775, 1973.

[51] R. Gholizadeh, A. Shibata, and N. Tsuji. Grain refinement and texture evolution in highly deformed ferrite during high-temperature torsion deformation of IF steel. In *Proceedings of the 6th International Conference on Recrystallization and Grain Growth (ReX&GG 2016)*, pages 71–78. Springer, 2016.

[52] J. Baczynski and J. J. Jonas. Torsion textures produced by dynamic recrystallization in α-iron and two interstitial-free steels. *Metallurgical and Materials Transactions A*, 29(2):447–462, 1998.

[53] A. Najafi-Zadeh, J. J. Jonas, and S. Yue. Grain refinement by dynamic recrystallization during the simulated warm-rolling of interstitial free steels. *Metallurgical Transactions A*, 23(9):2607–2617, 1992.

[54] N. Tsuji, Y. Matsubara, and Y. Saito. Dynamic recrystallization of ferrite in interstitial free steel. *Scripta Materialia*, 37(4), 1997.

[55] G. H. Akbari, C. M. Sellars, and J. A. Whiteman. Microstructural development during warm rolling of an IF steel. *Acta Materialia*, 45(12):5047–5058, 1997.

[56] G. H. Akbari, C. M. Sellars, and J. A. Whiteman. Quantitative characterisation of substructural development during warm working of an inter-

stitial free steel. *Materials Science and Technology*, 16(1):47–54, 2000.

[57] A. Oudin, M. R. Barnett, and P. D. Hodgson. Grain size effect on the warm deformation behaviour of a Ti-IF steel. *Materials Science and Engineering: A*, 367(1-2):282–294, 2004.

[58] A. Oudin, P. D. Hodgson, and M. R. Barnett. EBSD analysis of a Ti-IF steel subjected to hot torsion in the ferritic region. *Materials Science and Engineering: A*, 486(1-2):72–79, 2008.

[59] T. Ukena. Effect of high temperature deformation on the texture of cold rolled steel sheet. *CURRENT ADVANCES IN MATERIALS AND PROCESSES*, 8:1385–1385, 1995.

[60] W. F. Hosford. *The mechanics of crystals and textured polycrystals*. Oxford University Press(USA), 1993.

[61] E18-17$^{\varepsilon 1}$. Standard test methods for rockwell hardness of metalic materials. Technical report, ASTM, 2017.

[62] ASTM E8/E8M-16a. Standard test methods for tension testing of metallic materials. Technical report, ASTM, 2016.

[63] ASTM A370-17a. Standard test methods and definitions for mechanical testing of steel products. Technical report, ASTM, 2017.

[64] W. Köster and W. Rauscher. Beziehungen zwischen dem elastizitätsmodul von zweistofflegierungen und ihrem aufbau. *Zeitschrift für Metallkunde*, 39(4):111–120, 1948.

[65] N. A. Pedrazas. *Dynamic abnormal grain growth of selected refractory metals*. PhD thesis, The University of Texas at Austin, 2013.

[66] Wolfram Research, Inc. Mathematica, Versions 11.0.1–11.2. Champaign, IL, 2016–2017.

[67] F. Bachmann, R. Hielscher, and H. Schaeben. Texture analysis with MTEX–free and open source software toolbox. *Solid State Phenomena*, 160:63–68, 2010.

[68] MATLAB. *Version R2014b*. The MathWorks Inc., Natick, Massachusetts, 2014.

[69] BYU Microstructure of Materials. OpenXY. https://github.com/BYU-MicrostructureOfMaterials/OpenXY, August 2016.

[70] C. N. Tomé and R. A. Lebensohn. *Visco-plastic self-consistent (VPSC)*. Los Alamos National Laboratory (USA), 7c edition, 2009.

[71] R. A. Lebensohn and C. N. Tomé. A self-consistent anisotropic approach for the simulation of plastic deformation and texture development of polycrystals: application to zirconium alloys. *Acta Metallurgica et Materialia*, 41(9):2611–2624, 1993.

[72] U. F. Kocks, C. N. Tomé, and H. R. Wenk. *Texture and anisotropy: preferred orientations in polycrystals and their effect on materials properties*. Cambridge University Press, 2000.

[73] H. J. Bunge. *Texture analysis in materials science.* Butterworth's, London, 1982.

[74] S. Suwas and R. K. Ray. *Crystallographic Texture of Materials.* Springer Verlag, 2014.

[75] Rollett A. D. Typical Textures, part 2 FCC Torsion, BCC textures. http://pajarito.materials.cmu.edu/rollett/27750/L23-Metal_Textures-Torsion_BCC-part2.pdf, April 2014.

[76] S. I. Wright, M. M. Nowell, and D. P. Field. A review of strain analysis using electron backscatter diffraction. *Microscopy and Microanalysis*, 17(3):316–329, 2011.

[77] ASTM E112-13. Standard test methods for determining average grain size. Technical report, ASTM, 2013.

[78] A. J. Wilkinson. A new method for determining small misorientations from electron back scatter diffraction patterns. *Scripta Materialia*, 44(10):2379–2385, 2001.

[79] D. A. Molodov. *Microstructural design of advanced engineering materials.* John Wiley & Sons, 2013.

[80] P. J. Noell. The morphology and microstructure of dynamic abnormal grain growth in commercial-purity molybdenum. Master's thesis, The University of Texas at Austin, 2014.

[81] D. J. Dingley. High angular resolution EBSD for measurement of strain and residual dislocation density. *Analyse par diffraction des electrotrons retrodiffuses*, pages 217–276, 2015.

[82] T. Jäpel. *Feasibility study on local elastic strain measurements with an EBSD pattern cross correlation method in elastic-plastically deforming materials: Application on high manganese TWIP steels.* PhD thesis, Rheinisch -Westfälischen Technischen Hochschule Aachen, 2014.

[83] J. W. Barnes. *Statistical analysis for engineers and scientists: a computer-based approach.* McGraw-Hill, Inc., 1994.

Vita

Ryann Elizabeth Rupp graduated in 2009 as valedictorian from Ball High School in Galveston, Texas. Two high school science fair projects sparked her interest in engineering. In 2009, she began her studies in mechanical engineering at the University of Texas at Austin. She graduated in 2013 with honors, a mathematics minor, and the Business Foundations certificate. During this time, she worked as an undergraduate researcher in Dr. Paulo Ferreira and Dr. Eric Taleff's research groups. She thoroughly enjoyed research and decided to continue working in Dr. Taleff's research group as a graduate student. In 2013, Ryann started working towards her doctor in philosophy in Materials Science and Engineering.

Email address: ryannrupp@gmail.com

This dissertation was typeset with LaTeX[†] by the author.

[†]LaTeX is a document preparation system developed by Leslie Lamport as a special version of Donald Knuth's TeX Program.